A minerals research contract report
January 1981

INSTRUMENTS AND TECHNIQUES FOR DYNAMIC PARTICLE SIZE MEASUREMENT OF COAL DUST

Contract H0177026
Particle Technology Laboratory
University of Minnesota

OFR
83-173

BUREAU OF MINES ★ UNITED STATES DEPARTMENT OF THE INTERIOR
Minerals Health and Safety Technology

DISCLAIMER

The views and conclusions contained in this document are those of the authors and should not be interpreted as necessarily representing the official policies or recommendations of the Interior Department's Bureau of Mines or of the U. S. Government.

50272-101

REPORT DOCUMENTATION PAGE	1. REPORT NO.	2.	3. Recipient's Accession No.

4. Title and Subtitle
Instruments and Techniques for Dynamic Particle Size Measurement of Coal Dust

5. Report Date
January, 1981

6.

7. Author(s)
Virgil A. Marple and Kenneth L. Rubow

8. Performing Organization Rept. No.
PTL No. 434

9. Performing Organization Name and Address
University of Minnesota Particle Technology Lab
130 Mechanical Engineering
111 Church St. SE
Minneapolis, MN 55455

10. Project/Task/Work Unit No.

11. Contract(C) or Grant(G) No.
(C) DOI/BOM H0177026
(G)

12. Sponsoring Organization Name and Address
U.S. Bureau of Mines, Department of Interior
Washington, D. C. 20241

13. Type of Report & Period Covered
Final 12/1/76 to 11/30/80

14.

15. Supplementary Notes

16. Abstract (Limit: 200 words)
It was the purpose of this contract to conduct research in several different areas of instrumentation used to determine the quantity of respirable dust in the mining atmosphere. One area of research was in evaluation of instruments including several respirable dust monitors, several types of photometers, and a QCM cascade impactor. An instrument evaluation chamber was developed to aid in evaluating the instruments in a dust atmosphere. Another area of research was investigations into new instrumentation concepts, such as a virtual impactor/photometer instrument, a new optical device which can be used as either an optical particle counter or photometer, a new personal respirable sampler, which employs an impactor instead of a cyclone as a preclassifier, and the development of a new cascade impactor, which deposits the particles uniformly on the impaction plate. Another area of research included the use of many of these instruments in two field studies, including a silica sand plant and a tungsten mine.

17. Document Analysis a. Descriptors
Dust, particle, instrumentation, coal

b. Identifiers/Open-Ended Terms
mine dust instrumentation

c. COSATI Field/Group 08/I

18. Availability Statement	19. Security Class (This Report)	21. No. of Pages
Release Unlimited	unclassified	240
	20. Security Class (This Page) unclassified	22. Price

(See ANSI-Z39.18) See Instructions on Reverse

OPTIONAL FORM 272 (4-77)
(Formerly NTIS-35)
Department of Commerce

83

FOREWORD

This report was prepared by the University of Minnesota, Department of Mechanical Engineering, Minneapolis, Minnesota, under U. S. Bureau of Mines Contract No. H0177026. The contract was initiated under the Coal Mine Health and Safety Program. It was administered under the technical direction of Twin Cities Mining Research Center with Mr. H., W. Zeller acting as the Technical Project Officer. Mr. J. A. Herickes was the Contract Administrator for the Bureau of Mines.

This report is a summary of the work recently completed as part of this contract during the period December 1, 1976 to November 30, 1980. This report was submitted by the authors in January, 1981.

Reference to specific brands, equipment, or trade names in this report is to facilitate understanding and does not imply endorsement by the Bureau of Mines.

TABLE OF CONTENTS

		Page No.
CHAPTER 1	Executive Summary	14
	1.1 Background	14
	1.2 Purpose and Scope of the Contract	14
	1.3 Results	14
	1.4 Recommendation for Future Work	15
CHAPTER 2	Dichotomous Impactor/Photometer Aerosol Analyzing System	16
	2.1 Introduction	16
	2.2 Theoretical Studies	16
	2.3 Experimental Studies	18
CHAPTER 3	Laser Diode Optical Particle Counter	21
	3.1 Introduction	21
	3.2 The Instrument	21
	3.3 Calibration	24
	3.4 Current Status	26
CHAPTER 4	Instrument Evaluation Chamber	28
	4.1 Introduction	28
	4.2 Aerosol Chamber	28
	4.3 Concentration Reducer	31
	4.4 Monodisperse Aerosol Classifier	32
	4.5 Chamber Evaluation	36
CHAPTER 5	Instrument Evaluations and Calibrations	40
	5.1 Introduction	40
	5.2 SRI Portable Mine Dust Concentration Instrument	40
	5.3 Photometer Evaluation and Calibration	40
	5.4 GCA RDM-1 Calibration	59
	5.5 TSI Model 3500 Respirable Aerosol Mass Monitor Calibration	62
	5.6 Evaluation of Berkeley Controls QCM Cascade Impactor	71
CHAPTER 6	Personal Respirable Impactor	86
	6.1 Introduction	86
	6.2 MESA Disposable Respirable Impactor	86
	6.3 University of Minnesota Personal Respirable Impactor	86
CHAPTER 7	Uniform Deposition Impactor	88
	7.1 Introduction	88
	7.2 Impactor Design	88
	7.3 Current Status	89

Page No.

CHAPTER 8 General Impactor Calibration, Calculations, and Development....90
8.1 Introduction....90
8.2 Calibration of Berkeley Controls QCM Cascade Impactor....90
8.3 Further Investigations of Inertial Impactors....90

CHAPTER 9 Field Studies....94
9.1 Objectives and Instrumentation....94
9.2 Instrument Calibration....94
9.3 Silica Sand Plant....95
9.4 Tungsten Mine....98

References....106

APPENDIX A A Theoretical Study of Virtual Impactors....108

APPENDIX B Optical Particle Counter/Photometer Design Report....141

APPENDIX C Evaluation of SRI Portable Mine Dust Concentration Instrument....181

APPENDIX D Evaluation of MESA Disposable Respirable Impactor....203

APPENDIX E Impactors with Respirable Penetration Characteristics: Personal Sampler Size....210

APPENDIX F A Uniform Deposit Impactor....231

LIST OF FIGURES

Page No.

1. Schematic diagram of dichotomous impactor/photometer setup.....17

2. SRI portable coal dust concentration instrument response to small particle aerosol stream (<3.5 μm diameter) of dichotomous impactor.....19

3. SRI portable coal dust concentration instrument response to large particle aerosol stream (>3.5 μm diameter) of dichotomous impactor.....20

4. Laser diode optical particle counter/photometer and multichannel analyzer.....22

5. Laser diode optical particle counter/photometer.....22

6. Schematic diagram of optical system and light beam path.....23

7. Laser diode optical particle counter ideal particle calibration curve.....25

8. Laser diode optical particle counter coal calibration curve.....27

9. Schematic diagram of aerosol chamber.....29

10. Aerosol chamber.....30

11. Schematic diagram of concentration reducer.....33

12. Schematic diagram of monodisperse aerosol classifier.....34

13. Monodisperse aerosol classifier particle collection efficiency and penetration curves.....35

14. Strip chart records from photometer showing stability of aerosol concentration in aerosol chamber as a function of time.....39

15. ACGIH, BMRC and TBF 50-II respirable penetration curves.....42

16. Size distributions of test dusts in aerosol chamber.....44

17. Calculated respirable size distributions of test dusts in aerosol chamber based on ACGIH criteria.....45

18. Calibration curves for GCA RAM-1 serial number 1012B. (Data presented in Table 3.).....49

19. Calibration curves for GCA RAM-1 serial number 1018B. (Data presented in Table 3.).....50

Page No.

20. Calibration curves for GCA RAM-1 serial number 1097. (Data presented in Table 3.).....51

21. Calibration curves for GCA RAM-1 serial number 1098. (Data presented in Table 3.).....52

22. Calibration curves for SIMSLIN II serial number 126. (Data presented in Table 3.).....53

23. Calibration curves for SIMSLIN II serial number 133. (Data presented in Table 3.).....54

24. Calibration curves for Leitz Tyndallometer TM Digital serial number 575. (Data presented in Table 3.).....55

25. Calibration curves for Leitz Tyndallometer TM Digital serial number 586. (Data presented in Table 3.).....56

26. Calibration curves for TSI Model 5150 respirable aerosol photometer serial number 98343. (Data presented in Table 3.).....57

27. Response comparison between 2 GCA RAM-1 photometers.....60

28. Response comparison between 2 Leitz Tyndallometer TM Digital photometers.....61

29. Calibration curve for GCA RDM 101-1 serial number 2046.....66

30. Calibration curve for GCA RDM 101-1 serial number 2060.....66

31. Calibration curve for GCA RDM 101-1 serial number 2319.....67

32. Calibration curve for GCA RDM 101-1 serial number 2320.....67

33. Calibration curve for GCA RDM 101-1 serial number 2334.....68

34. Calibration curve for GCA RDM 101-1 serial number 2371.....68

35. Calibration curve for GCA RDM 101-1 serial number 2372.....69

36. Calibration curves for GCA RDM 101-1 serial number 2154. (Data presented in Table 3.).....70

37. Calibration curves for TSI Model 3500 serial number 104. (Data presented in Table 3.).....72

38. Calibration curves for TSI Model 3500 serial number 79485. (Data presented in Table 3.).....73

39. Schematic diagram of test setup used for Berkeley Controls QCM calibration with submicron particles.....75

Page No.

40. Berkeley Controls QCM particle collection characteristics of each stage....76

41. Berkeley Controls QCM particle loss per stage....79

42. Particle loss curve for the Berkeley Controls QCM cascade impactor....80

43. Relative response of Berkeley Controls QCM as a function of accumulative frequency shift for Arizona road dust loading on each stage....83

44. Relative response of Berkeley Controls QCM as a function of accumulative frequency shift for coal dust loading on each stage....84

45. Theoretically predicted impactor particle collection efficiency curves based on point-mass and interception methods....91

46. Effect of particle density on theoretically predicted impactor particle collection efficiency curves based on interception method....93

47. Laser diode optical particle counter coal calibration curve and estimated calibration curve for silica and Arizona road dust....96

48. Aerosol size distribution for silica bagging operation measured with laser diode OPC....99

49. Schematic diagram of tungsten mine layout....100

50. Aerosol size distribution at sampling site B in tungsten mine measured with Sierra Model 266 cascade impactor....105

APPENDIX A

1. Nomenclature, streamlines, particle trajectories and efficiency curves for a virtual impactor....111

2. Grid and flow field for virtual impactor at base case conditions....113

3. Particle trajectories at base conditions....116

4. Collection efficiency and loss curves for base conditions....118

5. Comparison of theoretical and experimental large particle collection efficiency curves at the following conditions:.... 120

6. Theoretical streamlines at the specified values of Re.... 121

Page No.

7. Influence of the Reynolds number on the axial velocity profile at the nozzle exit.....122

8. Large particle collection efficiency and collection probe loss curves at the specified values of Re.....123

9. Theoretical streamlines at the specified values of Q_1/Q_0.....125

10. Large particle collection efficiency and collection probe loss curves at the specified values of Q_1/Q_0.....126

11. Theoretical streamlines at the specified values of D_1/D_0.....127

12. Large particle collection efficiency and collection probe loss curves at the specific values of D_1/D_0.....128

13. Theoretical streamlines at the specified values of L_0/D_0.....130

14. Large particle collection efficiency and collection probe loss curves at the specific values of L_0/D_0.....131

15. Theoretical streamlines at the specified values of S/D_0.....132

16. Large particle collection efficiency and collection probe loss curves at the specific values of S/D_0.....133

17. Large particle collection efficiency and collection probe loss curves at the specified values of Θ_0.....134

18. Theoretical streamlines for various collection probe designs.....135

19. Large particle collection efficiency and collection probe loss curves for various collection probe designs.....137

APPENDIX B

1. Laser power output as a function of input current and diode temperature.....144

2. Input current of the laser diode as a function of voltage drop and diode temperature.....145

3. Diode current as function of temperature for a given output power...146

4. Thermistor component network for laser diode and network resistance as a function of diode temperature.....147

5. Schematic of laser diode intensity control circuit.....148

6. Laser diode cross section showing the location of the laser pellet.....150

Page No.

7. Calculated laser beam shape in the vicinity of the view volume.....152

8. Ideal intensity profile of laser beam at view volume.....154

9. Waist of laser beam at the view volume.....155

10. Schematic of microscope knife edge scanner.....156

11. Beam power profile in waist region along particle flow direction.....157

12. Beam power profile in waist region mutually perpendicular to the particle flow direction and laser beam axis.....157

13. Schematic of optical system and light path.....159

14. Schematic of laser light projector cell.....160

15. Schematic of modified Royco 218 inlet.....161

16. Removable inlet design.....163

17. Air flow system.....165

18. Clean rod mechanism.....166

19. Inlet and receiver optic block design.....167

20. Schematic cross section of assembled optical head.....169

21. Normalized accumulative light scattering curves for coal dust.....170

22. Laser diode optical particle counter ideal particle calibration curve.....172

23. Laser diode optical particle counter coal calibration curve.....174

24. Circuit diagram for photo cell and preamp.....175

25. Output pulse shaping circuit diagram.....178

APPENDIX C

1. Schematic of SRI portable coal dust concentration instrument (from Reference 1).....183

2. Particle size distribution of test dust aerosols.....185

3. Test set-up for calibrating the SRI instrument with an impactor removing large particles.....187

Page No.

4. Test set-up for demonstrating use of SRI instrument with a dichotomous impactor.....188

5. Calibration curve of SRI portable mine dust concentration instrument on coal dust.....190

6. SRI portable coal dust concentration instrument response on coal dust, with large particles removed by an impactor.....191

7. SRI portable coal dust concentration instrument response on silica dust, with large particles being removed by an impactor.....192

8. Dependency of SRI instrument response to flow rate due to leakage in the instrument.....196

9. SRI instrument response to small particle air stream (<3.5 μm diameter) of dichotomous impactor (13.7 lpm flow rate).....198

10. SRI instrument response to large particle air stream (<3.5 μm diameter) of dichotomous impactor (0.28 lpm flow rate).....199

11. Response for an instrument similar to the SRI portable coal dust concentration instrument.....200

12. Schematic of optical system of SRI instrument.....200

APPENDIX D

1. Schematic of the MESA Plastic Disposable Respirable Impactor (from Ref. 1).....205

2. Theoretical and experimental collection efficiency curves for MESA Plastic Disposable Impactor.....207

3. Comparison of penetration curves of the MESA Plastic Disposable Impactor with AEC and BMRC Respirable curves.....208

APPENDIX E

1. BMRC, AEC and ACGIH respirable penetration curves.....213

2. Approximation of a respirable curve by a single-stage impactor with three nozzle sizes.....215

3. Cross-sectional view of a personal sampler.....219

4. Respirable personal sampler.....220

5. Comparison of experimental data and the theoretical penetration curves to the AEC respirable curve for the two nozzle size impactor.....221

Page No.

6. Comparison of experimental data and the theoretical penetration curve to the AEC respirable curve for the three nozzle size impactor.....222

7. Comparison of experimental data and the theoretical penetration curve to the BMRC respirable curve for the three nozzle size impactor.....223

8. Penetration of particles through the impactor with an oil impregnated porous impaction plate as a function of time.....225

9. Deposits on the oil impregnated porous impaction plate after sampling a coal dust aerosol (9 mg/m^3) for 1.0, 2.0 and 6.5 hours...226

1A. ACGIH respirable penetration curve and modified ACGIH curve.....229

APPENDIX F

1. Annular rings of equal area.....234

2. Photograph of a 200 hole uniform deposit impactor nozzle plate.....235

3. Design schematic of the uniform deposit impactor.....239

LIST OF TABLES

Page No.

1. Gravimetrically Determined Mass Concentration as a Function of Filter Location Within Chamber.....37

2. Sierra Model 266 Cascade Impactor Stage Cutoff Diameters.....43

3. Respirable Mass Instrument Calibration Data.....48

4. Regression Coefficients for Photometer Response Calibration Curves.....58

5. Relative Photometer Response as Function of Aerosol.....58

6. Standard Filter Sampler Evaluation.....63

7. GCA RDM 101-1 Calibration for Respirable Arizona Road Dust.....64

8. GCA RDM 101-1 Calibration Data for Respirable Coal Dust.....65

9. Berkeley Controls QCM Calibration Summary.....74

10. Berkeley Controls QCM Cutoffs for Each Stage.....77

11. Comparison Between QCM and Gravimetrically Determined Mass Concentration.....82

12. Comparison Between QCM and Electrically Determined Liquid Aerosol Mass Concentration.....82

13. Activity and Average Respirable Aerosol Mass Concentration for Silica Sand Plant Bagging Operation.....97

14. Aerosol Mass Concentration as a Function of Source and/or Location and Time of Day in Tungsten Mine.....102

15. Log for Cascade Impactor Operation.....103

APPENDIX A

1. Values of Design Parameters Used in This Study.....115

A-I Values of St for the Large Particle Collection Efficiency Curves...139

A-II Values of St for the Small Particle Collection Efficiency Curves...140

APPENDIX C

1. Impactor Cut-Off Sizes (2 lpm).....186

2. Sensitivity of SRI Portable Coal Dust Concentration Instrument in Different Size Ranges.....193

Page No.

3. Comparison Between SRI Instrument Ranges.....195

APPENDIX E

1. Impactor Designs With Penetration Characteristics at 2 l/min Flow Rates Which Simulate the AEC (or ACGIH) Respirable Penetration Curve.....216

2. Impactor Designs With Penetration Characteristics at 2 l/min Flow Rate Which Simulates the BMRC Respirable Penetration Curve.....217

1-A Impactor Designs With Penetration Characteristics at 2 l/min Flow Rates Which Simulate the Modified ACGIH Respirable Penetration Curve.....230

APPENDIX F

1. Example of Uniform Deposit Impactor Nozzle Placement.....236

CHAPTER I
EXECUTIVE SUMMARY

1.1 Background

One of the concerns in the mining industry is the quantity of respirable dust to which coal miners are exposed. It is important that the dust concentrations in the coal mine be kept low enough to ensure a safe working atmosphere and yet not so low as to make the mining of coal unreasonably expensive.

Before any standards can be enforced, it is necessary that instruments be available to measure the dust concentrations within the mining atmosphere. Furthermore, it is important that the instruments be properly calibrated and their response characteristics understood.

1.2 Purpose and Scope of the Contract

It was the purpose of this contract to conduct research in several areas of instrumentation used to determine the quantity of respirable dust in the mining atmosphere. The contract was divided into tasks which are described in the various chapters of this report as follows:

Chapter 2 - A feasibility study of using a dichotomous impactor in conjunction with two photometers for a machine mounted dust monitor.
Chapter 3 - The development of a laser diode optical particle counter.
Chapter 4 - The development of an instrument evaluation chamber.
Chapter 5 - Instrument evaluations and calibrations.
Chapter 6 - The development of a new personal respirable dust sampler.
Chapter 7 - The development of a uniform deposit cascade impactor.
Chapter 8 - Inertial impactor calibrations and theoretical investigations.
Chapter 9 - Description of field studies.

1.3 Results

There have been many significant results from this contract. In Chapters 2 and 3, two of the most important results were the theoretical evaluation of dichotomous impaction devices and the development of an optical device which can be used either as an optical particle counter to obtain particle size distributions or a photometer to obtain the mass concentration.

The primary result of the work described in Chapter 4 has been the development of an evaluation chamber. This chamber provides a means by which many instruments can be exposed to a uniform dust concentration over long periods of time.

Photometers, mass monitors and cascade impactors were evaluated and calibrated as reported in Chapter 5. It was found that the instruments measured aerosol mass concentration with varying degrees of accuracy and detailed evaluations are necessary to thoroughly understand the operating characteristics of such instruments.

The results in Chapter 6 have been both an evaluation of the previously developed MESA personal respirable impactor and the development of a new personal respirable impactor which can approximate any respirable curve at any flow rate. Both devices use impactors instead of a cyclone as a preclassifier to remove the large nonrespirable particles.

In Chapter 7 the results are again the development of a new device; a uniform deposit impactor. This impactor collects the particles over the entire surface of the impaction plate rather than at discrete points. Some of the advantages of this impactor are its ease of operation, a low tareweight compared to the mass collected upon the impaction plate, and the substrates can be used in x-ray fluorescence analysis.

In Chapter 8 the results of the QCM cascade impactor evaluation are discussed and as a result of this evaluation several impaction characteristic phenomena were observed. A theoretical investigation into this phenomena has increased the understanding of the impaction process. For example, it was found that the efficiency curve of the cascade impactor is an "S" shaped curve which has been demonstrated experimentally and now is shown from theory. It has also been proven that there are real discrepancies between theoretical and experimental efficiency curves for large particle collection and low Reynolds numbers.

Chapter 9 discusses the results of dust measurement in a silica sand plant and a tungsten mine. Dust size distributions and concentration from various operations in these facilities are presented.

1.4 Recommendations for Future Work

Much of the effort in this contract has been in the development and characterization of the instrument evaluation chamber. Although evaluation of photometers was the initial application of the chamber, many more experiments can be performed. These experiments will be primarily in the area of detailed evaluation of instruments used in measuring mine dust size distributions and concentrations and in special studies such as inlet sampling efficiencies.

Now that the chamber has been constructed, further areas of investigation should include developing procedures and methods which can be used as standards. For example, the particle size distribution and concentration of the dust can be measured and the correct respirable efficiency curve applied to the data, or the classification device can be one with the same penetration characteristics as that of a particular respirable curve and the penetrating dust measured gravimetrically to determine the concentration.

Another area of future work should be in the further understanding of impaction devices. As pointed out in this report, there have been areas of impactor operation where the experimental and theoretical efficiency curves do not agree. Since the theoretical efficiency curves have been determined from basic laws of fluid mechanics and particle motion within a fluid, there is seemingly no reason for these differences. However, such secondary effects as electrostatic forces, turbulence, gravity, and the motion of particles in a shear flow have not been thoroughly investigated and may be significant in some cases. Since impaction devices are some of the most basic instruments used in aerosol studies, a complete understanding of their characteristics is imperative.

CHAPTER 2
DICHOTOMOUS IMPACTOR/PHOTOMETER AEROSOL ANALYZING SYSTEM

2.1 Introduction

One of the techniques investigated for a machine mounted dust monitor was the feasibility of utilizing two photometers monitoring the two air streams from a dichotomous impactor. The reason for using two photometers instead of one is that the output of a photometer has been shown to be sensitive to the size distribution of the aerosol as described in the SRI photometer evaluation section of the report (Section 5.2). To reduce this sensitivity, the particles can be classified into various size ranges with each range monitored by a photometer. In this manner, the sensitivity of the photometers to the particle size distribution is not a significant source of error, if the size range of the particle is not too large. For this technique to be feasible, however, the particles in the different size ranges must remain airborne to pass through the photometer. Thus, it is not possible to use size classification devices such as cascade impactors or cyclones. Instead a dichotomous impactor, which classifies particles in a manner similar to a real impactor but with the particles remaining airborne, must be used.

A schematic diagram of a dichotomous impactor/photometer system is shown in Figure 1. As indicated in the figure, the dust particles pass through the nozzle of the dichotomous impactor and impinge into a collection probe through which a small fraction of the air is being passed. The large particles, which have high inertia, cross the streamlines and enter the collection probe, while the small particles with low inertia remain in the airstream and pass out through the side of the dichotomous impactor. Each of these aerosol streams then passes through a photometer.

2.2 Theoretical Studies

The dichotomous (virtual) impactor has been studied quite extensively experimentally by other investigators (1) but the effect of the various parameters, such as the distance from the nozzle to the jet, the fraction of the flow passing through the central probe, and other geometric variables, on the classification characteristics of the dichotomous impactor has not been known. Thus, a theoretical technique which has been used by our laboratory in other studies was employed to thoroughly theoretically study the dichotomous impactor. In this technique the full Navier-Stokes equations which govern the flow within the impactor and the continuity equation are solved by a finite difference technique over a grid of node points covering the area of interest to determine the flow field. Particles are then placed into the flow field and their trajectories through the dichotomous impactor theoretically traced. From this information it is possible to determine the classification characteristics for any given set of conditions.

The details of this analysis can be found in references 2 through 4. Further details and results of this particular study are presented in Appendix A. As shown in Appendix A, it was found that the theoretical calculations agreed well with the experimental work of other investigators. Also, since the entire study was performed with dimensionless parameters such as the Reynolds number, Stokes number, etc., it should be possible to scale a virtual

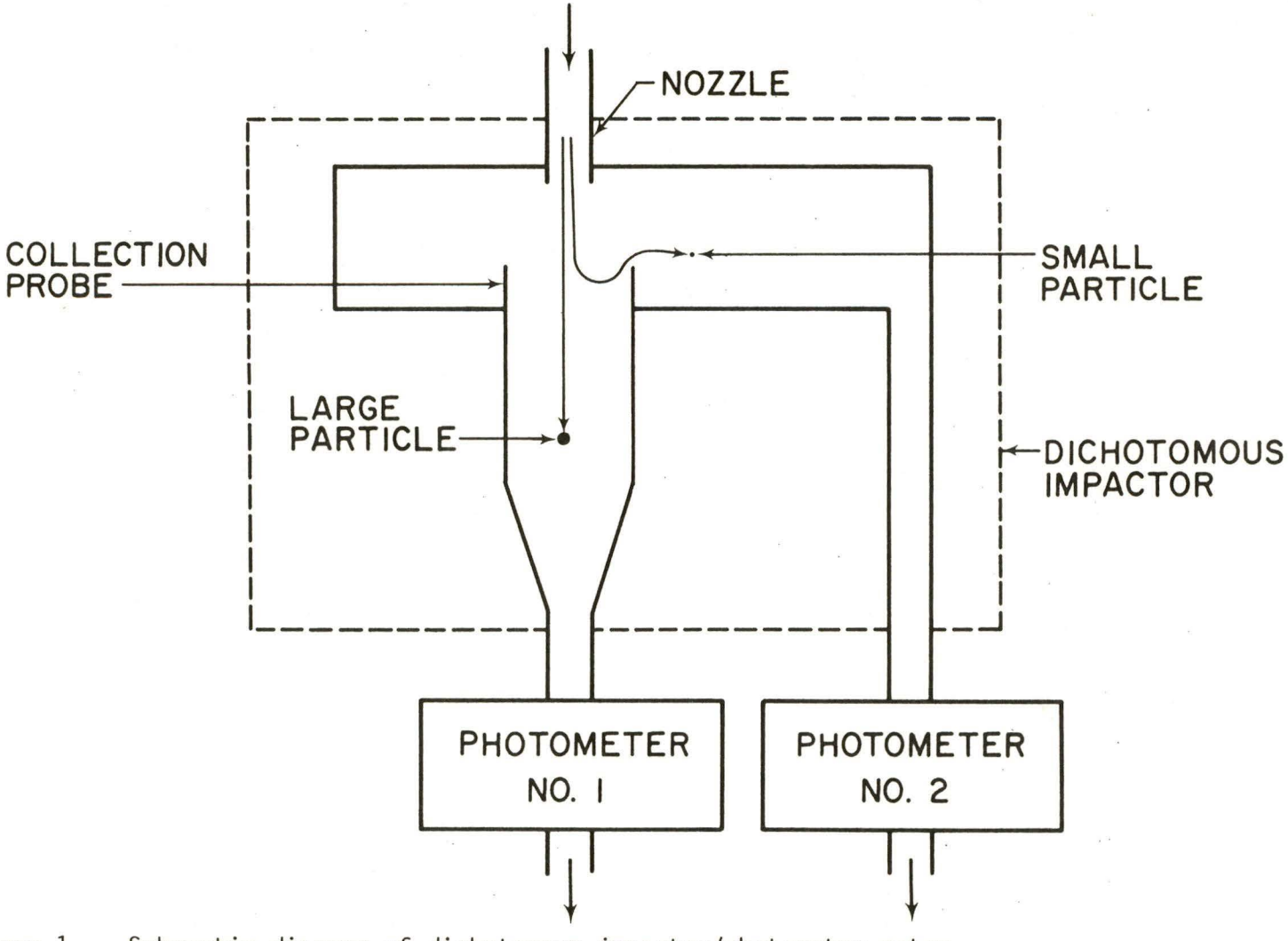

Figure 1. Schematic diagram of dichotomous impactor/photometer setup.

impactor to separate particles at nearly any size. However, this must be verified experimentally.

2.3 Experimental Studies

To demonstrate the feasibility of this technique, a commercial dichotomous (virtual) impactor was used to classify coal dust generated in a fluidized bed type of dust generator. At the time of the study the only photometer available in our laboratory was a unit built by Stanford Research Institute (SRI), which has been evaluated and described in Section 5.2. Since only one photometer was available, the concept was checked by first using the photometer on one air stream of the dichotomous impactor and then the other. Results of these tests are shown in Figures 2 and 3. In Figure 2, the SRI photometer output on range zero is compared to the gravimetrically determined concentration of the particles less than 3.5 μm (the cut size of the dichotmous impactor). The gravimetric samples were obtained by replacing the photometer with a filter to obtain a sample. In Figure 3, the SRI photometer output on range 1 is compared with the gravimetrically determined concentration of particles greater than 3.5 μm in the same manner. Again, gravimetrically determined concentrations were used as standards. It can be seen in these figures that the output is linear for both of the aerosol streams. The reason for the high mass concentration of particles larger than 3.5 μm is due to the dichotomous impactor acting as a concentrator for the large particle aerosol stream. Thus, the concentration of the large particles in this aerosol stream is much greater than the concentration of large particles in the aerosol stream entering the dichotomous impactor.

Since the theoretical studies indicate that the dichotomous impactor is an acceptable method for the classification of aerosols into two distinct sizes while keeping the particles airborne, and the experimental studies showed that results can be obtained from this combination of instruments, the concept is feasible. In addition, dichotomous impactors and photometers are both commerically available. However, since the system requires a dichotomous sampler plus two photometers, it was determined that the system would be expensive. In addition, the system would be rather large, unless a miniature photometer was developed. Therefore, even though the system has been shown to be feasible, it was felt that the primary effort should be concentrated on the development of the laser diode opticle particle counter (OPC) which was the other device considered in our studies for a machine mounted dust monitor. It was felt that the OPC device would provide more information on the size distribution, be smaller in size, and less expensive, than the dichotomous impactor/photometer system.

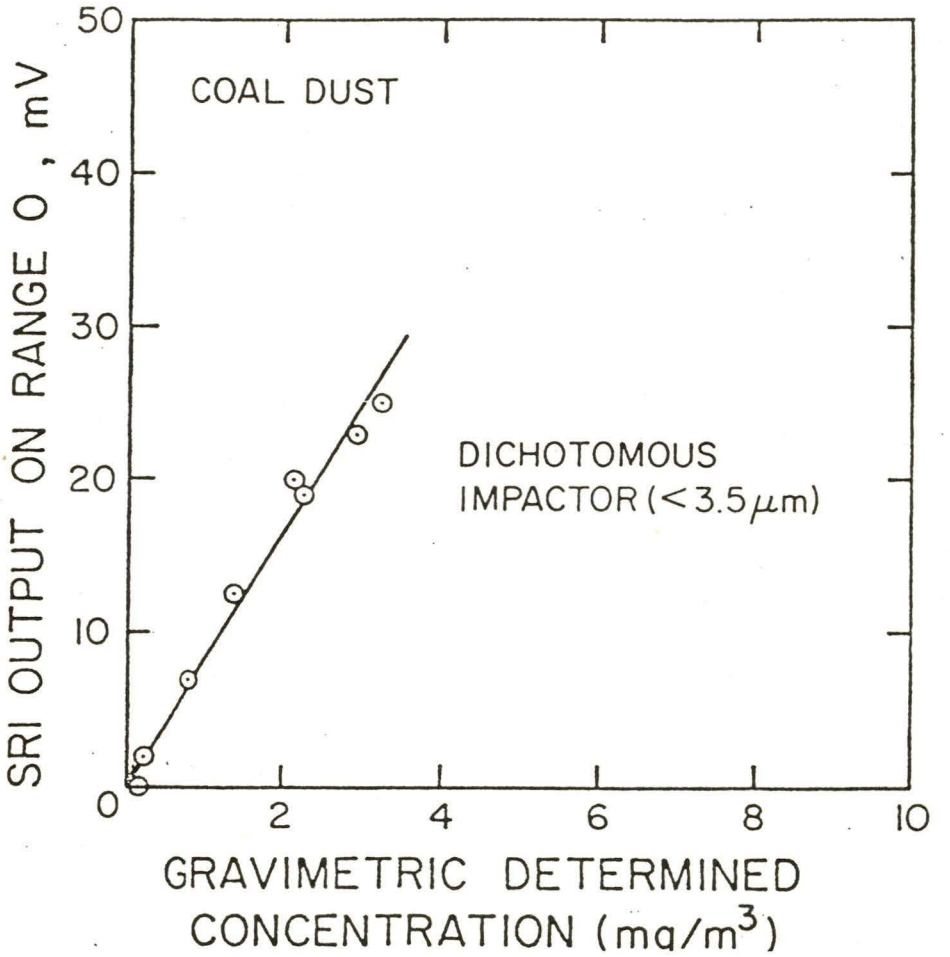

Figure 2. SRI portable coal dust concentration instrument response to small particle aerosol stream (<3.5 μm diameter) of dichotomous impactor.

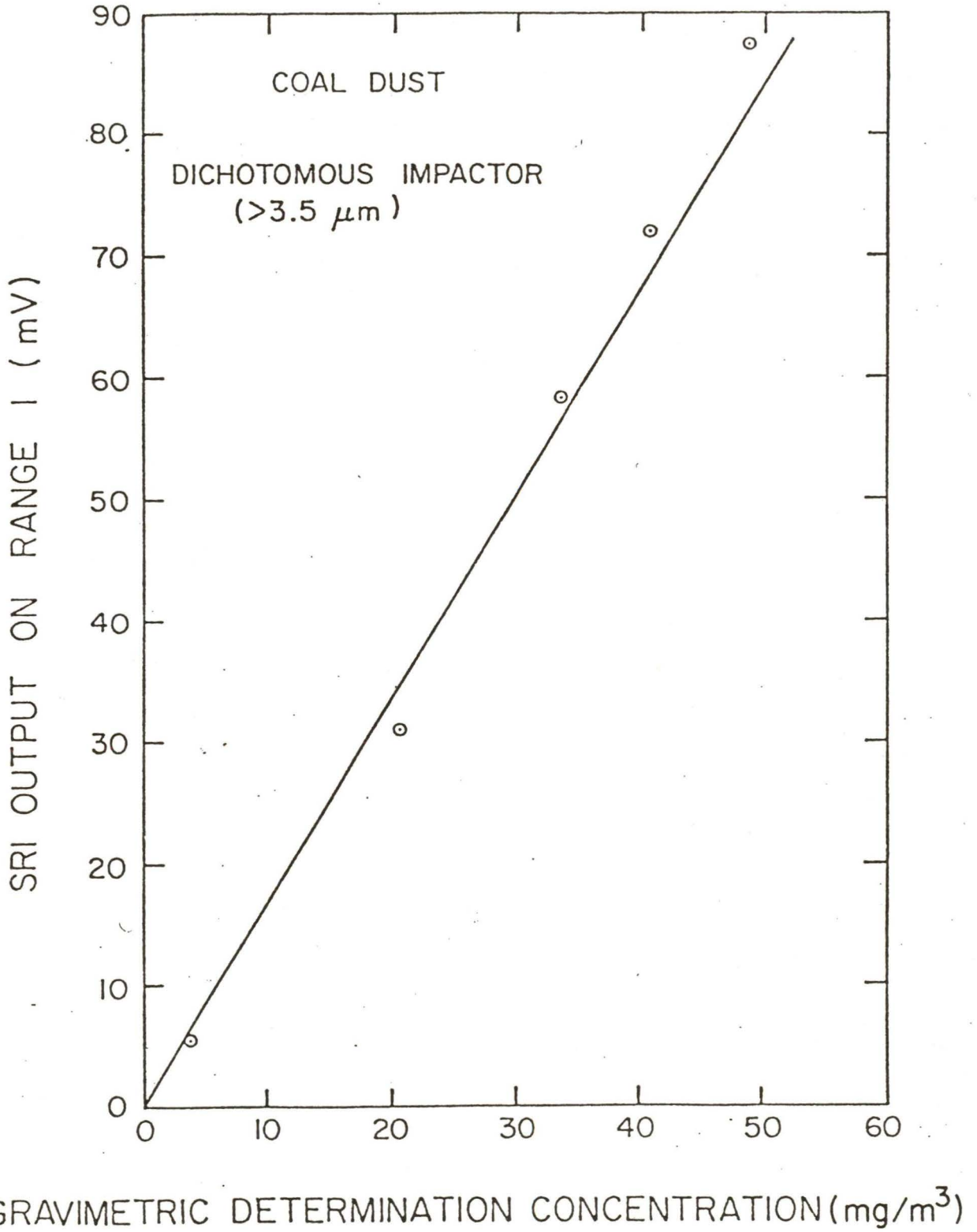

Figure 3. SRI portable coal dust concentration instrument response to large particle aerosol stream (>3.5 μm diameter) of dichotomous impactor.

CHAPTER 3
LASER DIODE OPTICAL PARTICLE COUNTER

3.1 Introduction

Previously, our laboratory developed two optical particle counter (OPC) systems for the Bureau of Mines for the purpose of measuring the size distribution of coal dust aerosols. The first of these systems was a Bausch and Lomb OPC with a Hewlett Packard multichannel analyzer (5). This system was used to measure a size distribution of dust particles generated during laboratory cutting processes. The second system utilized a portable Royco 218 OPC, which was modified for use in mines (6), and an 8 channel analyzer developed in our laboratory (7). Both of these components were powered by a single battery pack. The latter system was portable and could be used in field studies.

One concern with the Royco 218 OPC system was the use of an incandescent light bulb as the light source. It was felt that it was possible for this bulb to break and be an ignition source for an explosion, making it difficult for the OPC to be intrinsically safe for coal mine use. Thus, for the OPC described in this chapter, the incandescent light bulb was replaced by a laser diode light source and the size of the system was reduced so that it could be more easily used in field studies or possibly as a machine mounted dust monitor. In addition, the use of a laser diode, which requires little power, rather than an incandescent light source allowed for a smaller battery pack.

Finally, a technique was devised so that the individual pulses from the single particle pulses could be continuously conditioned and summed to provide an output proportional to the volume or mass of particles passing through the OPC. In this manner, the optical device also serves as a photometer with an output completely independent of the size distribution of the particles passing through it. This feature is in contrast to most conventional photometers which have outputs somewhat dependent on the dust size distribution (see Chapter 5).

3.2 The Instrument

The laser diode optical particle counter is shown in Figures 4 and 5. The instrument is contained in a Zero Model ZIP-810 instrument case (Zero Corp., Burbank, CA) and weighs 6.6 kg including the pump. The case dimensions are 28 by 18 by 25 cm. Aerosol is drawn through the OPC by a personal sampler pump which is attached to the cover of the instrument. Currently a Bendix Micronair II permissible air sampling pump (Bendix Environmental Process Instruments Div., Lewisburg Plant, Lewisburg, WV 24901) is used but any pump can be employed. The instrument as shown only contains the electronics to operate as a photometer. However, if data from the single optical particle counting circuit is to be used in determining the size distribution, the 8 channel analyzer, also shown in Figure 4, must be added to the system. A description of the design and use of the MCA is given in a previous Bureau of Mines final report (7). The analyzer can be operated on batteries in the same manner as with the Royco 218 OPC system.

The details of the optical particle counter design and operation specifications are presented in Appendix B. A schematic diagram of the optics is shown in Figure 6. The light from the laser diode is focused to form a light beam with a slit cross-sectional shape at the viewing volume by passing the light

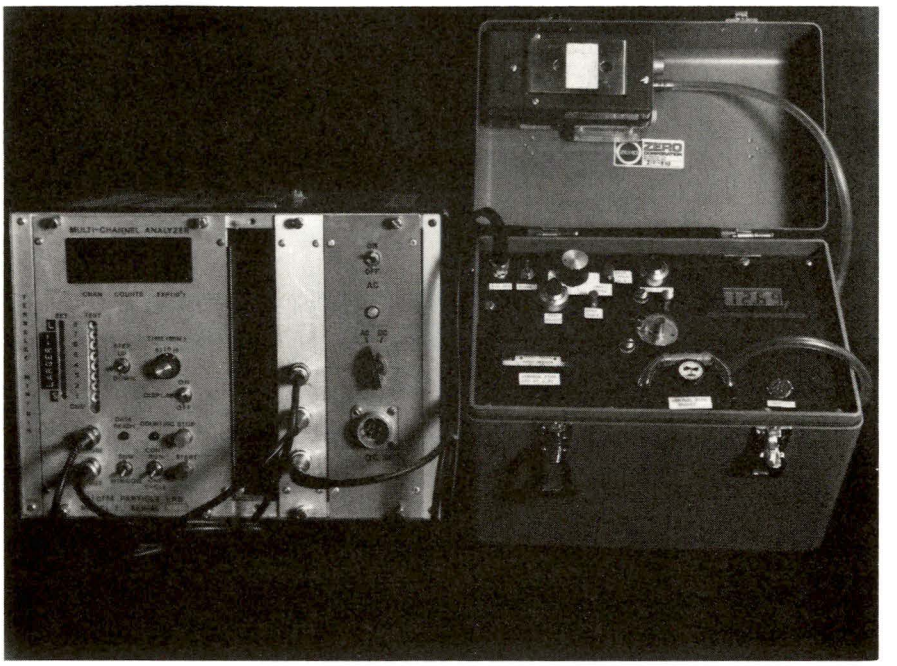

Figure 4. Laser diode optical particle counter/photometer and multichannel analyzer.

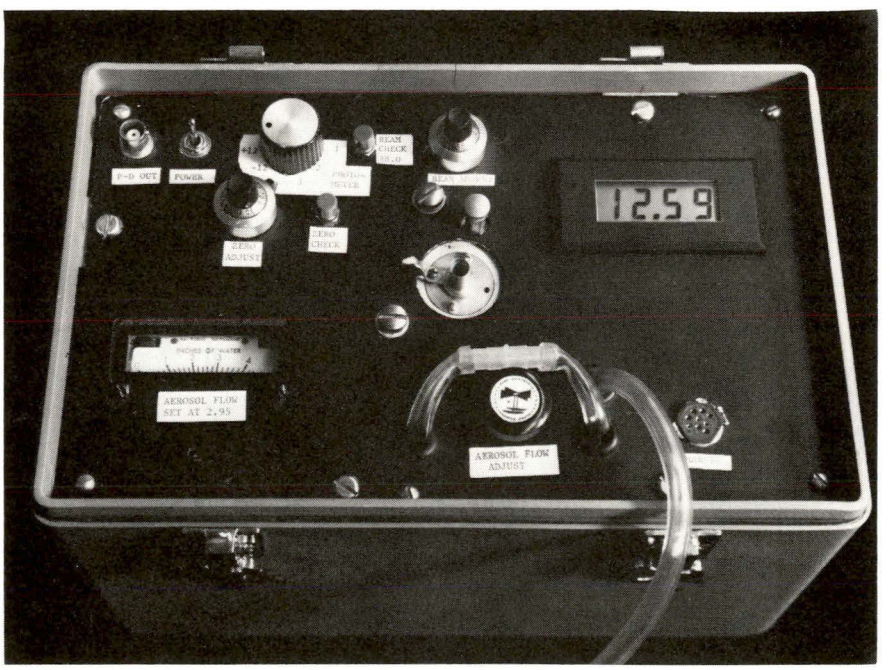

Figure 5. Laser diode optical particle counter/photometer.

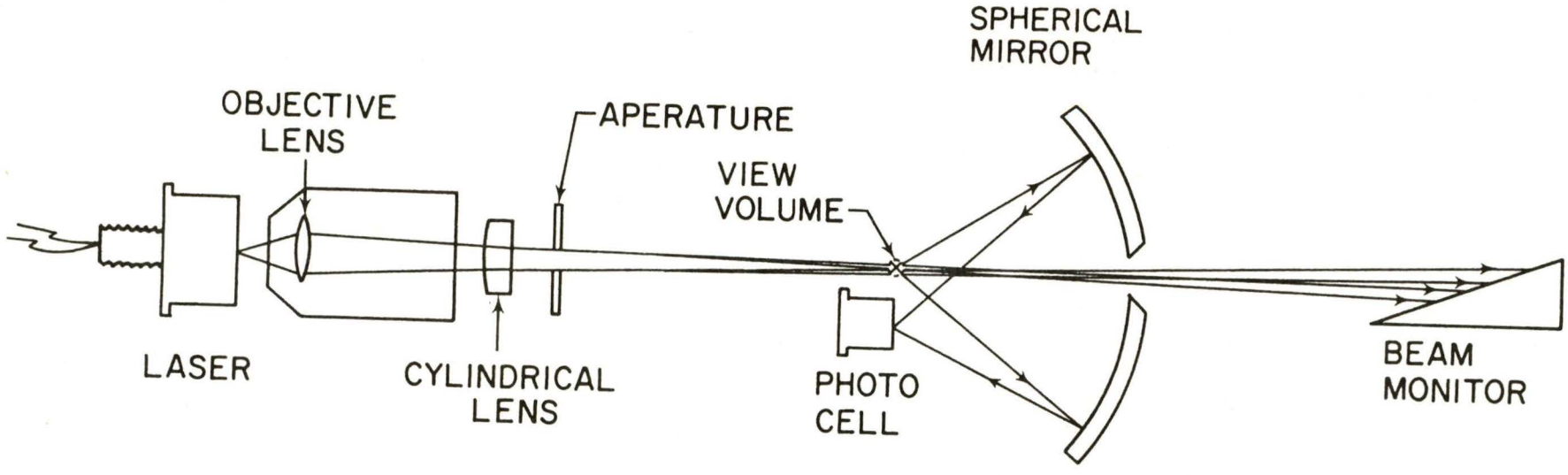

Figure 6. Schematic diagram of optical system and light beam path.

through a cylindrical lens. The particle scattered light for a scattering half-angle of 6° to approximately 33° is reflected from a mirror and focused onto a photosensor which is located near the view volume. The light passing into the light trap from the main beam is monitored by another photosensor which allows the operator to regulate the power to the light source to provide a constant intensity light beam.

The particles passing through the optics are surrounded by a sheath of clean air. This is accomplished by use of an inlet which divides the airstream into two parts, cleaning one part and reintroducing it as a sheath of clean air around the particles. In this manner recirculated air does not contaminate the optics with particles. For an inlet flowrate of 2.0 lpm, the sheath air flowrate is 1.8 lpm, or 90% of the total flowrate. Provisions have also been made for a dryer to be inserted in the sheath air line to remove excess humidity.

Experience has shown that an inlet of this type can become partially clogged with large particles, such as lint, in the sampled aerosol. Thus, the OPC is equipped with a means for cleaning the aerosol sampling tube. This cleaning mechanism is a wire located below the view volume which passes through the sampling tube and dislodges any particles collected within or on top of it as a shaft is pulled upward.

Figure 5 shows the front panel of the OPC. On this panel are located the aerosol sample inlet, panel meters, and controls for the electronics, flow and inlet cleaning rod. The controls include the instrument on/off switch (labeled "POWER"), instrument "ZERO ADJUST" and "BEAM ADJUST" potentiometers which control the electronic circuitry reference zero and laser diode output beam intensity level. The zero and laser beam voltage levels are displayed on the panel voltmeter (which is located in the upper right corner) by pushing the "ZERO CHECK" or "BEAM CHECK" switch. The 3 battery voltage levels and photometer output in one of three concentration ranges are displayed on the voltmeter when the rotary switch is set in the "+12", "-12", "-9", or "PHOTOMETER 1, 2, 3" positions, respectively. The control valve labeled "AEROSOL FLOW ADJUST" regulates the flow split between the aerosol sample and the sheath air flowrates. The pressure gage labeled "AEROSOL FLOW" monitors the pressure at the exit of the aerosol view volume. A pressure of 2.95 inches of water at a total inlet sample flow rate of 2.0 lpm corresponds to an aerosol sample flow rate of 0.2 lpm. The tubing union allows for the insertion of a silica gel dryer in the sheath air line. The cable connection labeled "P-D OUT" and "CHARGE" are for the signal cable to the MCA and the battery charger cable, respectively.

3.3 Calibration

The laser diode OPC was calibrated on both ideal aerosols and dust aerosols. The ideal aerosol calibration was obtained using oleic acid and PSL particles. The oleic acid particles were generated with a vibrating orifice monodisperse aerosol generator (8) and the PSL particles were generated by aerosolizing a PSL particle/water suspension with a nebulizer and subsequently evaporating the water from the PSL particles.

The calibration curve for these ideal aerosols is shown in Figure 7, along with a theoretical calibration curve as predicted by Mie scattering. The

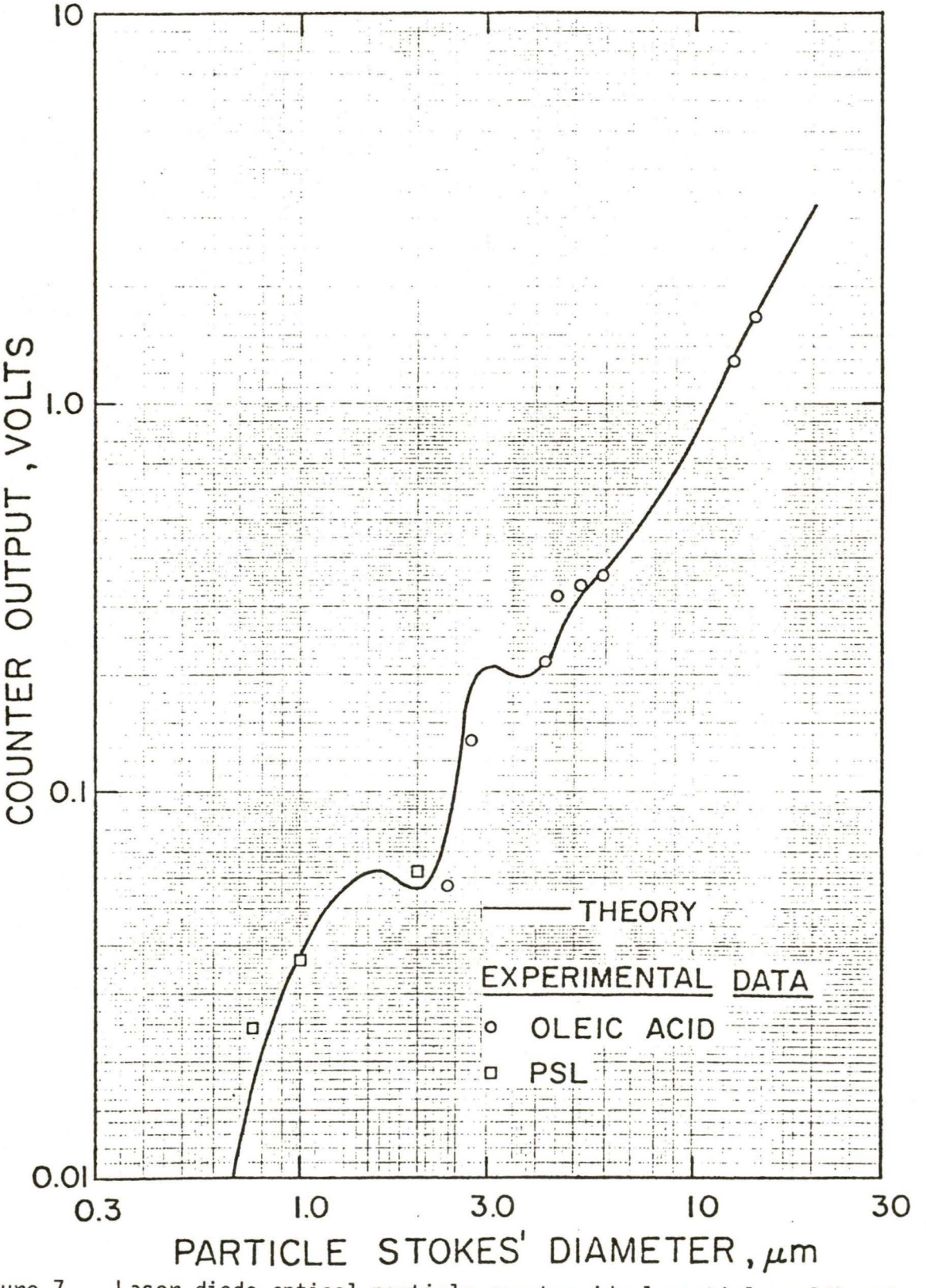

Figure 7. Laser diode optical particle counter ideal particle calibration curve.

theoretical predictions are based on an index of refraction of 1.49. It can be seen that there is good agreement between the theoretical and experimental curves.

The Mie scattering theoretical curve was obtained from a computer program which assumed spherical particles with scattering half-angles of 6° to 33°, and a light wave length of 0.82 μm. This program was employed in the preliminary design of the laser diode OPC to obtain a response curve for coal particles which would be a monotonically increasing function with particle size.

For coal particles, the calibration utilized the inertial impactor technique so that the calibration would be in terms of the aerodynamic diameter (9). The experimental and theoretical coal dust calibration curves are shown in Figure 8. The agreement between theory and experiment was found to be not quite as good as with the ideal aerosols. However, it must be noted that the theoretical coal calibration is based on spherical particles with a 1.95 - .66i index of refraction. Thus, perfect agreement was not expected, since coal particles are certainly not spherical and the true index of refraction is not known. In addition, light scattering characteristics may vary from particle to particle. With these uncertainties, the agreement between the theoretical and experimental calibration curves was determined to be satisfactory.

3.4 Current Status

The development of the electronics for this instrument has been a rather slow process due to a combination of extremely short pulses from the particles passing through the optical particle counter, malfunctioning laser diodes and temperature control elements, and a change in the personnel developing the electronics. Currently, the single particle counting portion of the instrument is operating satisfactorily and has been used on two field studies described later in this report. However, the extremely short pulses from the optical particle counter are still providing problems in the summation circuitry, which is a critical part of the photometer electronics of this instrument. Thus, this portion of the development is still in progress. Most of the photometer electronics, however, including the linearizing and squaring circuit, (see Appendix B) are operating properly.

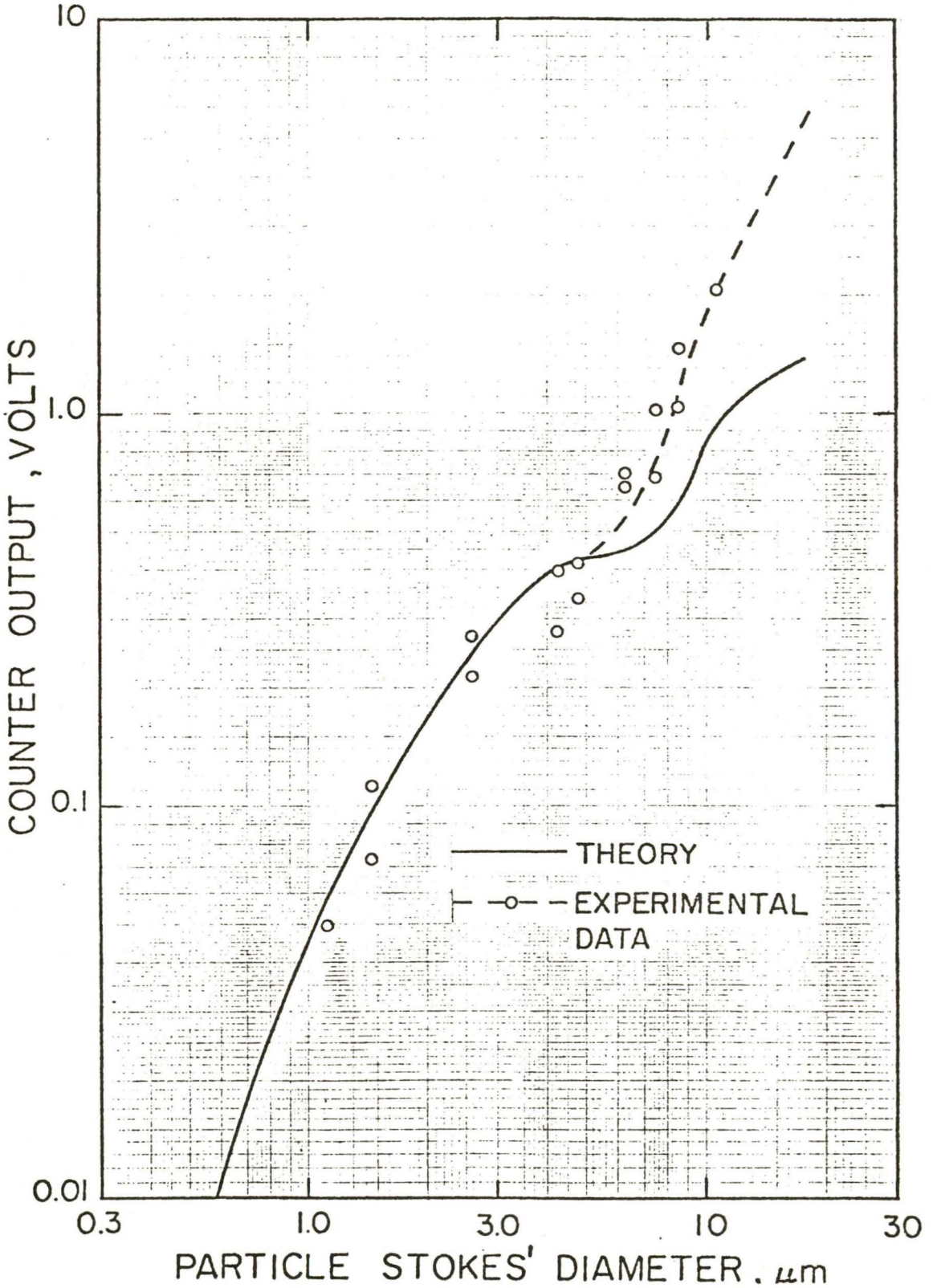

Figure 8. Laser diode optical particle counter coal calibration curve.

CHAPTER 4
INSTRUMENT EVALUATION CHAMBER

4.1 Introduction

In previous instrument evaluation programs, dust was supplied to the instrument's inlet from a dust generator by means of a flexible hose (10). Essentially this allowed only one instrument to be evaluated at a time and did not allow for inlet particle sampling efficiency effects to be determined, since the velocity of the dust was on the order of 40 cm/sec and normally directed into the inlet of the instrument.

To increase the quality of the instrument evaluations and to also increase the speed at which they could be performed, an instrument evaluation chamber was constructed. This chamber consists of three items (three tasks in this contract); the chamber body, a concentration reducer, and a monodisperse aerosol classifier. These three tasks are discussed in the following sections.

4.2 Aerosol Chamber

The design of the dust chamber, which has a hexagonal cross-section, is shown in Figures 9 and 10. The chamber is approximately 2.4 m high with an inside "diameter" of 1.2 m. Aerosol from a suitable source, such as a fluidized bed dust generator (11) or a vibrating orifice monodisperse aerosol generator (8), plus dilution air is introduced at the top of the chamber. The aerosol is thoroughly mixed in this portion of the chamber by a fan consisting of two 50 cm long wire mesh blades which rotate at approximately 60 rpm. The aerosol then flows downward through a 10 cm thick honeycomb structure where turbulence in the air caused by the fan blades is reduced, thereby providing a low velocity downward flow through the test section area of the chamber. The honeycomb material used is 3/8-inch cell Hexcel water resistant structural kraft paper (Hexcell Corp., 2710 Ave. E., Arlington, TX 76001). The instruments are located on a rotating 114 cm diameter table near the lower end of the chamber. The table is made to rotate so that any variation of dust concentration within the chamber would not be a factor in an instrument evaluation test. As will be discussed in the following section, the dust concentration was very uniform throughout the test section and the rotating of the table was not necessary. Below the rotating table the excess aerosol passes through the lower distribution plate and absolute filters, where the particles are removed from the airstream. The particle free air is then exhausted from the chamber by a blower. The absolute filters used were MSA Model B2141 8x8x4 inch HEPA filters (Mine Safety Appliances Co/Filter Products Division, 400 Penn Center Blvd. Pittsburgh, PA 15235).

Three of the six sides of the chamber are equipped with plexiglas windows and a pair of glove ports. The windows, which are 50 cm by 76 cm, are held in place by quick acting toggle clamps and can be removed to provide access into the chamber. The chamber is equipped with a pair of neoprene dry box gloves at each work station, allowing up to three people to operate the instrumentation within the chamber.

The chamber is split horizontally between the plexiglass windows and the glove ports. Thus, the upper portion of the chamber can be removed for the

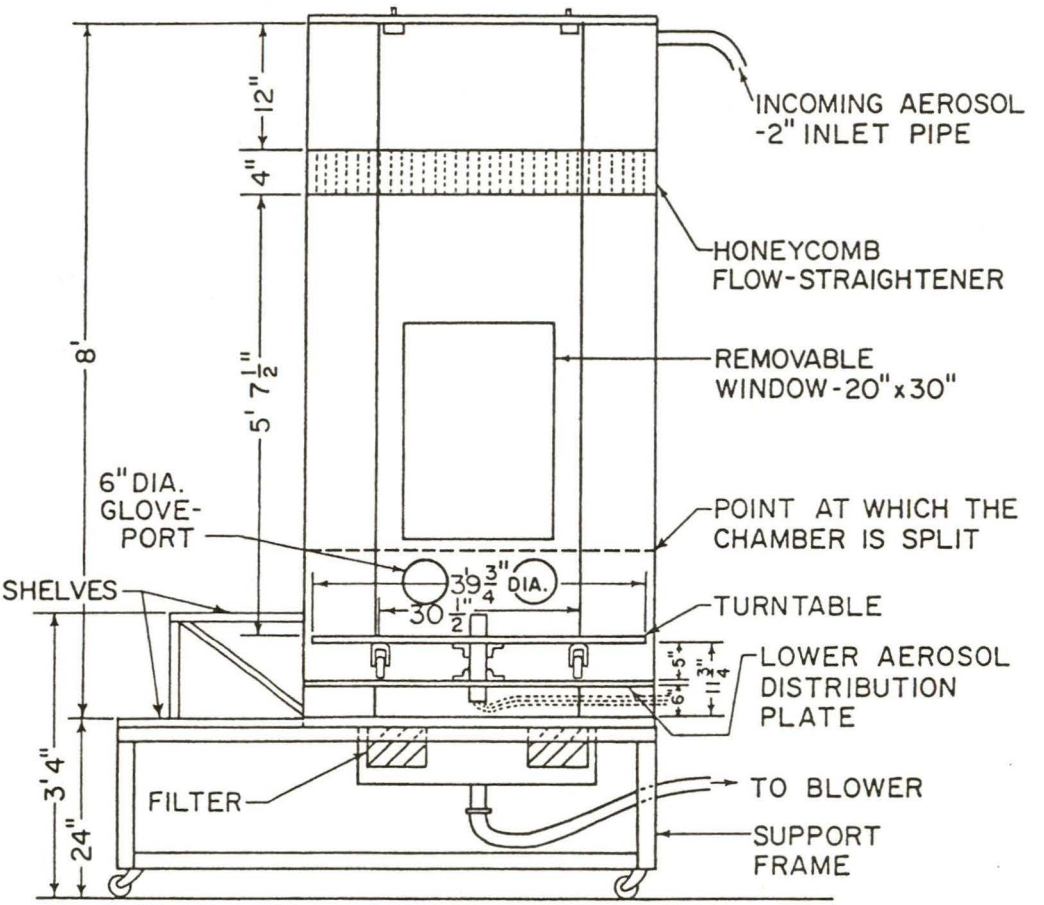

Figure 9. Schematic diagram of aerosol chamber.

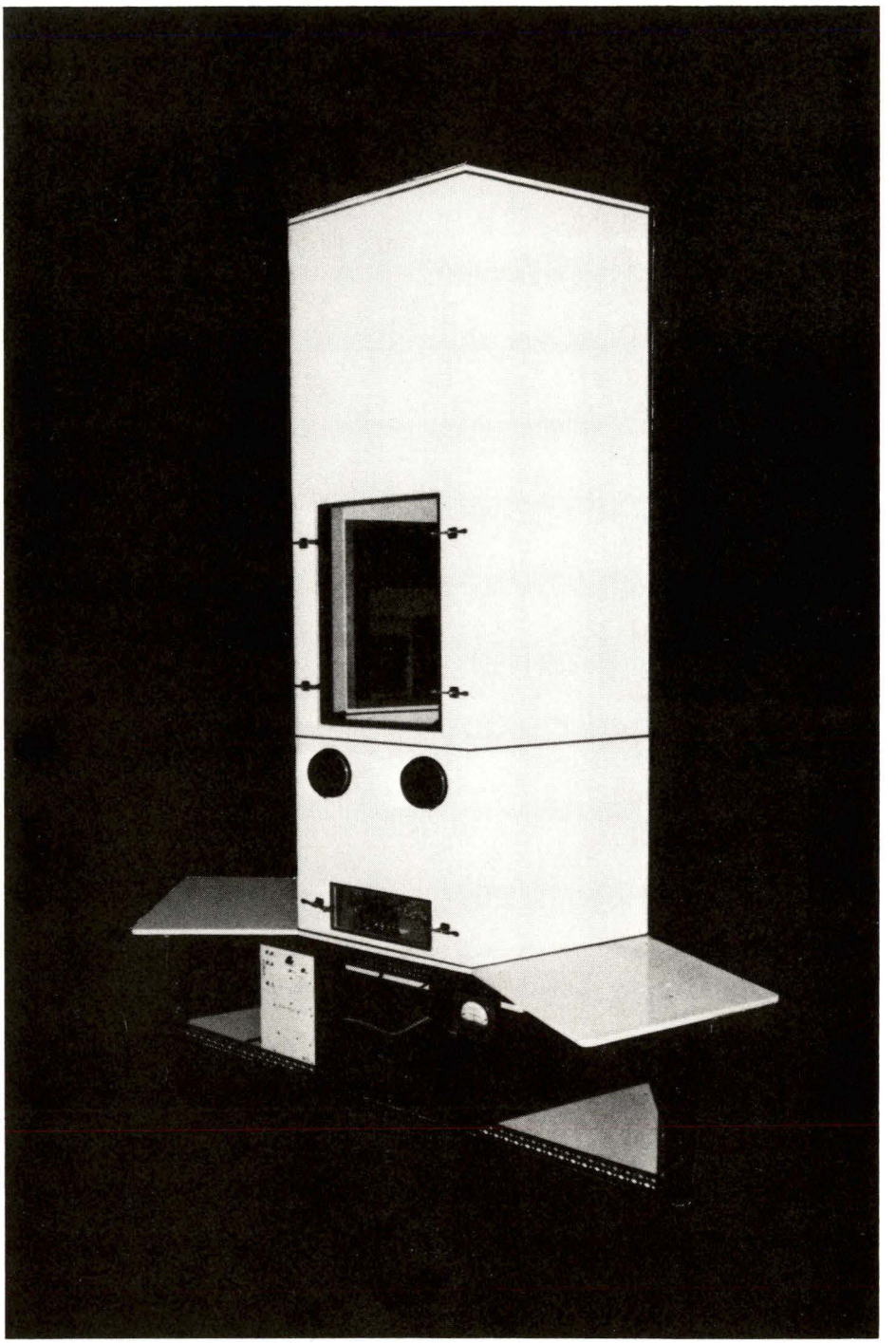

Figure 10. Aerosol chamber.

assembly of the table within the chamber or for the installation of any very large instruments. This also aids in transporting the chamber through doors, etc., if this is necessary.

The chamber is supported by a triangular frame of such a size that the three sides of the chamber containing the windows will be coincident with the three sides of the triangle. The three apexes extend beyond the three sides without windows and are used as platforms for supporting aerosol generation systems, strip chart recorders, etc.

In many instances, electrical leads or air lines must pass from the instruments to the exterior of the chamber. This would be necessary for attaching strip recorders to an instrument or an air line from a pump to a filter sampler or cascade impactor. To accomplish this, the axis of the turntable was made from a pipe so that the leads could pass through the axis of the turntable into the chamber above the absolute filters. The electrical leads and air lines are then brought into the chamber by use of bulkhead fittings attached to the horizontal plate supporting the absolute filters. An access door was provided into this lower part of the chamber to aid in threading leads through the table axis and also for attaching them to the bulkhead fittings. The door can be seen in Figure 10.

The standard instrumentation within the chamber consisted of several devices. First, a photometer is operated continuously with its output recorded on a strip chart. This aids in determining the concentration stability within the chamber. It is not necessary that the calibration of the photometer be known, but only that it be sensitive to changing concentrations. Second, the mass concentration of dust within the chamber is determined by use of open faced filters and the mass collected on the filters determined gravimetrically. It should be noted that in all tests two filters were used for the measurement of the dust concentrations. Third, the size distribution of the dust must also be measured and this is accomplished with a cascade impactor. The impactor currently being utilized is a Sierra Model 266 cascade impactor (Sierra Instruments, Inc., PO Box 909, Carmel Valley CA 93924). It is not necessary to operate the cascade impactor to determine the size distribution for all tests if the conditions of the dust generator remained constant.

In all of the tests performed so far, the fluidized bed dust generator has been the dust source. Besides using the generator air output to force the aerosol through the chamber, it was found advantageous to also use a blower to exhaust air from the chamber. Using this technique, the differential pressure between the interior and exterior of the chamber could be kept at 0.05 cm of water vacuum to ensure that no aerosol could pass into the room. Under this condition the leakage into or out of the chamber was negligible and it was possible to remove the windows for brief periods of time without disturbing the dust concentration equilibrium within the chamber. It was found that a window could be removed and an instrument transfered into or out of the chamber without any indication of a change of dust concentration within the chamber.

4.3 Concentration Reducer

Although the fluidized bed dust generator is capable of maintaining a constant concentration over long periods of time, it was found that if the con-

ditions of the dust generator are changed, such as increasing the feed rate or changing the bed flow rate, the dust generator must be operated several hours before a constant concentration is again obtained. Thus, it is desirable to operate the bed at a high concentration and control the dust concentration entering the chamber by means of a dust concentration reducer.

The concentration reducer that has been developed for this chamber is shown in Figure 11. The principle of operation of the concentration reducer is to split the dust stream output of the dust generator into two parts, remove the particles from one of the parts and reintroduce the clean air into the stream containing the dust. The initial split of the air stream is made isokinetically with a knife edge so as to preserve the size distribution in both of the air streams.

As shown in Figure 11, the dust passes into a flow channel with a semi-circular cross-section at the inlet of the concentration reducer. At the end of this semi-circular channel a knife edge, bisecting a second tube, can be rotated from 0° to 180°. On one side of the knife edge the particles are removed in an absolute filter, while on the other side of the knife edge the particles pass on to the chamber. By correctly positioning the knife edge and regulating the flow of air through the filter, it is possible to have isokinetic conditions at the knife edge. The filtered air is then passed through a pump and reintroduced downstream of the concentration reducer to maintain constant airflow.

It has been found that with this device the concentration can be reliably reduced to 10% of the initial concentration. Thus, the concentration reducer provides the capablility of supplying a dust concentration from 10% to 100% of the dust generator output.

4.4 Monodisperse Aerosol Classifier

Often times it is desirable to expose the instruments to dust particles of a specific size to determine what the instruments' output will be as a function of particle size. To do this type of test with an ideal aerosol, such generators as a vibrating orifice monodisperse aerosol generator can be used. However, to obtain a monodisperse dust, a polydisperse dust must first be generated and then the large and small particles removed from the dust laden stream.

The method that was attempted on this project was to use a virtual impactor to remove the small particles and a real impactor to remove the large particles. As indicated in Appendix A, a virtual impactor can be designed so that the cutoff characteristics are relatively sharp. This is also the case for real impactors (3). Thus, by passing the aerosol through both types of impactors as shown in Figure 12, it should be possible to obtain a fairly monodisperse aerosol. It should be noted that the aerosol can not be perfectly monodisperse since the sharpness of cut of the real and virtual impactors are not ideal. The type of distribution that can be expected from this type of system is shown in Figure 13. Here, the efficiency curves for both real and virtual impactors have been applied to a polydisperse size distribution.

Several virtual impactors were tested in attempting to develop this system. These consisted of two commercial units and three which had been constructed in

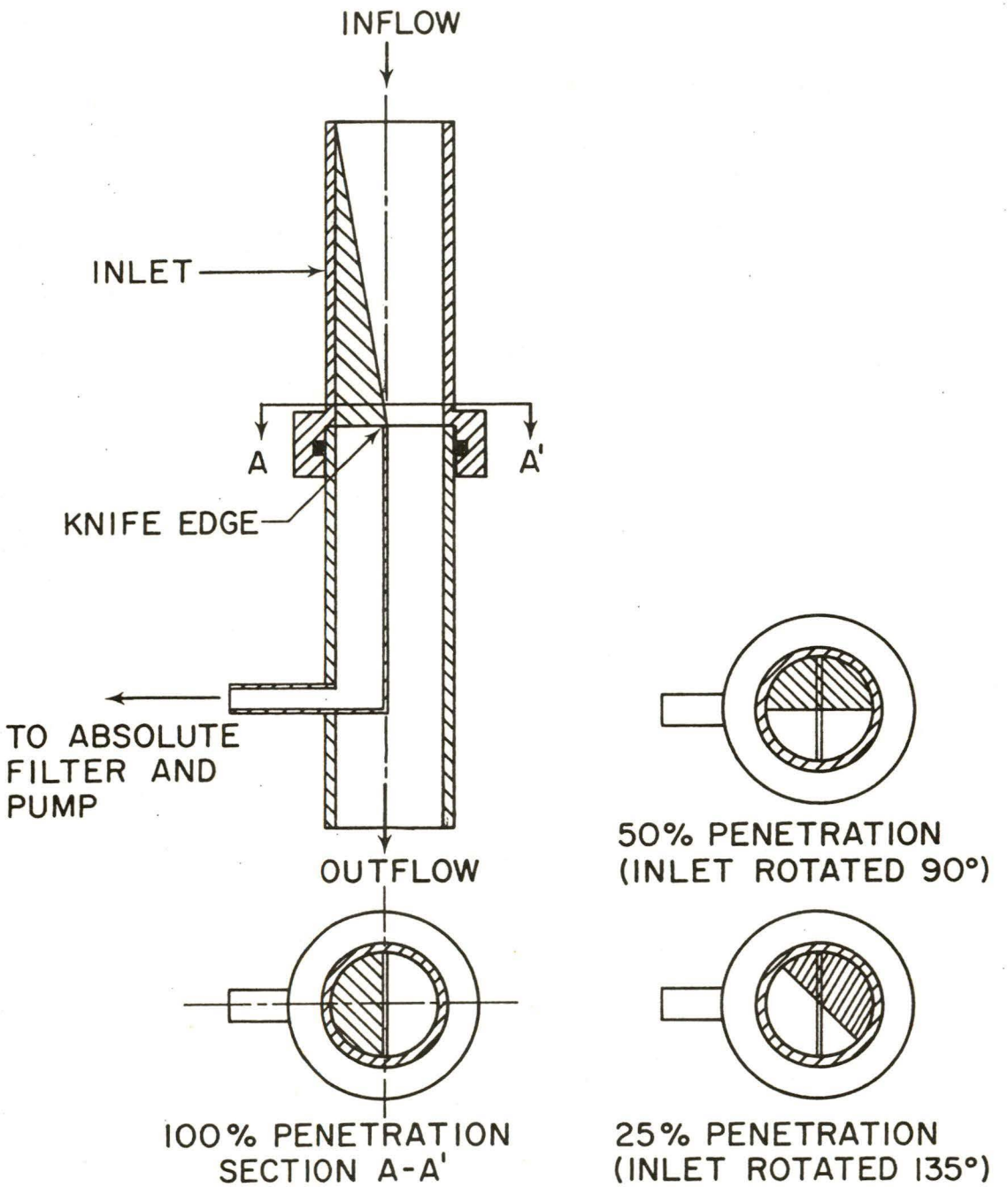

Figure 11. Schematic diagram of concentration reducer.

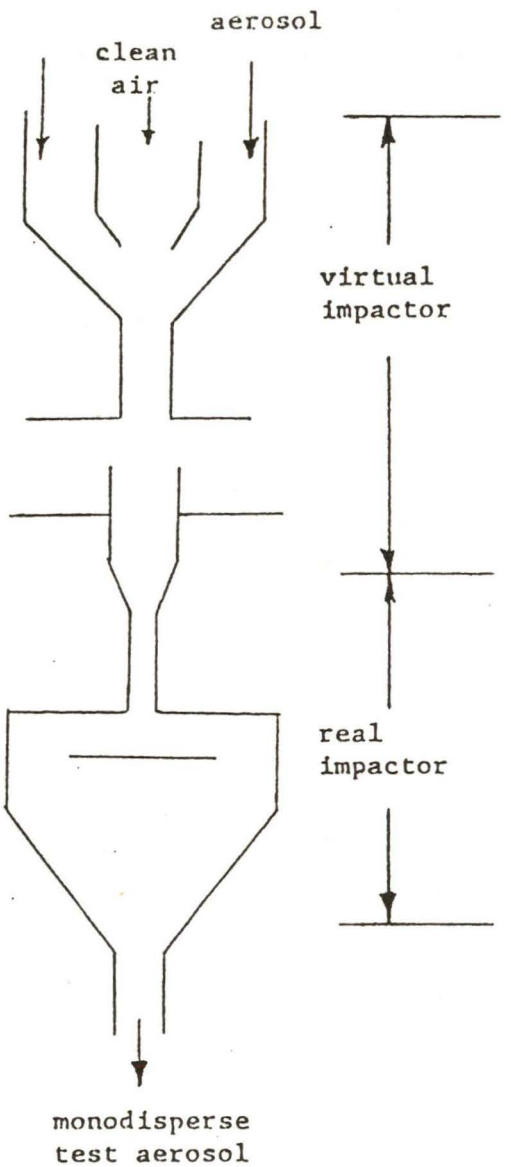

Figure 12. Schematic diagram of monodisperse aerosol classifier.

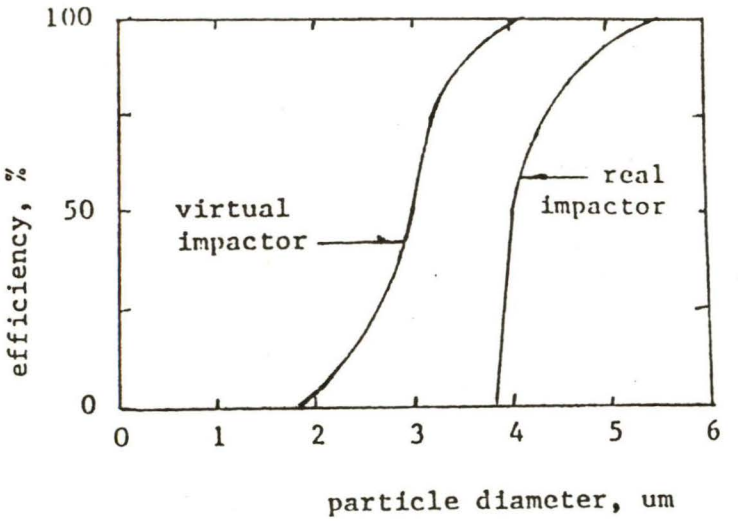

a. Collection efficiency curves

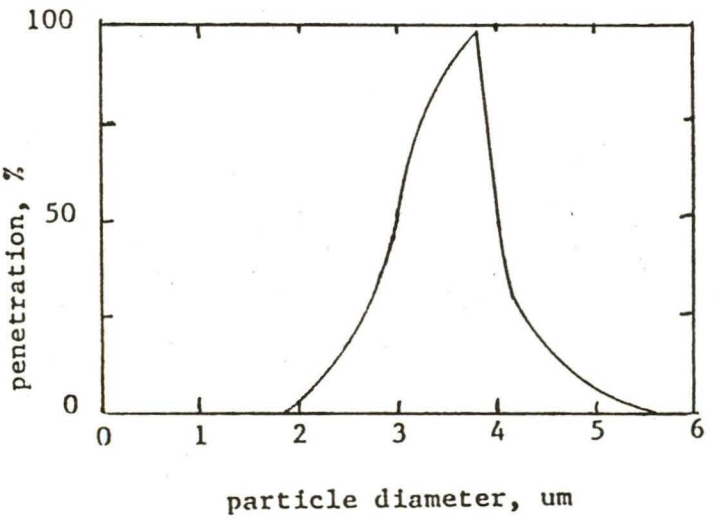

b. Penetration curve

Figure 13. Monodisperse aerosol classifier particle collection efficiency and penetration curves.

our laboratory. In all cases it was found that the aerosol passing through the central tube contained an excess amount of small particles. This indicated that the virtual impactors were not operating as expected. Currently, we are in the process of experimentally investigating virtual impactors, and once they are operating correctly, one will be incorporated into the system with the real impactor to aid us in obtaining monodisperse aerosols.

4.5 Chamber Evaluation

The chamber was evaluated to determine the uniformity of the dust concentration at various points within the chamber and also to determine how constant the concentration was with time. The primary method used to determine the dust concentration was to sample the aerosol using open faced filter samplers, each of which consisted of a Millipore model XX 50 047 10 open faced 47 mm filter holder and a Millipore AA filter (Millipore Corp., Bedford, MA 01730). The flow rate through the samplers was 20 lpm.

Two filters were placed at a distance of 37 cm from the center of the chamber and at the height comparable to the test instrument inlets. The location of the two filter holders was varied to simultaneously examine the spatial concentration within the chamber at any two of four points. These four sampling points were chosen so as to determine the spatial concentration within the chamber relative to the point of aerosol input into the chamber. Each point varied by 90° with 1 being defined as the point of aerosol input into the chamber. The points were then numbered starting with the first position at 1 and proceeding counterclockwise around the chamber.

Table 1 contains the mass concentration data which was gravimetrically determined using the open faced filters as a function of filter location within the chamber. The relative deviation from the average concentration is also listed. The data were obtained using the respirable fraction of the dust from the dust generator (i.e., the dust was passed through a respirable cyclone located at the fluidized dust generator exit). The first eight sets of data were obtained using Arizona road dust and the last two sets using coal dust. The sampling time for these tests ranged from 15 to 20 minutes. The data indicate that the variation in mass concentration between filter samplers is less than 5%, which is the estimated measurement uncertainty, and independent of the level of mass concentration or type of dust material. Note here that the deviation of the mass concentrations from the average of each run ranges from 0.3% to 4.6% with an average relative deviation of 1.8%.

Several different types of aerosol monitoring instruments were used to determine the variation of the aerosol concentration within the chamber for sampling times of two minutes or less. A modified Royco 218 OPC (6) was used to sample the dust for one minute intervals and these results indicate that the number concentration and particle size distributions were uniform throughout the chamber. Also, a TSI Model 3500 respirable aerosol mass monitor and a TSI Model 5150 respirable aerosol photometer (TSI, Inc., 500 Cardigan Rd., St. Paul, MN 55112) were used to study the aerosol concentration both as a function of time and location. The results from these instruments also showed less than 5% variation in dust concentration in the chamber.

Table 1

Gravimetrically Determined Mass Concentration

as a Function of Filter Location Within Chamber

Mass Concentration, mg/m^3 at location -				Average Concentration	Relative Deviation, %
1	2	3	4		
1.03	-	1.12	-	1.08	4.2
2.49	-	2.56	-	2.53	1.4
2.52	-	2.64	-	2.58	1.6
4.00	-	4.14	-	4.07	1.7
7.07	-	-	7.11	7.09	0.3
7.88	-	-	7.91	7.90	1.9
-	2.86	-	3.12	2.99	4.3
-	3.76	-	3.80	3.78	0.5
-	2.77	-	2.84	2.80	1.2
-	3.02	-	2.98	3.00	0.7

In addition to the uniformity of the dust concentration within the chamber, studies were performed to determine the stability of the dust concentration with time. For these studies the voltage output from the TSI photometer was monitored with a strip chart recorder. Two typical strip charts are shown in Figure 14. The test aerosol used for this evaluation was the respirable fraction of Arizona road dust.

The gravimetrically determined mass concentrations were 3.0 and 3.8 mg/m^3 for the data shown in Figures 14a and 14b, respectively. The length of sampling times for the strip chart data shown in the figures were 35 and 25 minutes. As can be seen from this photometer data, the aerosol concentration is indeed steady with time.

The time required for the dust concentration to reach equilibrium in the dust chamber was determined based on the time required for the photometer output to stabilize. It was found that the equilibrium time, which was dependent on the aerosol flow rate, ranged from 10 to 25 minutes for aerosol input flow rates of 300 and 100 lpm, respectively. This is about the same time required for one change of air in the chamber.

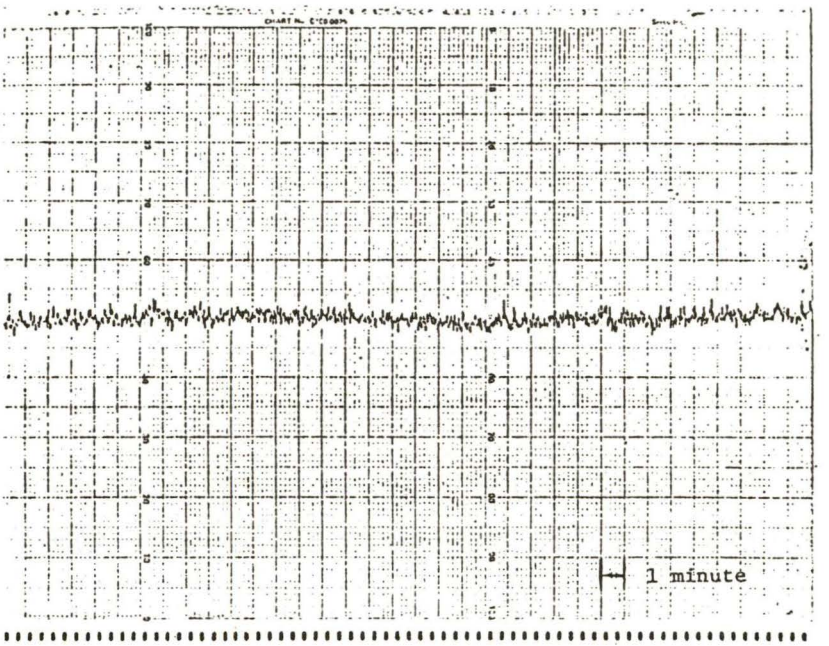

a.

Respirable Arizona road dust, mass concentration = 3.0 mg/m^3

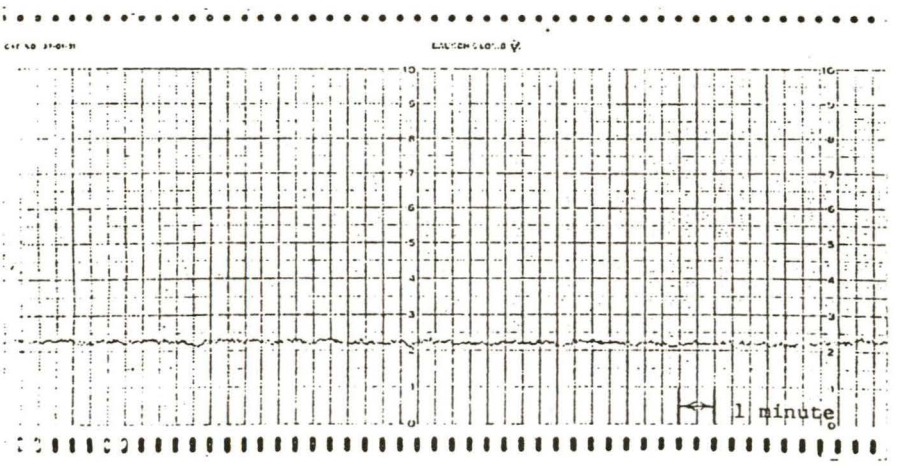

b.

Respirable Arizona road dust, mass concentraion = 3.8 mg/m^3

Figure 14. Strip chart records from photometer showing stability of aerosol concentration in aerosol chamber as a function of time.

CHAPTER 5
INSTRUMENT EVALUATIONS AND CALIBRATIONS

5.1 Introduction

Although there were many instances in which instruments and devices were evaluated and calibrated, these were often associated with other tasks. However, there were several cases in which the tasks were specifically performed for the purpose of an instrument evaluation or calibration. Five such cases described in this chapter include the evaluation and calibration of the SRI portable mine dust instrument, the calibration of several GCA RDM 101-1 and TSI Model 3500 respirable dust monitors, the calibration of several different photometers and the evaluation of the Berkeley Controls QCM cascade impactor.

5.2 SRI Portable Mine Dust Concentration Instrument

Two SRI instruments (12) were obtained from the Bureau of Mines for evaluation. One of the instruments had a severe instability in the electical baseline and air leakage into the viewing chamber. Thus, only one of the instruments was satisfactory for evaluation. A complete report on the instrument and the evaluation is presented in Appendix C.

Several conclusions were drawn from the study. First, it was difficult to eliminate the leakage into the viewing chamber and thus quite difficult to use the photometer in a reliable manner. In addition, there were problems with the electrical system and some electrical baseline drift. However, since these problems could be corrected with a redesign of the instrument, the evaluation was performed to determine the sensitivity of the photometer to varying particle size distributions. The size distributions were varied by eliminating the larger particles with an impactor and performing a calibration at various impactor cutoff sizes. These tests showed that the instrument was quite sensitive to the size distribution. However, the instrument was sensitive to changing concentrations and was easy to use. Thus, it is believed that the instrument could be useful for monitoring dust concentrations with some electrical or mechanical redesign. Full details of these items are presented in Appendix C.

5.3 Photometer Evaluation and Calibration

An investigation into the response as a function of respirable mass concentration of nine commercially available photometers to different types of aerosols, and in particular, coal dust was initiated during the last portion of this contract. Consequently, the results to be presented in this report are only preliminary and part of an on-going project. The photometers used in this study are four GCA Model RAM-1 (GCA/Environmental Instruments, Burlington Rd., Bedford, MA 01730), two SIMSLIN IIs (Rotheroe and Mitchell Ltd., Victoria Road, South Ruislip, Middlesex, England), two Leitz Tyndallometer TM digitals (Ernst Leitz, GmbH., Wetzler, Germany), and one TSI Model 5150 Respirable Aerosol Photometer (TSI, INC., 500 Cardigan Road, St. Paul, MN 55112). From the resulting data, comparisons can be made between each manufacturers' photometer as well as comparisons between several photometers from a given manufacturer.

The response of each photometer is designed to correspond to one of several different respirable dust criteria. Consequently, each photometer has a different type of particle preseparator incorporated into its inlet and in most

cases, the preseperator is an integral part of the instrument. The three different criteria utilized by the photometers studied here are the American Conference of Governmental Industrial Hygienist (ACGIH), British Medical Research Council (BMRC) and the German TBF 50-II. These criteria correspond respectively to those used for the GCA, SIMSLIN, and the Leitz photometers. An additional approximation criteria employed by the TSI photometer is obtained by using an impactor with a cut at 3.5 μm as the aerosol preseparator. This criteria approximates the ACGIH criteria which classifies 50% of the 3.5 μm diameter particles as respirable. Figure 15 illustrates the fraction of respirable dust as a function of particle size for the ACGIH, BMRC and the TBF 50-II criteria.

The respirable dust mass concentration used in the calibration of these photometers was computed from the aerosol size distribution as measured with a Sierra Model 266 cascade impactor (Sierra Instruments, Inc., PO Box 909, Carmel Valley, CA 93924). The respirable dust mass concentration was calculated from the size distribution data by applying the appropriate respirable dust criteria. Table 2 contains the cutoff diameters as theoretically determined for the Sierra Model 266 cascade impactor when operated at a flow rate of 4.0 lpm. For the case of the TSI photometer, the respirable mass concentration was determined by plotting the aerosol mass size distribution as an accumulative size distribution and then determining the amount of mass less than 3.5 μm. This type of analysis was required since no stage within the cascade impactor had a particle cutoff at 3.5 μm.

The photometers currently have been evaluated with several different aerosols to determine their response as a function of particle size distribution and particle composition. These aerosols, which were generated with the fluidized bed dust generator, have included coal (Illinois no. 6) and the AC Fine Arizona road dust (AC Spark Plug Div., General Motors Corp., 1300 N. Dort Hwy., Flint, MI 48556). The intrinsic density of the coal and Arizona road dust was measured to be respectively 1.45 and 2.61 gm/cm^3 (7).

To further vary the test aerosol, two different size distributions of coal were used, "Coal-I" and "Coal-II", where the "Coal-II" aerosol is the respirable fraction of the "Coal-I" aerosol. "Coal-II" aerosol is obtained by passing the aerosol through a respirable cyclone placed at the exit of the fluidized bed dust generator which removed the large nonrespirable particles.

The size distributions of these test dust aerosols as obtained from the cascade impactor, for the three different aerosols are presented in Figure 16. Assuming that these aerosols have log-normal size distributions, the value of the aerosol mass mean diameter (MMD) and geometric standard deviation (σ_g) have been calculated and are presented in the figure.

Although the size distributions of the aerosol in the chamber are those shown in Figure 16, the aerosol size distributions in the instruments' sensors were different for the instruments which only monitor the respirable fraction of the aerosol. For example, the aerosol size distributions presented in Figure 17 are for the case of instruments equipped with aerosol preseparators based on the ACGIH criteria. Since the preseparator preferentially removes only the larger particles, the difference between the resulting size distributions decreases from that which existed in the original sampled aerosol size distribution. For the case of the two coal size distributions, the ratio of the MMD decreased from

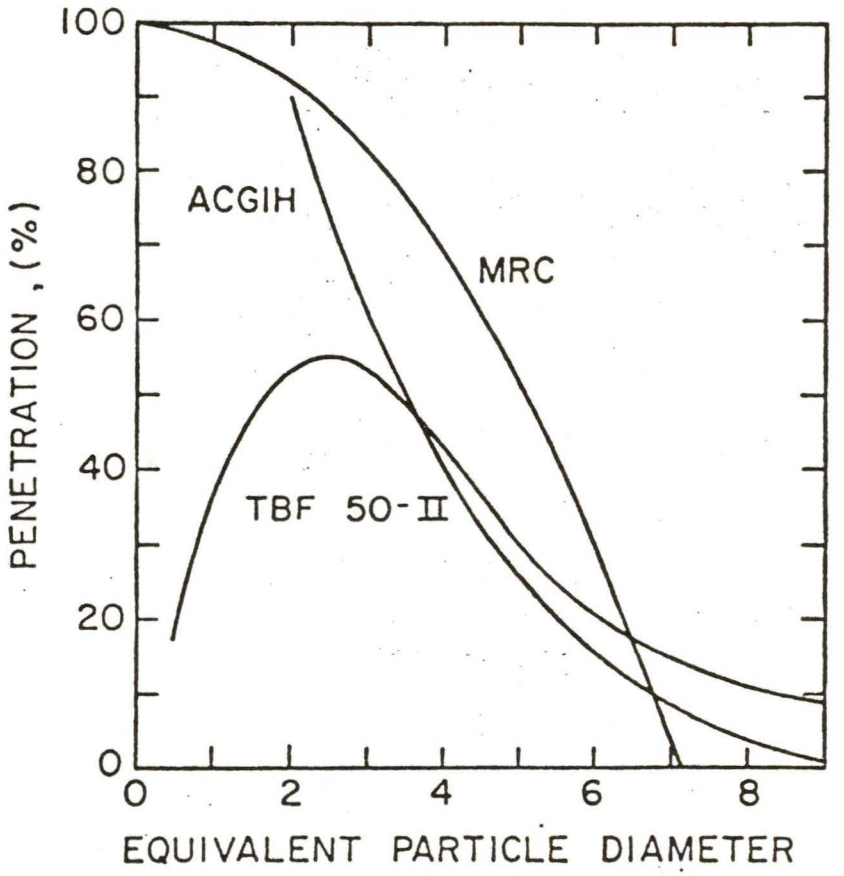

Figure 15. ACGIH, BMRC and TBF 50-II respirable penetration curves.

Table 2

Sierra Model 266 Cascade Impactor
Stage Cutoff diameters

Impactor stage No.	Aerodynamic Cutoff Diameter, µm*
1	14.5
2	9.5
3	5.2
4	2.5
5	1.1
6	0.55

* Theoretically determined for flowrate of 4.0 lpm.

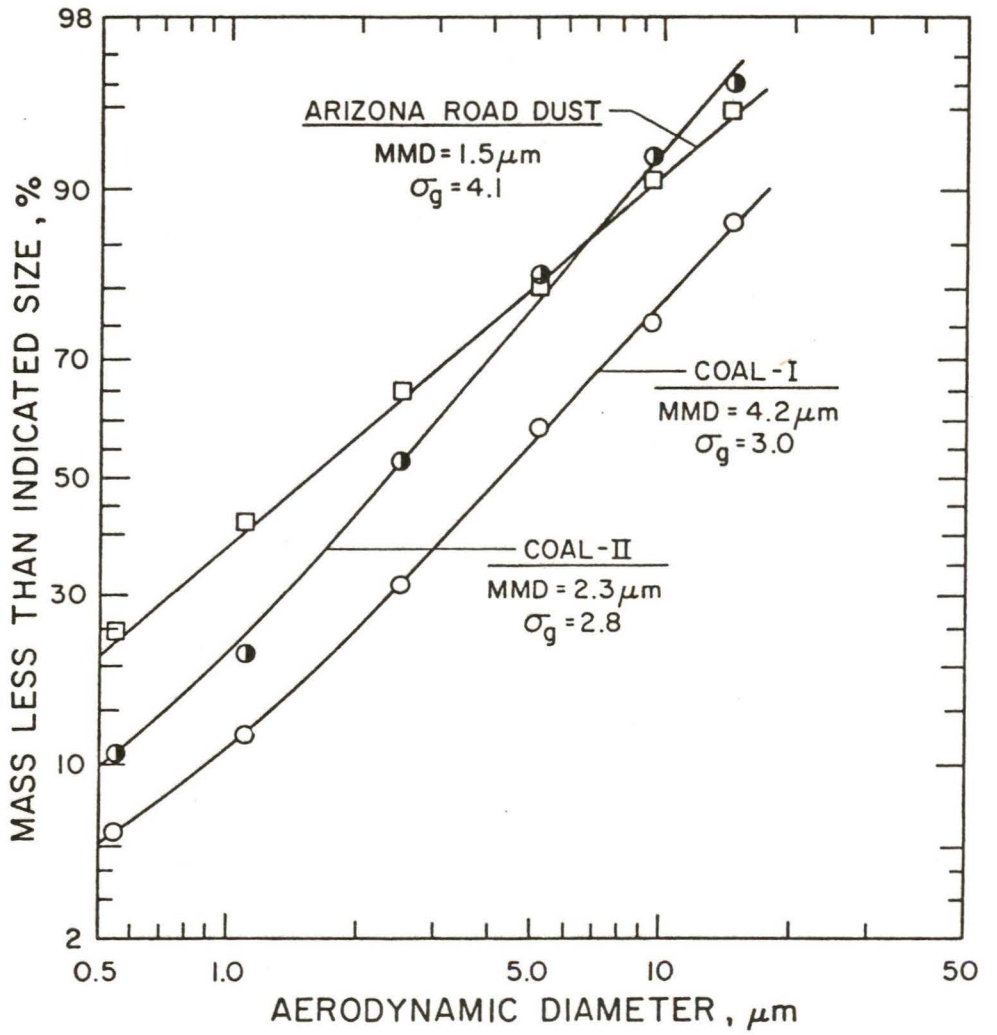

Figure 16. Size distributions of test dusts in aerosol chamber

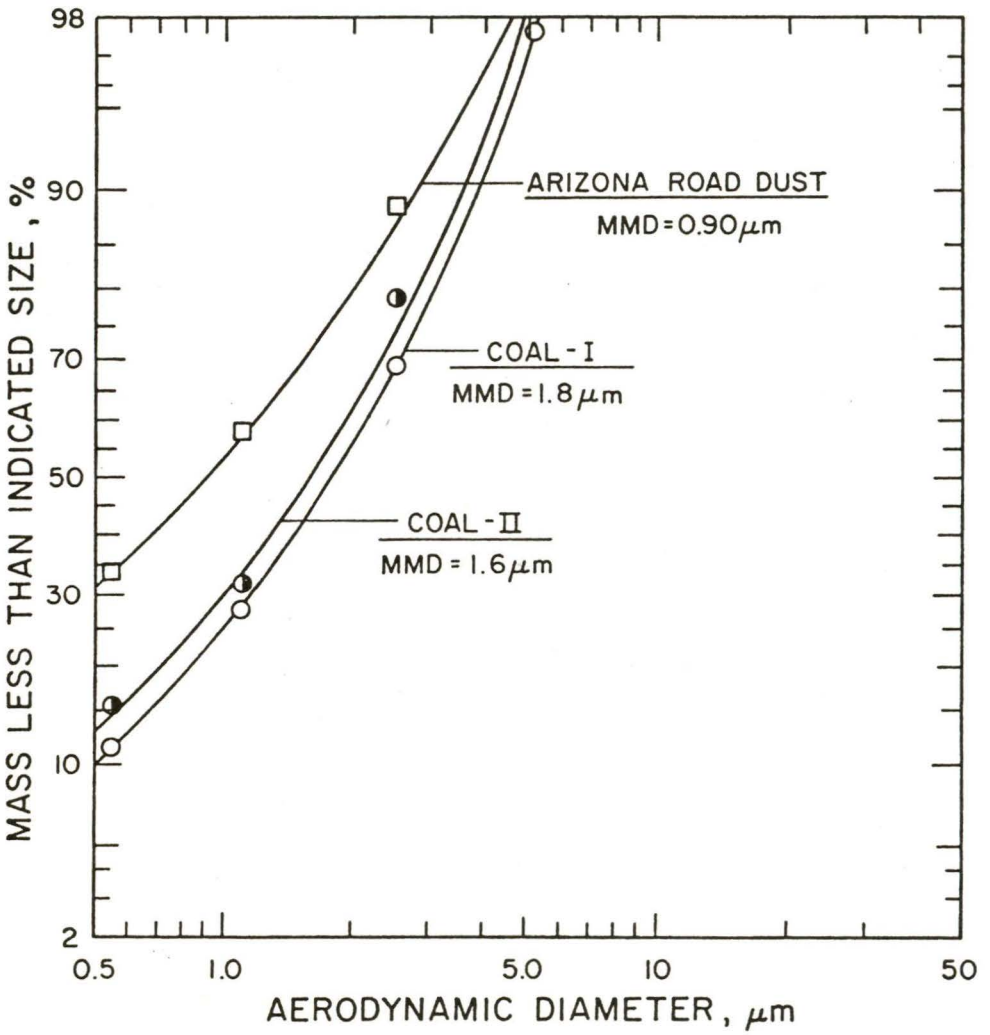

Figure 17. Calculated respirable size distributions of test dusts in aerosol chamber based on ACGIH criteria.

1.8 to 1.1. Consequently, the differences between the test aerosols actually monitored as compared to those sampled by the instruments are significantly decreased.

The entire instrument is evaluated as a consequence of comparing the instrument response to the calculated respirable mass concentration, based on each respirable criteria. This means that any discrepancies between the instrument response and the calculated concentration could result from the aerosol mass sensing technique, preseparator, or particle loss within the instrument. This consideration is especially important for the GCA instruments since the cutoff characterisitics of the 10mm nylon cyclone preseparator do not exactly match the ACGIH criteria. Also, the recommended flow rate for this cyclone is 2.0 lpm when sampling coal dust and 1.7 lpm for all other materials. Consequently, since the cyclone's particle cutoff is a function of flow rate, the use of these two different flow rates represents an additional source of uncertainty between actual and calculated aerosol size distribution passing into the instrument's sensing region.

All manufacturers state that their photometers must be calibrated with the particular aerosol that the instrument will later be used to monitor. This calibration is necessary since the response of a photometer is dependent on aerosol composition, size distribution, shape, and index of refraction. Consequently, all photometers are equipped with calibration or gain controls. In addition, all photometers used in this evaluation, except the SIMSLIN II are equipped with some type of reference scatterers. Through use of these reference scatterers, the instruments' gains can be set at a value provided by the manufacturer or at a value which has been obtained through instrument calibration with a particular aerosol.

For this study all photometer gains were set at the manufacturers' provided values. These values were used since the intent of this study was to evaluate the relative response of these photometers to different aerosols and determine the applicability of the manufacturers' calibration value to various aerosols.

Since the SIMSLIN II instruments did not have reference scatterers, the instruments' gains were adjusted to provide a response approximately equal to that gravimetrically determined for the Coal-I test aerosol. The gains were then left constant for all other test aerosols.

The flow rate of each instrument was at the value supplied by the manufacturer. These values were 0.625 and 1.0 lpm respectively for the SIMSLIN and TSI photometer. The GCA photometers were operated at 2.0 lpm when sampling coal aerosol and 1.7 lpm when sampling all other aerosols. The Leitz photometer has a passive sampling system. The GCA and SIMSLIN photometers were operated with the mass concentration range switch in the 0 to 20 mg/m^3 range.

The photometer evaluation data presented in this report is considered only preliminarily since the Sierra impactor has not been experimentally evaluated. Possible sources of error which would affect the resulting aerosol mass size distribution are the discrepancy between the actual and theoretically predicted impactor particle cutoff and particle losses within the impactor. The discrepancy is especially important for the largest cut sizes and will be discussed in greater detail in Chapter 8. While this impactor has been designed to minimize

the effects of particle loss, losses are known to exist. Thus, once the impactor has been calibrated, the aerosol size distributions can be corrected to account for these two sources of error. However, the resulting respirable mass concentration correction is expected to be small since both sources of potential error primarily affect the larger nonrespirable particles.

The photometer calibration data are presented in Table 3 and Figures 18 to 26. These data are presented as the response of the instrument as a function of mass concentration and type of test aerosol. Listed in the table for each test are the mass concentrations corresponding to the four respirable dust criteria and the mass concentration readings from the nine instruments. One must be careful to compare the instrument response to the appropriate respirable dust criteria. The respirable mass concentration ranged from approximately 0.5 to 25 mg/m^3. The limited amount of data reported for the SIMSLIN (serial number 126) is the result of mechanical problems with the unit.

The responses from all instruments except the TSI photometer are read out directly as mass concentration in units of mg/m^3. For the TSI photometer, the mass concentration is read out in units of counts/minute. Consequently the user must either use the instrument's calibration curve or the empirically determined conversion factor in order to relate counts/minute to mass concentration.

The results indicated that the response of all photometers is a linear function of respirable mass concentration for all test aerosols up to mass concentrations of 6 mg/m^3. Based on the limited higher concentration data, the response no longer appears to be linear. Since this observation is based on only three data points at most for each instrument, additional tests are currently being performed at these higher mass concentrations.

Linear regression analysis was performed for each photometer by assuming that the photometer's responses were proportional to respirable mass concentration. The analysis utilized all data for mass concentrations less than 6 mg/m^3. The resulting regression coefficients are presented in Table 4 and the lines drawn in Figures 18 to 26 are those resulting from the regression analysis. For the GCA and Leitz photometers, the coefficient represents the ratio of the instruments response when the span adjust is set at the manufacturers' provided value to the actual span value for each test aerosol. In general, these coefficients show that the instruments' response for these aerosols agrees well with the calculated mass concentration.

The comparison of the regression coefficients provides a relative measure of how the test aerosol composition and size distribution effects the photometer response. In Table 5, the ratio of the average regression coefficients for Coal-II and Arizona road dust to Coal-I for each manufacturers' photometer is presented. The comparison indicates that the photometers' sensitivities are from 1 to 36% greater for the test aerosol containing the larger fraction of smaller particles. This result is expected since the amount of light scattered per unit mass of aerosol increases with decreasing particle size for supermicron particles. The comparison also shows excellent relative agreement between the coal and Arizona road dust. This agreement is especially important for the RAM-I, since GCA calibrates the RAM-I using Arizona road dust (13).

In addition to comparing the photometers' response to a standard, the correlations of the responses between photometers from the same manufacturer

Table 3
Respirable Mass Instrument Calibration Data

Dust Type	Respirable Mass Concentration, mg/m^3, For Criteria (4):				Instrument Response, mg/m3 (1), for listed instruments (2) (5)											
					GCA RAM -I (3)				GCA/RDM 101-1(3)	Leitz Tyndallometer		SIMSLIN II		TSI no. 5150	TSI model 3500	
	ACGIH	BMRC	TBF 50II	<3.5μm	1098	1097	1012B	1018B	2154	575	586	126	133	98343	104	79485
Coal I	0.62	0.61	0.48	0.52	--	--	0.69	0.71	--	0.38	0.46	--	0.65	27	--	--
	1.07	1.24	0.80	0.92	--	--	1.40	1.44	1.38	0.84	0.89	--	1.14	54	--	--
	1.33	1.49	0.88	1.21	--	--	1.02	1.08	1.14	0.60	0.65	1.22	--	38	--	--
	1.48	1.61	0.86	1.38	--	--	1.15	1.24	1.29	0.68	0.78	1.27	1.01	45	--	--
	1.55	1.62	0.58	1.50	1.95	1.80	1.59	1.61	--	--	--	1.30	1.40	65	--	--
	3.12	3.41	1.71	2.96	--	3.72	--	3.72	3.75	1.89	2.00	--	2.69	126	--	--
	3.63	3.97	2.30	3.52	4.30	4.27	3.37	3.73	5.11	2.04	2.00	--	3.27	--	--	--
	3.82	4.19	2.31	3.61	3.79	3.95	3.18	3.53	3.54	1.92	2.07	--	3.20	128	--	--
	4.07	4.36	2.23	4.11	4.08	3.88	3.16	3.55	4.27	1.98	1.97	--	--	126	--	--
	4.35	4.84	2.49	4.19	--	--	--	--	--	--	2.79	--	4.02	162	--	--
	7.06	7.19	3.66	7.79	5.58	5.06	4.39	5.03	5.30	2.89	2.86	--	4.24	178	--	--
Coal II	1.64	1.83	0.92	1.66	2.30	1.88	1.65	1.84	--	1.02	1.05	--	1.67	--	--	--
	1.78	1.76	0.76	1.76	--	--	--	--	--	1.25	1.27	--	1.96	78	--	1.60
	1.98	2.15	1.10	2.00	2.81	2.30	2.14	2.20	--	1.23	1.30	--	2.00	80		--
	2.07	2.29	1.22	2.09	--	--	--	--	--	1.49	1.50	--	2.36	84	--	1.85
	2.37	2.57	1.28	2.18	--	--	--	--	--	1.91	1.89	--	2.98	110	--	2.18
	2.40	2.67	1.22	2.50	--	--	--	--	--	1.45	1.41	--	2.31	84	--	1.83
	3.57	3.88	2.06	--	5.66	4.89	4.20	4.91	--	--	--	--	--	--	--	--
	3.74	4.14	2.10	--	5.16	4.84	3.98	4.39	--	--	--	--	--	--	--	--
	3.98	4.19	1.98	4.04	--	--	--	--	--	2.06	2.04	--	3.22	120	--	2.83
	5.06	5.46	2.74	--	7.67	6.69	5.85	6.60	--	--	--	--	--	--	--	--
	5.19	5.58	2.67	--	7.54	7.14	5.78	6.65	--	--	--	--	--	--	--	--
Arizona Road Dust	2.46	2.51	0.86	2.49	3.19	3.04	2.47	2.67	--	--	1.38	--	1.55	86	1.98	1.50
	2.49	2.52	0.90	2.45	3.00	2.96	2.44	2.71	--	--	1.31	--	1.81	--	1.95	1.49
	5.95	6.28	2.79	5.76	5.98	5.38	4.29	5.82	--	3.09	2.97	3.48	3.86	185	--	3.62
	7.02	7.19	2.74	7.10	8.24	7.90	6.22	6.80	--	3.50	3.53	--	4.96	227	4.86	4.04
	11.3	11.8	4.34	11.6	9.35	8.55	6.55	7.44	--	3.92	3.83	--	5.45	259	4.11	6.39
	25.0	25.6	9.33	24.7	18.5	18.8	15.6	17.0	--	--	8.17	--	11.3	551	--	--

1. Except for TSI RAP, counts/min.
2. Instruments listed by serial number.
3. GCA sample flowrate: for coal-2.0 lpm; for Arizona raod dust - 1.7 lpm.
4. Calculated from aerosol mass size distribution.
5. Respirable criteria associated with each instrument:

Instrument	Criteria
GCA RAM-1 & RDM	ACGIH
Leitz Tyndallometer	TBF 50-II
SIMSLIM II	BMRC
TSI 5150 & 3500	<3.5 μm

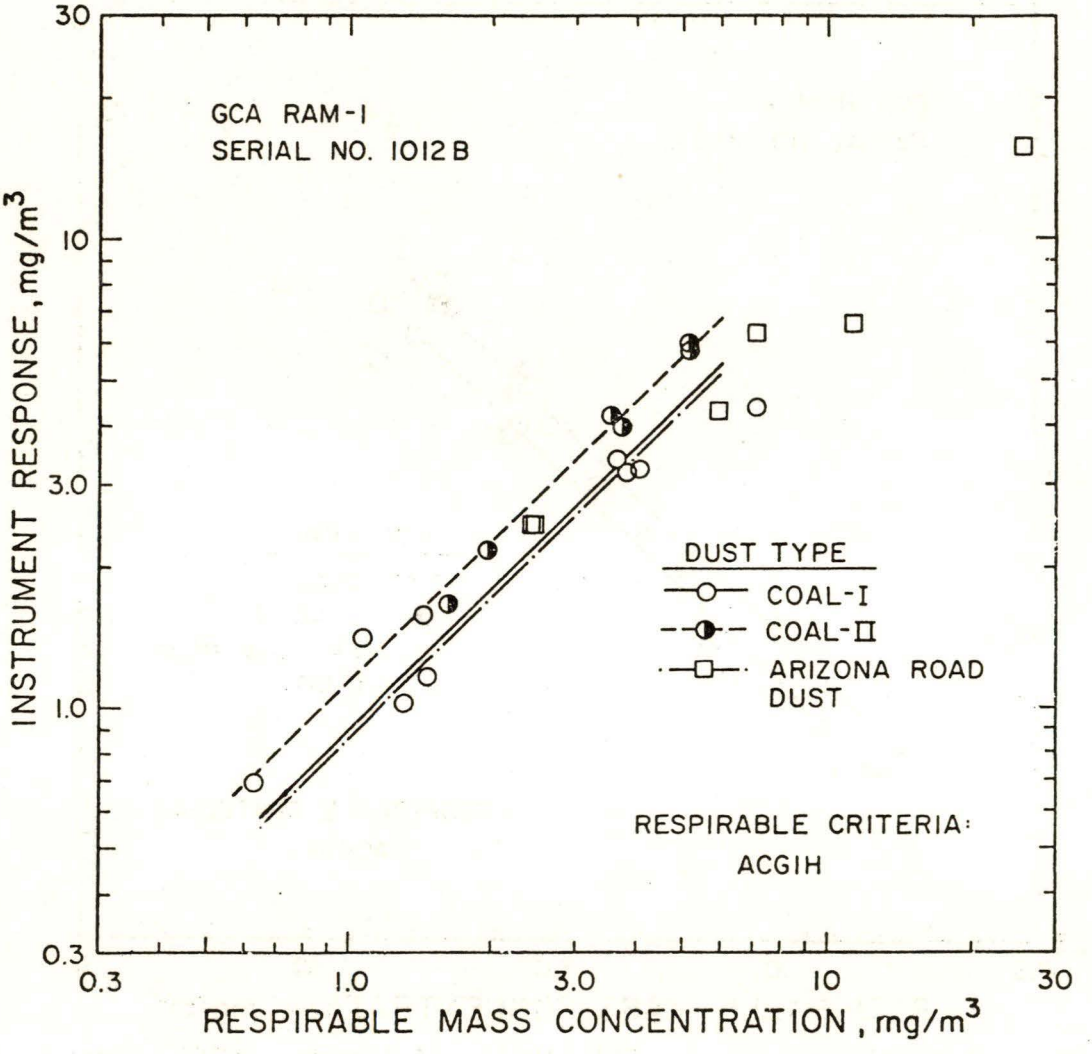

Figure 18. Calibration curves for GCA RAM-1 serial number 1012B. (Data presented in Table 3.)

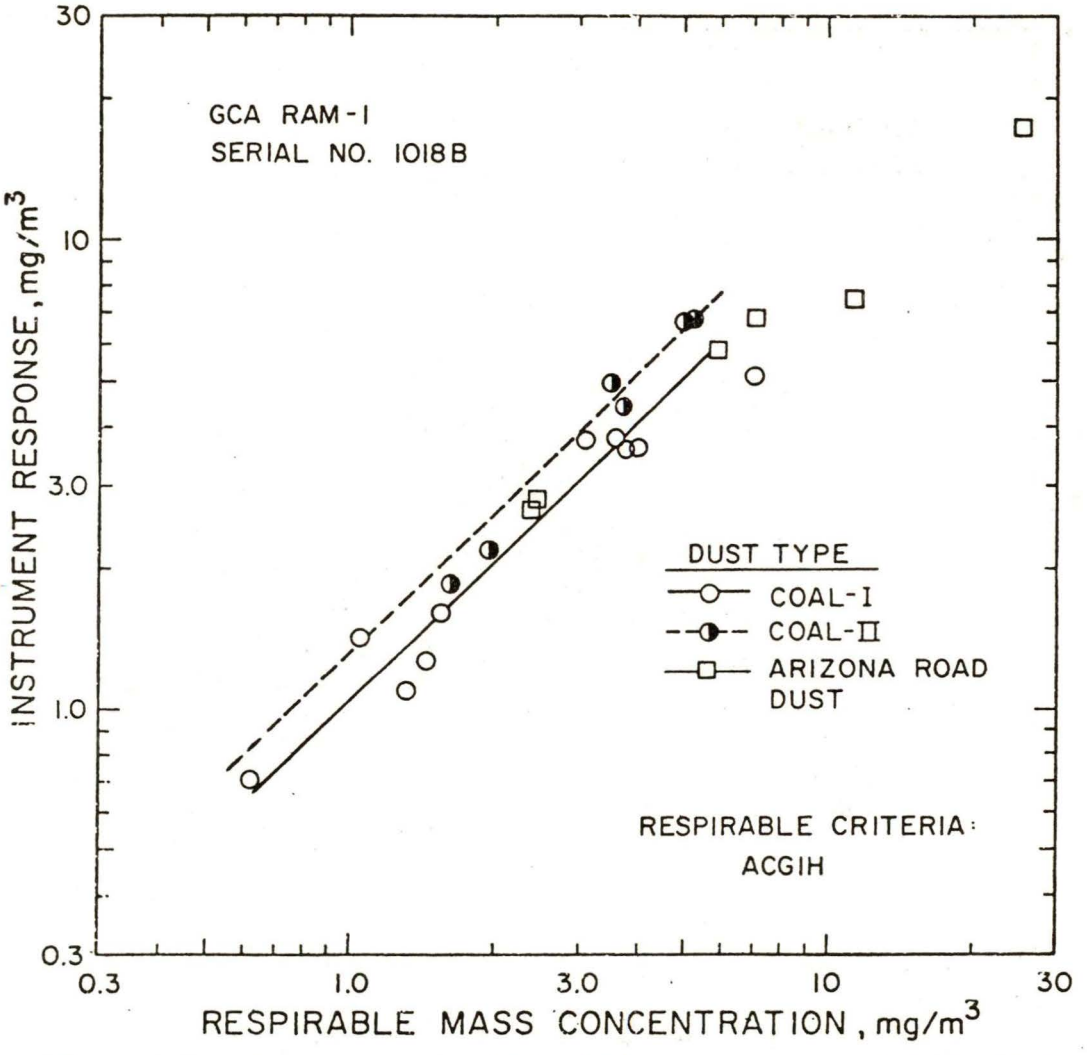

Figure 19. Calibration curves for GCA RAM-1 serial number 1018B. (Data presented in Table 3.)

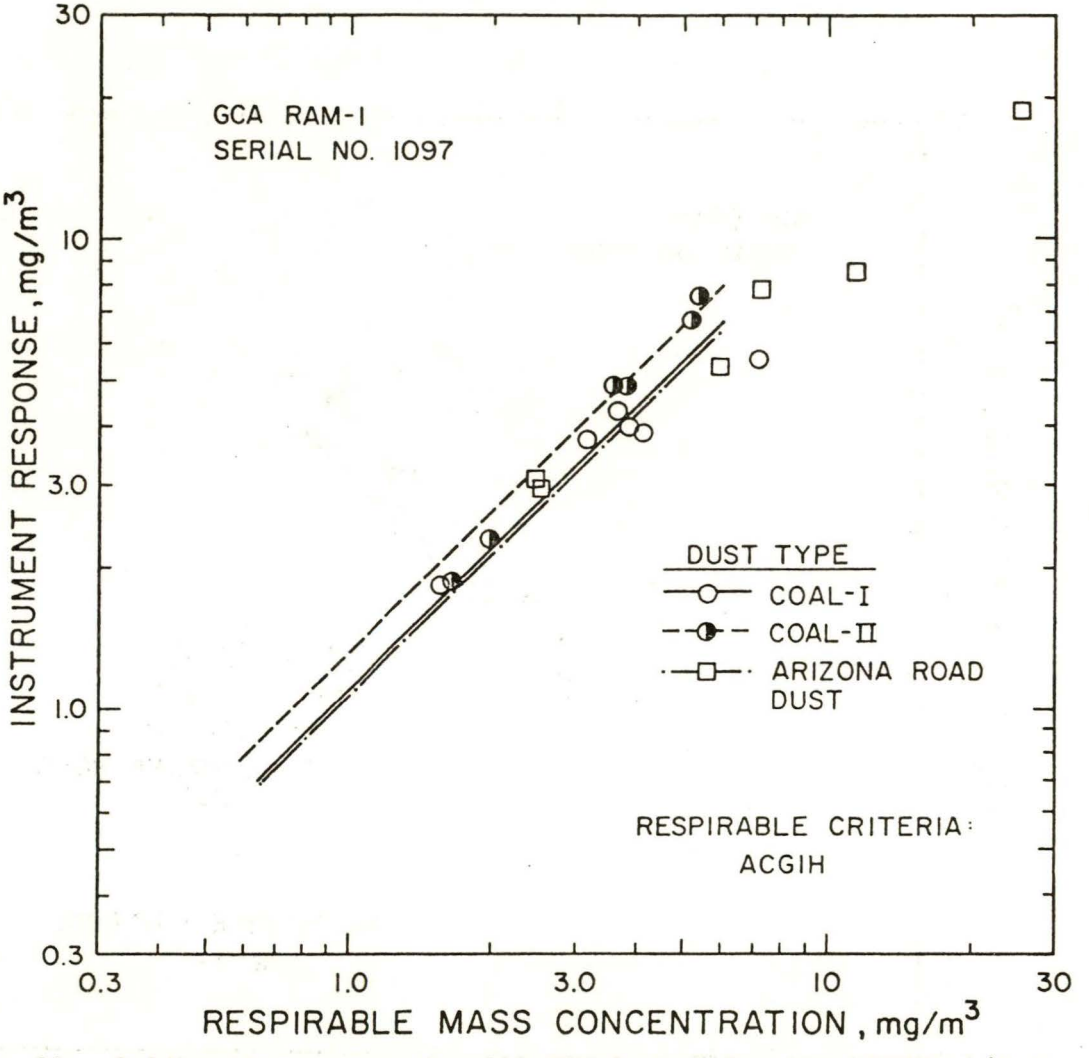

Figure 20. Calibration curves for GCA RAM-1 serial number 1097. (Data presented in Table 3.)

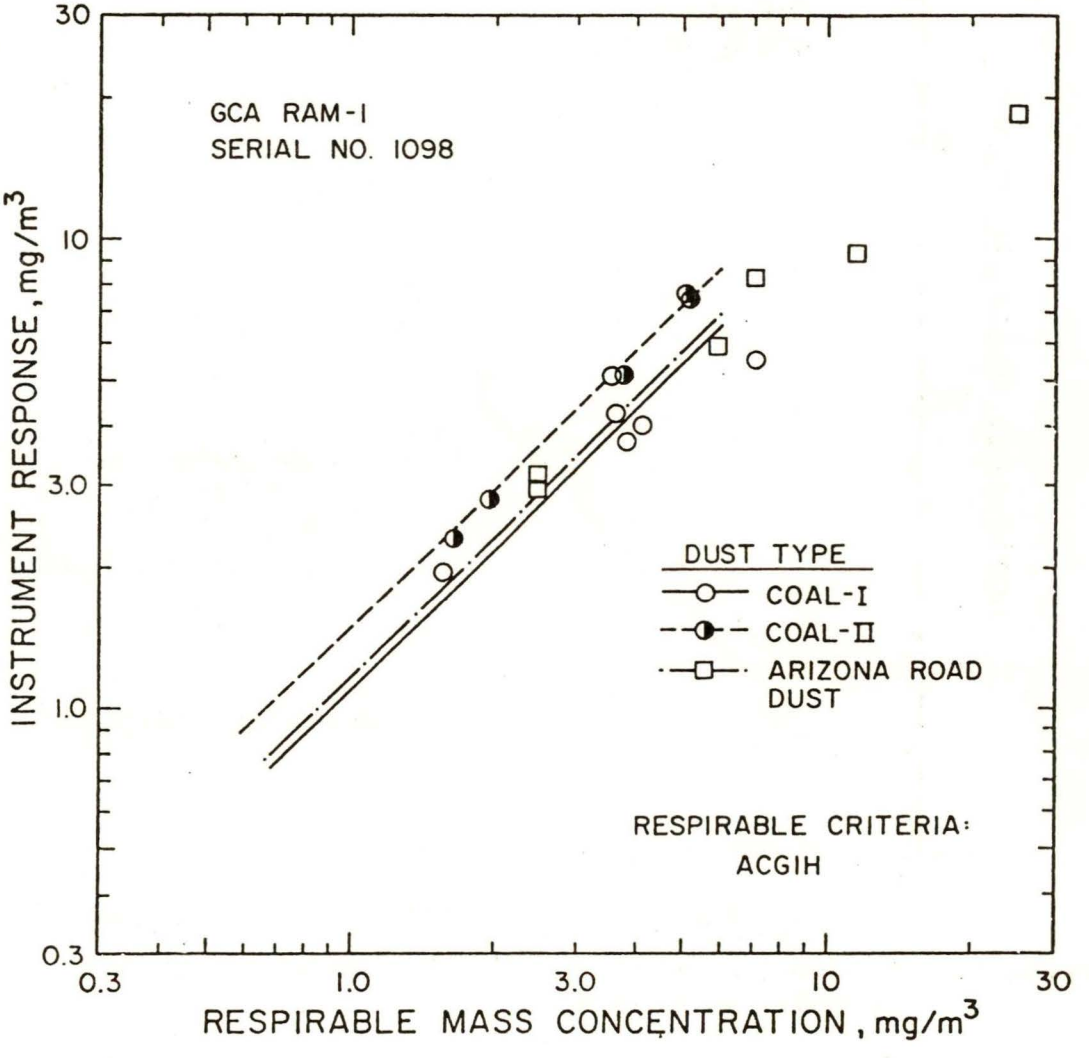

Figure 21. Calibration curves for GCA RAM-1 serial number 1098. (Data presented in Table 3.)

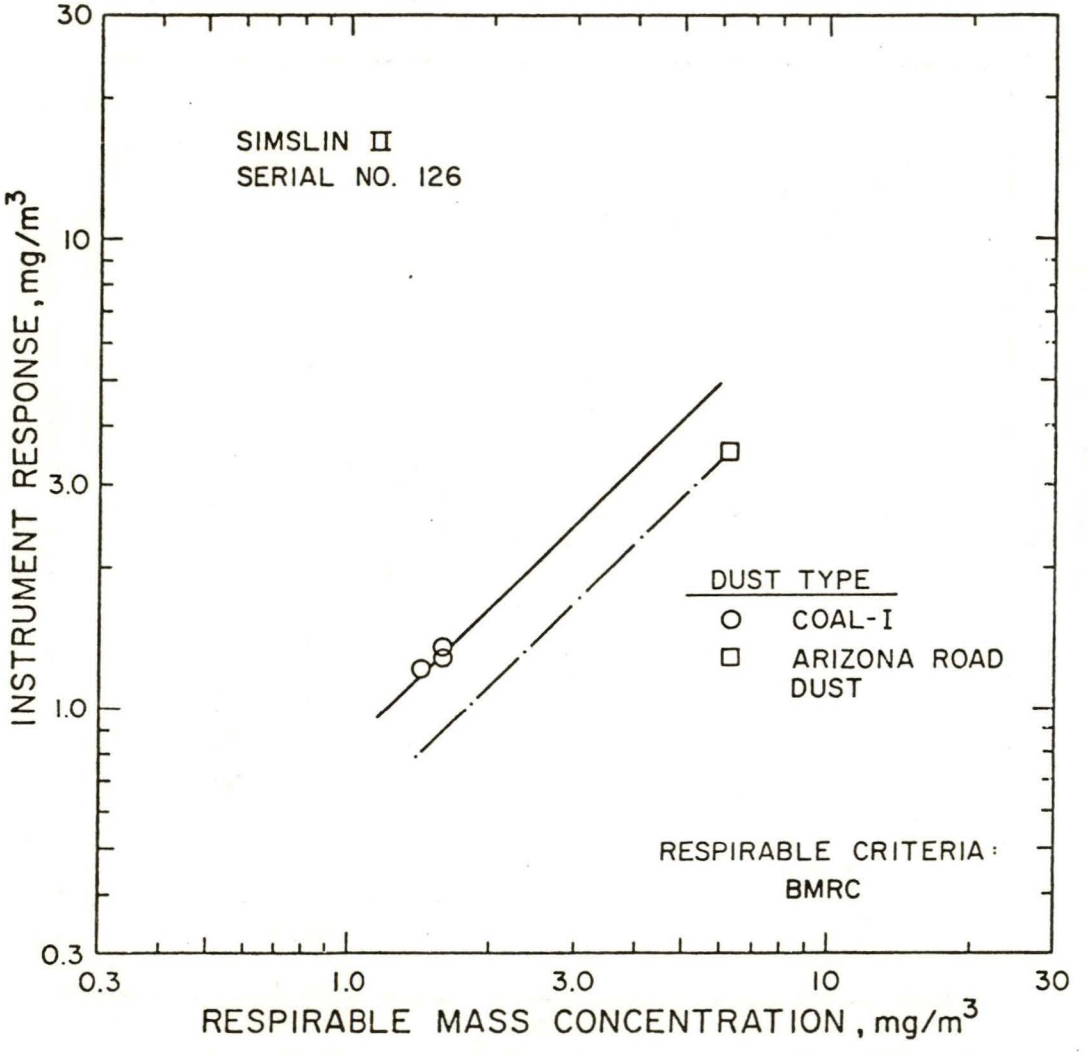

Figure 22. Calibration curves for SIMSLIN II serial number 126. (Data presented in Table 3.)

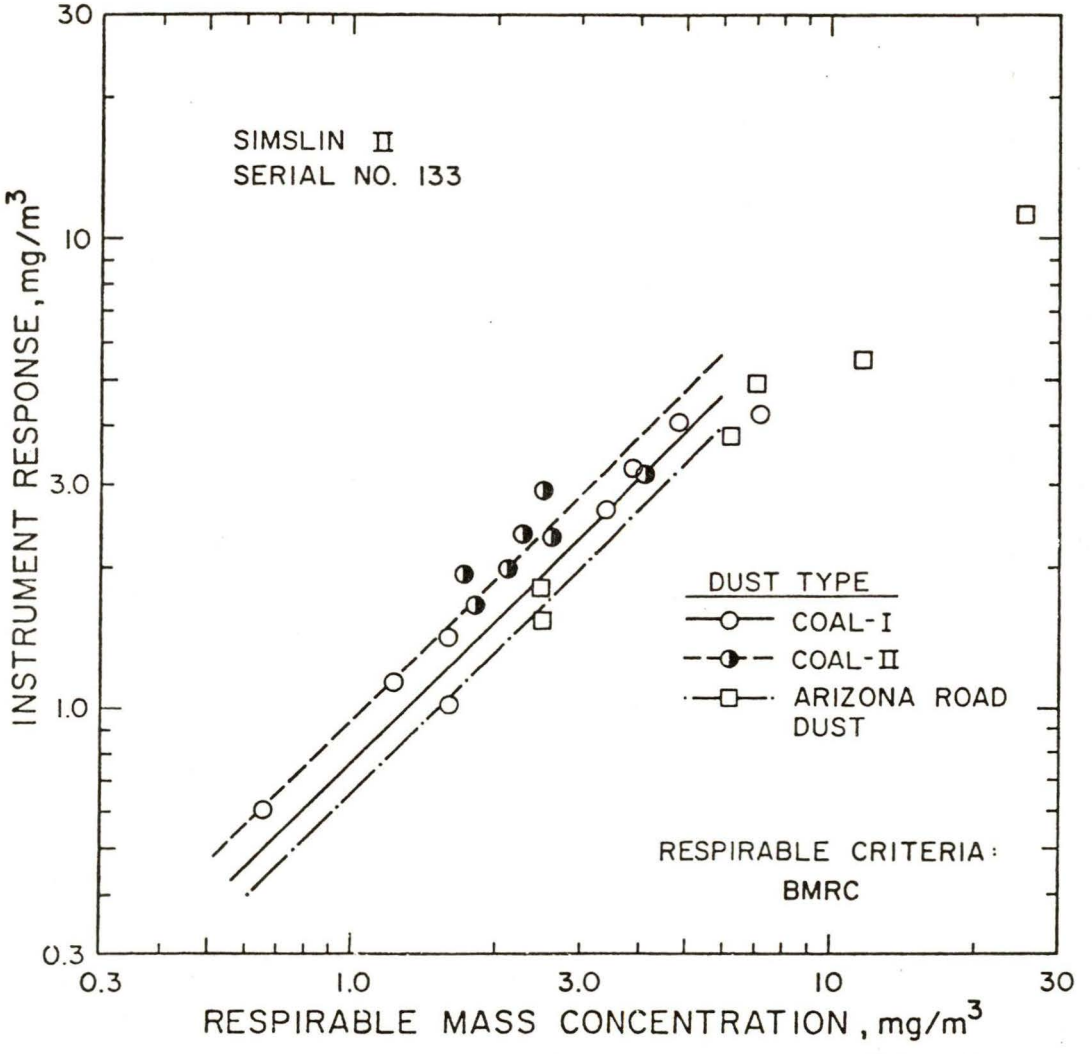

Figure 23. Calibration curves for SIMSLIN II serial number 133. (Data presented in Table 3.)

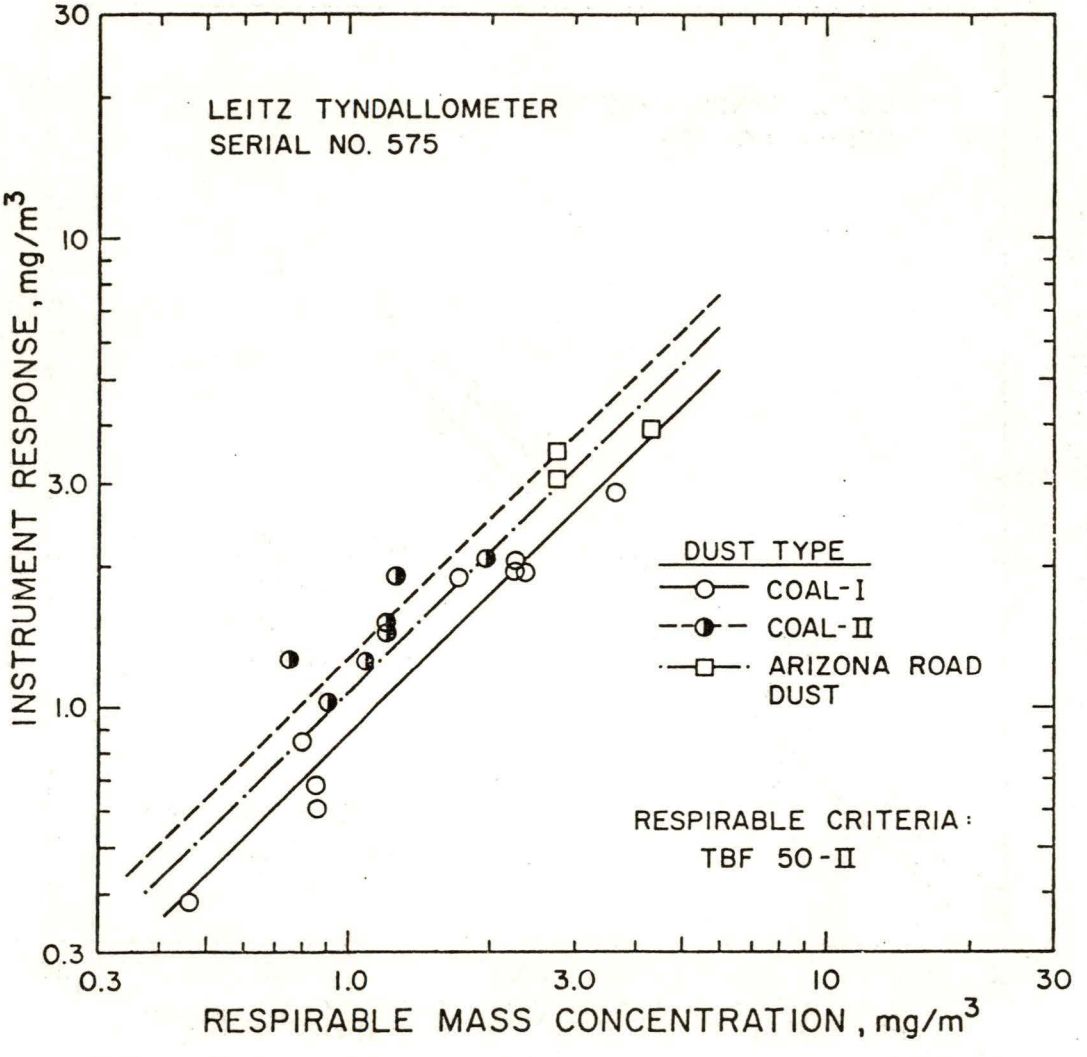

Figure 24. Calibration curves for Leitz Tyndallometer TM Digital serial number 575. (Data presented in Table 3.)

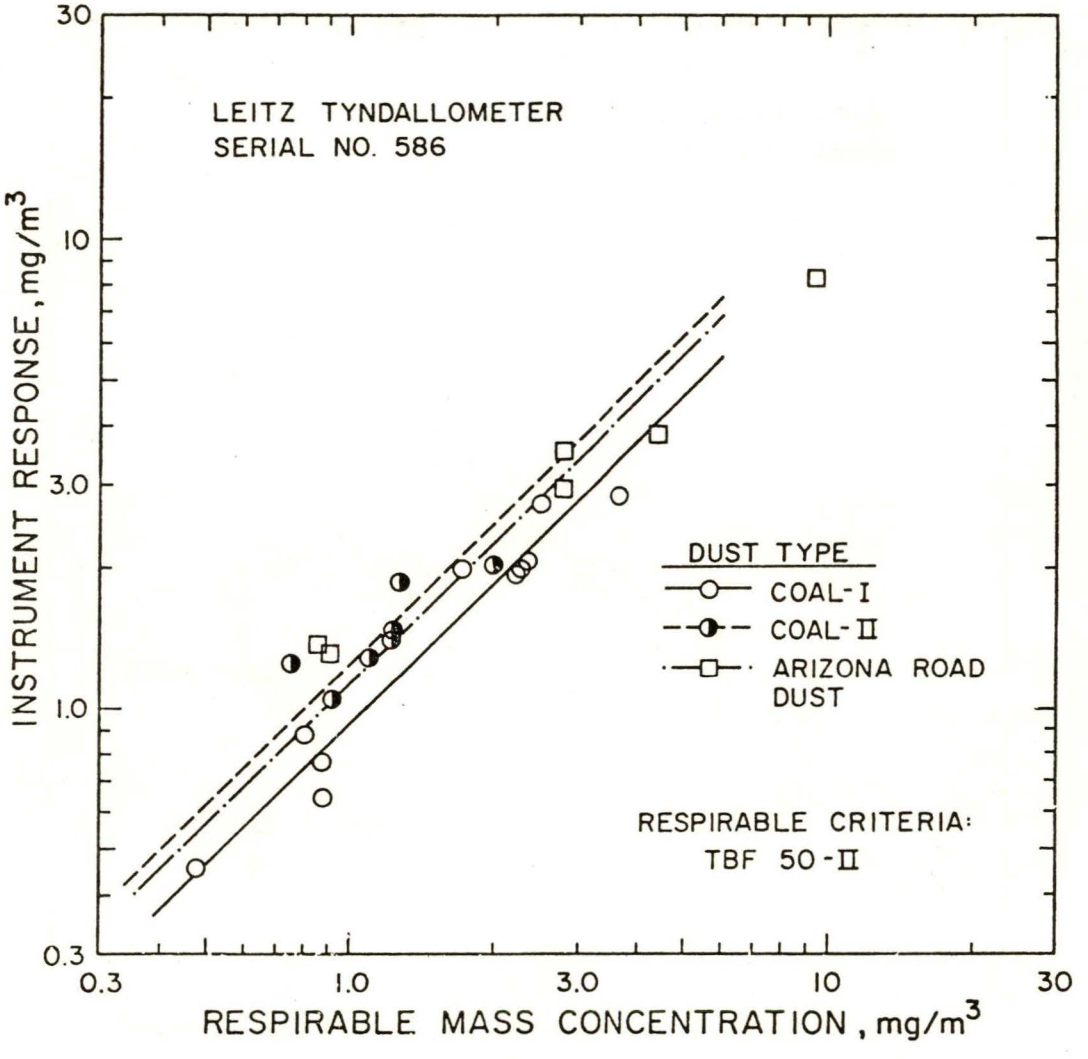

Figure 25. Calibration curves for Leitz Tyndallometer TM Digital serial number 586. (Data presented in Table 3.)

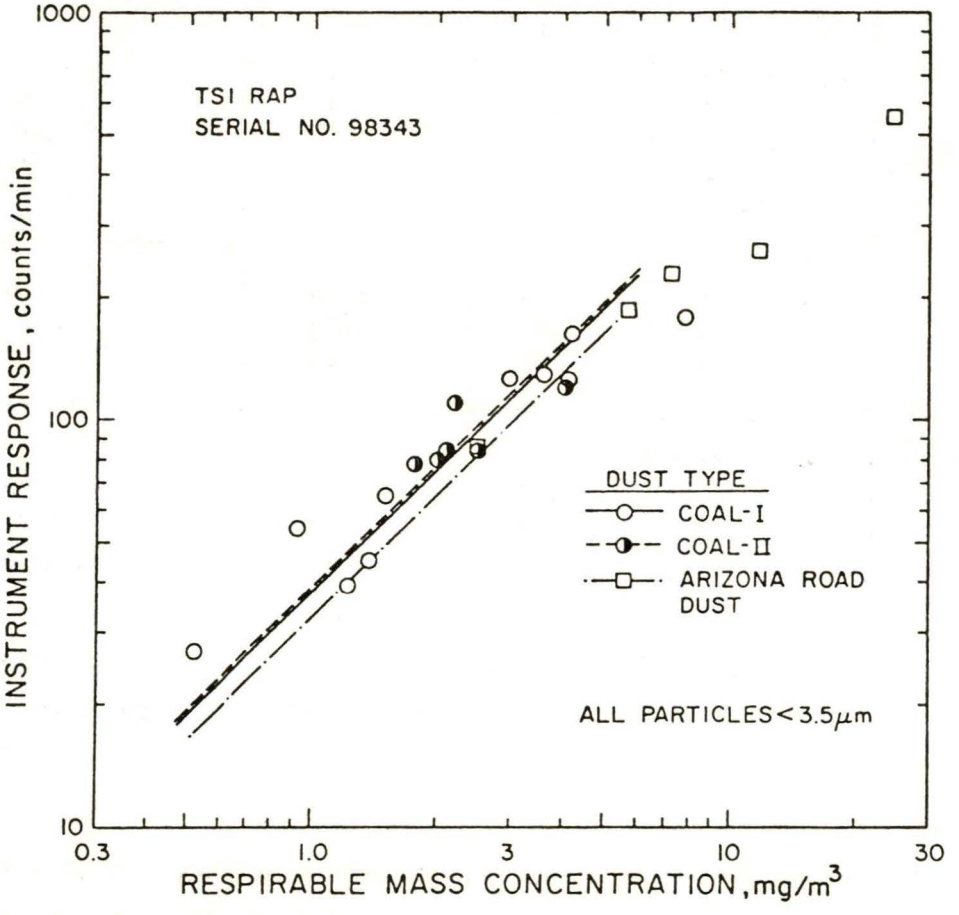

Figure 26. Calibration curves for TSI Model 5150 respirable aerosol photometer serial number 98343. (Data presented in Table 3.)

Table 4

Regression Coefficients
for Photometer Response Calibration Curves

Instrument	Regression Coefficient[1] for: Coal-I	Coal-II	Arizona Road Dust
GCA: #1098	1.08	1.47	1.14
#1097	1.09	1.31	1.08
#1012B	0.89	1.11	0.86
#1018B	1.00	1.26	1.00
average	1.02	1.29	1.02
Leitz: #575	0.87	1.23	1.06
#586	0.93	1.23	1.12
average	0.90	1.23	1.09
SIMSLIN #126	0.80	--	0.55
#133	0.77	0.95	0.66
average	0.78	0.95	0.60
TSI: #98343	37.8	38.2	32.8

1. Based on respirable mass concentration less than 6.0 mg/m^3.

Table 5

Relative Photometer Response as Function of Aerosol

	Ratio of Regression Coefficient for Aerosols of	
Photometer	Coal-II / Coal-I	Arizona Road Dust/ Coal I
GCA	1.27	1.00
Leitz	1.36	1.21
SIMSLIN	1.23	0.78
TSI	1.01	0.86

were also investigated. This type of investigation was straightforward since all photometers were simultaneously exposed to the same test aerosol in the aerosol chamber. To illustrate this correlation, scatter plots of the response of two photometers from the same manufacturer are shown in Figures 27 and 28, respectively, for the GCA RAM-I and Leitz Tyndallometer TM digital. These data show good agreement between each photometer as a function of instrument response regardless of the type of test aerosol. The average correlation coefficient obtained from statistical analysis was 0.998.

The data scatter in the photometer calibration plots, Figure 18 to 26, is due to systematic variations in the photometer response and random errors in the aerosol mass size distribution determination with the cascade impactor. Based on the excellent correlation between photometers from the same manufacturer, the data scatter does not result from significant random variation in photometer response. However, the scatter could be due to systematic variations which would affect all photometers equally. One such example would be a shift in the respirable aerosol size distribution which would affect the amount of light scattered, but not the actual mass concentration. The random errors in calculating the respirable mass concentration result from the uncertainty in the weighing of the impactor deposits, estimated to be approximately ±15%.

Additional work is planned in the areas of the effect of particle size distribution and higher mass concentrations on the photometer response. The response of all photometers was found to be affected by the relatively small difference in the size distributions between Coal-I and Coal-II. Thus, further studies need to be performed using test aerosols with larger differences between the particle size distributions to determine the significance of this size distribution dependency. Additional data are also needed for mass concentration in excess of 6 mg/m^3 to determine the linearity of the photometer response at high mass concentrations. The very limited data currently obtained indicate a possible decrease in the instrument sensitivity at these higher mass concentrations.

5.4 GCA RDM 101-1 Calibrations

Several GCA RDM 101-1 (GCA/Environmental Instruments, Burlington Road, Bedford, MA 01730) respirable aerosol mass monitors were calibrated in the aerosol chamber during this contract. These calibrations were made with and without the 10 mm nylon cyclone, which is used as a particle preseparator, on the inlet of the instruments. For the initial series of tests, the cyclone was removed from the inlet and respirable dust, as generated by the fluidized bed dust generator, was injected into the aerosol chamber. The second series of tests involved calibrating the unit with the cyclone mounted on its inlet.

The initial GCA RDM 101-1 study involved the calibration of seven GCA RDM 101-1 instruments for the Twin Cities Mining Research Center. These calibrations were performed by placing the instruments into the chamber without the respirable cyclone on their inlets and determining the mass concentration in the chamber with two filter samplers. The filter samplers used were Millipore Model XX 50 047 10 open faced filters placed 180° apart. These open faced filters became the standards to which the instruments were compared.

Tests were made to insure that the mass concentration, as determined through use of the open faced filters, was the true concentration and not biased by

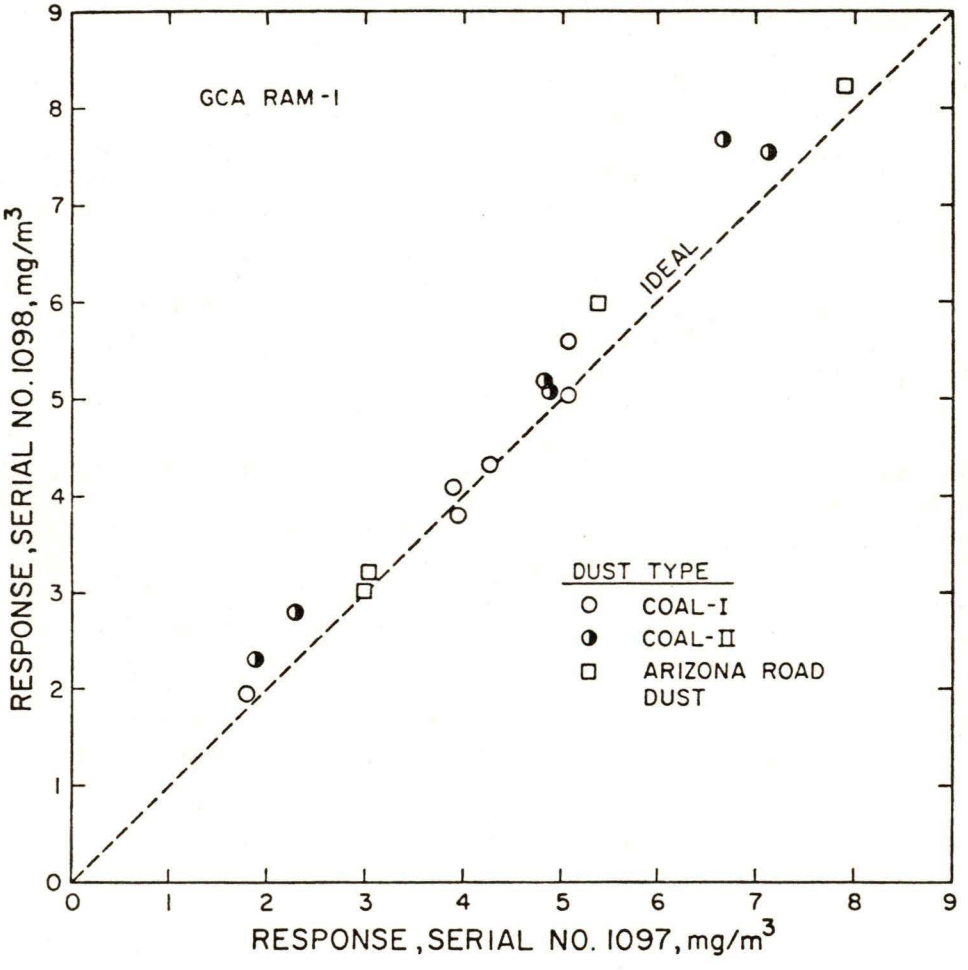

Figure 27. Response comparison between 2 GCA RAM-1 photometers.

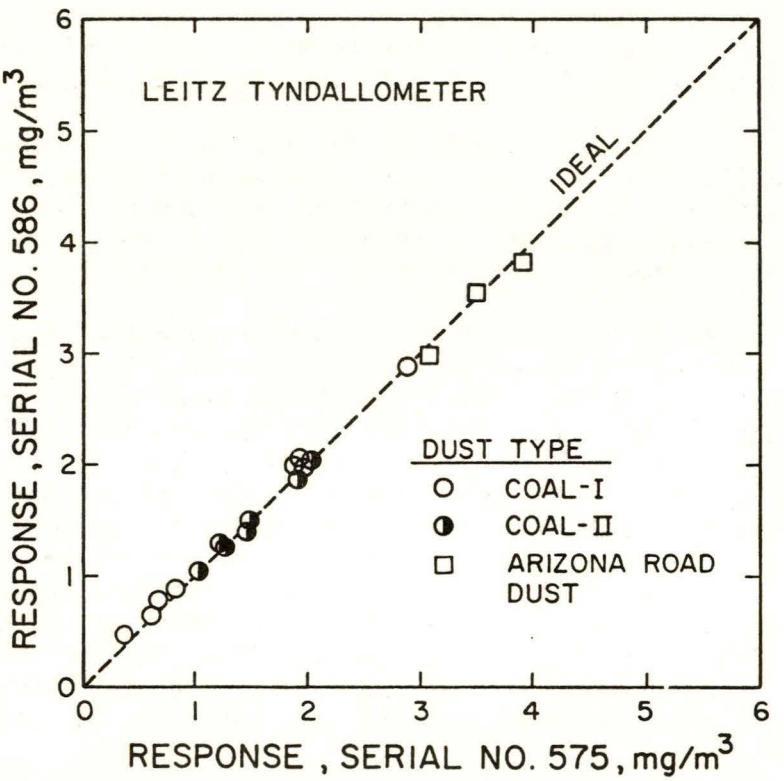

Figure 28. Response comparison between 2 Leitz Tyndallometer TM Digital photometers.

large particles settling onto the filters. For this study, two identical adjacent open faced filter samplers (one upright and the other inverted) collected the respirable fraction of Arizona road dust. The resulting mass concentration data obtained for these two filter samplers for several sampling runs are shown in Table 6. The average relative difference between the mass concentration determined from the upright and inverted filter was 3.2% which is within the experimental test uncertainty.

The theoretical inlet sampling efficiency of the open faced filter was also investigated using the numerical results obtained by Agarwal and Liu (14). Based on their work, the open faced filter when mounted in an upright position and sampling at a flow rate of 20 lpm from calm air should have a particle sampling efficiency near 100% for all particles less than 10 μm.

The results of RDM 101-1 calibrations are shown in Tables 7 and 8 and Figures 29 to 35. Here the gravimetrically determined mass concentration is given along with the average concentration provided by each instrument. The uncertainty bar associated with each data point is the standard deviation of the RDM 101-1 readings averaged together for that data point.

The test aerosols used for this evaluation were the respirable fraction of the aerosol from the fluidized bed dust generator. All seven units were initially calibrated using Arizona road dust and later two units were calibrated using coal dust. From the calibration data two distinct calibration curves were observed. Units with the serial numbers 2046 (Figure 29) and 2372 (Figure 35) had calibration curves which were similar to the calibration data obtained in past calibrations performed in our laboratory (10). While the other five units all have similar calibration curves, these curves indicate lower instrument mass sensitivity. One should note that all seven units were adjusted so that they correctly determined the appropriate mass concentration indicated on their calibration disks. The instrument sampling flow rate for the Arizona road dust tests was 1.7 lpm; whereas, it was 2.0 lpm for the coal tests. For the lower flow rate case, the instrument outputs were corrected to account for the lower sampling flow rate.

In the second series of tests the mass concentration response of one unit with a cyclone on the inlet was calibrated. For this study, the respirable dust concentration was calculated from the test dust mass size distribution as explained in Section 5.3. The tests were made using both coal and Arizona road dust aerosol. The resulting data is presented in Table 3 and Figure 36. The unit used in this evaluation was serial number 2154, which is the same unit used in a previously published study (10). These results are in excellent agreement with the results from that study.

5.5 TSI Model 3500 Respirable Aerosol Mass Monitor Calibration

Two TSI Model 3500 respirable aerosol mass monitors (TSI, Inc., 500 Cardigan Road, St. Paul, MN 55112) were briefly evaluated using coal and Arizona road dust aerosols. The instruments have impactors with a 3.5 μm diameter cutoff as an integral part of their inlets. Consequently, the instruments' responses were compared to the mass concentrations of particles less than 3.5 μm in diameter, as calculated from the test aerosol mass size distribution. This technique is described in Section 5.3.

Table 6

Standard Filter Sampler Evaluation

Mass concentration, mg/m^3		Relative Difference, %
Upright filter	Inverted filter	
2.64	2.60	+ 1.5
2.56	2.49	- 2.7
4.14	3.85	- 7.0

Table 7

GCA RDM 101-1 Calibration

for Respirable Arizona Road Dust

Gravimentric Mass Concentration, mg/m^3	Average GCA Reading, mg/m^3						
	Ser. No. 2320 (AA), mg/m^3	Ser. No. 2319 (BB),	Ser. No. 2060 (CC),	Ser. No. 2046 (DD),	Ser. No. 2334 (EE),	Ser. No. 2371 (FF),	Ser. No. 2372 (GG),
2.53	2.3	2.7	-	2.1	2.4	2.6	-
2.58	2.5	2.5	-	3.0	1.9	2.9	-
2.99	3.9	-	-	-	3.1	-	-
4.07	3.3	3.6	-	3.0	3.1	-	-
4.49	4.0	4.0	-	-	-	-	-
4.91	3.9	3.8	3.8	4.9	3.7	-	4.6
5.05	3.7	4.4	-	-	-	-	-
5.75	5.1	5.9	3.8	5.3	3.6	-	4.9
6.90	4.7	4.8	4.8	7.0	6.1	-	6.3
7.90	5.3	4.9	6.4	7.7	5.3	5.7	6.6

Table 8

GCA RDM 101-1 Calibration Data

for Respirable Coal Dust

Gravimetric Mass Concentration, mg/m^3	Average GCA Reading, mg/m^3 Ser. No. 2046 (DD),	Ser. No. 2372 (GG),
1.58	-	1.5
2.80	2.3	2.7
3.00	-	3.2

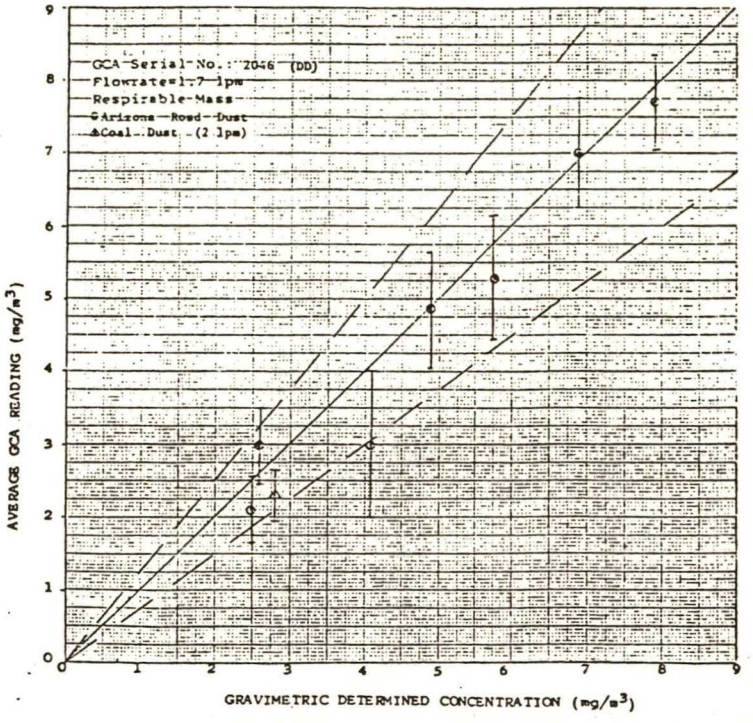

Figure 29. Calibration curve for GCA RDM 101-1 serial number 2046.

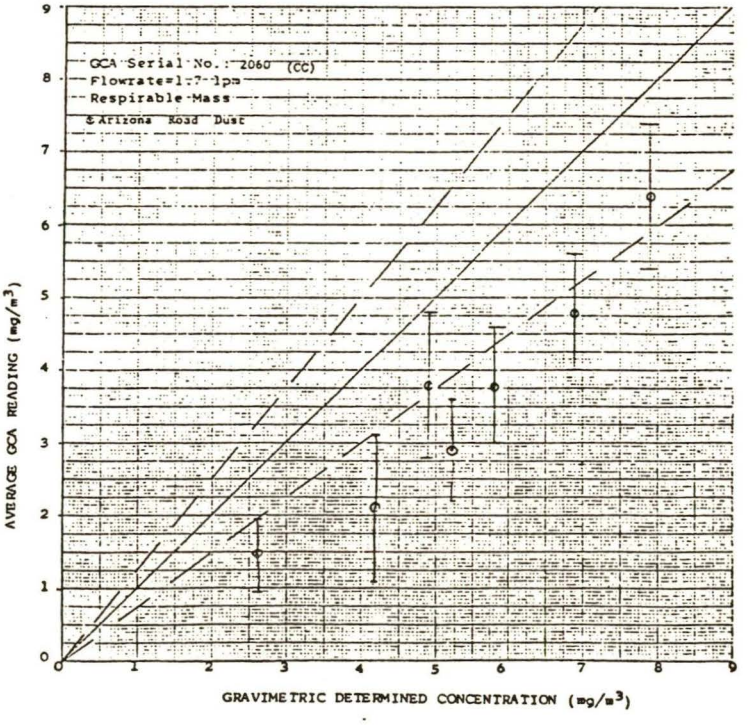

Figure 30. Calibration curve for GCA RDM 101-1 serial number 2060.

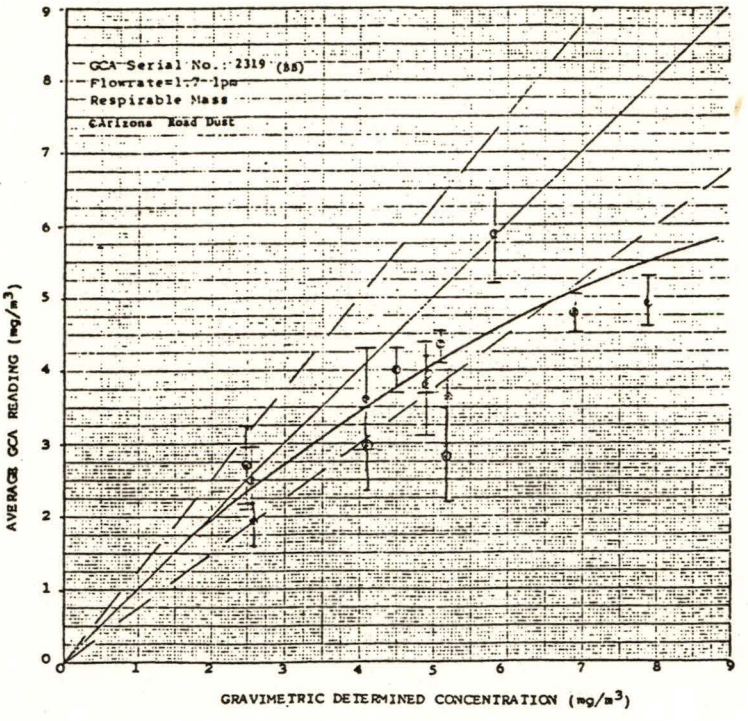

Figure 31. Calibration curve for GCA RDM 101-1 serial number 2319.

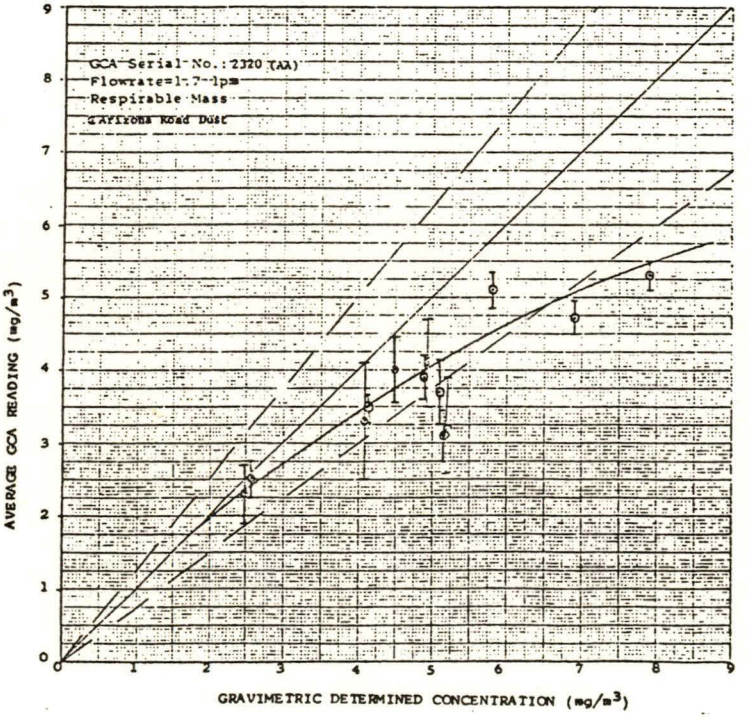

Figure 32. Calibration curve for GCA RDM 101-1 serial number 2320.

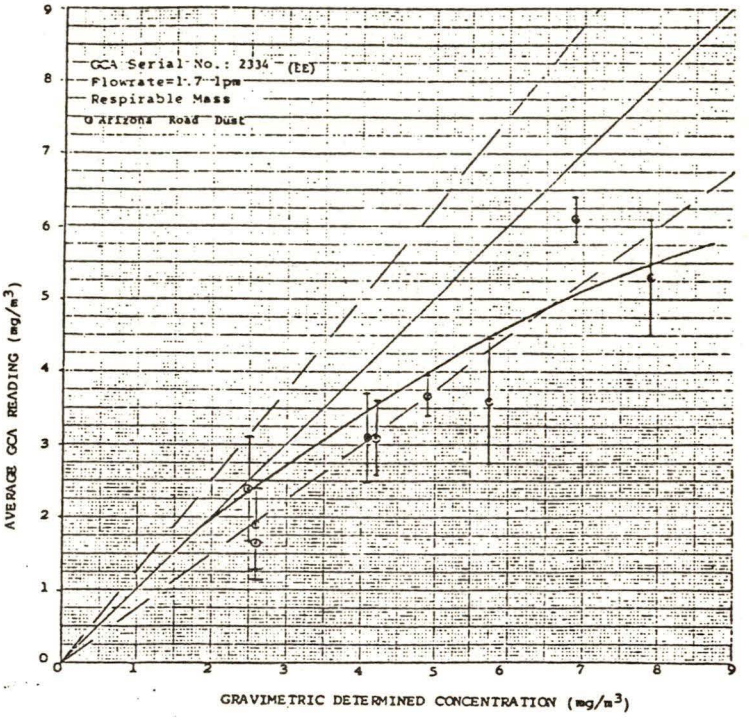

Figure 33. Calibration curve for GCA RDM 101-1 serial number 2334.

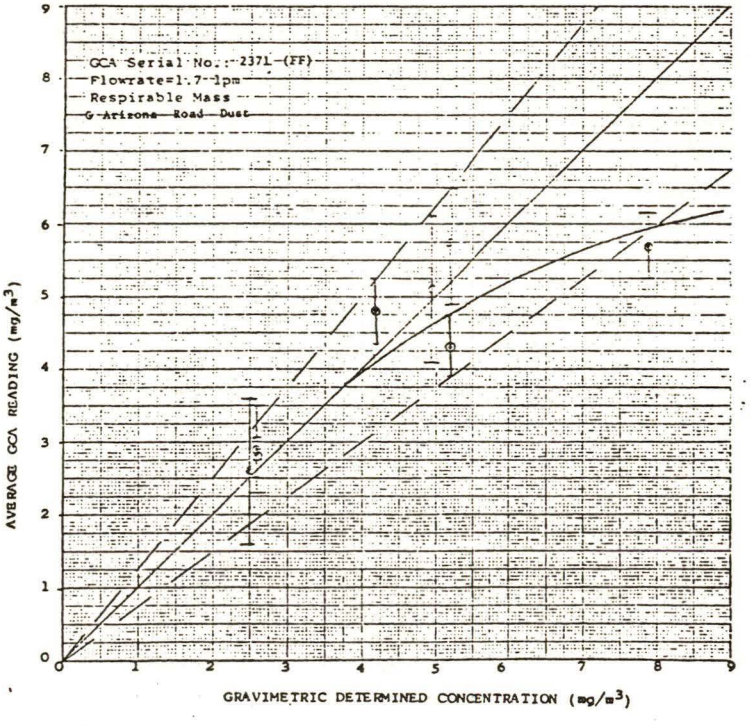

Figure 34. Calibration curve for GCA RDM 101-1 serial number 2371.

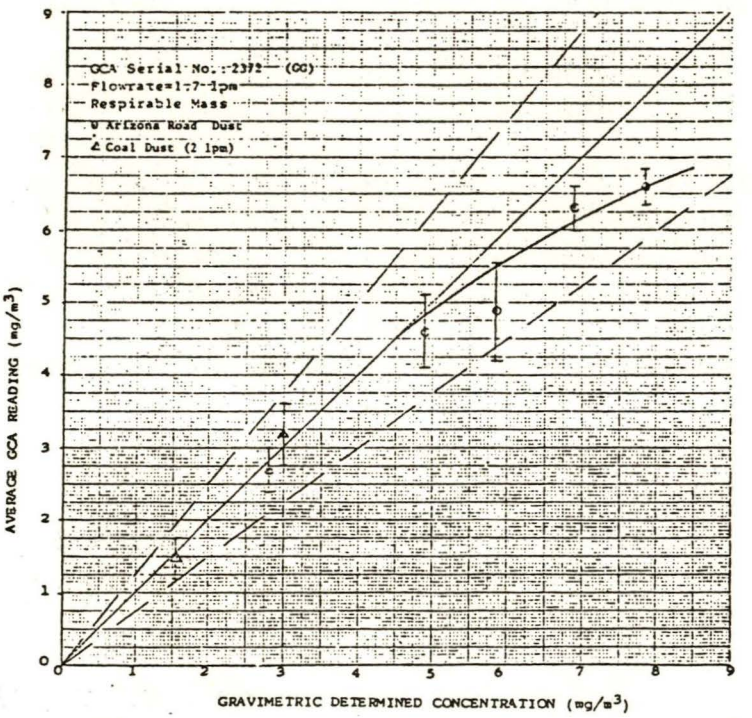

Figure 35. Calibration curve for GCA RDM 101-1 serial number 2372.

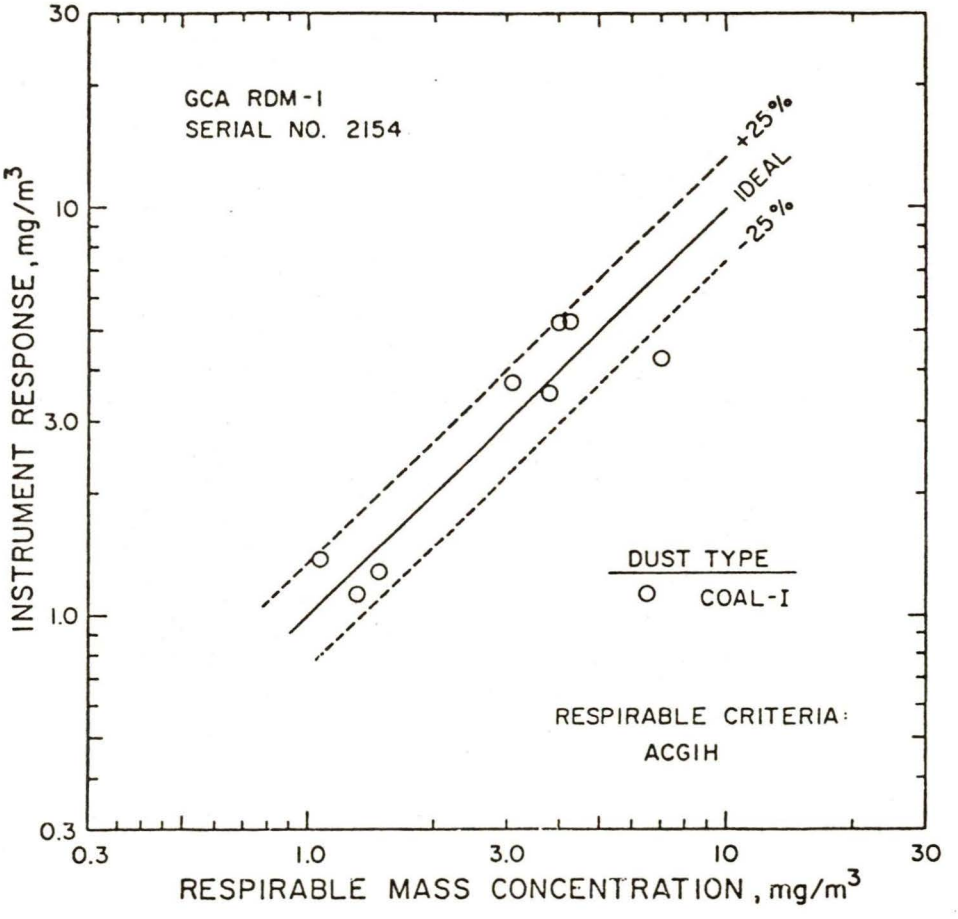

Figure 36. Calibration curves for GCA RDM 101-1 serial number 2154. (Data presented in Table 3.)

Table 3 and Figures 37 and 38 contain the resulting calibration data for the two mass monitors. For these tests the quartz crystals were cleaned prior to each series of runs. The results indicate that the responses of the mass monitors are a linear function of mass concentration. However, the responses are less than the respirable mass concentrations. Linear regression analysis shows the responses to be 0.82 and 0.58 of the respirable mass concentration for unit serial number 79485, respectively, for Coal-II and Arizona road dust test aerosols. For unit serial number 104, the response is 0.73 of the respirable mass concentration for Arizona road dust if one excludes the data point at a response of 4.11 mg/m^3. One possible explanation for the lower response is that the dry irregularly shaped particles are not completely coupled to the oscillating quartz crystal.

5.6 Evaluation Of Berkeley Controls QCM Cascade Impactor

An extensive evaluation of the Berkeley Controls Model C-1000A QCM cascade impactor (Berkeley Industries, Inc., 2825 Laguna Canyon Road, Laguna Beach, 92652) was performed during this contract. The evaluation, as summarized in Table 9, included the determination of the particle collection efficiency of each impactor stage, the interstage particle loss as a functon of particle diameter, the evaluation of the mass sensing capabilities of the quartz crystal as a function of type of aerosol, and the effect of particle loading on crystal response.

One result of the study is the particle collection efficiency curves for each impactor stage. The test aerosols were monodisperse liquid droplets. The submicron aerosol was DOP droplets generated by an evaporation condensation aerosol generator (15). This aerosol was passed through the differential mobility analyzer (DMA) electrostatic classifier to obtain the monodisperse test aerosol (16). The particle collection efficiency data was obtained by measuring the particle concentration upstream and downstream of each stage with a TSI Model 3070 electrical aerosol detector (EAD) (TSI, Inc., 500 Cardigan Road, St. Paul, MN 55112). This test setup is schematically shown in Figure 39. For these tests, the aerosol was drawn out of the impactor through pressure tap ports located on each stage.

The evaluation for particles larger than 1 μm was performed using oleic acid particles produced by the vibrating orifice monodisperse aerosol generator (VOMA). The particle number concentration was determined using a Royco Model 215 optical particle counter (OPC), (Royco Instruments, Inc., 141 Jefferson Drive, Menlo Park, CA 94025).

The experimental as well as theoretical collection efficiency curves (3) for each impactor stage are shown in Figure 40. This figure shows that the experimental data agree well with the theoretical curves for stages 5 - 10 but deviates for the larger particle collection stages (stages 1 - 4) with the amount of deviation increasing with increasing particle size. As will be discussed in Chapter 8, there is no apparent reason for this deviation. Based on the results presented in Figure 40, the particle cutoff diameters for each stage are listed in Table 10. For particle cutoffs less than 2.1 μm, the experimental results confirm the theoretically predicted values. Thus, the theoretical values are used to predict the cutoff. However, experimentally determined cutoff values are listed for cutoffs above 2.1 μm.

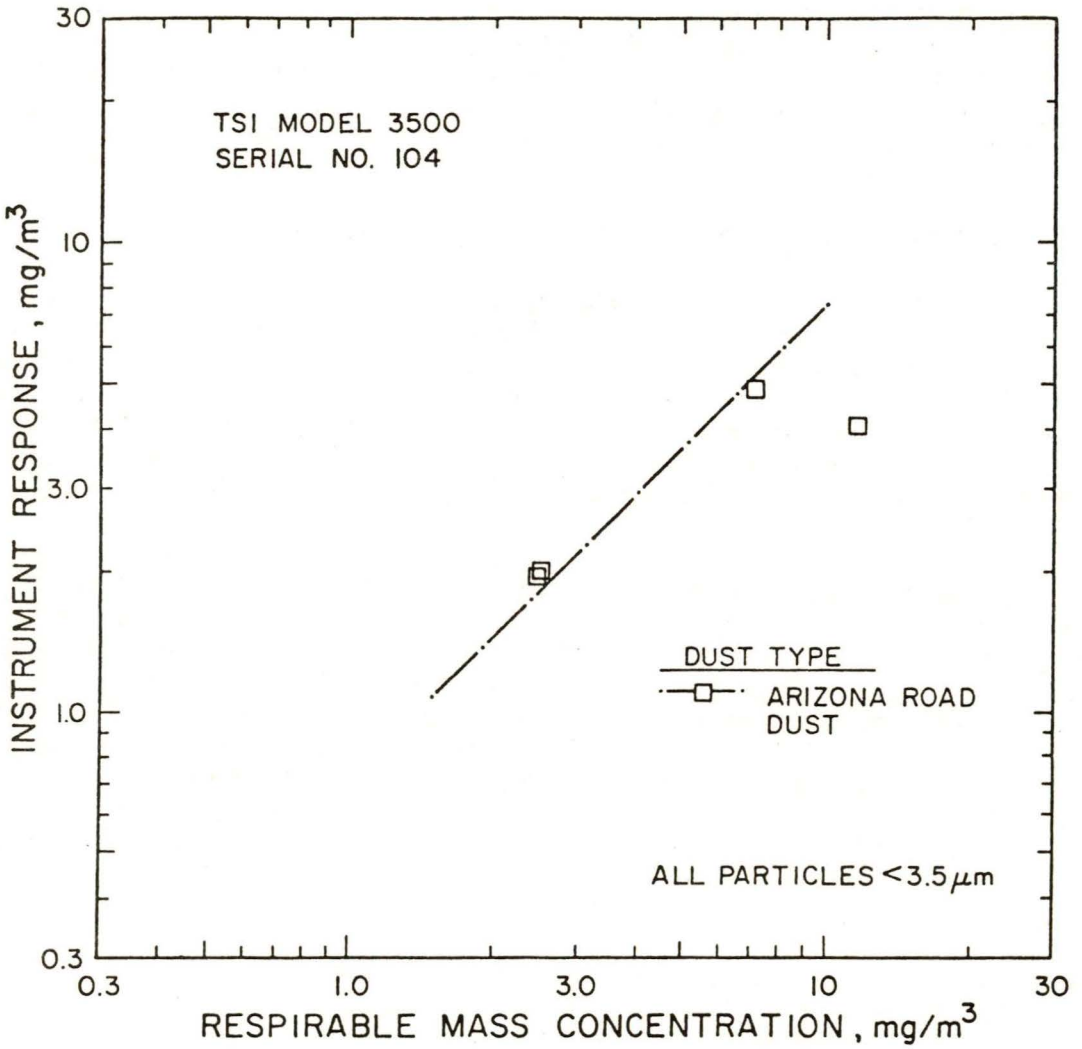

Figure 37. Calibration curves for TSI Model 3500 serial number 104. (Data presented in Table 3.)

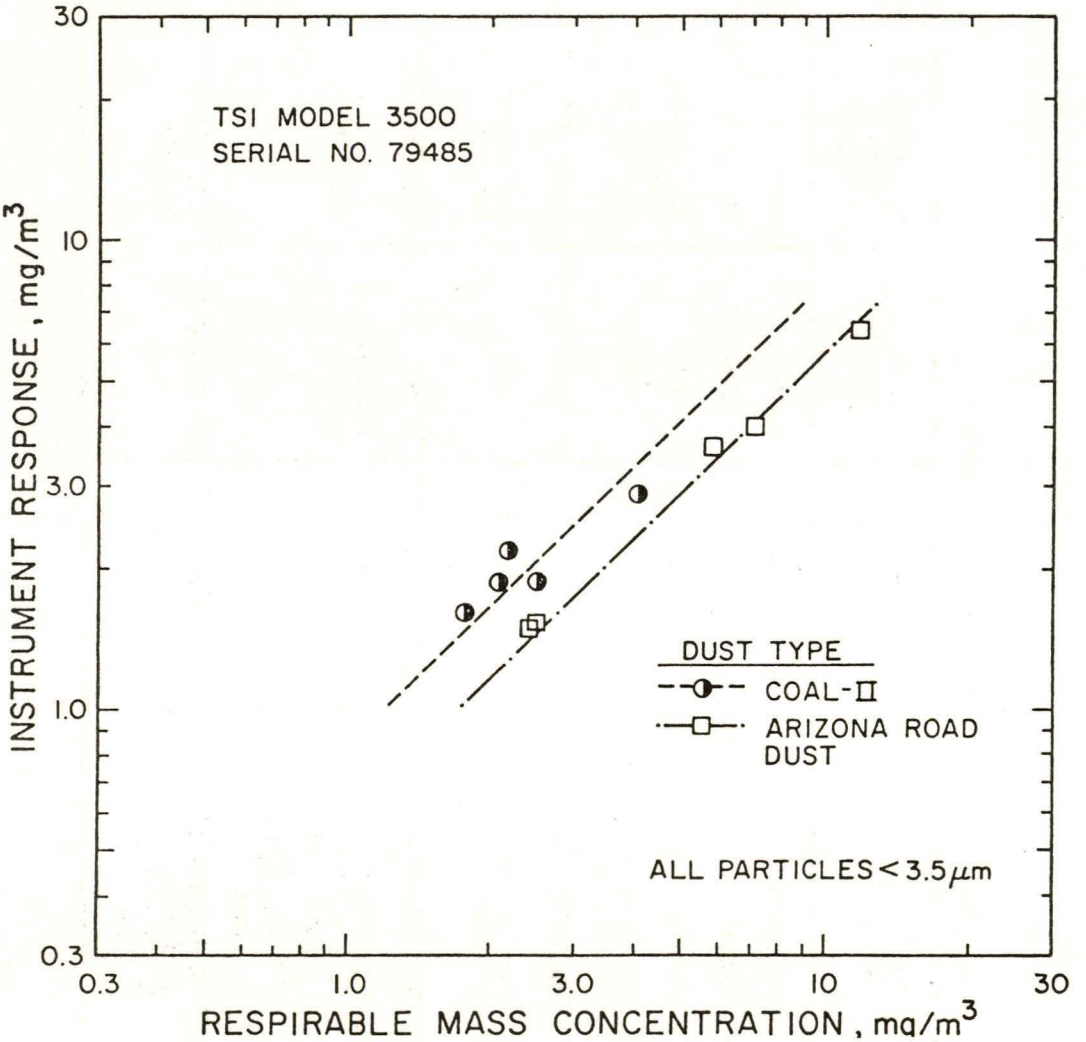

Figure 38. Calibration curves for TSI Model 3500 serial number 79485. (Data presented in Table 3.)

TABLE 9
Berkeley Controls QCM Calibration Summary

Type of Evaluation	Type of Aerosol	Particle Size - μm	Aerosol Generating System	Measurement Technique Analysis
Stage Collection Efficiency (Cutoffs)	1. Monodisperse DOP	0.05 to 0.46	DMA	EAD
	2. Monodisperse Oleic Acid	1.1 to 18.0	VOMA	OPC
	3. Monodisperse DOP	0.15 to 0.2	DMA	Mass sensing from QCM
	4. Monodisperse Oleic Acid and Uranine	2.3, 3.5, 7, 15	VOMA	Fluorometric Analysis
Interstage Losses	1. Monodisperse DOP	0.05	DNA	EAD
	2. Monodisperse Oleic Acid and Uranine	2.3, 3.5, 7, 15	VOMA	Flurometric Analysis
Mass Sensitivity	1. Monodisperse DOP	0.15 to 0.2	DMA	Electrometer
	2. Polydisperse Dust a. Respirable Coal Dust b. AC Fine Arizona Road Dust	Sub 3.5 μm	Fluidized Bed	Gravimetric Analysis
Mass Loading	1. Polydisperse Dust a. Coal Dust b. Arizona Road Dust	Sub 3.5 μm	Fluidized Bed	Gravimetric Analysis

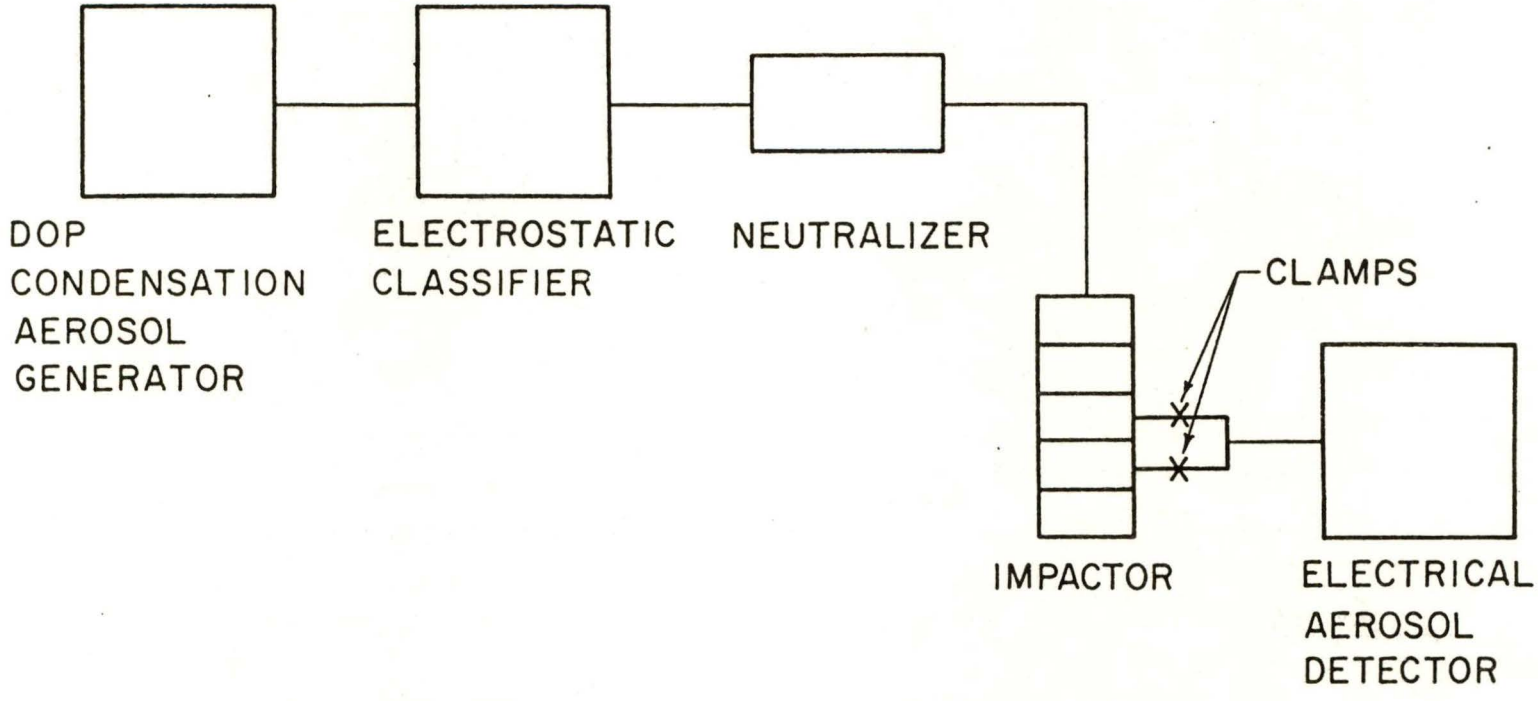

Figure 39. Schematic diagram of test setup used for Berkeley Controls QCM calibration with submicron particles.

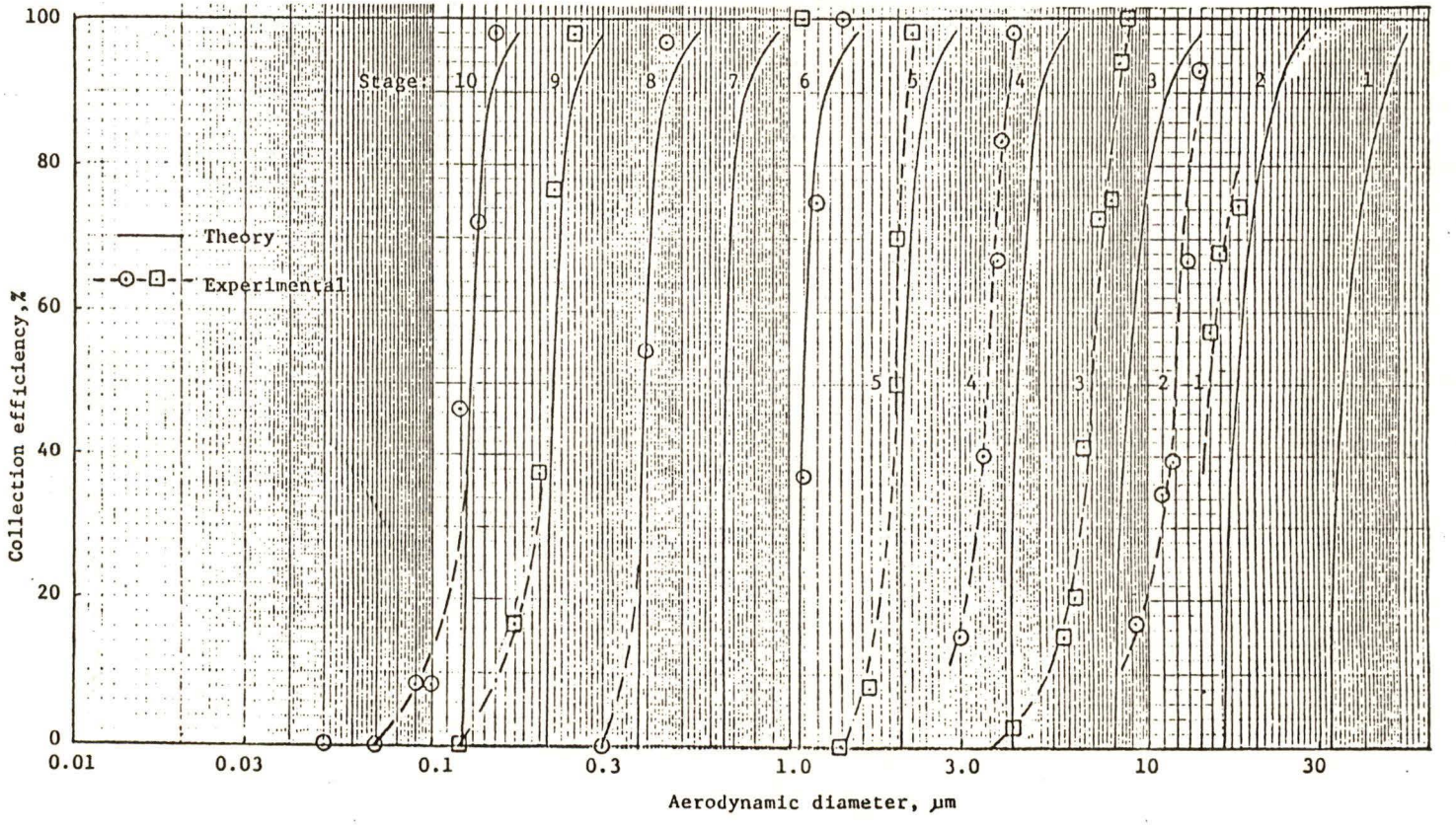

Figure 40. Berkeley Controls QCM particle collection characteristics of each stage.

Table 10

Berkeley Controls QCM Cutoffs
For Each Stage

Stage	Aerodynamic Cutoff Diameter, µm	
1	15.0	Experimental Calibration (Liquid Particles)
2	12.0	
3	7.0	
4	3.6	
5	2.1	Experimentally Confirmed Theoretical Values
6	1.11	
7	0.67	
8	0.40	
9	0.22	
10	0.127	

Another technique utilized to determine both the impactor collection efficiency and interstage losses for particles larger than 1 μm was to sample oleic acid particles which contained a uranine dye tracer. Particles of 2.3, 3.5, 7.0, and 15.0 μm diameter were generated with the VOMA. After sampling each size of particle, the QCM impactor stages were disassembled and all internal surfaces individually washed with known quantities of 0.02 N aqueous solution of NaOH. Then, by use of a fluorometer (Model 110, G. K. Turner, Associates, Palo Alto, CA), the concentration of uranine dye present in the wash, which was proportional to the amount of particles collected on a given surface, was determined. From this data, the determination of the particle collection efficiency and loss curves for each impactor stage, as well as the overall loss curve, could be made. The collection efficiency data determined by this method was found to be in agreement with results presented in Figure 40.

From this calibration technique, it was possible to not only determine the overall and per stage particle loss within the impactor, but to also determine what collection mechanisms were predominant in the losses. For example, it was found that most of the losses were on the upper surface of either the impactor chamber or the reference crystal. Thus, it appears that the losses were primarily due to settling, which might be expected, since the flow rate is only 0.25 lpm. In Figure 41 the particle loss per stage is presented for the particle size range of 2.3 to 15 μm.

The overall loss curve as shown in Figure 42 indicates maximum losses at about 10 μm. Greater losses are not found for larger particle sizes because they are collected upon the first stages and there is little time for them to be lost. However, for particles collected several stages into the impactor, which still have appreciable loss per stage, the accumulated loss is larger than for larger particles collected on the initial stages of the impactor. The small particles which penetrate deep into the impactor have very small losses per stage and thus, their total loss is small.

As was shown in Figure 41, the particle loss decreases with decreasing particle size due to diminishing gravitational and inertial effects. However, as the particle size decreases, the effects of diffusional loss increases. To investigate diffusion losses, an experiment was performed using a particle size which was smaller than the smallest particles collected by the QCM. The test aerosol was 0.05 μm diameter DOP obtained from the DMA. The particle concentrations upstream and downstream of all 10 stages of the QCM were measured using the EAD. The overall particle penetration was found to be 70%. Thus, for all collectable submicron aerosols, the particle loss will be less than 30% and should be negligible for particle sizes just below 1 μm.

The manufacturer's reported mass sensitivities for the quartz crystals were evaluated by investigating the ability of the QCM to accurately sense various types of aerosols. This evaluation was performed using several different types of particles including dry irregularly shaped dust particles (coal and Arizona road dust), diesel particles, and liquid particles.

The aerosol test chamber was utilized for experiments involving the dust aerosols. A 47 mm open faced filter sampler and a filter sampler which had a 3.5 μm particle cutoff impactor mounted on it's inlet were operated adjacent to the QCM. The test duration was 20 to 30 minutes, but the QCM only sampled the

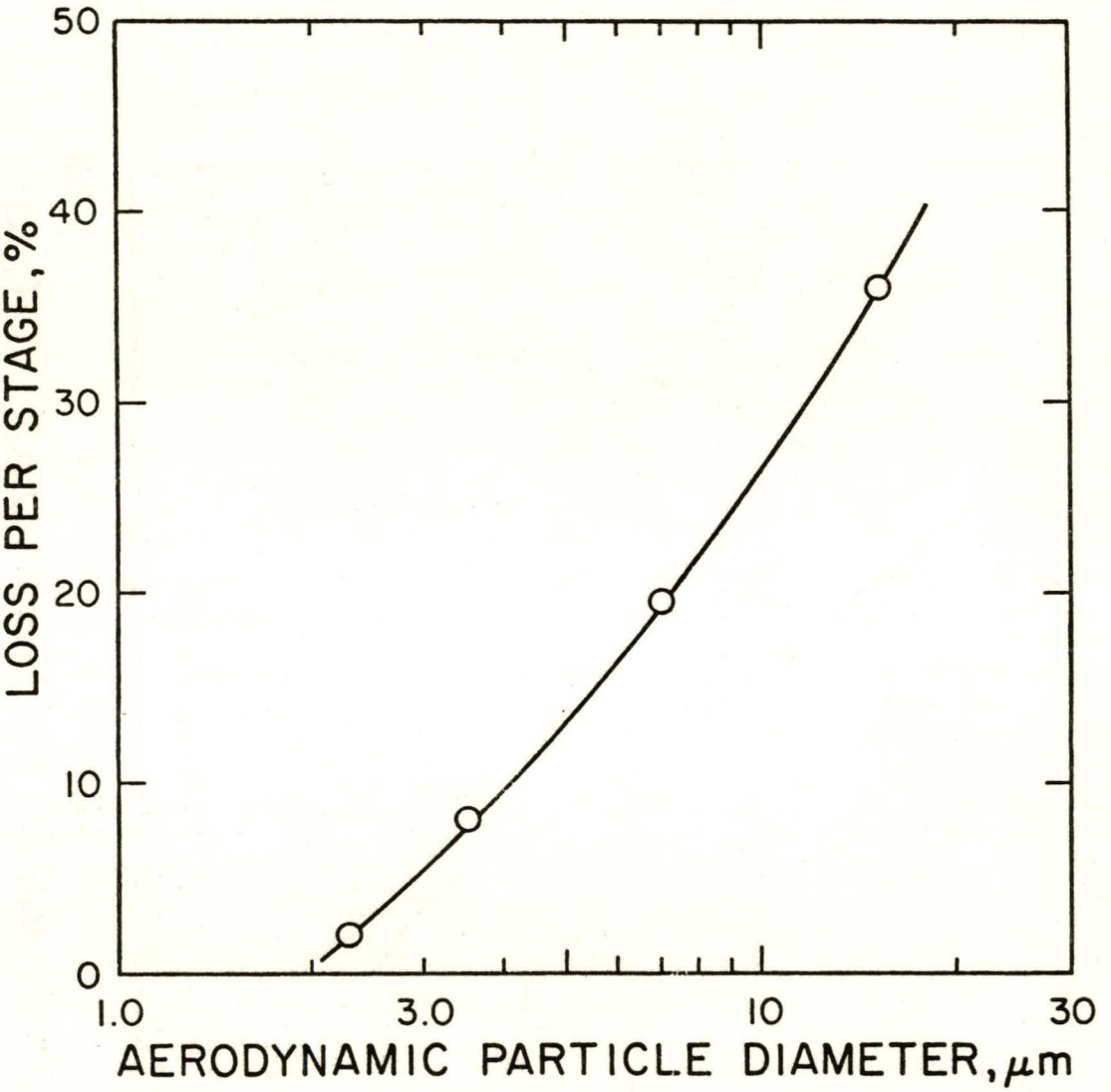

Figure 41. Berkeley Controls QCM particle loss per stage.

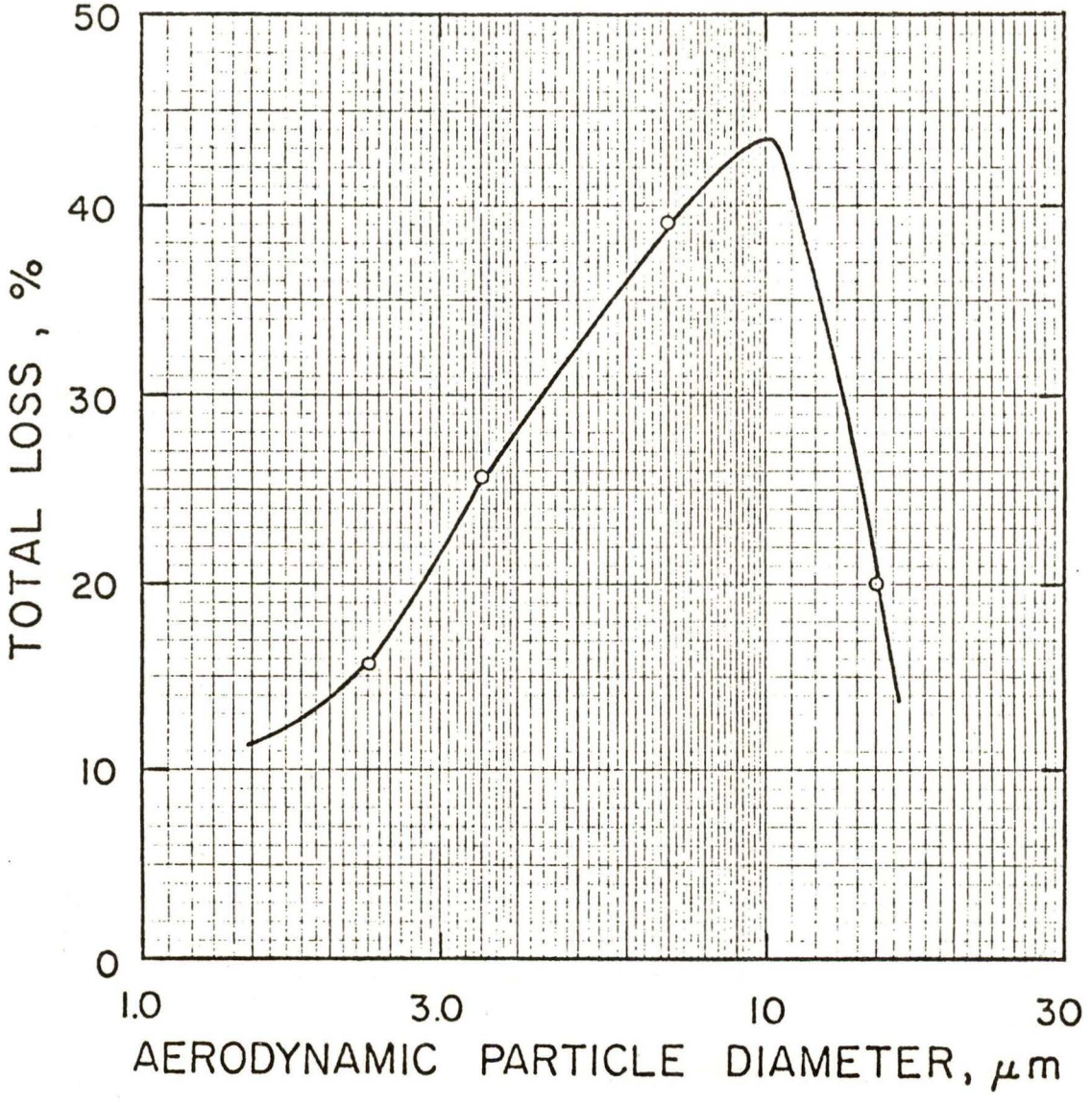

Figure 42. Particle Loss Curve for the Berkeley Controls QCM Cascade Impactor.

dust for 30 seconds. However, since the dust concentration and size distribution was constant within the chamber, the mass concentration as determined from the filter sample could be compared to the mass concentration as determined from the QCM. The QCM had freshly greased impactor crystals.

Table 11 contains the filter sampler and QCM indicated mass concentration for both coal and Arizona road dust aerosols. As can be seen, the comparison for the particles less than 3.5 μm showed less than 10% discrepancy. However, for the total mass concentration comparison, the QCM indication averages about 19% less than that obtained from the filter sampler. This discrepancy is primarily due to the high particle loss which occurs for particles greater than 3.5 μm.

The liquid particle test was performed using monodisperse DOP particles with one elementary unit of charge produced by the DMA. Thus, the particle number concentration could be determined with an electrometer. The aerosol concentration was measured using a Cary Model 401 electrometer (Varian Instrument Div., Cary Products, Inc., Palo Alto, CA 94303) and compared to the concentration as determined by the QCM. The resulting mass concentration data and the corresponding ratio of QCM to electrometer mass concentration ratio are presented in Table 12.

The QCM was also evaluated using diesel aerosol. For dry diesel aerosols, the QCM was found to have essentially no mass sensing capabilities, even though the particles were visually observed to be deposited upon the crystal. Apparently the diesel particles do not couple to the quartz crystal.

The effects of mass loading on crystal sensitivity was investigated using coal and Arizona road dust aerosols. The experiments were performed in the aerosol test chamber. A photometer which was used to monitor the chamber dust concentration showed a constant dust concentration for the duration of the tests, which lasted 20 to 30 minutes with 30 second samples taken by the QCM approximately once every 3 minutes.

Figures 43 and 44 show the resulting effects of mass loading on crystal sensitivity. The mass concentration for particles less than 3.5 μm was 2.10 and 3.4. mg/m^3, respectively, for the coal and Arizona road dust aerosols. The data obtained for stages 1, 2, 3, and 10 are not included due to insufficient mass loading. For stages 1, 2, and 3, the total accumulative frequency shift was less than 50 Hz per stage. However, these three stages should perform similarly to stage 4, due to their large particle deposition area. The crystals were freshly greased at the beginning of each series of tests. The accumulation frequency shift was obtained by summing each sample frequency shift. The relative sample frequency is the ratio of the frequency shift for each sample period to the frequency shift obtained during the first sample period. In computing the ratio, the amount of deposited mass is assumed to remain constant for each sample. Also, the effect of mass loading is assumed to be insignificant for the first sample. Thus, this ratio is the relative crystal sensitivity as a function of accumulative frequency.

The QCM's response, in general, decreases with mass loading as shown in Figures 43 and 44 for Arizona road dust and coal, respectively. This effect becomes more pronounced with decreasing particle cutoff size (increasing stage

Table 11

Comparison Between QCM and Gravimetrically Determined Dust Mass Concentration

Aerosol Type	Filter Mass Conc.,mg/m3		QCM Cascade Conc.,mg/m3		Total Mass QCM/Filter	Mass < 3.5 μm QCM/Filter
	Total Mass	Mass < 3.5μm	Total Mass	Mass < 3.5μm		
Arizona Road Dust	---	3.43	---	3.66	---	107.0%
Arizona Road Dust	2.99	2.06	2.42	2.05	81.0%	99.6%
Coal Dust	1.58	0.98	1.18	0.88	74.7%	90.1%
Coal Dust	3.00	2.10	2.62	2.25	87.2%	106.0%

TABLE 12

Comparison Between QCM and Electrically Determined Liquid Aerosol Mass Concentration

D_p, μm	Measured Mass Concentration, $\mu g/m^3$		
	Electrometer	QCM	QCM/Electrometer
0.15	38.3	42.5	1.11
0.20	184.7	178.7	0.97

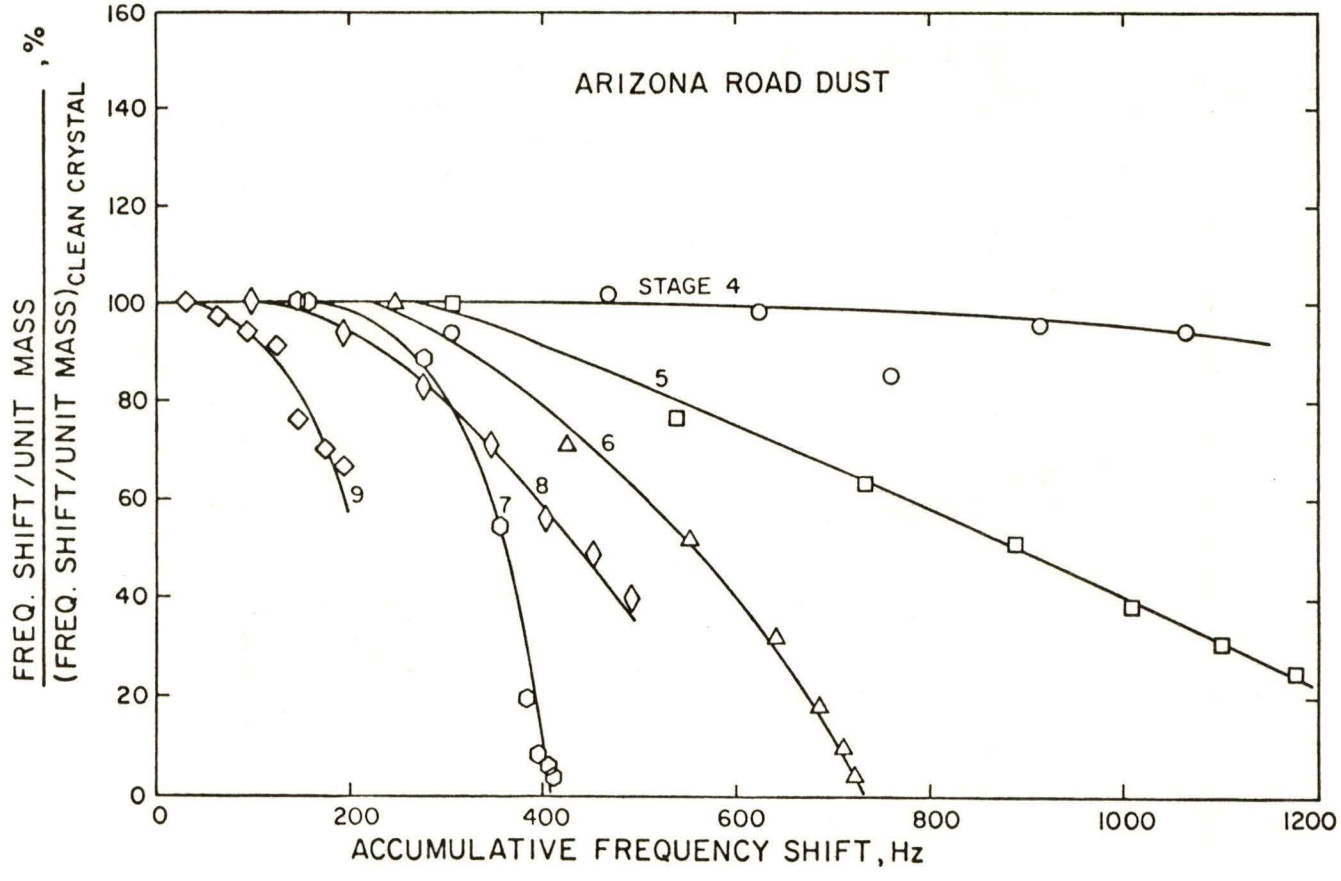

Figure 43. Relative response of Berkeley Controls QCM as a function of accumulative frequency shift for Arizona road dust loading on each stage.

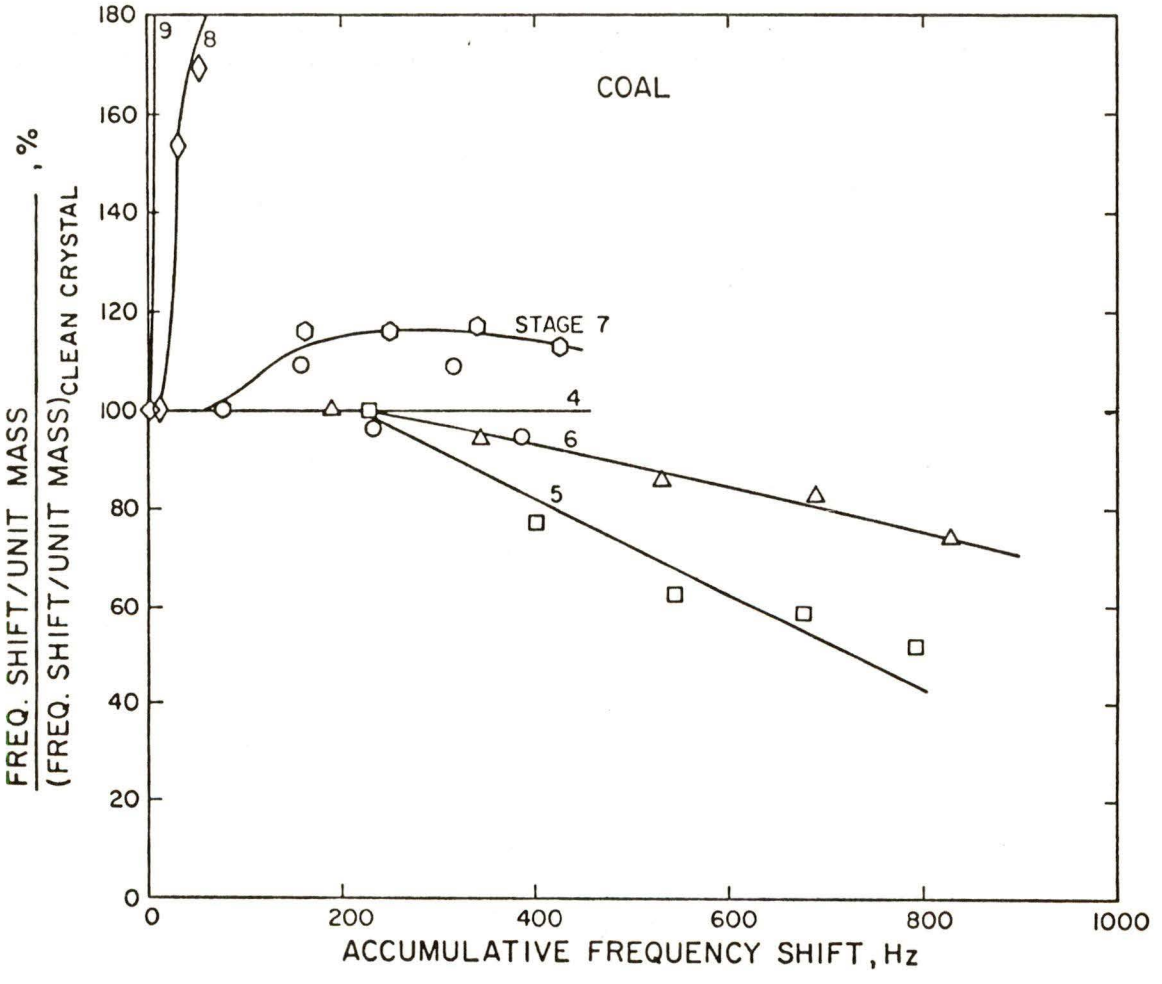

Figure 44. Relative response of Berkeley Controls QCM as a function of accumulative frequency shift for coal dust loading on each stage.

number). One explanation of this trend is that with decreasing particle cutoff size, the area of the sample collection depositon decreases. Thus, for the same mass loading (frequency shift), the depth of particle deposit will increase with the decrease in particle cutoff size. Consequently, the effects of mass loading become more pronounced.

For the case of the coal aerosol, particle bounce is the probable reason for the increase in relative crystal sensitivity. For particle bounce to occur, the deposited coal must be in some way impeding the wicking process of the grease through the particle deposit. This effect should be more pronounced on stages experiencing high mass loading. The experimental results indicate that the increase in relative crystal sensitivity occurred for stages downstream of those stages which received high mass loading.

The manufacturer's instrument manual acknowledges the existence of mass loading effects by stating that the maximum allowable crystal mass loading "normally" corresponds to 1000 Hz accumulative frequency shift. While this can be assumed to be true for stages 1 to 4, the maximum frequency shift decreases to less than 200 Hz for stage 9.

The effects of mass loading are also dependent on the type of aerosol. The effect is expected to be different for liquid and solid particles. But, even for solid particles, the effect is dependent on particle composition and perhaps on particle shape. Additional work is currently being performed to further characterize these effects.

CHAPTER 6
PERSONAL RESPIRABLE IMPACTORS

6.1 Introduction

The normal method of obtaining a personal respirable dust sample is to use the Dorr Oliver 10 mm cyclone/filter personal respirable dust sampler. However, in the course of this contract, two samplers which use inertial impactors as the respirable classifier have been evaluated. One of these devices is the MESA disposable respirable impactor and the other is a respirable personal impactor developed in our laboratory. Both of these are discussed in the following sections.

6.2 MESA Disposable Respirable Impactor

The evaluation of the MESA Disposable Respirable Impactor (17) was performed using monodisperse aerosols generated by a vibrating orifice monodisperse aerosol generator to determine the efficiency curve for the impactor. The details of the test are given in Appendix D.

The results of this study show that the efficiency curve presented in Figure 3 of Appendix D has approximately the same shape as the BMRC curve but is displaced to the right. This implies that the penetration characteristics of the impactor are such that the percent penetration for all particle sizes is larger than that of the BMRC criteria. As indicated in reference 17, the BMRC concentration values can be obtained by multiplying the concentrations determined with the MESA impactor by a factor of 0.5. However, it must be realized that this factor will be a function of the particle size distribution of the aerosol.

By changing the impactor nozzle head of this personal sampler as described in the following section, it is possible to obtain a penetration curve which approximates either the BMRC or the ACGIH respirable curves very closely.

6.3 University of Minnesota Personal Respirable Impactor

A method for designing impactors so that the penetration characteristics are approximately that of any respirable curve was previously developed in our laboratory (18). This technique involved using a single stage impactor with multiple nozzles of different sizes. By proper selection of the flow rate, nozzle sizes, and number of nozzles of each size, it is possible to approximate a curve in a stepwise fashion. The number of nozzle sizes determines the number of steps in the approximation.

In reference (18) the design parameters are given for impactors which would approximate the ACGIH curve at a flow rate of 2 lpm. To evaluate the feasibility of using this device as a personal sampler, three special heads containing nozzles and impaction plates were designed and built to fit on the filter holder and body of the MESA disposable respirable impactor described in the previous section. The three different heads corresponded to approximating the ACGIH curve with two nozzle sizes and three nozzle sizes and approximating the BMRC respirable curve with three nozzle sizes.

The results of this study and the details of the design are presented in Appendix E. As indicated in this appendix, the experimental curves determined by using monodisperse aerosols with a dye tracer are in good agreement with the theoretically expected curves for both the ACGIH and the BMRC criteria.

Another important aspect of the work presented in Appendix E is the use of an oil saturated porous impaction plate. As particles impact upon the impaction plate, the oil wicks up through the deposit and presents the oncoming particles with a fresh surface, and the problem of particle bounce and blowoff is minimized.

It was found in this study that sampling coal dust with a total mass concentration of approximately 8 mg/m^3 and a respirable concentration of 2 mg/m^3, the performance of the impactor did not deteriorate over approximately six hours. It was found, however, that the deposits on the impaction plate were large tree-like structures but it did not appear as through they were detrimental to the performance of the impactor.

The conclusion for this study was that impactor classifiers could be used as an alternate for the respirable cyclone. It appears as through the impaction device would be lighter, smaller, and could also be operated with the same personal sampler pump. Two important advantages of using the impactor as compared to a cyclone are as follows. First, the impactor could be designed to operate at any flow rate so that a flow rate larger than 2 lpm could be used and more material collected. For example, a 4 lpm impactor would provide twice the mass or one half the sampling time for the same mass. Second, the impactor can be designed to approximate the BMRC curve directly, then no correction factor would have to be applied to the data. This would be a more accurate method of obtaining the BMRC equivalent respirable dust concentration than using the Door Oliver 10 mm cyclone, since the conversion factor between the BMRC and the ACGIH must be a function of particle size distribution.

CHAPTER 7
UNIFORM DEPOSIT IMPACTOR

7.1 Introduction

One characteristic of conventional cascade impactors is that the deposits are collected in discrete locations. This characteristic leads to several problems including those of particle bounce and reentrainment, particles being collected on only a small part of the impaction plate requiring a larger tareweight than necessary when performing gravimetric analysis, and deposits not being suitable for analysis by techniques which require the particles to be uniformly distributed over a larger area such as x-ray fluorescence elemental analysis techniques. Thus, to correct these problems, a new type of cascade impactor, known as the uniform deposit cascade impactor, was developed in our laboratory.

Under partial support of this contract a prototype unit was built and has been used on several field projects. The principle of operation and the details of the design are presented in Appendix F. Basically, the technique is to use an impaction plate assembly containing a number of nozzles of uniform diameter. Each nozzle is located at a different distance from the center of an impaction plate which is rotating. The radial distances of the nozzles are such that the deposit on the impaction plate will be evenly distributed. The specific requirements as to the positioning of these nozzles is presented in Appendix F.

7.2 Impactor Design

The particular impactor that has been used under this contract has a design somewhat different than that described in Appendix F. However, the principles of operation are still the same. One of the differences is that the impaction plates are driven by worm and worm gear sets instead of bevel gears. Another change is that the coupling between the drive assembly and the impaction plate assembly is through the use of magnets instead of shafts. A thin sheet of metal has been used to make an airtight chamber for the cascade impactor. Two disk magnets are used for each impaction plate, one on each side of the thin metal sheet. The lower magnet is driven by the worm gear assembly and the magnetic attraction between the magnets rotates the upper magnet which is attached to the impaction plate.

Some problems have arisen because of these changes. One has been that the worm and worm gear sets have been difficult to align and there has been some wearing of the gears. Secondly, it has been difficult to precisely locate the center of rotation of the impaction plates since they are attached to magnets. Thus, the deposit is sometimes uneven.

Besides the uniform deposit feature of the impactor, another advancement in impactor development has been that the nozzles have been machined by a photo chemical etching process. With this technique it has been possible to machine very small diameter nozzles (as small as 25 μm diameter) which means that the cutoff sizes of the impactor can be very small. The cutoff size of this particular impactor has been about 0.06 microns aerodynamic diameter at a flow rate of approximately 30 lpm. Thus, a high volume of gases can be sampled by the impactor and yet the cutoff size can be kept small. This makes the instrument

usable for separating combustion aerosols, such as diesel exhaust particles, from other mining type aerosols.

Another feature of the instrument is that by removing the impaction plate assembly from the nozzle plate and drive assemblies, all of the impaction plates can be changed at one time. In addition, by placing a cover on these impaction plates, it is possible to not have to touch the impaction plate substrates in the field. The impactor surfaces can be prepared in a laboratory before the test and disassembled in the laboratory after the test.

Finally, by spreading the deposits over a large area the deposits can be analyzed by x-ray fluorescence analysis. In all of the field tests where this impactor has been used, this has been the analysis method.

7.3 Current Status

The development of the instrument is still in progress. However, the instrument has been used in several field tests for both the Bureau of Mines and EPA. In most cases the instrument has operated satisfactorily. The most recent application of this impactor has been in the field study at a tungsten mine. The details of that study are presented in Chapter 9 of this report.

CHAPTER 8
GENERAL IMPACTOR CALIBRATION, CALCULATIONS, AND DEVELOPMENT

8.1 Introduction

During the course of this contract there have been intermittent studies concerning the calibration of impactors. Many of these studies have led to significant results and insights into the operation of impactors and, in some cases, new problem areas have been defined for which no answer has yet been obtained. Brief descriptions of these studies are presented in the following sections.

8.2 Calibration of Berkeley Controls QCM Cascade Impactor

The results of the Berkeley Controls QCM impactor stage cutoff evaluation have been presented in Section 5.6. In all cases it was expected that the cutoff characteristics would agree well with that predicted by theory. However, as shown in Figure 40, the agreement between theory and experiment is only completely satisfactory for particles of size less than approximately 2 μm diameter. For larger particles there is a difference between the experimental and theoretical efficiency curves which becomes more pronounced as the size increases. There is no apparent reason for this discrepancy and this phenomena has initiated some further work which is described in the following section.

8.3 Further Investigations of Inertial Impactors

The problem of the differences between the experimental and theoretical efficiency curves for the larger particles is considered very important since the application of impactors is being applied to larger particles at an increasing rate. This is especially true since EPA became interested in inhalable particles at 15 microns in diameter. Thus, a program involving both theoretical and experimental studies was initiated.

From a theoretical point of view, there appears to be no reason why large particles should not be modeled as well as small particles. However, in the original theory the particles were assumed to be of such small sizes that they were considered to have all their mass at a point (no physical dimension). The finite size of the particles, however, becomes significant when the particles are near the impaction plate. Thus, since the time the original work on impactors had been performed, a technique had been developed by which the physical size of the particles can be expressed as a function of the Reynolds number, Stokes number, and the particle density.

Therefore, the theoretical programs were run again with the physical size of the particles being considered. A comparison of the efficiency curves for both round and rectangular impactors using these two techniques are shown in Figure 45. As expected, at the low values of collection efficiency, the particles are very near the impaction plate and would be collected if their physical size are considered. Thus, the characteristic 'S' shape, which is normally found only in experiments, has been shown to be the case in the theory as well. However, the 50% cutoff point has been essentially unchanged by this correction to the theory and does not predict a shift as was found in the QCM cascade study.

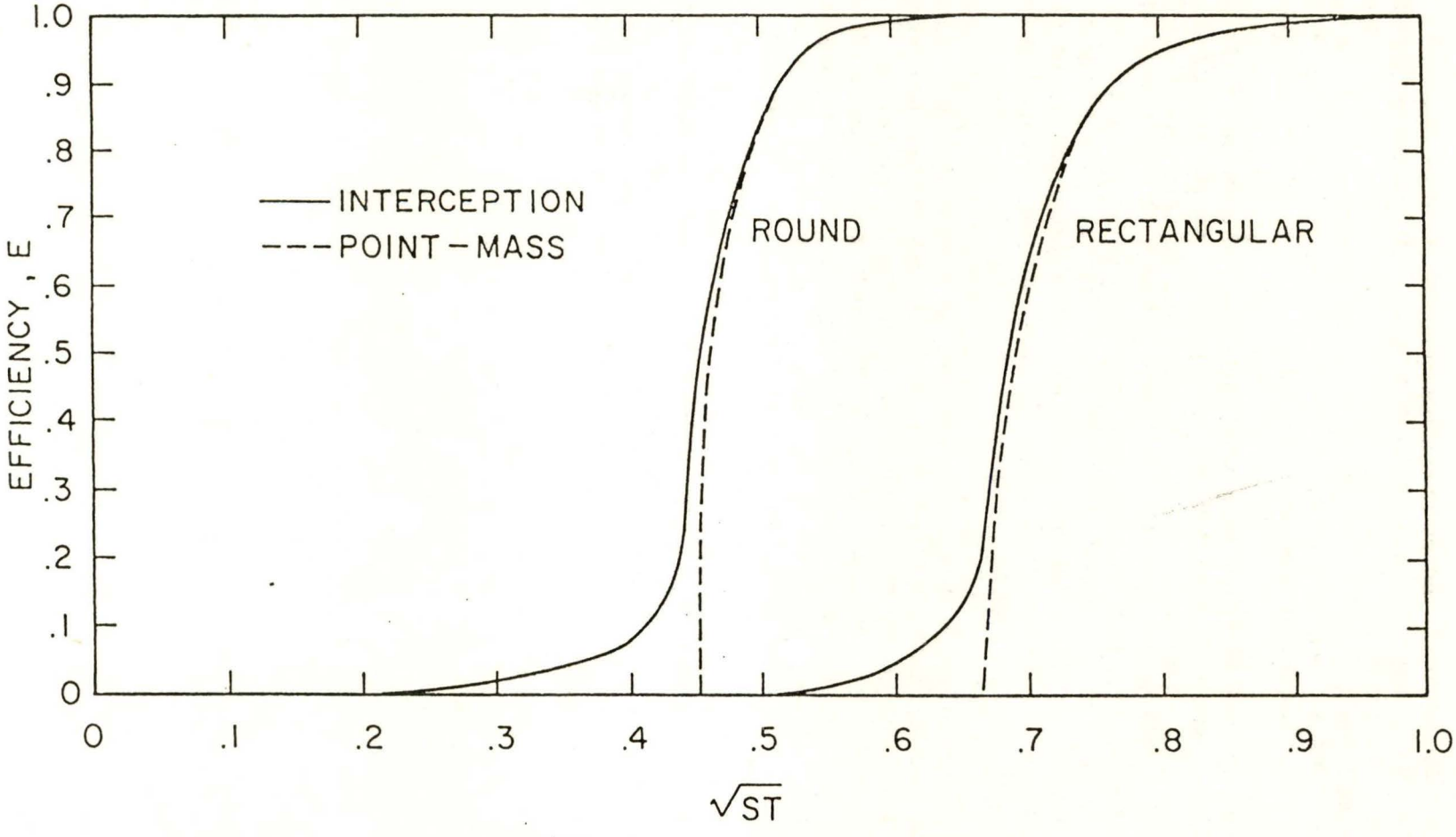

Figure 45. Theoretically predicted impactor particle collection efficiency curves based on point-mass and interception methods.

As a consequence of considering the physical size of the particles, the density of the particles is now a new parameter. This parameter can actually be defined as a ratio of the particle density to the fluid density and, thus, be kept in dimensionless form. However, this was not found to be a large factor as shown in Figure 46, where collection efficiencies for particle densities of 0.5, 1.0, 2.0, and 10.0 are presented.

Another parameter which was investigated was the value of the Reynolds number of the particles passing through the air. In the theory, the particles are assumed to be Stokesian, (particle Reynolds numbers less than 0.1) but a theoretical study indicated that the Reynolds numbers could be as large as 1.5. However, as the drag coefficients were modified for the larger particles' Reynolds number, it was found that there was little influence on the resulting efficiency curve. Thus, the ultra-Stokesian Reynolds numbers of the particles is not the reason for the differences between the experimentally and theoretically determined efficiency curves.

In the experimental study, calibrations were made on single stage impactors other than the QCM cascade and similar differences between the theoretical and experimental curves were found. However, for one set of tests, it was found that the theoretical and experimental efficiency curves agreed if the particles were solid but efficiency curves for liquid particles of the same size had a shift similar to that of the QCM cascade. Although these tests were interesting, when they were further investigated, the differences between solid and liquid particles were not found to be significant.

Due to the inconsistencies which have been found and scatter in the data, the experimental techniques for calibrating impactors of large sizes are being investigated further. It may be found that liquid particles are not completely dried or are becoming deformed as they pass through the nozzle and thus do not conform to the theory.

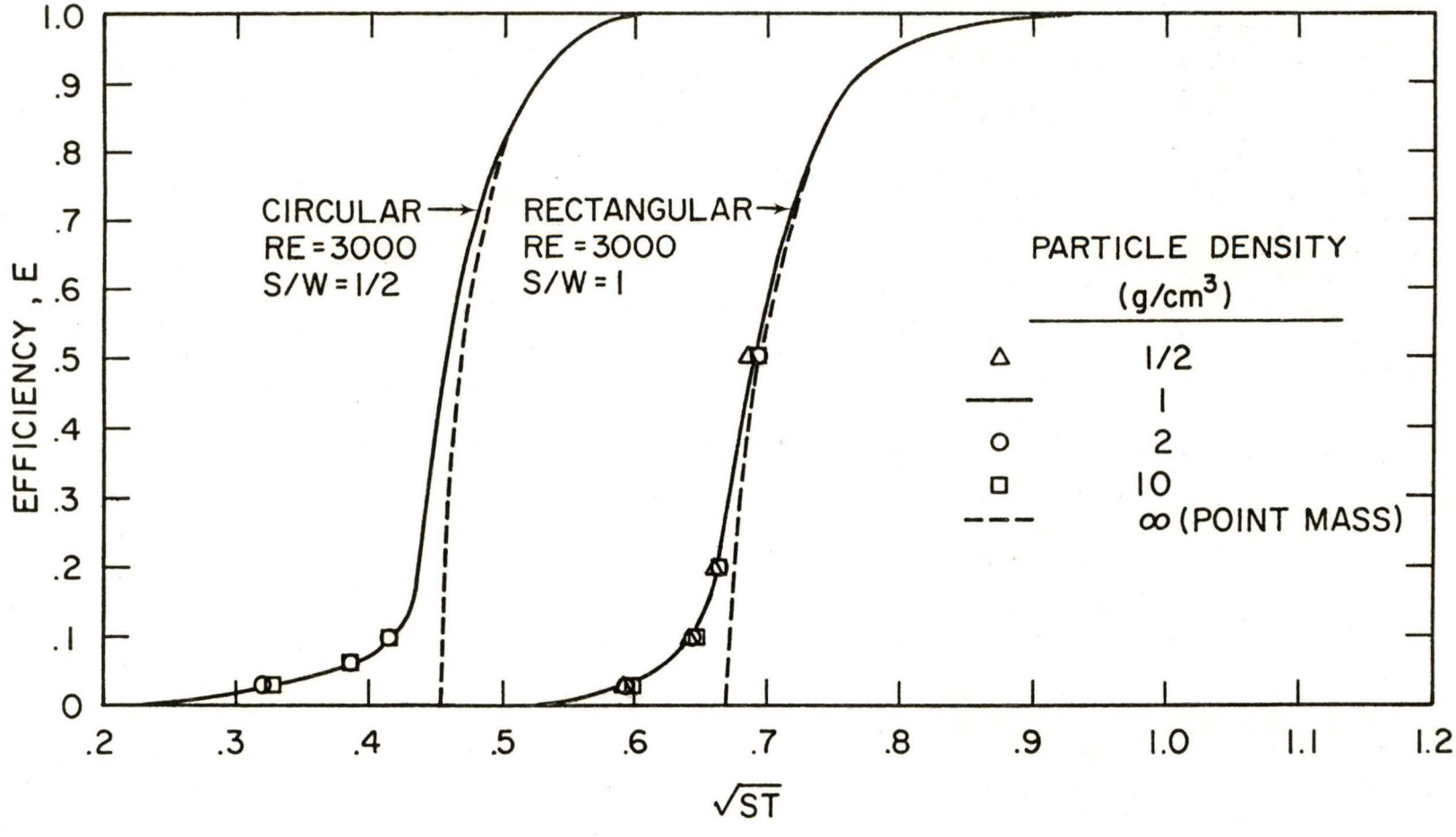

Figure 46. Effect of particle density on theoretically predicted impactor particle collection efficiency curves based on interception method.

CHAPTER 9
FIELD STUDIES

During the course of the contract period two experimental field studies were performed. The location of the two field studies were a silica sand plant and a tungsten underground mine. Both of these studies were performed in conjunction with the Twin Cities Mining Research Center (TCMRC) personnel and in the case of the tungsten mine, in conjunction with personnel from Illinois Institute of Technology Research Institute (IITRI). The work performed by the TCMRC personnel at the silica sand plant will be published as Bureau of Mines Information Circulars (IC). This report will only highlight some of the preliminary findings of the studies.

9.1 Objectives and Instrumentation

The primary purpose of these studies was to evaluate the instrumentation either developed and/or evaluated during the contract under actual field conditions and to determine aerosol size distributions and concentrations in the work place. The objectives of these two studies were as follows:

1. Evaluate the in-field use of the laser diode OPC by comparing the aerosol size distribution obtained with it to that measured with a cascade impactor.
2. Evaluate the response of photometers and mass monitors to changes in aerosol concentration and size distribution.
3. Evaluate the use of the uniform deposit impactor (UDI) to obtain elemental composition via x-ray fluorescence analysis of submicron aerosols.
4. Determine the aerosol concentration and size distribution as a function of specific work activity or location and time of day.
5. Determine the diesel aerosol concentration in the tungsten mine.
6. Assist the Bureau of Mines and IITRI personnel in obtaining data for their sampling programs.

Instrumentation used in one or both of these studies was either developed in our laboratory or was commercially available. The developmental instrumentation included the laser diode optical particle counter (OPC) and the UDI. The instrumentation used at the silica sand plant included:

1. laser diode OPC
2. TSI Model 3500 Respirable Aerosol Mass Monitor
3. TSI Model 5150 Respirable Aerosol Photometer

The Sierra Model 266 cascade impactor was also intended to be used, but the aerosol concentration was too low to obtain an adequate sample. The instrumentation used in the tungsten mine included:

1. laser diode OPC
2. uniform deposit impactor
3. TSI Model 3500 Respirable Aerosol Mass Monitor
4. GCA RAM-1 photometer
5. Sierra Model 266 Cascade Impactor

9.2 Instrument Calibration

The data analysis presented in this report is based on the instrument calibration data obtained with either coal or Arizona road dust aerosols. The results of these calibrations are presented in Chapters 3 and 5.

The laser diode OPC used in both of these studies has only been calibrated with coal dust and ideal particles. Therefore, the laser diode OPC calibration curve was estimated from the calibration curves obtained for the Royco 218 OPC (6) which has previously been calibrated on silica and Arizona road dust as well as coal and ideal particles. By comparing the response of the two OPCs for coal and ideal particles, the estimated calibration curve for silica and Arizona road dust for the laser diode OPC was obtained. This comparison was possible since both instruments had near forward scattering optics. However, both the actual light scattering angles and light wave length were slightly different. Figure 47 shows the laser diode OPC coal calibration as well as the estimated calibration curve for the silica and Arizona road dust.

For the tungsten mine preliminary data analysis, the GCA RAM-1 photometer sensitivity was assumed to be equivalent to the manufacturer's provided value. As presented in Section 5.3, the photometer's response for coal and Arizona road dust aerosols agrees well with this provided value. However, since the majority of the respirable aerosol in the mine was diesel aerosol, the photometer's sensitivity could significantly differ from the provided value. This is because almost all of the diesel aerosol is contained in particles less than 1 μm in diameter. Consequently, the fraction of the diesel aerosol large enough to scatter sufficient light to be detected by the instrument is unknown. The second source of uncertainty is the instrument's sensitivity to that portion of the diesel particulate matter which does scatter a detectable amount of light, since the index of refraction for diesel particulates is much different than for rock dust.

9.3 Silica Sand Plant

The silica sand plant study occurred on June 25, 1980 and involved 6 hours of aerosol sampling during the day shift. The particular area of the plant studied was the sand bagging operation. This plant is less than one year old and incorporates the latest sand bagging equipment. The air in the sand bagging room was not subject to any particle control measures and outdoor air freely could infiltrate into the room. The material being bagged was sifted and screened silica sand with a nominal particle size of approximately 100 μm. The instrumentation was set up approximately 8 m from the sand bagging machines at a height of approximately 0.3 m above the floor. During the sampling time, one or both of the machines were in operation, except for a 20 minute lunch break. One routine room cleanup also occured during the sampling period.

The TSI Model 5150 photometer was used to continuously monitor the aerosol concentration by recording the output analog signal with a strip chart recorder. Due to an improper instrument adjustment, the absolute aerosol concentration could not be obtained. Consequently, the photometer reading was used solely to obtain the relative information of the aerosol concentration and, in particular, periods of minimum and maximum concentration. This information was especially useful to determine the periods of maximum concentration which occured during the morning clean-up and minimum concentration which occured during the lunch break. The data also showed that, with the exception of brief periods of dust increases, the dust concentration was very stable during the time the bagging operations were being performed.

Table 13 contains a listing of the major activities which occured during the sampling period and corresponding respirable mass concentrations. The

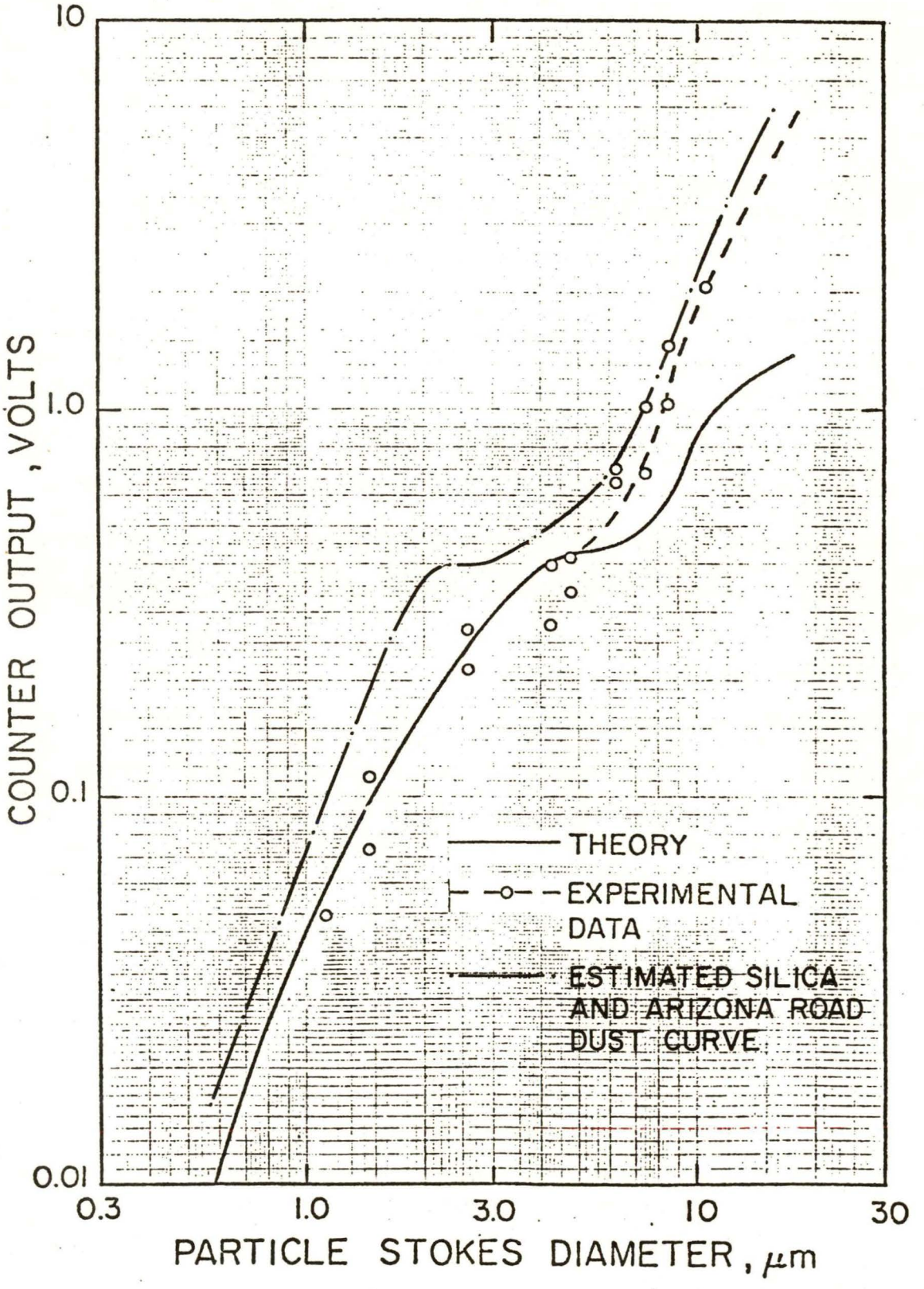

Figure 47. Laser diode optical particle counter coal calibration curve and estimated calibration curve for silica and Arizona road dust.

Table 13

Activity and Average Respirable Aerosol Mass Concentration for Silica Sand Plant Bagging Operation

Activity	Average respirable mass concentration [1,2] mg/m^3
Minimum during lunch break	0.08
Typical bagging operation	0.10
Sweeping floor around bagging machine	No Data
Maximum during general room clean up	0.41

[1] Data obtained with TSI Model 3500, serial number 79435. which monitors the mass of particles less than 3.5µm aerodynamic diameter.

[2] TLV is not known because quartz concentration was not determined.

respirable mass concentration was obtained with the TSI Model 3500 respirable aerosol mass monitor. These data were reduced using the calibration sensitivities reported in Section 5.5. Results show that the most significant respirable mass concentration increase occurred during the general morning cleaning, which involved sweeping and vacuuming of the building bulkheads, floors, and equipment. During this time the concentration increased by a factor of 5 over the minimum lunch break concentration. Otherwise, the respirable aerosol concentration was within a factor of 2 of the minimum value (lunch break). The TLV concentration is not known because the quartz concentration was not determined.

Typical aerosol size distributions obtained with the OPC are shown in Figure 48. Each curve represents the average of the two to seven one-minute-samples. The data is plotted at the geometric mean diameter for each particle size range as obtained from the multichannel analyzer. The four sets of data represent the episodes at lunch break, typical concentrations observed during the bagging operations, maximum concentrations which occured during the sweeping of the accumulated silica dust around the bagging machine, and the grand average of 15 runs made during the six hour work shift. Consequently, comparing the data obtained during the bagging operation to that observed at the lunch break indicates that there is a preferential increase in the larger particle concentration occuring during the bagging operation. However, when comparing the data for typical bagging operations to that of sweeping around the bagging machine, the concentration increased by approximately a factor of 2 for all particle sizes in the range of 1 to 20 μm. The grand average particle size distribution was also essentially the same as the typical bagging operation concentration size distribution. The concentration peak which occurred at approximately 10 μm may be real or may result from the use of the estimated calibration curve. This will be further investigated during the final data analysis.

9.4 Tungsten Mine

The study at the underground tungsten mine, which extensively used diesel powered equipment, occured from October 26-30, 1980. This mine was found to be extremely wet, which greatly reduced the mine generated dust concentration. The ore being mined contains tungsten, molybdenum, copper, and trace amounts of gold and silver, with the host rock being granite and metamorphosed limestone. The main ore body strikes were approximately due north-south and dipped almost vertically.

A schematic of the mine is shown in Figure 49. The main mine entrance and haulage track was at the 8100 ft level. All the mining activity took place at elevations above this level. The mine was divided into two working areas. The south workings were between the 8100 and 11,200 ft levels. Ore being mined in this area was dumped via diesel powered front-end loaders into the main vertical ore pass. The north workings were located above the 9400 ft level. Ore from this area was dumped into ore passes and loaded into ore haul cars at the 9400 ft level. The ore was dumped by a rotary car dump into the main ore pass. At the bottom of the main ore pass the ore was loaded from chutes (1 and 2) into ore cars at the 8100 ft level.

The mine ventilation air was brought in at the 9400 ft level where it was equally divided between the upper and lower portions of the mine. The mine's

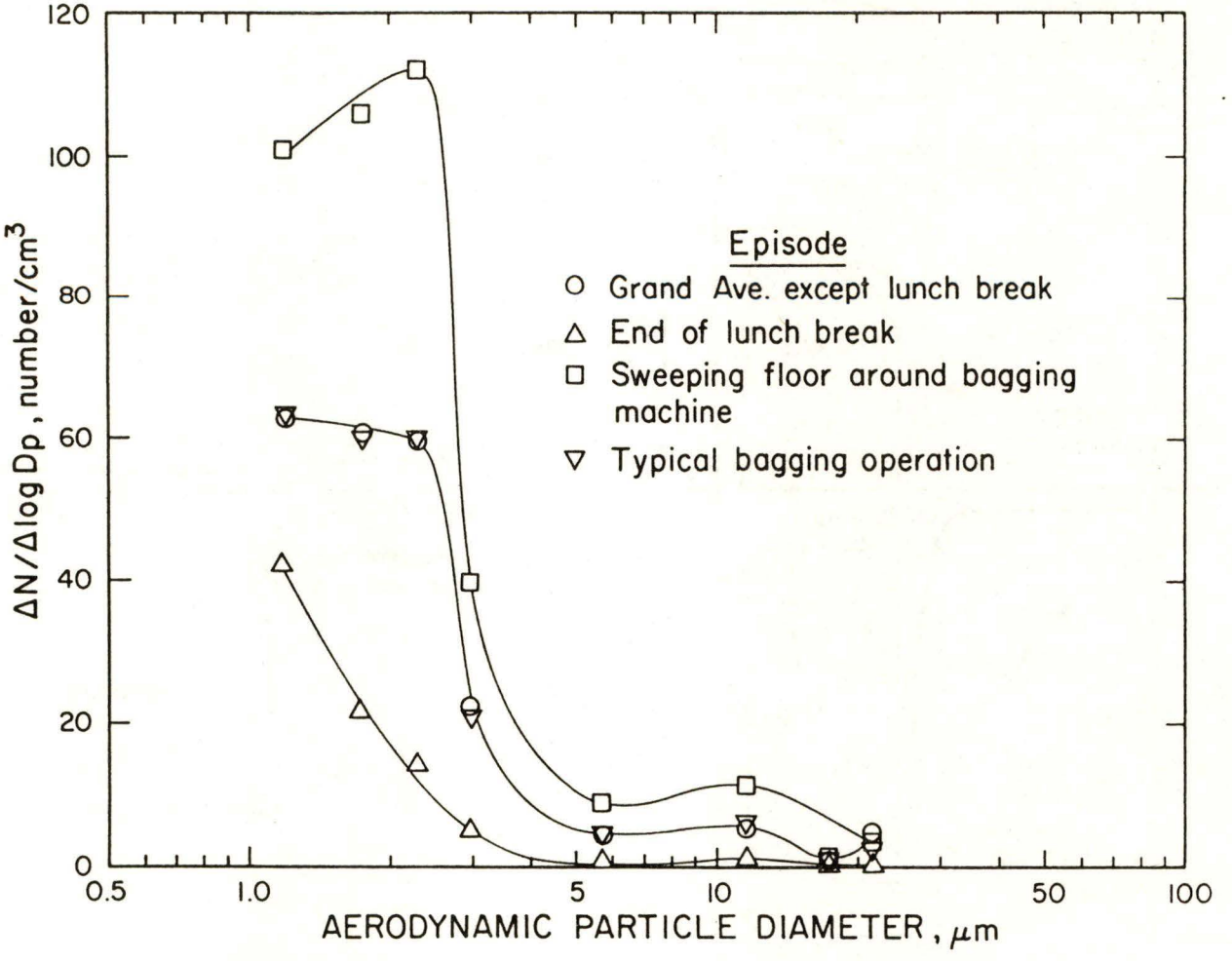

Figure 48. Aerosol size distribution for silica bagging operation measured with laser diode OPC.

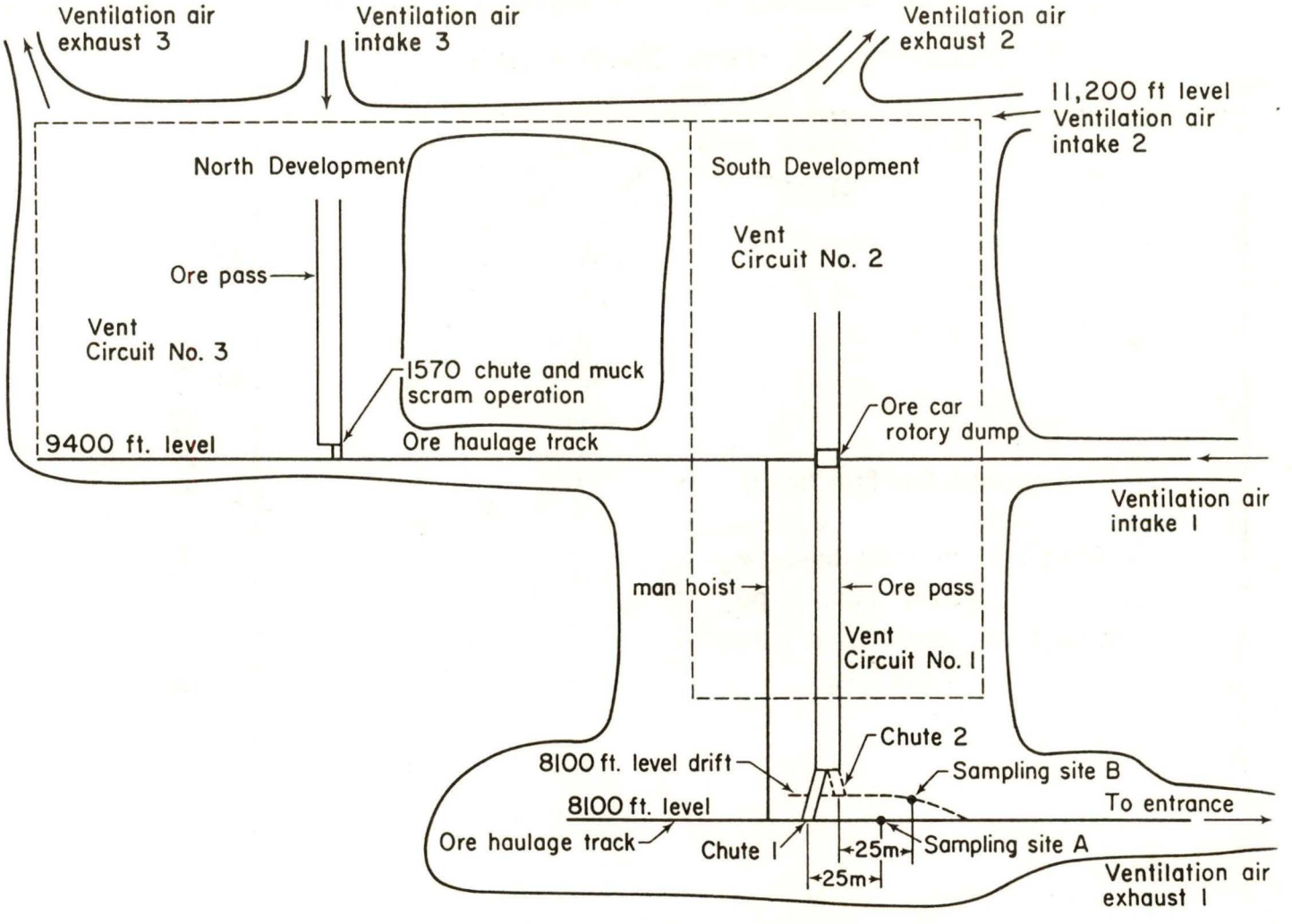

Figure 49. Schematic diagram of tungsten mine layout.

ventilation air, which was passed through the lower portion of the mine, traveled through the workings, vertical ore pass, and the elevator shaft to the 8100 ft level, where it was exhausted through the mine entrance.

The primary sampling sites were at the 8100 ft level, and approximately 25 m downwind of the chute areas used for loading ore cars. These sites are listed as sampling sites A and B in Figure 49. At these sites 110 v. AC power was available for operating non-battery powered instrumentation. These locations are also in the exit region of the mine ventilation system. Consequently, the aerosol sampled here would include aerosol from all mine operations. A total of 98 and 95 one minute sample runs were made with the laser diode OPC at sampling sites A and B, respectively. Data were simultaneously obtained with the GCA RAM-1 photometers.

On October 29, 1980, a sampling walk through tour was conducted in the lower portions of the mine. For this tour two GCA photometers were used, one monitoring the respirable aerosol concentration and the other monitoring the mass concentration of particles less than 1.5 μm in diameter. This tour included mine operations which occured between the 8100 and 9400 ft levels.

Table 14 presents the aerosol mass concentrations as a function of mine location or source and time of day. Two aerosol mass concentrations are listed, the respirable mass concentration and the mass concentration for particles less than 1.5 μm aerodynamic diameter (diesel particles). For the case of the mass less than 1.5 microns, the instrument's respirable cyclone was replaced with an impactor (9). These RAM-1s were a matched pair and read exactly the same aerosol concentration when operated with their respirable cyclones in place. With the exceptions of noted dust sources or ore dumping, as shown in Table 14, diesel particles are the major respirable aerosol source, since the respirable and <1.5 μm diameter particle concentrations are the same. The respirable aerosol concentration was approximately 0.08 mg/m^3 at the start of the morning shift at sampling site A and 0.04 mg/m^3 in the incoming ventilation air. The respirable concentration increases during the shift to values of 1 to 3 mg/m^3 at sampling site A and B as well as most locations surveyed in the work areas. The data also shows that 80-90% of the respirable aerosol is less than 1.5 μm.

Table 15 contains the date, time, and sampling locations for the cascade impactor runs made in the tungsten mine. Five runs were made with the Sierra cascade impactor and three runs were made with the UDI. The theoretically determined particle cutoff sizes of the Sierra impactor are listed in Table 2 for a flow rate of 4 lpm. The UDI had cut sizes of 0.4, 0.4, 0.16, and 0.16 μm aerodynamic diameter for a flow rate of 30 lpm. The redundant stages were used to evaluate possible particle bounce. An after filter collected all the material leaving the impactor. The UDI was operated with a cyclone preseperator mounted on the inlet of the impactor which had a cut size of 1.3 μm. The deposited material in the Sierra impactor was used to obtain the aerosol mass size distribution, whereas the deposited material in the UDI was used to determine elemental concentrations by x-ray fluoresence analysis. The laser diode OPC and the GCA photometer were operated continuously during the periods when the impactor samples were being obtained.

A mass stability problem for the coating used on the Sierra impactor impaction plates was found during this study. The impaction plates used in the

Table 14

Aerosol Mass Concentration as a Function of Source and/or Location and Time of Day in Tungsten Mine

Source and/or location	mass concentration [1], mg/m^3	
	respirable	aerosol <1.5 μm diameter
Incoming ventilation air shaft	0.04	0.04
Exhaust ventilation at sample sites A and B		
- 9:00 am[2]	0.08	0.06
- typical[3]	1.0	0.8
- maximum[3]	3.0	----
9100 ft level shaft at 1570 chute		
before blast	0.15	0.13
maximum during blast	1.20	0.13
Muck scram operation at 1570 chute operation station	0.095	0.07
Idling diesel powered front end loader		
upwind	0.04	0.04
downwind	1.10	1.10
Mucking operation with diesel powered front end loader		
typical	2.2	2.0
maximum	4.0	----
Adjacent to ore pass between 9100 and 8157 ft. level during dumping of ore	2.50	1.00
Cage hoist area at the 8157 ft. level	0.2-0.6	----

[1] Data obtained using GCA RAM-1 photometer serial number 1097 and 1098.

[2] Before any mining activity commenced.

[3] Due to water in ore, no detectable increase in aerosol concentration during ore car loading operation.

Table 15

Log for Cascade Impactor Operation

Impactor	Date	Time, Hr:min	Location
Sierra 266	27 Oct	14:33-15:02	A
	28 Oct	24:03-15:05	A
	30 Oct	10:24-11:34	B
	30 Oct	12:03-13:06	B
	30 Oct	13:31-14:35	B
UDI	28 Oct	11:20-14:44	A
	30 Oct	11:00-12:04	B
	30 OCt	12:47-13:44	B

Sierra impactor were 18 mm diameter glass microscope slide cover slips coated with Apiezon type L grease (James G. Biddle Co., Plymouth Meeting, PA 19462). The plates were weighed out of the mine before and after the mine sampling runs and were transported in Millipore 47 mm petri dishes. A study was performed with this particular coating in the laboratory using dehumidified air in the laboratory aerosol dust generators. In this case the coating instability was found to be less than 5 µg, which is the uncertainty in the mass determination procedure. However, control coating surfaces, when exposed to the mine atmosphere were found to gain on the average 48 µg. Because of the significant amount of mass gain by the control surfaces, the mass determined for each stage of the impactor was corrected for this weight gain. Consequently, there is significant uncertainty in the cascade impactor determined aerosol size distribution.

Figure 50 shows a typical size distribution obtained with the Sierra cascade impactor. Note that 53% of the mass was in a size range less than 0.55 µm diameter and collected on the after filter. This sample was obtained at sample site B on October 30, 1980 during the times from 12:03 to 13:06. The total mass concentration determined from the cascade impactor data was 1.35 mg/m^3. The average respirable concentration and mass concentration for particles less than 1.5 µm obtained with the GCA photometers during this time was 1.51 and 1.48 mg/m^3, respectively. Thus, the cascade impactor data correlates well with the photometer data indicating that most of the respirable mass is contained in particles less than 1.5 µm.

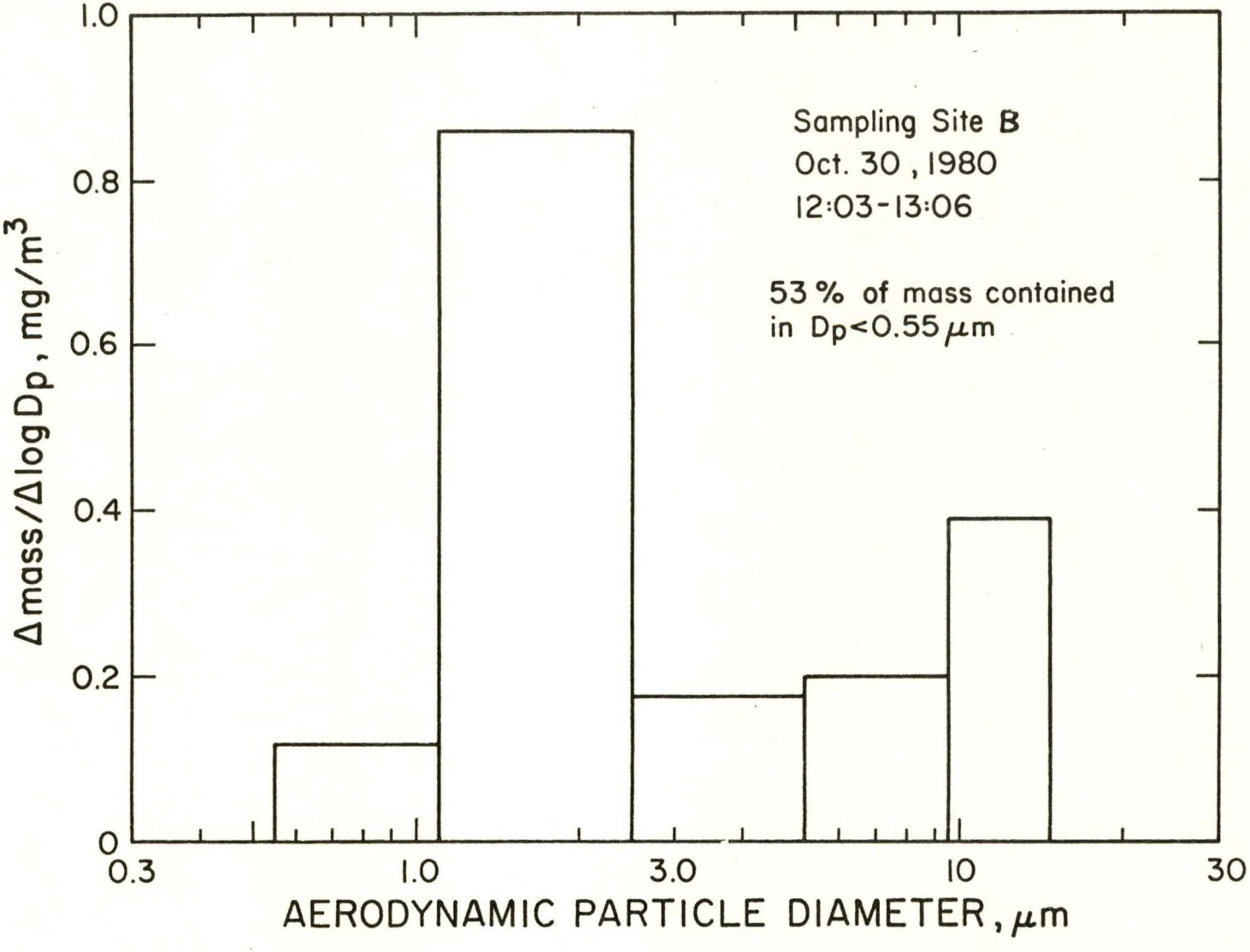

Figure 50. Aerosol size distribution of sampling site B in tungsten mine measured with Sierra Model 266 cascade impactor.

REFERENCES

1. Loo, B. W., S. M. Jaklevic, and F. J. Goulding, "Dichotomous Virtual Impactors for Large-Scale Monitoring of Airborne Particulate Matter," in Fine Particles Aerosol Generation, Measurement, Sampling, and Analysis, B. Y. H. Liu, ed. Academic Press, New York, pp. 311-350 (1976).

2. Marple, V. A., B. Y. H. Liu and K. T. Whitby, "Fluid Mechanics of the Laminar Flow Aerosol Impactor," J. Aerosol Sci. 5:1-16 (1973).

3. Marple, V. A. and B. Y. H. Liu, "Characteristics of Laminar Jet Impactors," Environ. Sci. Technol. 8:648-654 (July, 1974).

4. Marple, V. A., B. Y. H. Liu and K. T. Whitby, "On the Flow Fields of Inertial Impactors," presented at the ASME Symposium on Flow Studies in Air and Water Pollution, Atlanta, GA (June, 1973); J. Fluids Eng.96:394-400 (1974).

5. Liu, B. Y. H., V. A. Marple, K. T. Whitby and N. J. Barsic, "Size Distribution Measurement of Airborne Coal Dust by Optical Particle Counters," Am. Ind. Hyg. Assoc. J. 35:443-445 (Aug., 1974).

6. Marple, V. A. and K. L. Rubow, "A Portable Optical Counter System for Measuring Dust Aerosols," Am. Ind. Hyg. Assoc. J. 39:210-218 (March, 1978).

7. Marple, V. A. and K. L. Rubow, "Dynamic Particle Size Measurement of Coal Dust," Final Report, U. S. Bureau of Mines Contract No. H0133095 (Feb. 1977).

8. Berglund, R. N. and B. Y. H. Liu, "Generation of Monodisperse Aerosol Standards," Environ. Sci. Technol. 7:147-153 (Feb., 1973).

9. Marple, V. A. and K. L. Rubow, "Aerodynamic Particle Size Calibration of Optical Particle Counters," J. Aerosol Sci. 7:425-433 (1976).

10. Marple, V. A. and K. L. Rubow, "An Evaluation of the GCA Respirable Dust Monitor 101-1," Am. Ind. Hyg. Assoc. J. 39:17-25 (Jan., 1978).

11. Marple, V. A., B. Y. H. Liu and K. L. Rubow, "A Dust Generator for Laboratory Use," Am. Ind. Hyg. Assoc. J. 39:26-32 (Jan., 1978).

12. Lapple, C. E. and C. F. Schadt, Portable Mine Dust Concentration Instrument," Final Report, U. S. Bureau of Mines Contract No. H0111688, Stanford Research Institute Project PYU-1267 (June 27, 1977).

13. Lillienfeld, P., GCA Corp., Private communication (Sept. 1980).

14. Agarwal, J. K. and B. Y. H. Liu, "A Criterion for Accurate Aerosol Sampling in Calm Air," Am. Ind. Hyg. Assoc. J. 41:191-197 (March 1980).

15. Liu, B. Y. H. and K. W. Lee, "An Aerosol Generator of High Stability," Am. Ind. Hyg. Assoc. J. 36:861-865 (Dec., 1975).

16. Liu, B. Y. H. and D. Y. H. Pui, "A Submicron Aerosol Standard and the Primary, Absolute Calibration of the Condensation Nuclei Counter," J. Colloid Interface Sci. 47:155-171 (April, 1974).

17. Tomb, T. F. and H. N. Treaftis, "A New Two-Stage Respirable Dust Sampler," Am. Ind. Hyg. Assoc. J. 36:1 (1975).

18. Marple, V. A., "Simulation of Respirable Penetration Characteristics by Inertial Impaction," J. Aerosol Sci. 9:125-134 (1978).

APPENDIX A

A THEORETICAL STUDY OF VIRTUAL IMPACTORS

by

Virgil A. Marple and Chung M. Chien
Particle Technology Laboratory
Mechanical Engineering Department
University of Minnesota
Minneapolis, Minnesota 55455

Abstract

The characteristics of virtual impactors have been determined by the numerical solution of the Navier-Stokes equations and of the equations of motion of the particles. The effect of the nozzle Reynolds number, the fraction of flow passing through the collection probe, collection probe diameter, nozzle throat length, nozzle-to-collection probe distance, and collection probe inlet design on the small and large particle collection efficiencies has been studied. In addition, it was found that at the cutoff particle size there were significant losses on the inner surface of the collection probe. The results show that most parameters, with the exception of the nozzle Reynolds number, have little effect on the large particle collection efficiency. However, the effect on the small particle collection efficiency and collection probe losses was significant for many of these parameters.

INTRODUCTION

The virtual impactor is a device used for the inertial separation of airborne particles (1,2). In this impactor, shown schematically in Figure 1a, a jet of particle-laden air is directed at a collection probe which is slightly larger in diameter than the acceleration nozzle. The large particles cross the air streamlines and enter the collection probe, while the small particles follow the air streamlines into the side passage. To remove the large particles from the collection probe, a fraction of the total flow passing through the nozzle of the virtual impactor is allowed to pass through the collection probe. This flow will be referred to as the minor flow, while the flow through the side passage will be referred to as the major flow.

As is the case with real impactors, the virtual impactor's performance is characterized by a collection efficiency curve. For the ideal virtual impactor, the separation between the large and small particles should be perfectly sharp, as shown for the ideal case in Figure 1b. Note, however, that in the virtual impactor, there will always be some of the small particles with the large particles due to the air flow through the collection probe.

In an actual virtual impactor, the efficiency curve is not quite so simple, since there are not only large particles passing through the collection probe and small particles passing through the side passage, but also a fraction of the particles impacting upon the inner surfaces of the collection probe. Thus, as shown in Figure 1b, there are actually two efficiency curves separating the particles into the following three regions: (1) small particles passing out the side passage, (2) particles which are impacted upon the collection probe (losses), and (3) large particles passing through the collection probe. Since losses in the virtual impactor are highly undesirable, an impactor should be designed such that the displacement of the two efficiency curves shown in Figure 1b is as small as possible, with the two efficiency curves coinciding for the desirable case of a virtual impactor with no losses.

It is the purpose of this paper to use numerical methods to determine the flow fields, particle trajectories, and finally, the efficiency and loss curves for virtual impactors operating at different conditions of Reynolds numbers, fraction of flow passing through the collection probe, and virtual impactor design.

THEORETICAL TECHNIQUES

Although theoretical studies of virtual impaction devices have been made previously (3,4), the studies have assumed potential flow, which does not take viscous effects into account. The method used here to theoretically analyze the performance of the virtual impactor, which does include the viscous effects, is to first determine the flow field within the impactor by solving the full Navier-Stokes equations using numerical analysis techniques, and then to solve for the particle trajectory within this flow field by numerically integrating the particle's equation of motion. This method has been used successfully in a fundamental study of real impactors to determine the influence of various parameters on the characteristic collection efficiency curves (5). Comparisons of the theoretical efficiency curves with those of experimental investigations

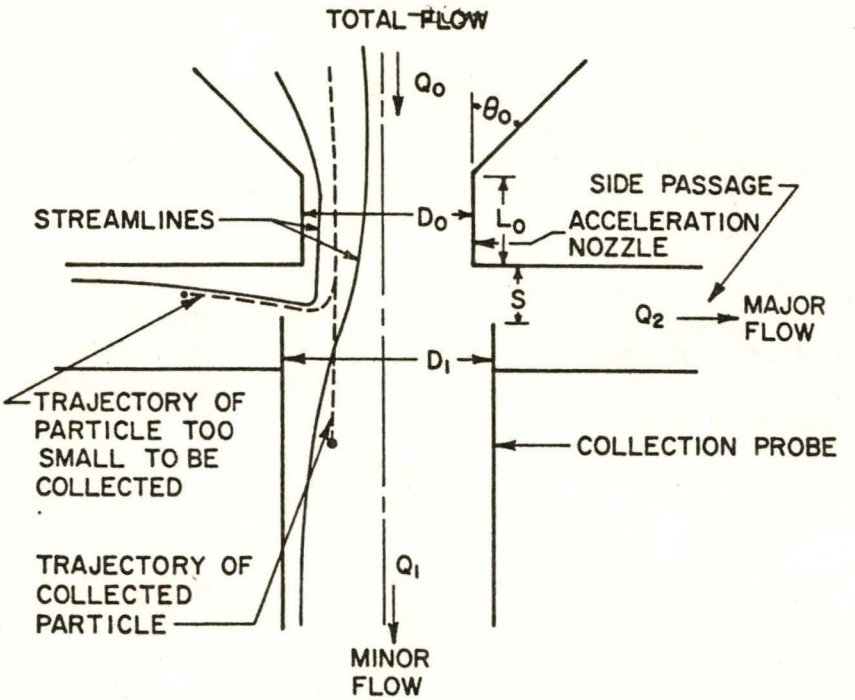

(a) VIRTUAL IMPACTOR

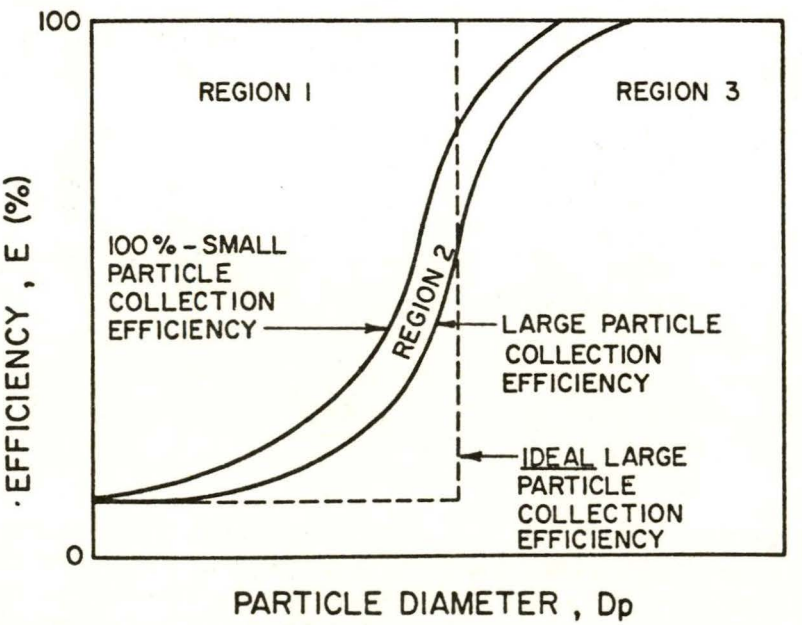

REGION 1-PARTICLES IN THE MAJOR FLOW
REGION 2-PARTICLES IMPACTED ON COLLECTION PROBE
REGION 3-PARTICLES IN THE MINOR FLOW

(b) COLLECTION EFFICIENCY CURVES

Figure 1. Nomenclature, streamlines, particle trajectories and efficiency curves for a virtual impactor.

(6,7,8,9,10) have shown that the agreement is good if the impactor inlet conditions, shape, and Reynolds number are similar. Since the flow field and particle trajectories are similar in real and virtual impactors, this theoretical technique should be equally successful in determining the efficiency curves of virtual impactors.

The general method of solution of the flow field is to first express the Navier-Stokes equations in terms of the vorticity and the stream function. The resulting differential equations are then made dimensionless, with the radial, r, and axial, z, dimensions being in units of the nozzle throat diameter, D_o. The Reynolds number

$$Re = \frac{\rho D_o V_o}{\mu} \qquad (1)$$

where ρ is the fluid density, V_o is the mean fluid velocity at the nozzle throat, and μ is the absolute viscosity of the fluid, will be a parameter in these equations. The dimensionless differential equations are next expressed in a finite difference form and solved by the method of relaxation over a grid of node points covering the field of interest, as shown in Figure 2a. (Note that the flow is symmetrical about the centerline.) Although the solution is the determination of the vorticity and stream function values at each node point, the values of the velocity components at the node points can be calculated from the stream function values. For details on the derivation of the finite difference equations, boundary conditions, and relaxation technique, the reader is referred to a previous paper by Marple et al. (11).

After the flow field has been determined, it is then necessary to follow particle trajectories through the virtual impactor. To accomplish this, the particle's equations of motion in the r and z directions are made dimensionless by again expressing the r and z dimensions in units of D_o. For these equations, the Stokes number, St, defined by Fuchs (12) as the ratio of the particle stopping distance to $D_o/2$, will be a parameter. The Stokes number is thus expressed as

$$St = \frac{\rho_p V_o C D_p^2}{9 \mu D_o} \qquad (2)$$

where ρ_p is the particle density, C is the Cunningham slip correction, and D_p is the particle diameter. Since St is dimensionless, Equation (2) indicates that $\sqrt{St}$ is a measure of the dimensionless particle diameter. The dimensionless equations of motion are next put in finite difference form and integrated numerically through the area of interest. This technique, which is described in detail by Marple and Liu (6), is capable of describing the particle's trajectory once the particle's initial position and velocity have been given.

The integration process is started by first assigning a specific value of $\sqrt{St}$ to a particle, and giving the particle an initial velocity equal to the local fluid velocity at a position near the entrance. By use of the Runge-Kutta integration method, the movement of the particle, Δz and Δr, during a small increment of time, Δt, is determined. This gives the position of the particle

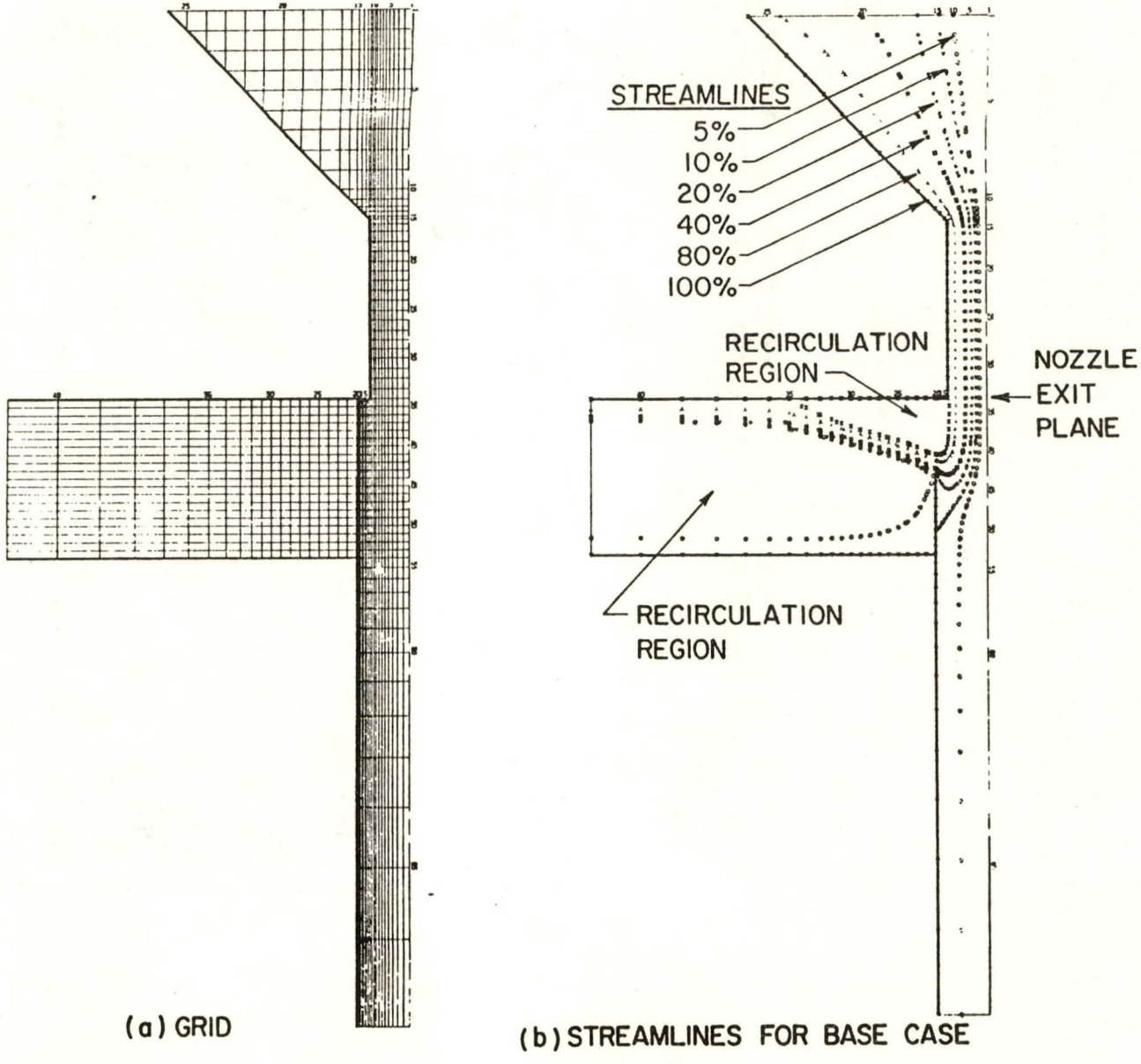

Figure 2. Grid and flow field for virtual impactor at base case conditions.

at the end of the time increment. This process is then repeated, and the movement of the particle through the impactor is followed until the particle either exits through the collection probe, exits to the side of the virtual impactor, or impacts upon the wall of the collection probe.

The particle is considered impacted when the center of the particle comes within one particle radius, r_p, of a surface. Since all dimensions of the virtual impactor are in units of the nozzle diameter, D_o, the particle radius must also be expressed in units of D_o. Thus, from Equations (1) and (2),

$$\frac{\sqrt{C}\, R_p}{D_o} = \sqrt{2.25 \frac{\rho}{\rho_p} \frac{St}{Re}} \qquad (3)$$

A detailed description of the numerical procedure and the computer program used has been given by Marple (5).

RESULTS

As described above, the flow fields, particle trajectories and corresponding efficiency curves of a virtual impactor will depend on the flow parameters, Re, Q_1/Q_o, and the physical design parameters, D_1/D_o, L_o/D_o, S/D_o, θ_o, and the shape of the entrance to the collection probe.

To initiate the parametric study, a set of base values for the parameters were chosen and are listed in the "boxed-in" portion of Table I. The other values of the parameters in Table I were then varied one at a time to the values listed, while the remaining parameters remained at the base values. Following is a discussion of the results for the base case, and then discussions of the effects of the various parameters.

Base Case

The grid used for the base case, corresponding to the parameters in Table I, is shown in Figure 2a. A thin-walled tube collection probe, which simulates a collection probe with its wall tapered to a sharp edge at the entrance, was chosen, since this design introduces no new variables such as wall thickness, or radius of curvature of the probe entrance.

The flow field streamlines for the base case are shown in Figure 2b for streamlines corresponding to 5%, 10%, 20%, 40%, 80%, and 100% of the flow inside that streamline. Note that the 0% streamline is at the center line, the 10% streamline intersects the collection probe (Q_1/Q_o = 10%), and the 100% streamline corresponds to the nozzle wall. Also note that the free streamline emitting from the nozzle reattaches to the surface defining the nozzle exit plane, forming a recirculation region between that surface and the free streamline. A second recirculation region is formed between the air flowing out the side passage and the lower surface, causing a 5% streamline to be indicated in this region.

In Figure 3a, the particle trajectories for five particles with different values of $\sqrt{St}$, all starting at the 50% streamline, are shown. These five particle trajectories include the three cases where particles (1) pass through the collection probe, (2) are impacted on the collector probe inner surface, and (3) pass through the side passage. Also included are the two critical tra-

Table I

Values of Design Parameters Used in Study

Re	Q_1/Q_o	D_1/D_o	L_o/D_o	S/D_o	θ_o	Collection Probe**	
1							
10						(B) 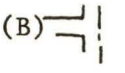	
100						(C) 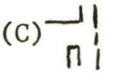	
500							
1,000	.05	1.16	.013	.25	30°	(D) 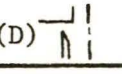	
5,000	.10	1.33	2.5	1	45°	(A) 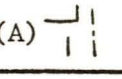	*
15,000	.15	1.49		2			
	.25						

* Base values from which parameters are varied.

** Collection probe A - thin wall

Collection probe B - infinite wall thickness

Collection probe C - finite wall thickness

Collection probe D - finite wall thickness with taper

(Collection probe designs are shown in Figure 18.)

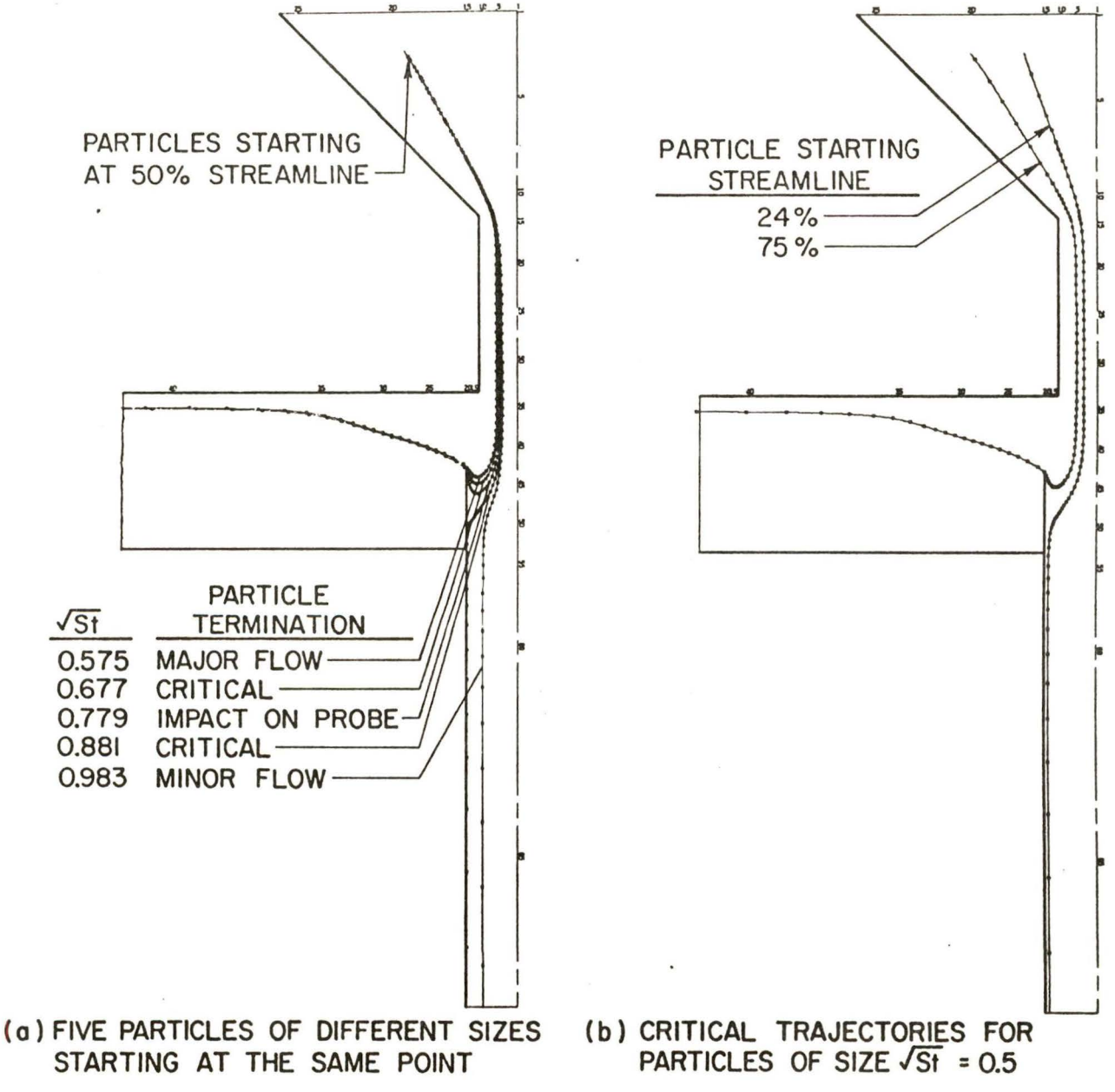

Figure 3. Particle trajectories at base conditions.

jectories between these three cases. For example, if the value of $\sqrt{St}$ of a particle is greater than 0.881, the particle will pass through the collection probe; if it is less than 0.677, the particle will pass through the side exit; and if it is between these two critical values, the particle will impact on the collection probe inner surface.

Another method by which the critical values of $\sqrt{St}$ can be determined is to keep $\sqrt{St}$ constant while varying the inlet starting position of the particle, as shown in Figure 3b. This shows that particles with $\sqrt{St}$ = 0.5 starting between the 24% streamline and the centerline will pass through the collection probe, those starting between the 24% and 75% streamlines will impact on the collection probe, and those starting at streamlines greater than 75% will pass out the side exit.

By using data such as represented in Figure 3a for particles starting at several positions, or as in Figure 3b for particles with different values of $\sqrt{St}$, the "large particle collection efficiency" and the "small particle collection efficiency" curves shown in Figure 4 can be determined. In either case, the collection efficiencies are the percent of particles emitting from the nozzle which pass through the collection probe or side passage, respectively. The value of $\sqrt{St}$ as a function of these efficiencies are presented as the base case in the two tables of the addendum to this Appendix. Also note that this information for all cases listed in Table I are presented in this addendum.

For the purpose of determining the percent of the particles being impacted on the inner surface of the collection probe, referred to as "collection probe loss" in this paper, it is best to construct the curve "100% - small particle collection efficiency." This curve, along with the large particle collection efficiency curve, represents the two efficiency curves in Figure 1b. As stated before, the difference in efficiencies at any value of $\sqrt{St}$ represents the collection probe loss, and thus the loss curve can be constructed.

It should be noted in Figure 4 that collection characteristics of a virtual impactor can be specified by the large particle collection efficiency curve and any one of the other three curves. However, since collection probe losses are of considerable importance, this curve will be used in this paper. Also note that the quantity of collection probe losses is quite large, being greater than has been reported in experimental investigations (13,14). However, investigations of the computer outputs indicated that nearly all losses occurred at the tip of the collection probe by particles that were traveling vertically upward directly adjacent to the probe inner surface. As will be shown later, it is possible to reduce these losses by proper contouring of the probe entrance. Therefore, the absolute values of the losses in this paper may be high, but the relative effects of the various parameters on these losses are of interest.

Although the contour of the collection probe entrance affects the probe losses, it has little effect on the large particle collection efficiency curve. Thus, this curve should be considered as the most significant characteristic curve for virtual impactors, and it is the curve by which virtual impactors will be characterized in this paper.

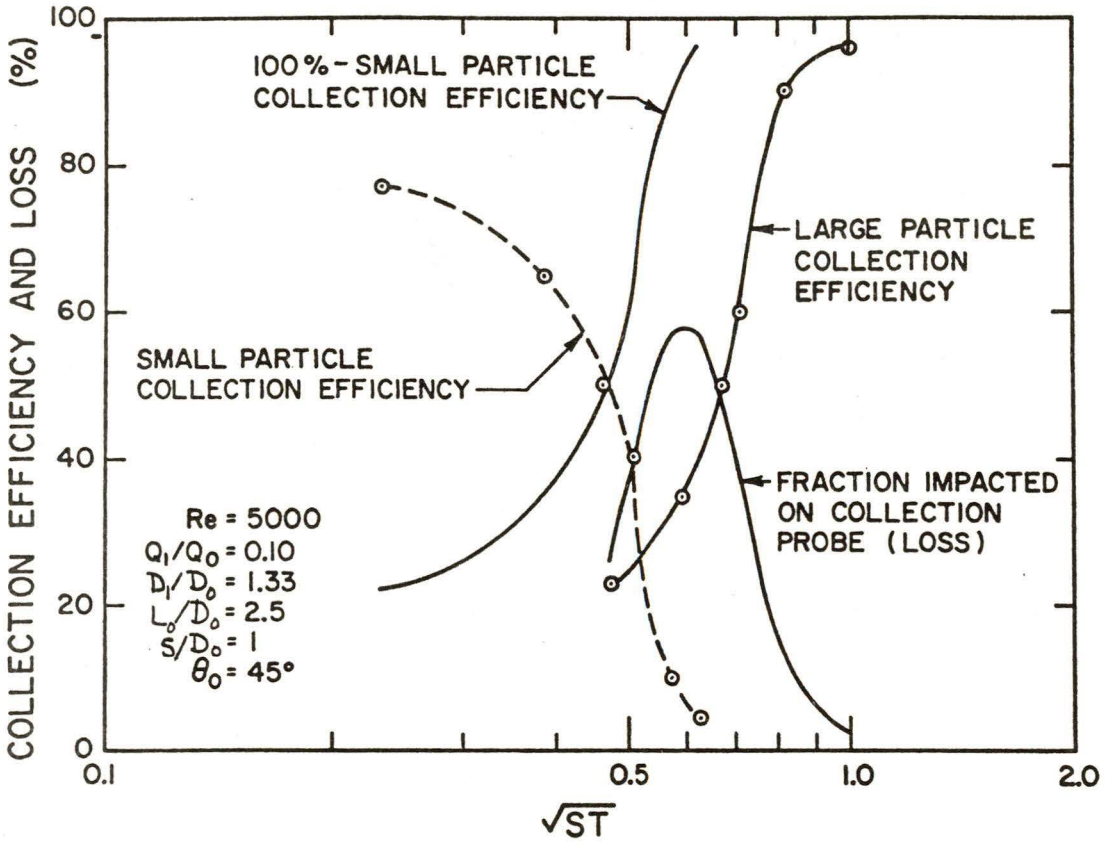

Figure 4. Collection efficiency and loss curves for base conditions.

It is of interest to compare the large particle collection efficiency curve determined theoretically to experiments by other investiagators (13, 14) in Figure 5. The value of the parameters listed in Figure 5 for each curve indicates that the virtual impactors are similar. The comparison shows that the theory agrees well with the experimental results, with the theoretical curve and experimental curve by Loo being nearly identical.

Having confidence that the theoretical solution of the virtual impactor is indicating collection curves that agree well with experimental results for the base case, the other cases listed in Table I were analyzed by varying the value of each parameter one at a time, while the other parameters were held at the base values. The influences of these parameters are discussed in the following sections.

Influence of Reynolds Number

To determine the influence of the Reynolds number, cases were run for the different values of Re listed in Table I, while the other parameters were held constant at base values. The flow fields are shown in Figure 6 for Re = 1, 10, 100, 500, 1,000, and 15,000, and in Figure 2b for Re = 5,000. In Figure 6, only the portion of the flow fields in the vicinity of the collection probe are shown, since the flow fields in other portions of the impactors are very similar to those in Figure 2b. It should be noted that the flow may not be laminar for Re = 15,000, but is presented as a limiting case.

Since the large particle collection efficiency curves are of primary interest, the flow fields within the collection probe are of most importance. It is in this region where we observe the unexpected result that the penetration of the 10% and 20% streamlines into the collection probe is greater for the cases of Re = 100 and 500 instead of for the higher values of Re, where the inertial effects of the flow should be larger. The reason for this can be seen by inspecting the velocity profiles at the nozzle exit plane shown in Figure 7. At high values of Re (Re = 5,000 and 15,000), the velocity profile is relatively uniform across much of the nozzle, making it difficult for any portion of the flow to penetrate into the air in the collection probe. For the cases of Re = 500 and 100, the velocity profile is more parabolic, and the relatively high velocity near the centerline makes it possible for the jet to penetrate farther into the collection probe. However, if the value of Re is small (Re = 10), there is insufficient inertia in the jet to penetrate into the viscous air in the collection probe. Thus, Re in the range of 100 to 500 is the correct combination of nozzle velocity profile and inertia to obtain maximum penetration of the 10% and 20% streamline into the collection probe.

The large particle collection efficiency curves are shown in Figure 8 with Re as a parameter. The influence of the flow penetration into the collection probe can be seen in the relative position of the large particle collection efficiency curves in Figure 8a. For the cases where the flow penetration into the collection probe is largest (Re = 100 and 500), the particle Stokes numbers must be larger in order for the particles to penetrate into the minor flow, since the Stokes number is defined as the particle stopping distance to the radius of the nozzle. Where the flow penetration into the collection probe is small, the required distance that the particle must travel, and thus the value of the Stokes number, will be smaller.

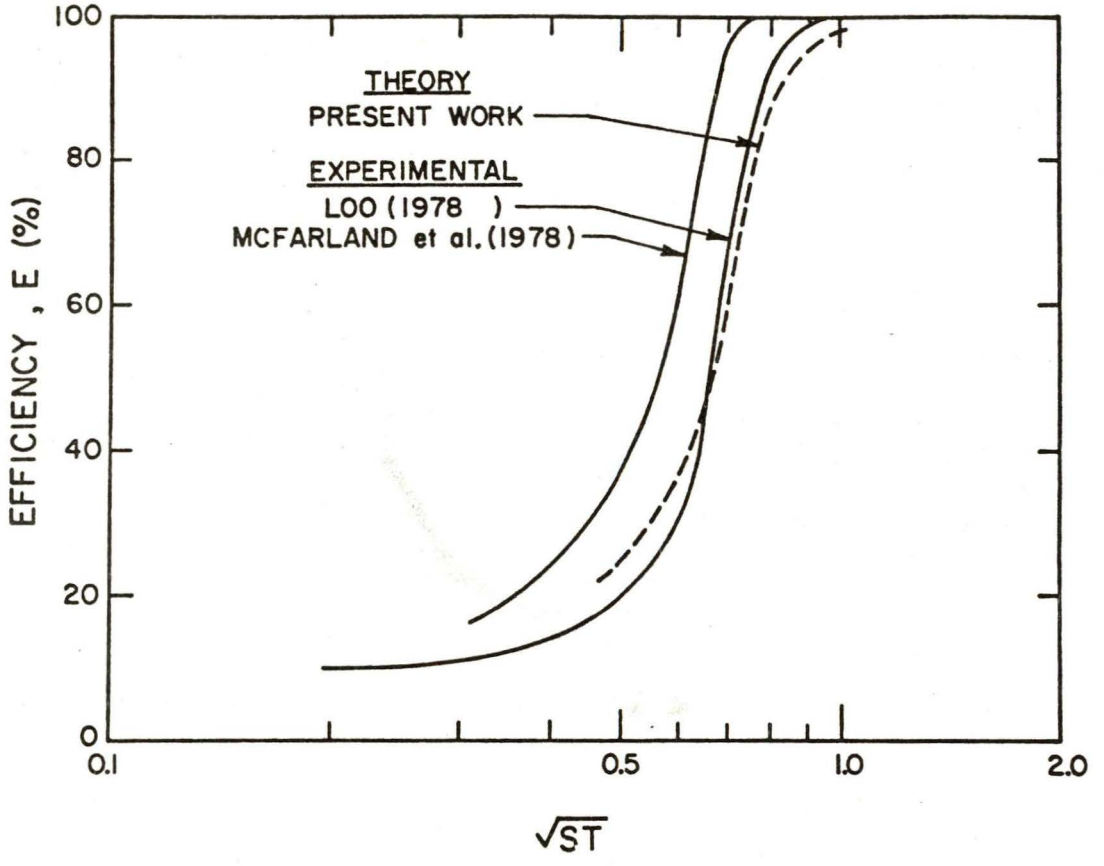

Figure 5. Comparison of theoretical and experimental large particle collection efficiency curves at the following conditions:

	Re	Q_1/Q_o	S/D_o	D_1/D_o	L_o/D_o	θ_o
Present theory	5000	0.1	1.0	1.33	2.5	45°
Loo (1978)	6000	0.1	0.8	1.38	0.8	45°
McFarland (1978)	4500	0.1	0.9	1.31	---	---

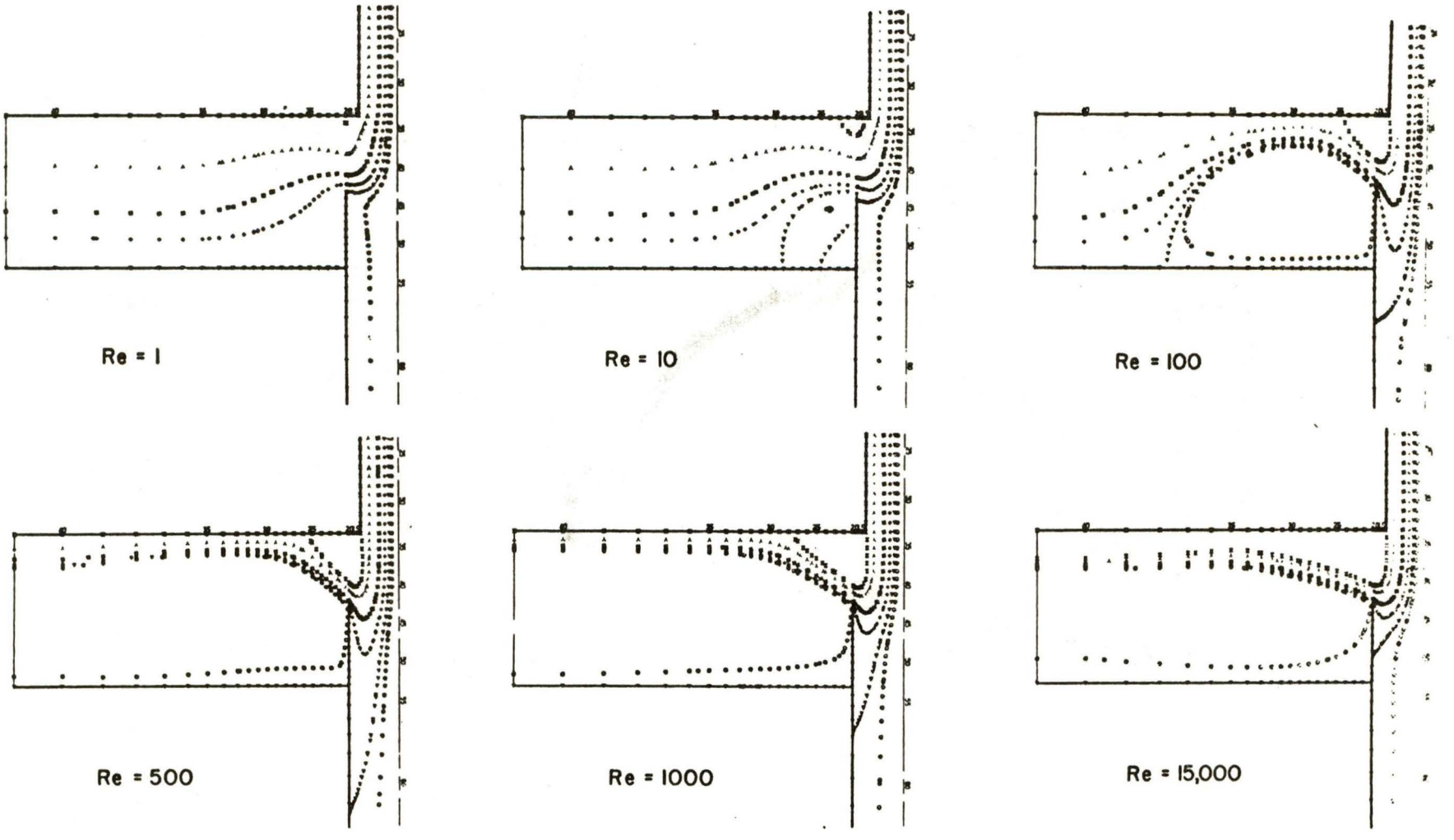

Figure 6. Theoretical streamlines at the specified values of Re (Q_1/Q_o = 0.1, D_1/D_o = 1.33, L_o/D_o = 2.5, S/D_o = 1, and θ_o = 45°).

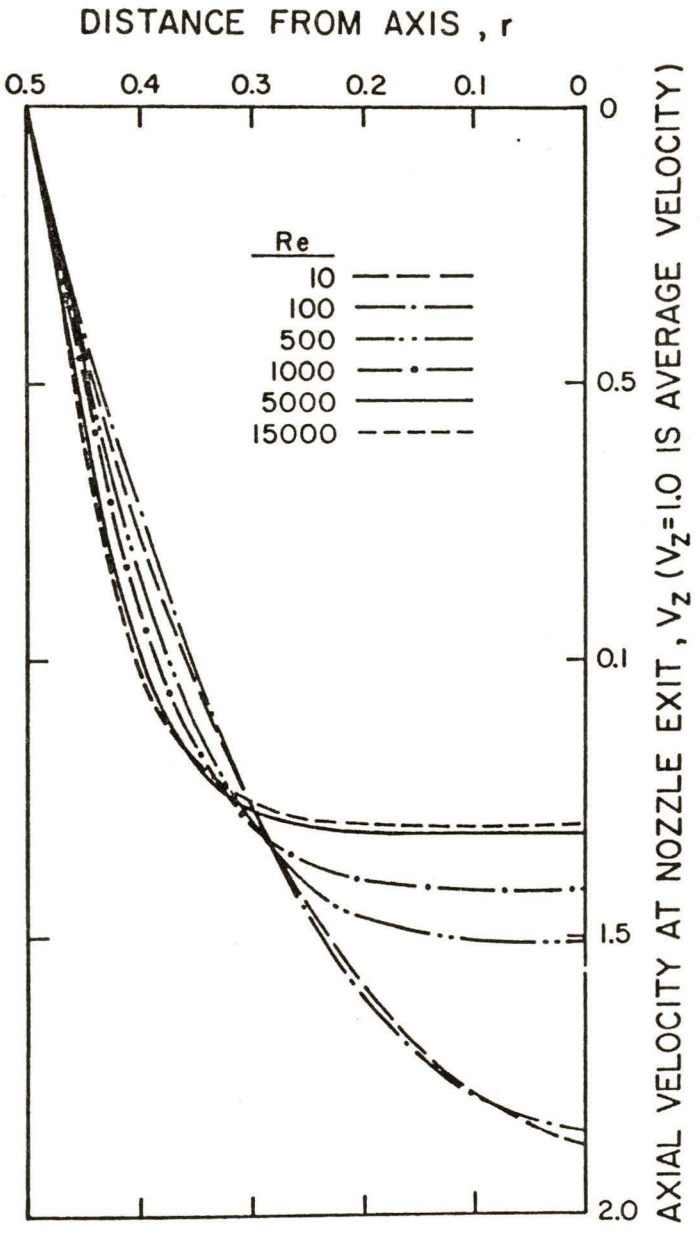

Figure 7. Influence of the Reynolds number on the axial velocity profile at the nozzle exit.

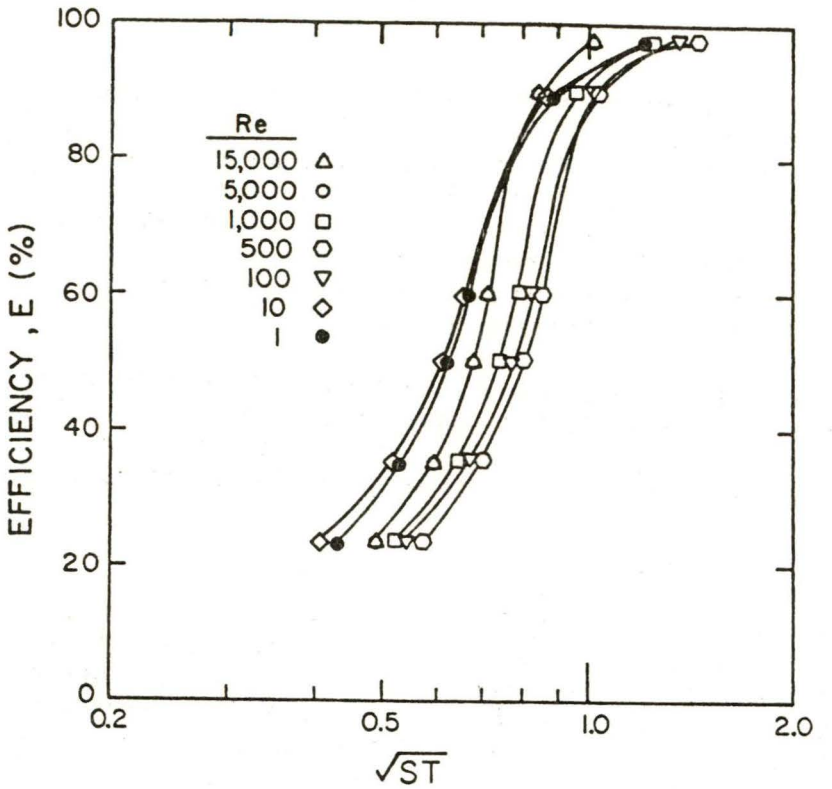

(a) LARGE PARTICLE COLLECTION EFFICIENCY

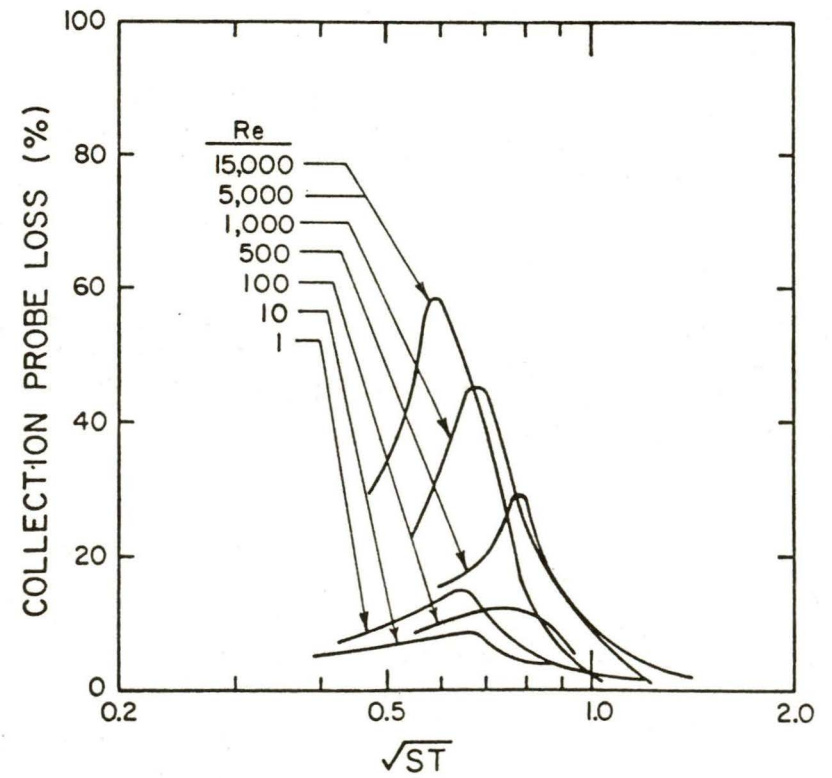

(b) COLLECTION PROBE LOSS

Figure 8. Large particle collection efficiency and collection probe loss curves at the specified values of Re (Q_1/Q_o = 0.1, D_1/D_o = 1.33, L_o/D_o = 2.5, S/D_o = 1, and θ_o = 45°).

It is of interest to note in Figure 8a that the efficiency curves are nearly identical for the cases of Re = 1 and 10, and for Re = 5,000 and 15,000, indicating that lower or higher Reynolds number than those listed should have little effect on these curves. It is also interesting to note that the slopes of the penetration curves are greater for the larger values of Re, indicating better cut-off characteristics. However, this effect is small, which is different from real impactors, where the cut-off characteristics are much poorer for low values of Re than for large values (6).

Concerning the influence of Re on the losses, Figure 8b shows that the influence is large. In general, the losses increase from a minimum of about 10% at low values of Re to about 60% at high values, with the maximum losses occurring at the value of $\sqrt{St}$ corresponding to 50% efficiency.

Influence of Q_1/Q_0

The flow fields corresponding to Q_1/Q_0 values of 0.05, 0.15, and 0.25 are shown in Figure 9, and should be compared to the base case of Q_1/Q_0 = 0.10 in Figure 2b. As can be seen from these figures, more streamlines pass through the collection probe for large values of Q_1/Q_0 and the small amount of flow in the side passage leaves more room for recirculation in this area. The flow field for Q_1/Q_0 = 0.05 shows reattachment to the lower surface of the side passage, much like the flow at Re = 100 in Figure 6. Whether or not the flow field in this region is correct is uncertain. However, since the flow in the region has no effect on the flow field in the important area within the collection probe, a more detailed investigation of the flow in this region was not made.

The corresponding large particle collection efficiency curves are shown in Figure 10. The large particle collection efficiency curves indicate that a "sharper" cut between large particles collected and those which are not is obtained for smaller values of Q_1/Q_0. Also, the cut-off size increases as Q_1/Q_0 decreases. This is expected, since particles must pass through more air to enter the minor flow stream when Q_1/Q_0 is small.

The loss curves show more losses associated with the lower Q_1/Q_0 values. This would be due to the larger percentage of the flow being exposed to the inlet of the collection probe where the losses generally occur, and should be decreased with proper inlet design.

Effect of D_1/D_0

Besides D_1/D_0 being equal to the base value of 1.33 (Figure 2b), D_1/D_0 was also set at 1.16 and 1.49 (Figure 11). Although, as shown in Figure 12, this parameter had only a small effect on the large particle collection efficiency and loss curves, there are substantial differences in the flow fields for these three cases. For example, the flow field attaches close to the nozzle exit when D_1/D_0 = 1.49 but does not attach when D_1/D_0 = 1.16. Experiments (15) have shown that for values of D_1/D_0 on the order of 1.49, the reattaching flow does cause particles to impact on the nozzle exit plane surface, increasing the losses in the virtual impactor. Therefore, it is recommended that the value of D_1/D_0 be kept less than 1.49, and preferably near 1.33.

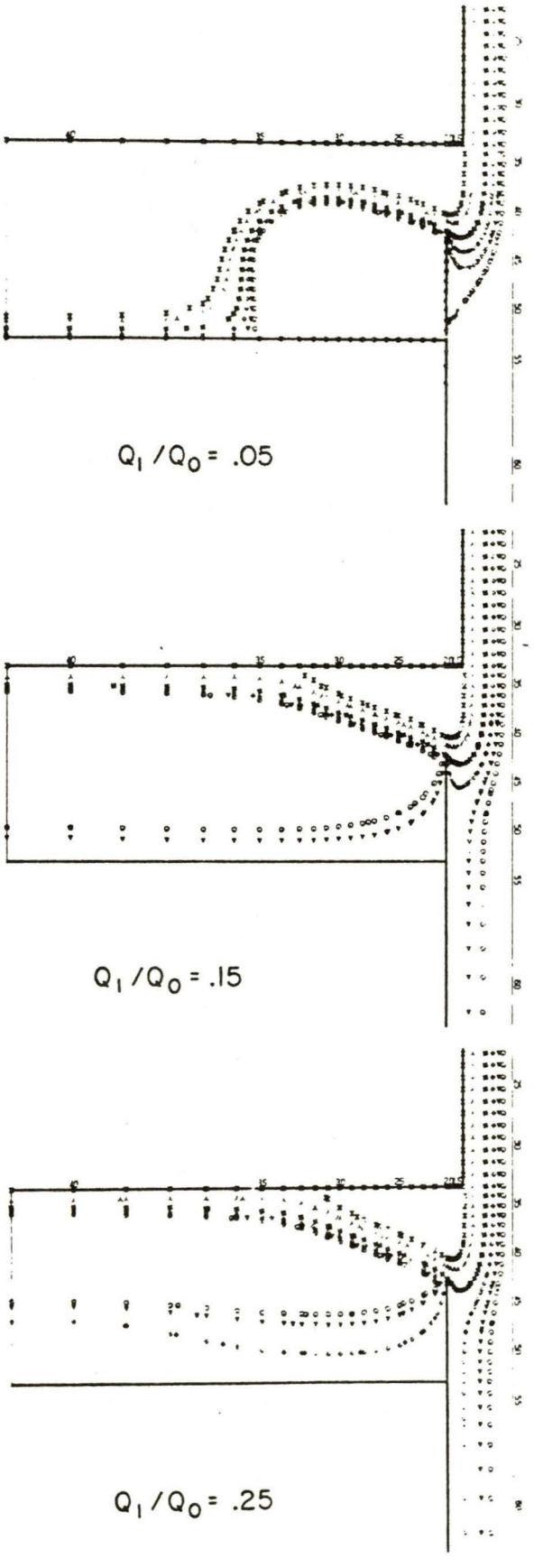

Figure 9. Theoretical streamlines at the specified values of Q_1/Q_o (Re = 5000, D_1/D_o = 1.33, L_o/D_o = 2.5, S/D_o = 1, and Θ_o = 45°).

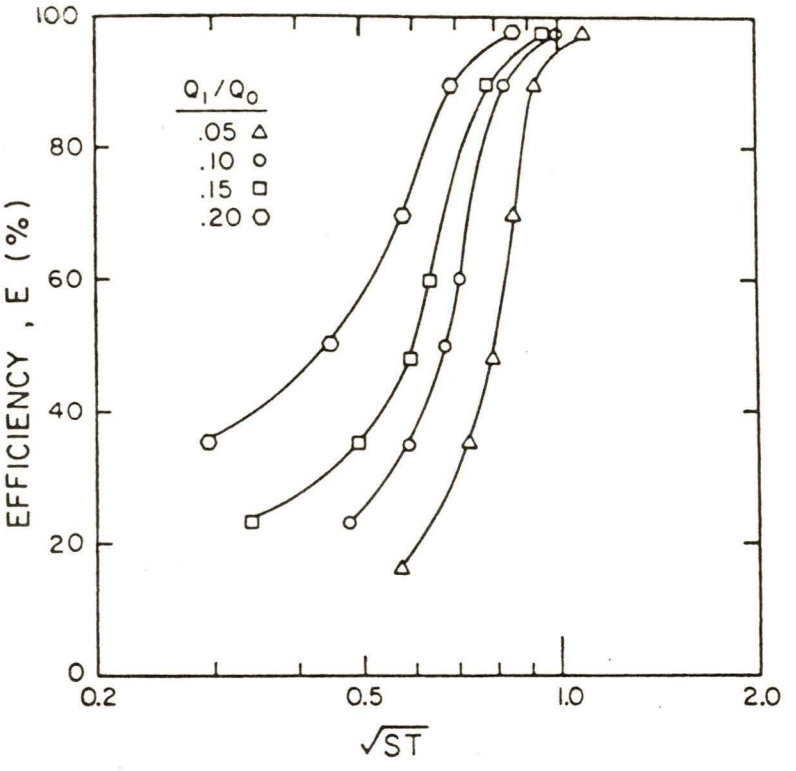

(a) LARGE PARTICLE COLLECTION EFFICIENCY

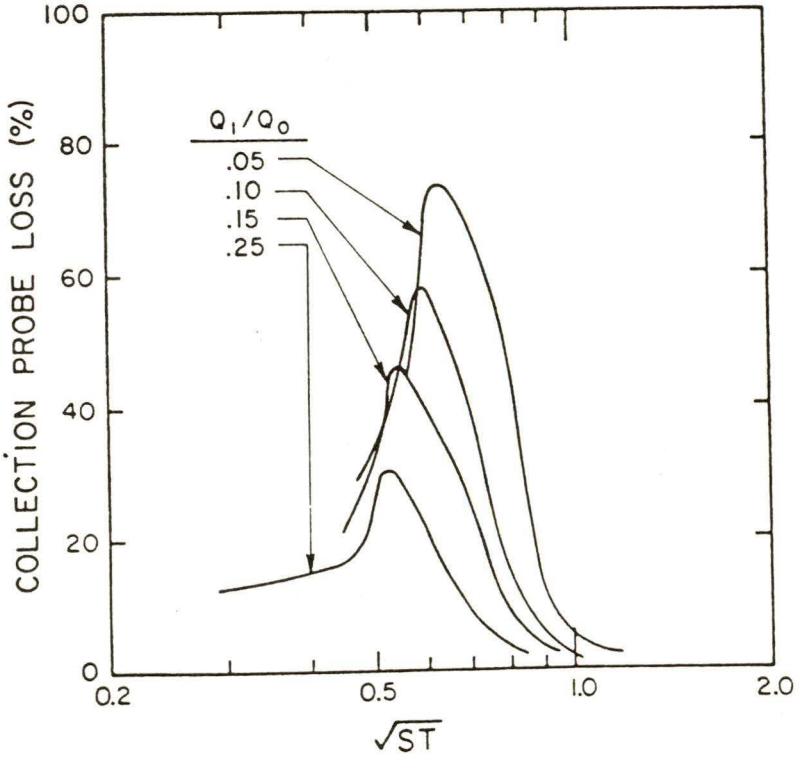

(b) COLLECTION PROBE LOSS

Figure 10. Large particle collection efficiency and collection probe loss curves at the specified values of Q_1/Q_o (Re = 5000, D_1/D_o = 1.33, L_o/D_o = 2.5, S/D_o = 1, and Θ_o = 45°).

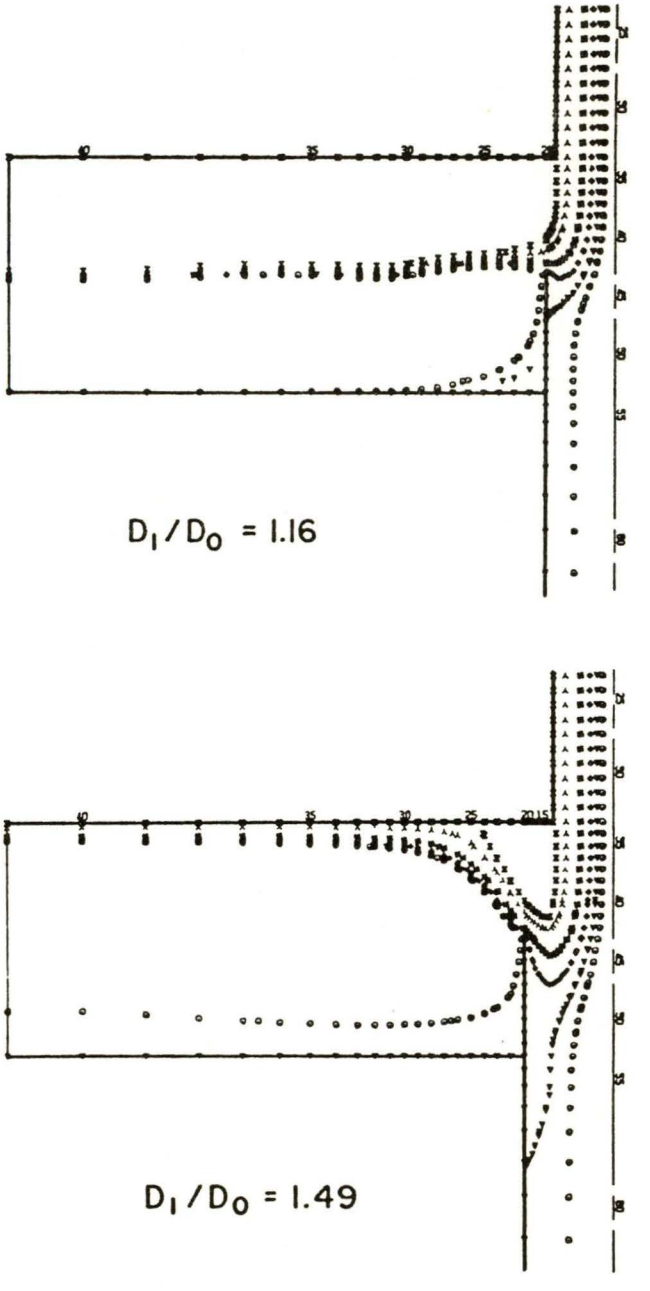

Figure 11. Theoretical streamlines at the specified values of D_1/D_o (Re = 5000, Q_1/Q_o = 0.1, L_o/D_o = 2.5, S/D_o = 1, and θ_o = 45°)

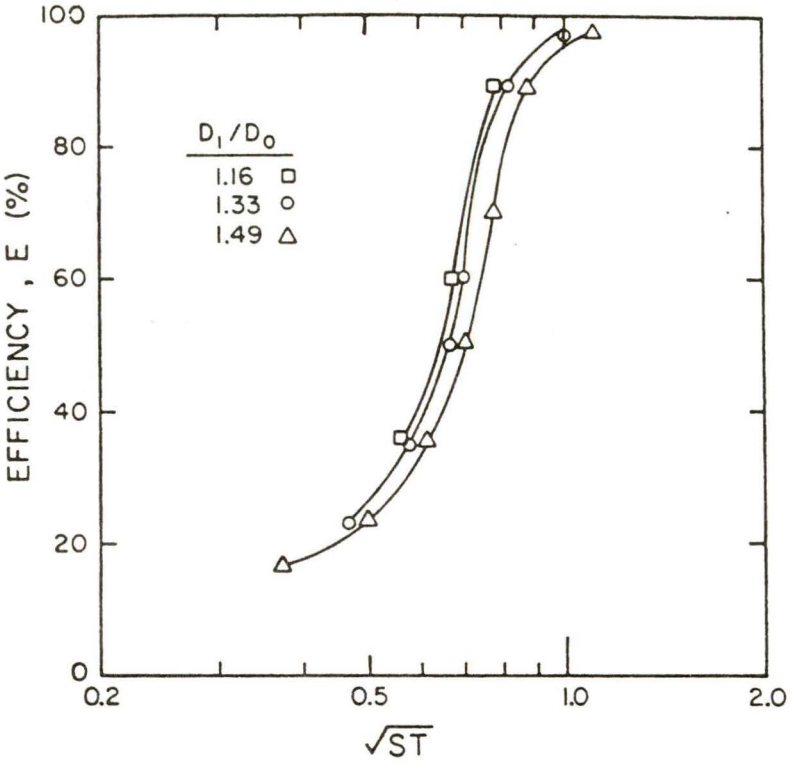

(a) LARGE PARTICLE COLLECTION EFFICIENCY

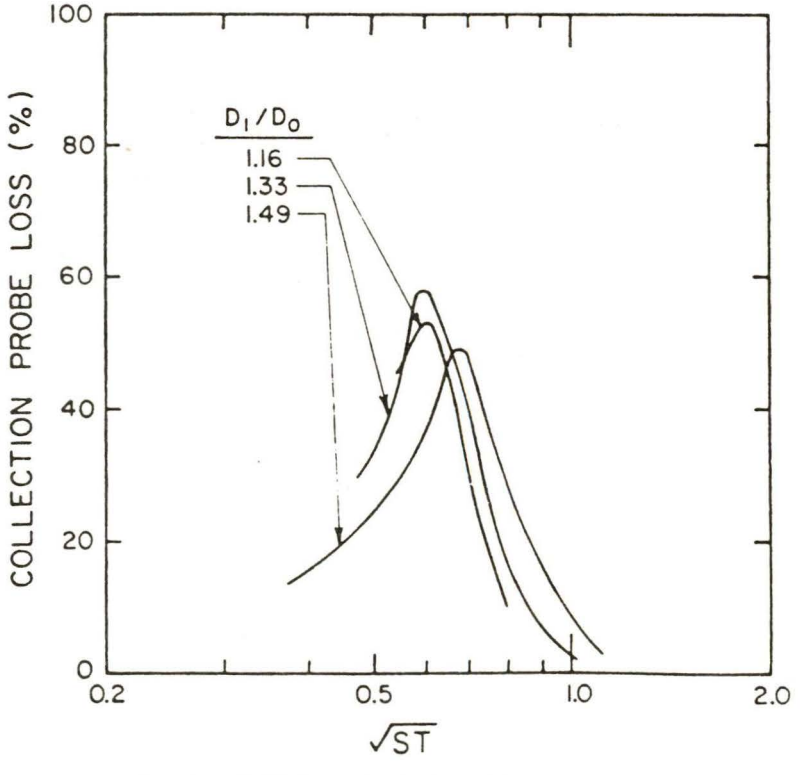

(b) COLLECTION PROBE LOSS

Figure 12. Large particle collection efficiency and collection probe loss curves at the specific values of D_1/D_o (Re = 5000, Q_1/Q_o = 0.1, L_o/D_o = 2.5, S/D_o = 1, and θ_o = 45°).

Effect of L_0/D_0

To investigate the effect of L_0/D_0, the results of a case where L_0/D_0 is small (L_0/D_0 = 0.013) is compared to the base case. Although the streamlines emitting from the nozzle are not parallel to the nozzle axis when L_0/D_0 = 0.013 (Figure 13) as they were when L_0/D_0 = 2.5 (Figure 2b), the effects on the large particle collection efficiency and the loss curves were negligible, as shown in Figure 14. Similar insensitivity to this parameter was found for real impactors (6).

Influence of S/D_0

The influence of S/D_0 was determined by using values of S/D_0 = 0.25, 1 (base), and 2. The flow fields shown in Figures 15 and 26 appear to be quite different. However, in the region in the collection probe where the 10% streamline attaches to the probe wall, the flow fields are similar. Thus, as expected, the resulting large particle collection efficiency curves shown in Figure 16 are nearly identical. Again, this is different from the effect found for real impactors (6) where small values of S/D_0 have a large effect on collection efficiency.

However, the probe loss curves shown in Figure 16 are influenced by S/D_0, with larger losses being found with small S/D_0 values. It may be expected that additional losses will be experienced on the nozzle exit plane surface and on the backside of the collection probe for small S/D_0 values due to turbulence in the restricted area between the collection probe and nozzle exit plane.

Influence of θ_0

The effects of the entrance angle on the large particle collection efficiency curve, and the probe loss curve are shown in Figure 17. Since the streamlines are very similar to those of the base case shown in Figure 2b, the streamlines for θ_0 =30° are not shown. In Figure 17, it can be seen that the large particle collection efficiency curves are similar in shape for both angles, but the curve for θ_0 = 45° is shifted to smaller particle sizes. This is due to the particles being thrown closer to the centerline for the larger θ_0 values, making the collection of particles in the probe slightly easier. The losses shown in Figure 17 indicate fewer losses for θ_0 = 45° than for θ_0 = 30°. Thus, it appears that θ_0 should be at least 45°.

Influence of the Collection Probe Inlet Design

Four receiving tube configurations were tested as shown in Figures 2b and 18. The base design was a thin wall shown as configuration A. In configuration B, the wall was infinite in width, and in configuration C, the wall had a finite thickness. In configuration D, the wall thickness was also finite, but the inner surface was tapered in an attempt to reduce losses.

The flow fields for these configurations are shown in Figures 2b and 18 and the resulting large particle collection efficiency and probe loss curves are

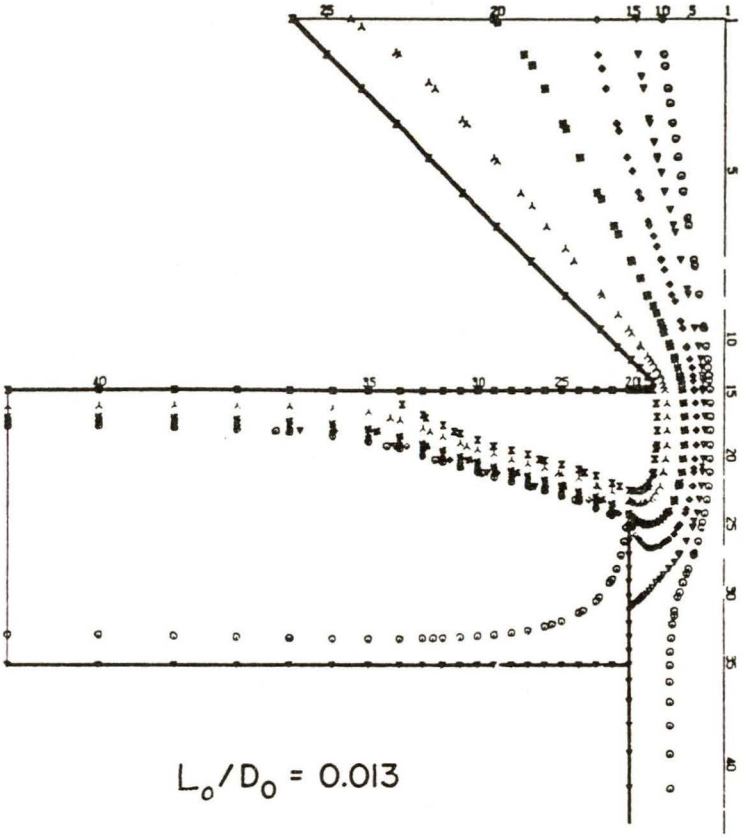

Figure 13. Theoretical streamlines at $L_o/D_o = 0.013$ (Re = 5000, $Q_1/Q_o = 0.1$, $D_1/D_o = 1.33$, $S/D_o = 1$, and $\theta_o = 45°$).

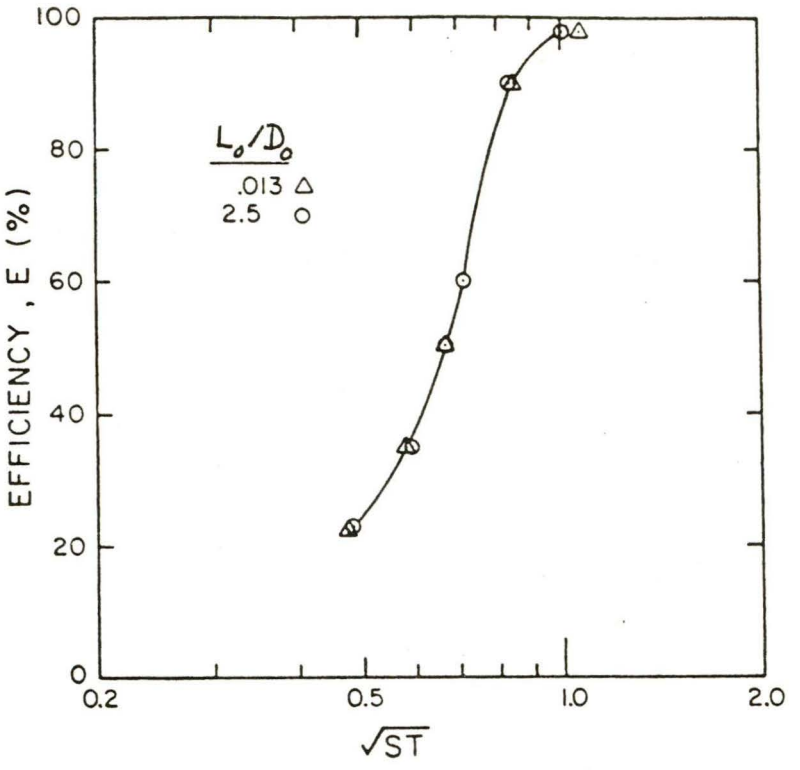

(a) LARGE PARTICLE COLLECTION EFFICIENCY

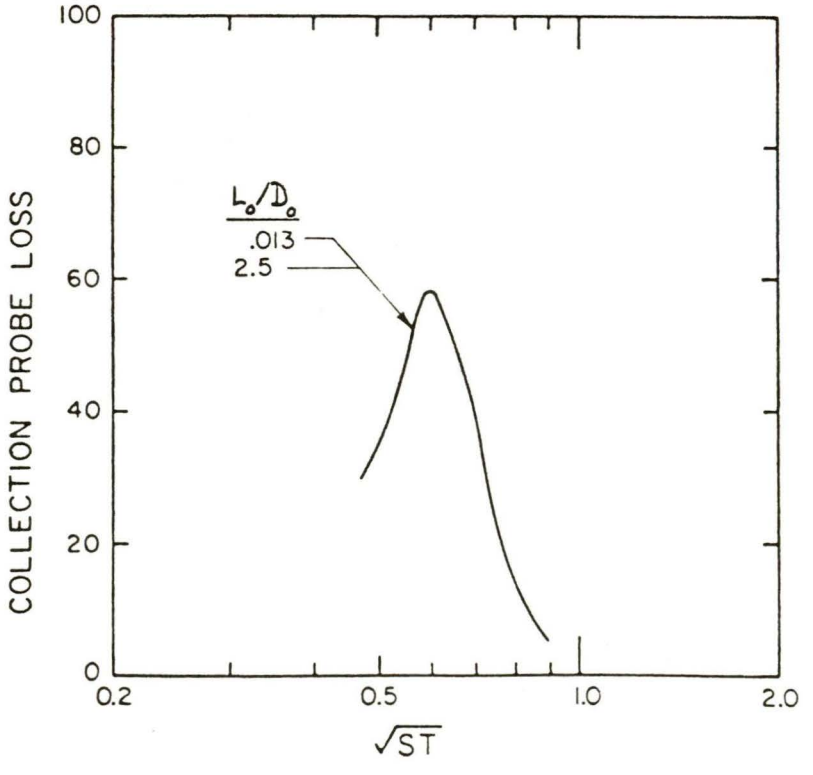

(b) COLLECTION PROBE LOSS

Figure 14. Large particle collection efficiency and collection probe loss curves at the specified values of L_o/D_o (Re = 5000, Q_1/Q_o = 0.1, D_1/D_o = 1.33, S/D_o = 1, and Θ_o = 45° .

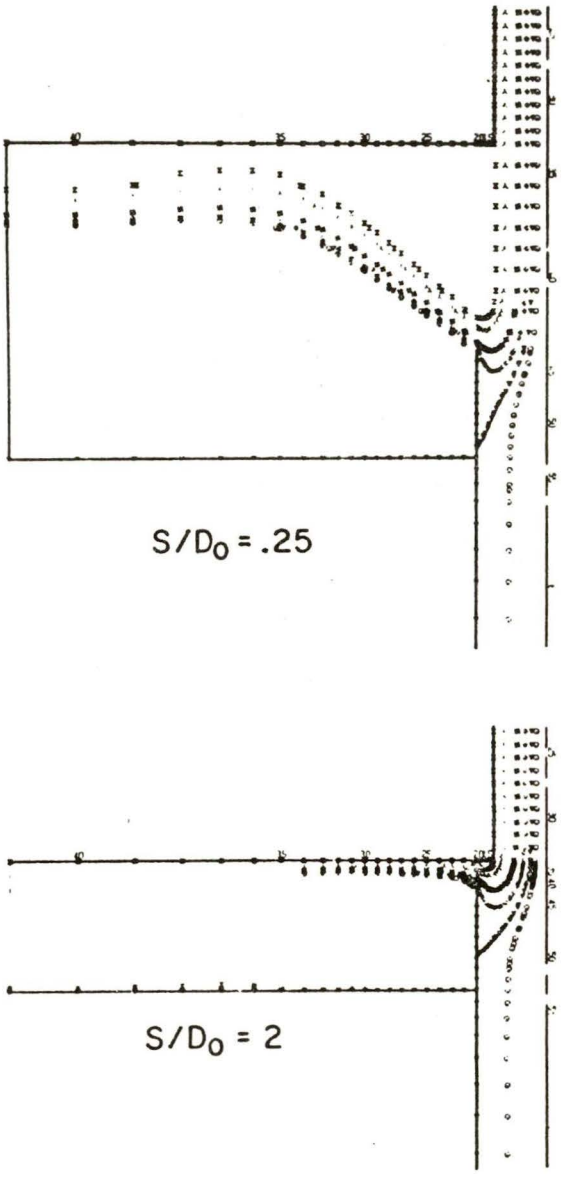

Figure 15. Theoretical streamlines at the specified values of S/D_o (Re = 5000, Q_1/Q_o = 0.1, D_1/D_o = 1.33, L_o/D_o = 2.5, and Θ_o = 45°).

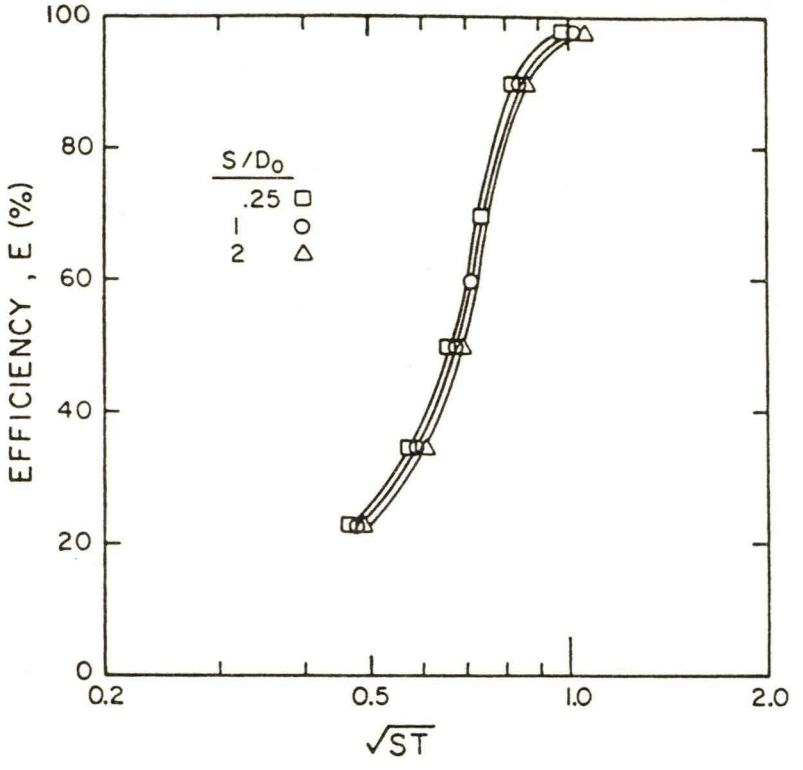

(a) LARGE PARTICLE COLLECTION EFFICIENCY

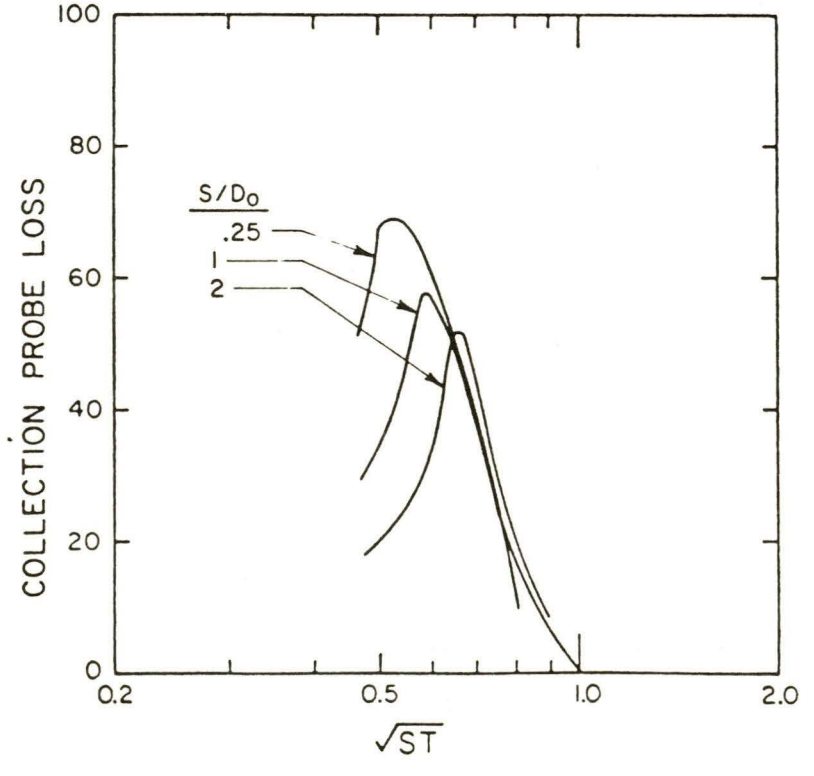

(b) COLLECTION PROBE LOSS

Figure 16. Large particle collection efficiency and collection probe loss curves at the specified values of S/D_o (Re = 5000, Q_1/Q_o = 0.1, D_1/D_o = 1.33, L_o/D_o = 2.5, and θ_o = 45°).

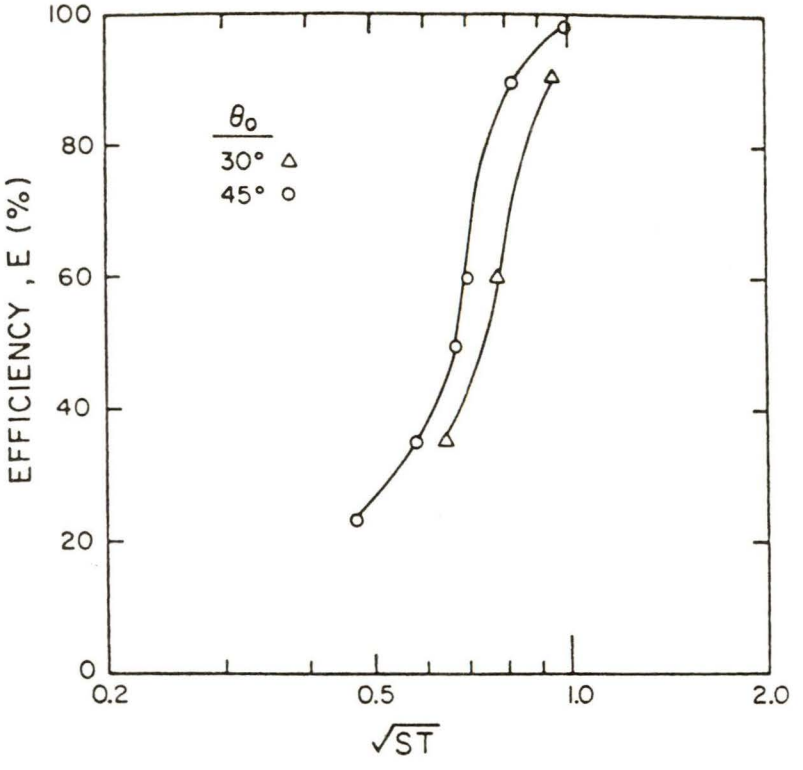

(a) LARGE PARTICLE COLLECTION EFFICIENCY

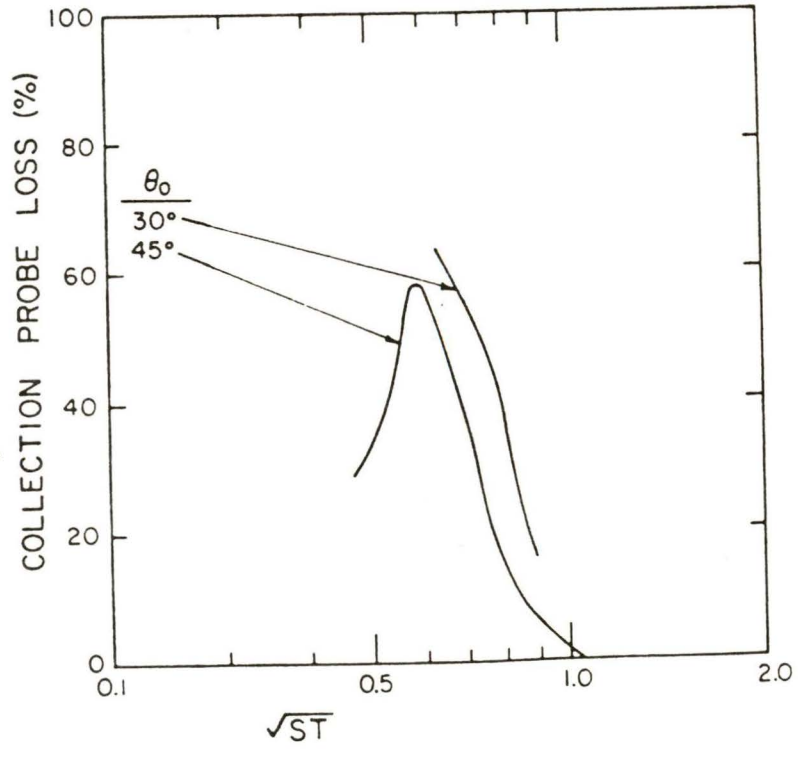

(b) COLLECTION PROBE LOSS

Figure 17. Large particle collection efficiency and collection probe loss curves at the specified values of Θ_o (Re = 5000, Q_1/Q_o = 0.1, D_1/D_o = 1.33, L_o/D_o = 2.5, and S/D_o = 1).

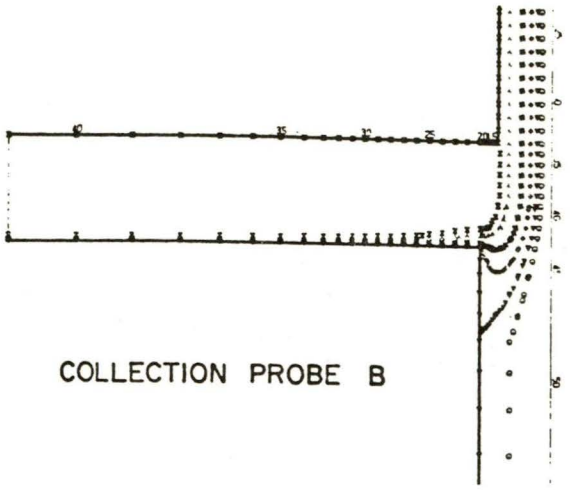

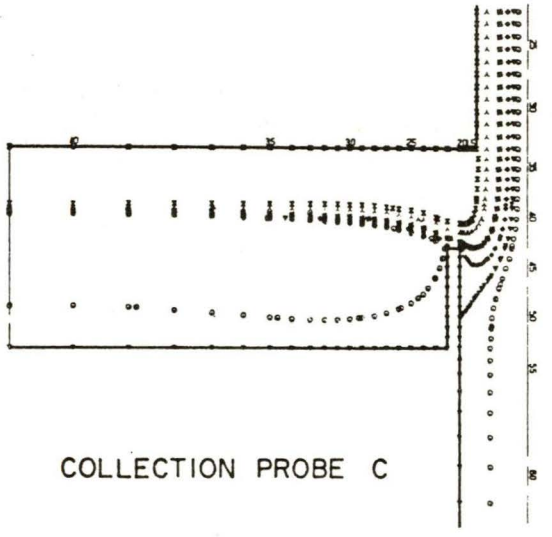

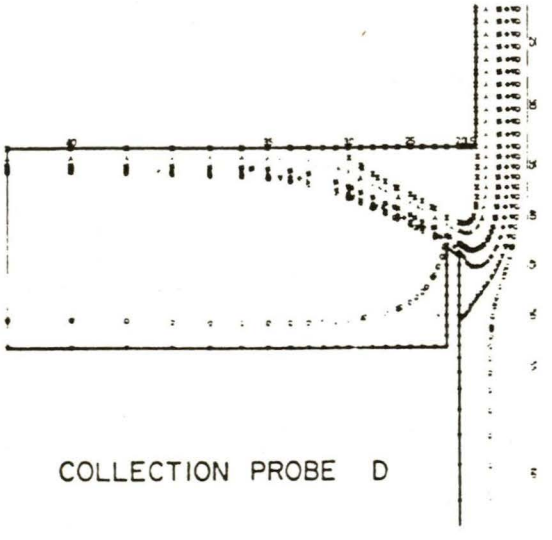

Figure 18. Theoretical streamlines for various collection probe designs (Re = 5000, Q_1/Q_o = 0.1, D_1/D_o = 1.33, L_o/D_o = 2.5, S/D_o = 1, and Θ_o = 45°).

shown in Figure 19. Since configuration B is essentially a real impactor impaction plate with a hole in its center, particles are collected on the plate, and thus losses are meaningless for this case and are not shown.

It is interesting to note that the configuration of the entrance to the collection probe had essentially no effect on the large particle collection efficiency curve. This would be expected, since this curve defines the separation of particles which impact upon the probe wall and those which pass through with the minor flow, and since the region of importance for this curve is inside the collection probe rather than at its entrance.

The losses, however, are influenced by the collection probe configuration. For configurations where there is a sharp edge at the upper entrance, such as configurations A and C, the probe losses are quite large and the loss curves are similar.

The losses that were found in these cases are from particles which are traveling vertically upward along the collection probe wall towards the major flow exit. The boundary layer in this region is very thin, and particles passing within one particle radius of this wall are collected as a loss. If there were some mechanism, such as aerodynamic forces, which would keep the particle from touching the wall, it would not be collected as a lost particle.

In addition, losses should be reduced by replacing the sharp corner in configuration C with a tapered entrance (configuration D) so the particles could not be collected as easily at the upper corner of the probe. As shown in Figure 19b, the losses were reduced. By replacing the taper with a radius, the losses should be reduced even farther.

CONCLUSIONS

An examination of the large particle collection efficiency curves reveals that they all have essentially the same shape and are not greatly influenced by any of the parameters. The only parameter which appears to influence the shape is Q_1/Q_0, because the collection efficiency curves are asymptotic to the different values of Q_1/Q_0 at low values of $\sqrt{St}$.

The reason none of the parameters have a large effect on the large particle collection efficiency curve is because this efficiency is governed by the flow field within the collection probe. The losses, however, are governed by the flow conditions at the tip of the collection probe inlet, and thus are influenced by many of the parameters. This is especially true for the case of the collection probe inlet design, where losses were reduced by adding a taper to the probe inlet.

References

1. Loo, B. W., Jaklevic, J. M. and Goulding, F. S. (1976). Dichotomous virtual impactors for large-scale monitoring of airborne particulate matter. In Fine Particles: Aerosol Generation, Measurement, Sampling, and Analysis (Edited by Liu, B. Y. H.). Academic Press, New York.

2. Dzubay, T. G. and Stevens, R. K. (1975) Environ. Sci. Technol. 9, 633-8.

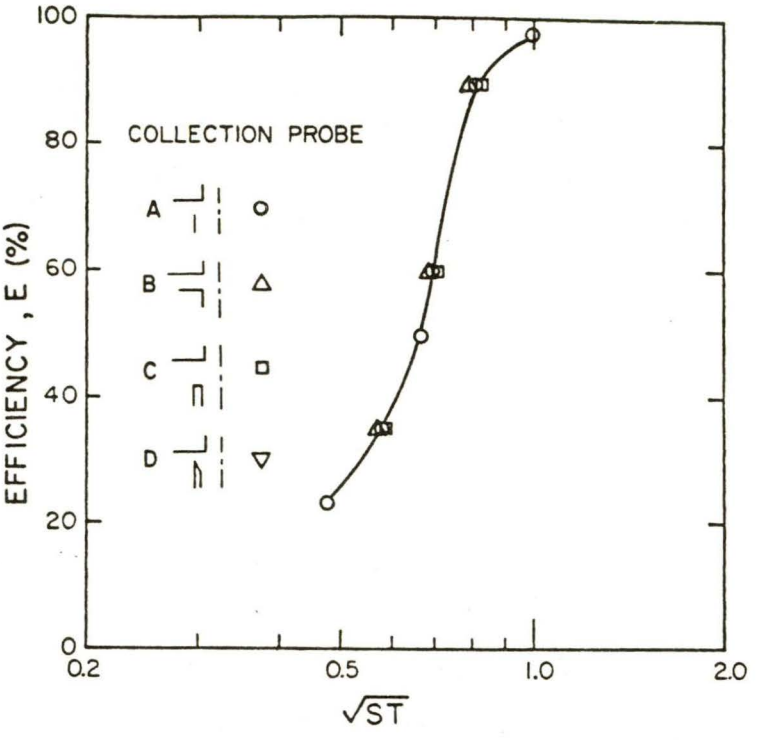

(a) LARGE PARTICLE COLLECTION EFFICIENCY

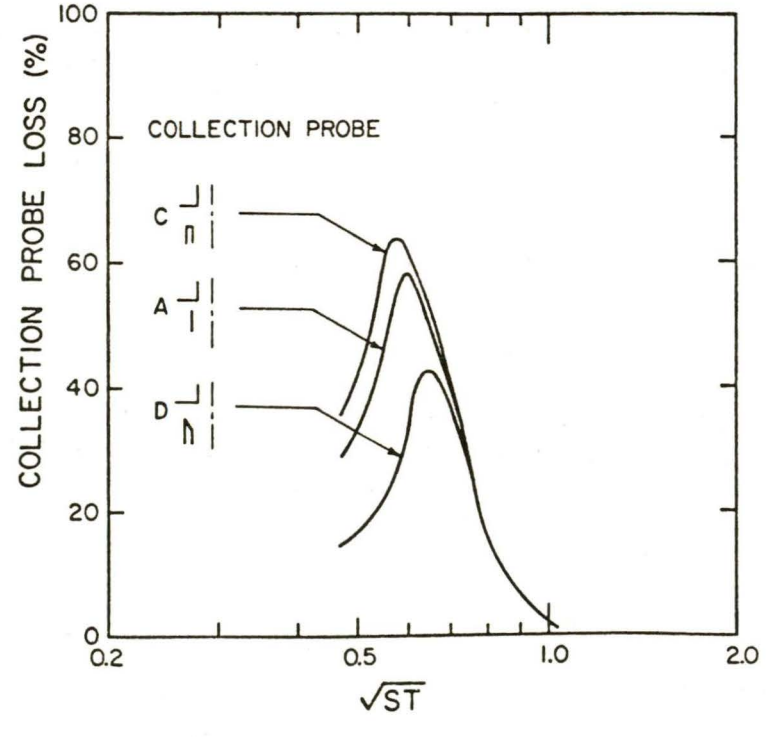

(b) COLLECTION PROBE LOSS

Figure 19. Large particle collection efficiency and collection probe loss curves for various collection probe designs (Re = 5000, Q_1/Q_o = 0.1, D_1/D_o = 1.33, L_o/D_c = 2.5, S/D_o = 1, and θ_o = 45°).

3. Fourney, L.J., D.G. Ravenhall, and D.S. Winn (1978). Aerosol impactors: a study of a fluid jet impinging upon void. J. Appl. Phys. 49 (4), 2339-45.

4. Ravenhall, D.G., L.J. Fourney, and M. Jazayer. (1978). Aerosol sizing with a slotter virtual impactor. J. Colloid Interface Sci. 65 (1).

5. Marple, V. A. (1970) A Fundamental Study of Inertial Impactors, Ph.D. Thesis, University of Minnesota, Minneapolis, Minnesota.

6. Marple, V. A. and Liu, B. Y. H. (1974) Environ. Sci. Technol. 8, 648-654.

7. Jaenicke, R. and Blifford, I. H. (1974) J. Aerosol Sci. 5, 457.

8. Willeke, K. and McFeters, J. J. (1975) J. Colloid Interface Sci. 53, 121-127.

9. Schott, J. H. (1973) Jet-Cone Impactors as Aerosol Particle Separators, M.S. Thesis, University of Minnesota, Minneapolis, Minnesota.

10. Willeke, K. (1975) Am. Ind. Hyg. Assoc. J. 36, 683-691.

11. Marple, V. A., Liu, B. Y. H. and Whitby, K. T. (1974) J. Fluids Eng. 96, 394-400.

12. Fuchs, N. A. (1964) The Mechanics of Aerosols, p. 154. Pergamon Press, New York.

13. Loo, B. W. and Cork, C. C. (1978). High Efficiency Virtual Impactor for Collecting Airborne Particulate Matter. Lawrence Berkeley Labs, University of California, Berkeley, Calif., Paper LBL-8204.

14. McFarland, A. R., Ortiz, C. A. and Bertch, R. W., Jr. (1978) Environ. Sci. Technol. 12, 679-682.

15. Loo, B. W. (1978) Lawrence Berkeley Labs, Berkeley, Calif., private communications.

Addendum to Appendix A

The values of $\sqrt{St}$ for the large particle and small particle collection efficiency curves are tabulated in Tables A-I and A-II, respectively. The cases are the same as those listed in Table I. The base case is presented first and subsequent cases are labeled by the value of the changed variable. For example, for the case Re = 1, all variables except Re are at the base values.

The large particle collection efficiency curves are presented in the appropriate figures. The small particle collection efficiency curves are not presented, but were used to determine the collection probe loss curves as described in Figure 4. The collection probe loss curves are then presented in this paper.

Table A-I

Values of $\sqrt{St}$ for
the Large Particle Collection Efficiency Curves

Case	Large Particle Collection Efficiency							
	16%	23%	35%	50%	60%	70%	90%	98%
Base		.48	.59	.67	.71		.84	1.01
Re = 1		.42	.53	.62	.67		.88	1.22
10		.40	.51	.60	.66		.86	
100		.54	.67	.76	.82		1.02	1.34
500		.56	.70	.80	.85		1.03	1.41
1,000		.51	.64	.73	.77		.94	1.23
15,000		.48	.59	.67	.71		.83	1.00
Q_1/Q_o = .05	.57		.73	.79		.85	.93	1.11
.15		.34	.49	.59	.64		.78	.96
.25			.29	.45		.57	.69	.86
D_1/D_o = 1.16			.57		.69		.80	
1.49	.37	.51	.62	.71		.80	.89	1.13
L_o/D_o = .013		.48	.58	.67			.85	1.06
S/D_o = .25		.47	.58	.65		.73	.87	.98
2		.49	.60	.69			.87	1.07
θ_o = 30°			.65		.78		.96	
Collection Probes**								
(B)			.57		.69		.80	
(C)			.59		.71		.83	
(D)			.59		.71		.84	

**Collection probe A - thin wall
Collection probe B - infinite wall thickness
Collection probe C - finite wall thickness
Collection probe D - finite wall thickness with taper

(Collection probe designs are shown in Figure 18.)

Table A-II

Values of $\sqrt{St}$ for
the Small Particle Collection Efficiency Curves

Case	Small Particle Collection Efficiency							
	84%	77%	65%	50%	40%	30%	10%	2%
Base		.23	.39	.47	.51		.58	.64
Re = 1		.35	.46	.55	.60		.79	1.00
10		.35	.47	.56	.61		.79	
100		.41	.57	.68	.75		.96	1.23
500		.34	.54	.66	.72		.92	1.13
1,000		.28	.45	.55	.59		.71	
15,000		.24	.39	.47	.51		.58	.64
Q_1/Q_o = .05	.23		.46	.53		.58	.60	.66
.15			.32	.43	.48		.56	.63
.25			.08	.32	.39	.45	.53	.60
D_1/D_o = 1.16			.40		.51		.59	
1.49		.23	.43	.52		.61	.67	.74
L_o/D_o = .013		.23	.38	.46		.53	.56	.63
S/D_o = .25		.10	.31	.40		.46	.49	.55
2		.29	.44	.53		.60	.64	.69
θ_o = 30°			.43		.55		.62	
Collection Probes**								
(B)			---		---		---	
(C)			.34		.47		.54	
(D)			.45		.57		.65	

**Collection probe A - thin wall
Collection probe B - infinite wall thickness
Collection probe C - finite wall thickness
Collection probe D - finite wall thickness with taper

(Collection probe designs are shown in Figure 18.)

APPENDIX B

OPTICAL PARTICLE COUNTER/PHOTOMETER

DESIGN REPORT

Report prepared by

Frank D. Dorman
Scientist in Mechanical Engineering

Kenneth L. Rubow
Research Fellow in Mechanical Engineering

Donald J. Nieken
Research Fellow in Mechanical Engineering

Submitted by

Dr. Virgil A. Marple
Associate Professor of Mechanical Engineering

Particle Technology Laboratory
Department of Mechanical Engineering
University of Minnesota
Minneapolis, Minnesota 55455

U. S. Bureau of Mines
Contract No. H0177026

Introduction

The optical particle counter/photometer described in this appendix has been designed specifically for use in underground coal mines. Thus, some of the important features of this instrument are that it is battery-powered, small, portable, and to make the instrument more easily adaptable for use in explosive atmospheres, the light source is a laser diode instead of an incandescent light bulb. Although the instrument is designed for coal mines, it can also be used equally well in other areas.

The instrument can actually be used as a photometer or as a single particle optical counter. It is presently envisioned that separate instruments would be built for these two applications. However, it is possible that one instrument could be used as both a photometer and a single particle counter.

The two instruments are very similar in that the light source, optics, flow systems, and signal detection circuits are identical for both units. The primary difference between the two instruments is in the processing of the signal after detection by the photo sensor. For the photometer, the signals are linearized, so that the magnitude of the signal is proportional to the volume of the particle. The volumes are then summed to give a resulting output of the total volume (or mass) of the aerosol. The single particle counter outputs the signals as pulses of different magnitudes, and by use of a multichannel analyzer, the size distribution of the aerosol can be determined.

In the following sections, the design and testing of the various components of these instruments and their resulting design specifications are discussed. This report is divided into four sections, each section dealing with one of the main system components. The four section topics include light beam, particle sample port, scattered light receiver optics, and signal processing. The evaluation and final design for each component is presented in the section dealing with the appropriate component.

1 Light Beam

1.1 Laser Diode Light Source

The laser diode used is an RCA type C30130. This is a continuous wave, room temperature operation, Gallium Aluminum Arsenide Injection laser diode. The wavelength of peak radiant intensity is 820 nm. The rated power output is 6 mw with peak power of 15 mw. The radiation is from a 13 x 2 μm area source with a half-angle beam spread of 5° in plane parallel to junction, and 20° in plane normal to junction.

To insure long service life, the diode is run at 5 mw power output. In order to operate the diode at ambient temperature, the diode current is controlled by a temperature-sensitive circuit to maintain a constant power output.

The output power as a function of diode temperature was measured with the diode mounted on a thermoelectrically-cooled (and heated) aluminum block. The power output was measured by close coupling a United Detector Tech., Inc. PIN 10DF silicon photo cell to the diode. Due to the 1 cm^2 area of the photo cell and the close spacing, the photo cell intercepted almost all the diode output.

The optical power output as a function of current at different temperatures was measured, and the result is plotted in Figure 1. The diode voltage drop as a function of current at each temperature was also measured and is shown in Figure 2. By selecting points on the different temperature curves in Figure 1 that correspond to a 5 mw output, and replotting as a function of temperature, the curve of diode current needed for constant power output as a function of temperature can be plotted as shown in Figure 3.

1.11 Thermistor Current Control

The thermistor is a large area disc that is kept in thermal equilibrium with the diode heat sink. From the data in Figures 2 and 3, and by assuming constant supply voltage, a resistor-thermistor network can be calculated that will maintain constant power output to within about 1% over the range of 0°C to 30°C. The calculated networks for 4 V and 6 V are shown in Figure 4. The networks can be designed to operate directly from the a 6 V Gel/cell battery, or from a lower voltage regulated down from the battery voltage.

1.12 Beam Monitor

In order to control the photo diode output beam intensity, a photo cell is placed in the beam dump (Section 1.23) to intercept and absorb the unused portion of the beam. The energy lost to the particles is a small fraction of the total beam energy. The output of the photo cell is a measure of the beam intensity passing through the test section. The output is amplified and displayed on the meter to test the otherwise invisible infrared beam. The output is also fed back to the laser diode as negative feedback to maintain constant beam energy (Figure 5). The feedback is via a parallel resistor to the temperature compensation network, and has the ability to change the diode output by about 10%. If the correction needed is outside this range, the indicated output will drop, and corrective action, such as cleaning of the optical surfaces, is needed.

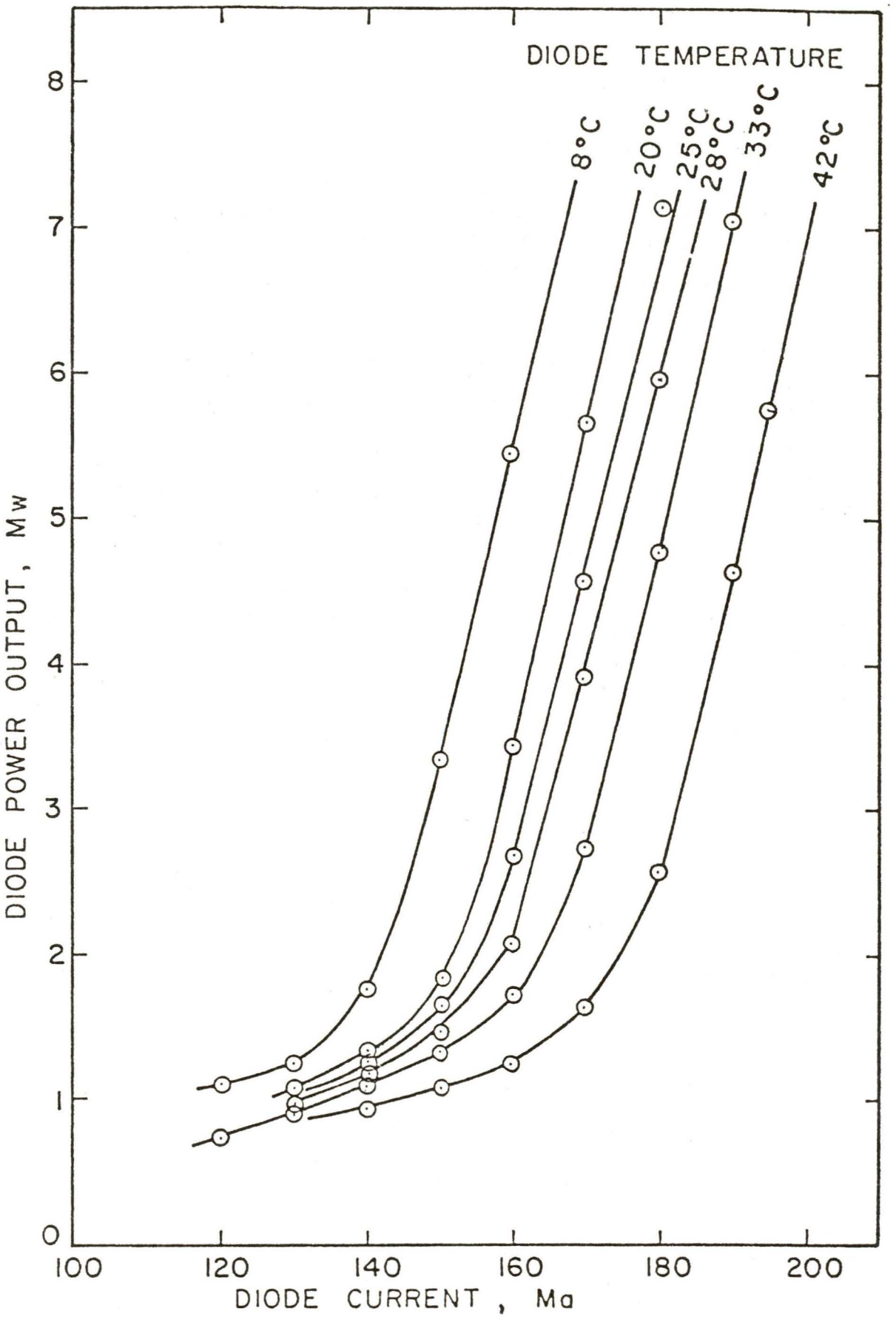

Figure 1 Laser power output as a function of input current and diode temperature.

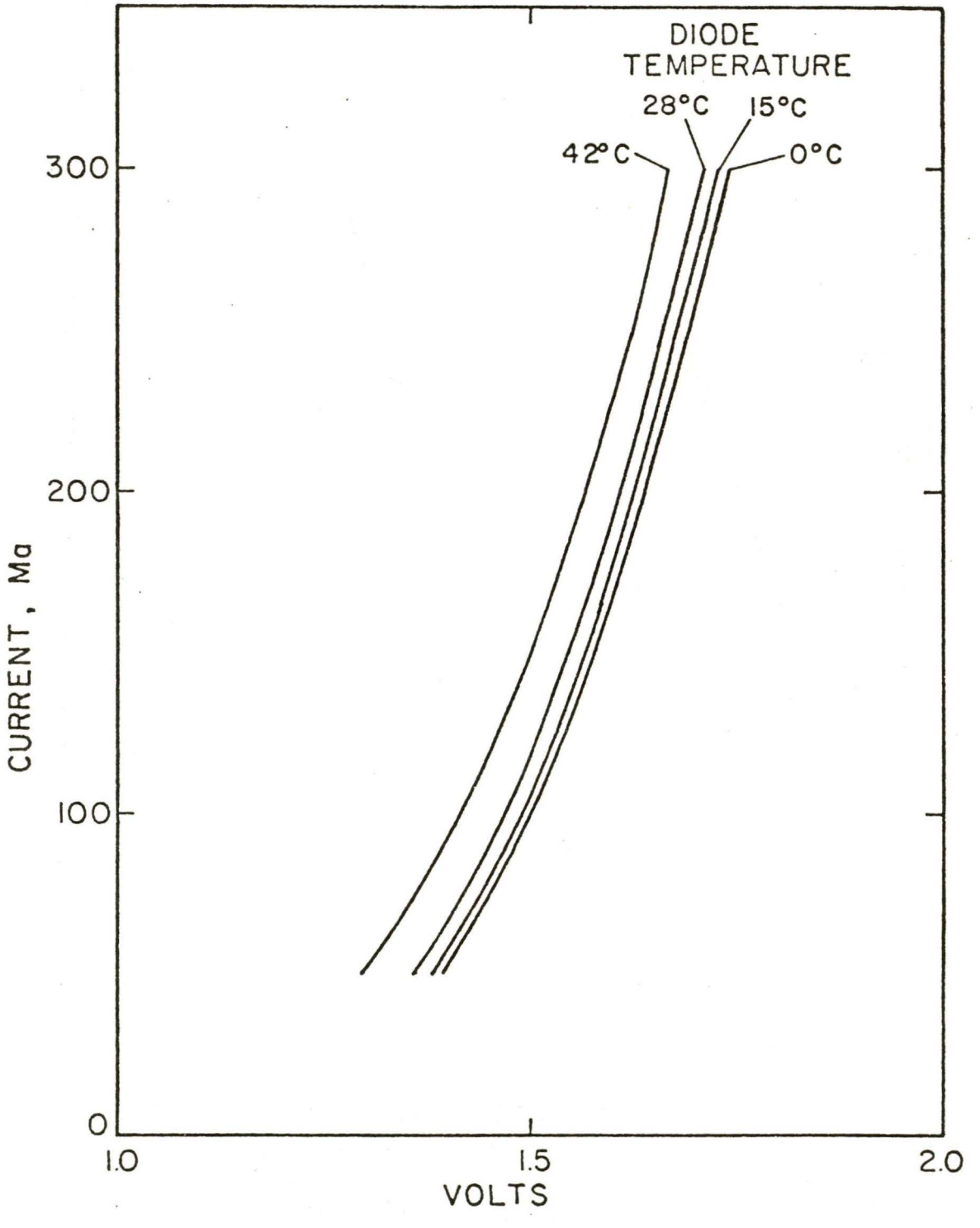

Figure 2 Input current of the laser diode as a function of voltage drop and diode temperature.

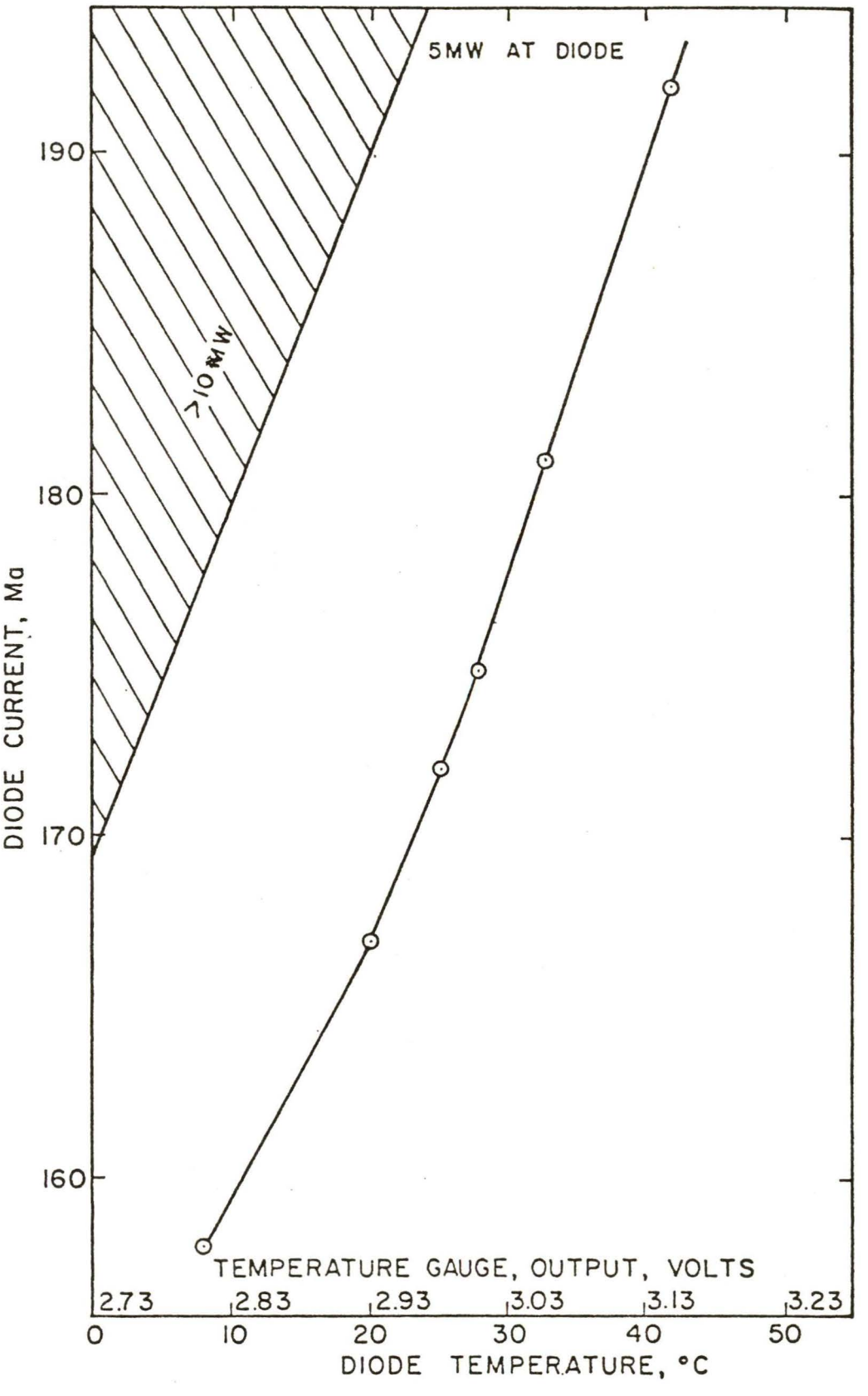

Figure 3 Diode current as a function of temperature for a given output power.

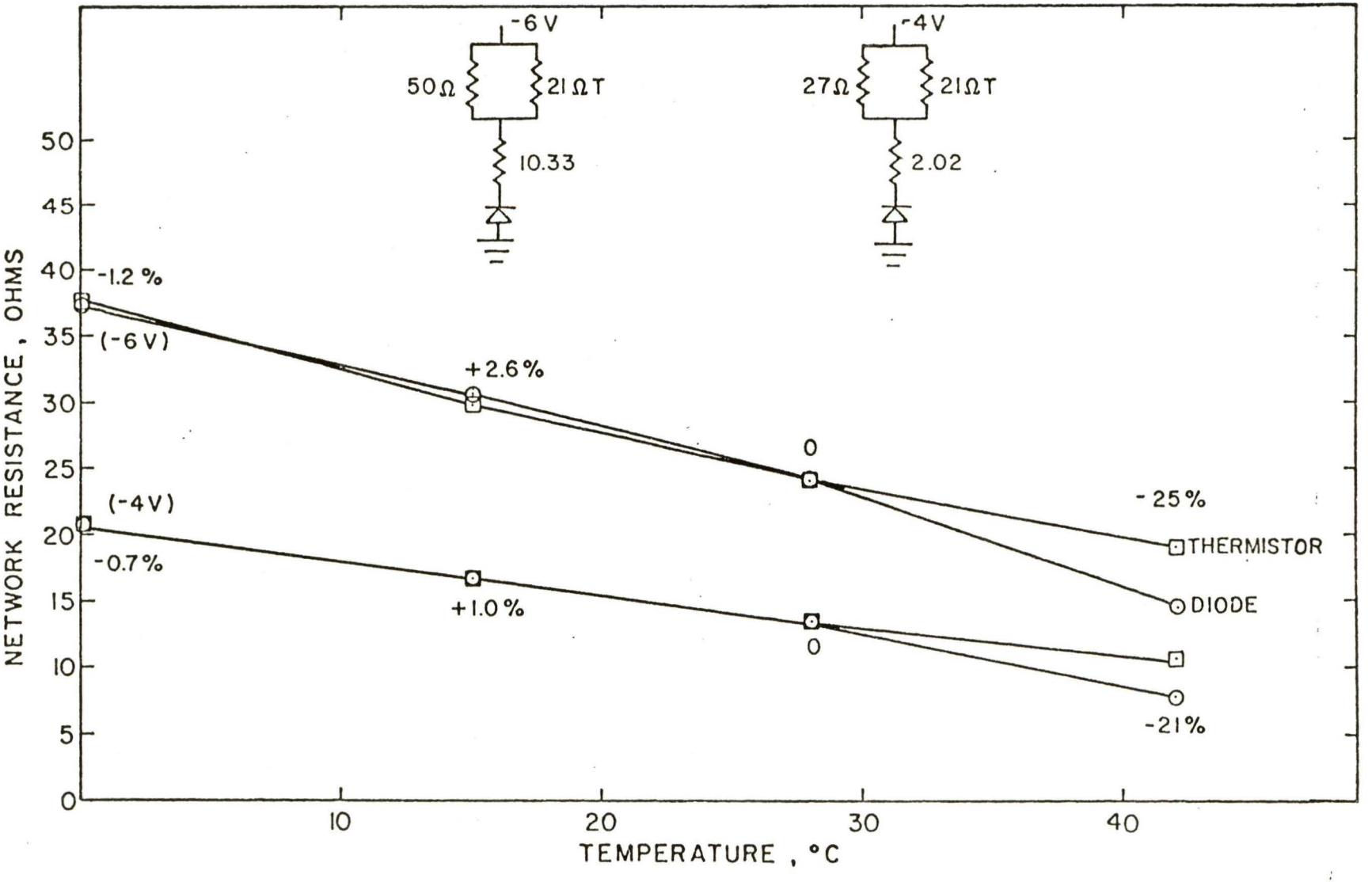

Figure 4 Thermistor component network for laser diode and network resistance as a function of diode temperature.

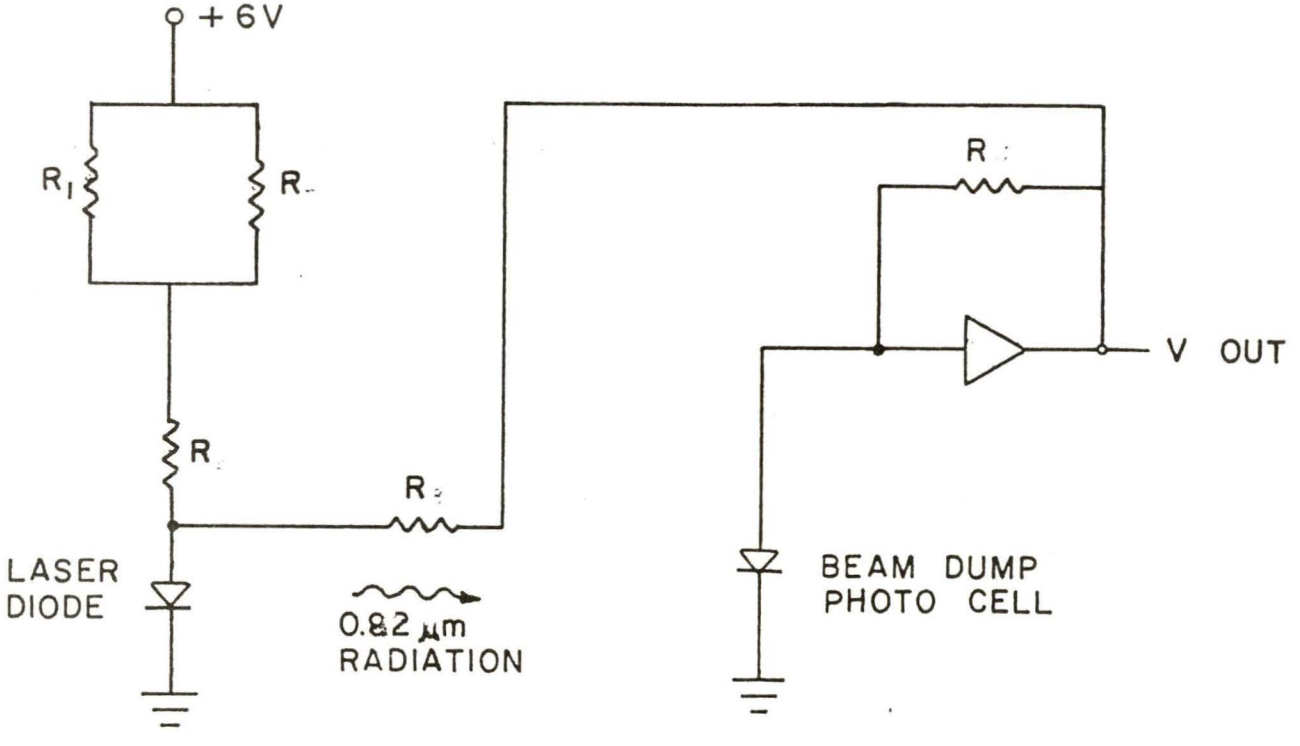

Figure 5 Schematic of laser diode intensity control circuit.

The feedback circuit will not compensate for loss due to particle scattering, since there is rarely more than one valid count in the beam at once. When more than one is present, the electronics detects them as a single particle. The maximum particle concentration limit is set by whatever error limit for multiple counts one deems acceptable. (See Section 4.1 for in-depth discussion.) The feedback circuit has not been incorporated into the system at this time. Consequently, the beam intensity is manually controlled to maintain a constant output which is monitored and displayed on the panel meter. However, after the initial electronic "warm up" time, there is no drift in the laser output.

1.2 Optics

1.21 Beam-Forming Optics

The light is emitted from a laser pellet inside the diode package. The pellet is 2.03 mm from the outside surface of a glass window 0.89-1.65 mm thick (Figure 6). These distances define the minimum free working distance of the objective lens used to collect and focus the light. The light exits from the edge of the pellet as an asymmetrical beam. The beam spread (1/2 power angle) has a maximum of 20° in the plane normal to junction, and this defines the lens numerical aperture, N.A., needed to collect the emitted light. The largest N.A. lens with the necessary working distance that is available at low cost is a 20 power microscope objective lens (Rolyn 80.3070). The N.A. is 0.35, and the working distance is 4.0 mm. From the definition of N.A. as:

$$\text{N.A.} = \sin \frac{\alpha}{2}$$

$$\frac{\alpha}{2} = 20.49°$$

Using a half-angle of 20.49°, the percent of the total emitted radiant flux collected should be about 40% from the published curves in RCA Data Sheet C 30130. When the power was measured with and without the objective lens in place, using the PIN 10DF large area photo cell, 34% was collected. Since the lens may not be the proper distance for the 0.35 N.A. to be valid, a corrected N.A. of 0.31 was calculated as the equivalent N.A. when used with the laser diode source. The N.A. is used to define the entrance aperture of the lens, and thus, the beam spread angle of the output. When used at a 150 mm back focal length, the beam angle is calculated at 1.91°.

From this beam angle, the beam waist at the focal point where the particles pass through can be calculated:

$$s = 1.22 \lambda F$$
$$= 0.92 \ \mu m$$

$$F = \text{beam F number} = \frac{1}{\tan \alpha}$$

$$\alpha = 1.19°$$

$$s = 33.6 \ \mu m$$

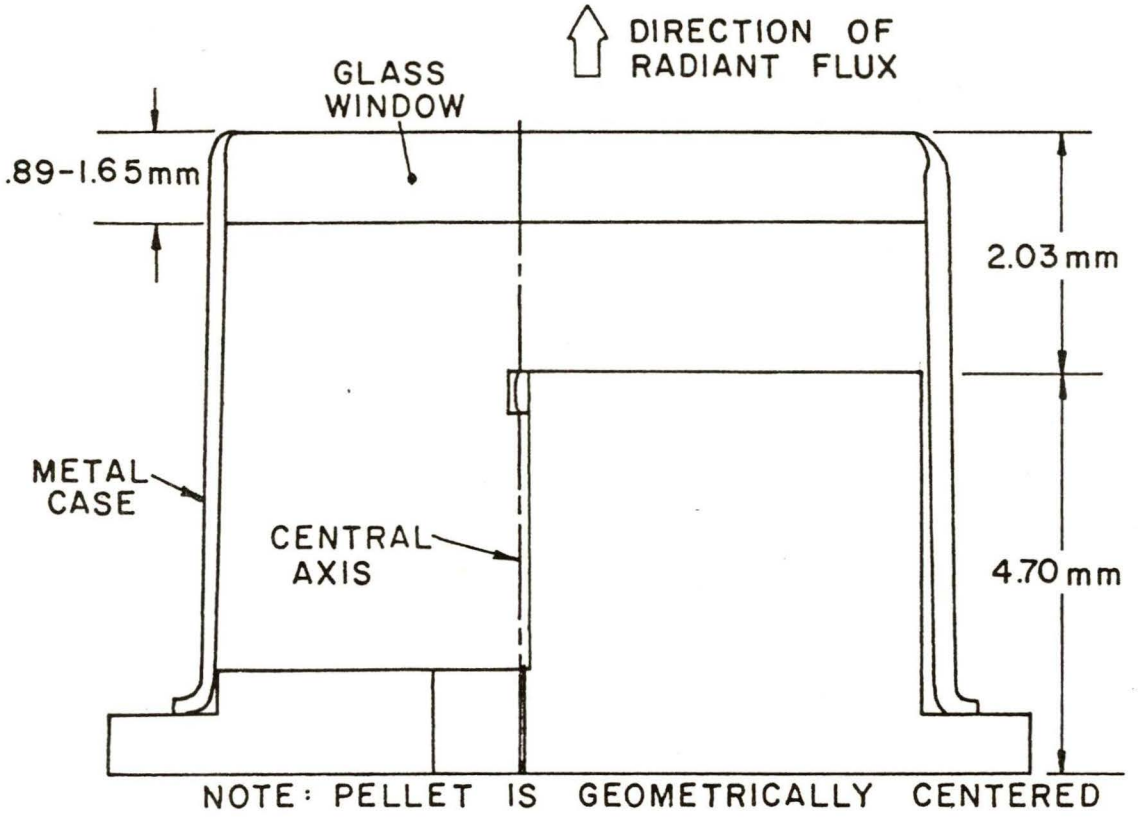

Figure 6 Laser diode cross section showing the location of the laser pellet.

1.22 Cylindrical Lens

The beam is focused to a line by the use of a cylindrical lens which has a back focal length of 150 mm in one plane and infinity in the other (parallel surfaces). This lens is placed 30 mm behind the objective lens and brings the beam to focus at 101 mm in one plane. The width of the beam at that point is calculated to be 1.15 mm. Thus, if the lens performance were perfect, the beam shape at the point where particles pass through it would be as shown in Figure 7.

1.23 Beam Shape Testing

An important feature of this instrument is the shaped light beam that allows high count rates. The aerosol flow field in the region of the light beam has a circular cross-section of about 0.6 mm in diameter. The ideal case would be to have the light pass through this region as a parallel beam. Any change in light intensity across or along the beam causes an error in the indicated particle size.

Several factors affect the beam shape:
1) Source shape
2) Lens characteristics
3) F number of beam

1) Source shape

The laser diode used has a multimode source. There are several lasing regions in the strip junction, and power is emitted from a series of points along the middle of the exposed junction.

The center spots tend to be the strongest, but there can be up to three or four nearly equal spots. It is the nature of lasing media to have opposite polarizations of adjacent regions. When the junction is focused to a remote spot, the difference in polarization causes a complete cancellation of light intensity at a point between the spots on the image. When the beam is expanded into a line source by the use of a cylindrical lens, the dark region can be oriented either parallel to the line or perpendicular to the line. If the dark region is perpendicular, there will exist a region where particles can pass through the beam without being illuminated, so the selected orientation is with the dark regions parallel to the line directions. The particles now pass through light and dark regions while going through the beam, but the average intensity is the same over the cross-section of all particle paths. The output light signal is a replica of a scan along the emitting surface of the exposed end of the junction of the laser diode. The response time of the photo cell receivers integrates this variation into a single Gaussian shaped pulse, however, and the electronics does not see the fine structure of the beam intensity profile.

The source region on the laser diode can now move about, with the only effect that the beam will intercept the particle paths at a different point along its path, but well within the focal spot of the photo cell receiver. Small changes within the diode junction and on the emitting surfaces can move the preferred lasing regions a few hundred nanometers.

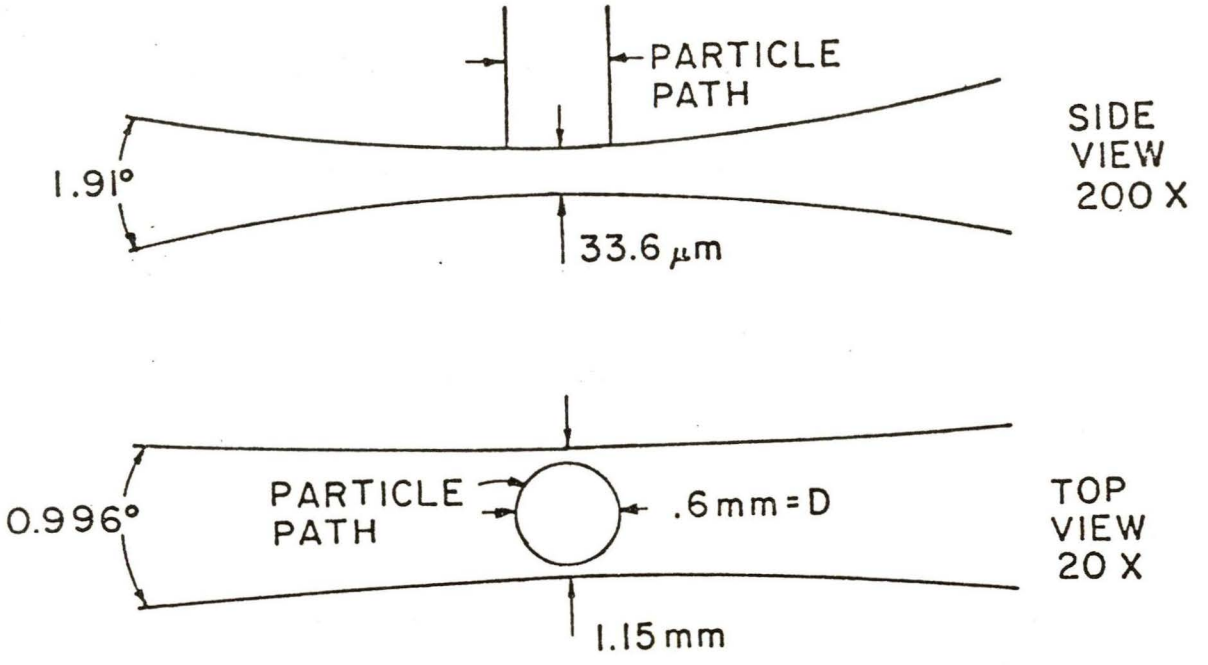

Figure 7 Calculated laser beam shape in the vicinity of the view volume.

2) Lens characteristics

The lenses used are standard and do not apodize the beam other than the normal limits of the aperture set by the N.A. The beams are thus focused as ideal Gaussian beams, since the source is coherent. The intensity distribution in space from each point source at the junction is defined by the equation

$$I_x = I_o \, e^{(-x)^2}$$

The shape is as shown in Figure 8. The beam width has been chosen to be the distance between the points where the intensity is 0.7 of the peak intensity. The actual beam will be a complex superposition of the intensity distributions of all the point sources focused to nearly the same region of space.

3) F number of beam

The F number of the back focal length of the lens determines the angle of convergence and divergence of the beam at the focal point. This number determines both the thickness of the beam at the waist and the depth of field of the focal point.

The depth of field is defined as the region where the beam diameter is not larger than 1/0.7 of the diameter at the waist. The depth of field, d, needed is defined by the diameter of the particle beam (Figure 9). Thus, the beam shape is a complex function of the optical components used, and is critical to the performance of the instrument.

A special instrument was made to measure the beam intensity distribution in space at the focal point. The source optics assembly (laser diode, objective lens, and cylindrical lens) was mounted on a short section of optical bench, so that it could be translated along the beam axis and rotated about the beam edge (Figure 10). At the focal point, a knife edge was mounted on a micrometer drive that would vertically translate 1 mm perpendicular to the knife edge surface. The position was transduced electrically using a precision 10 turn potentiometer on the drive knob. The knife edge was moved through the beam to block it progressively with an accuracy of about 1 μm.

The beam was directed into a large area photo cell (PIN 100f) positioned on the opposite side of the knife edge from the source, and the photo cell output was recorded on one axis of an x-y plotter. The transduced knife edge position was recorded on the other axis.

The knife edge is scanned manually through the beam at progressive locations along the beam in the regions of focus. The output plot is a curve that represents the unblocked portion of the beam. If this curve is differentiated, the result is the intensity profile of the beam. The beam intensity can thus be experimentally determined in both planes and along the beam. Figures 11 and 12 show examples of the output plots for a scan across the waist region parallel to the particle flow direction and a scan perpendicular to the particle flow direction. The differential, which is the beam power profile, is also shown for each scan.

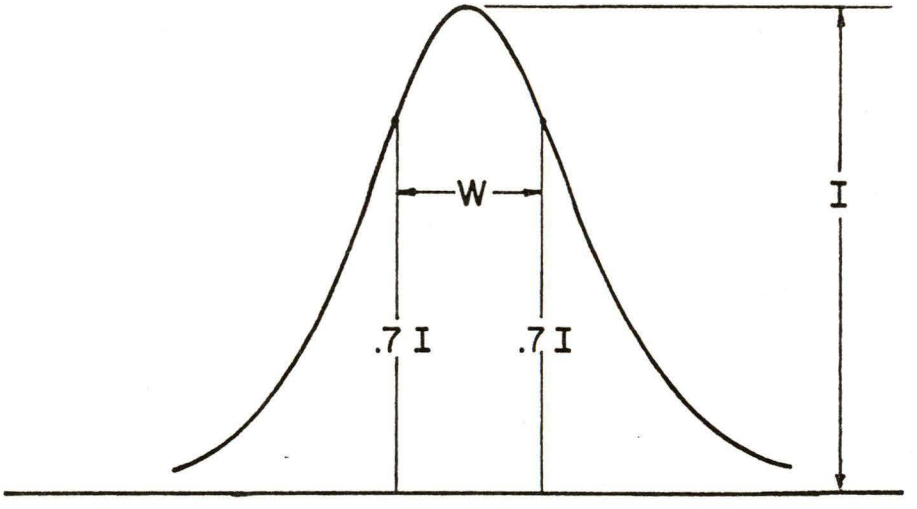

Figure 8 Ideal intensity profile of laser beam at view volune.

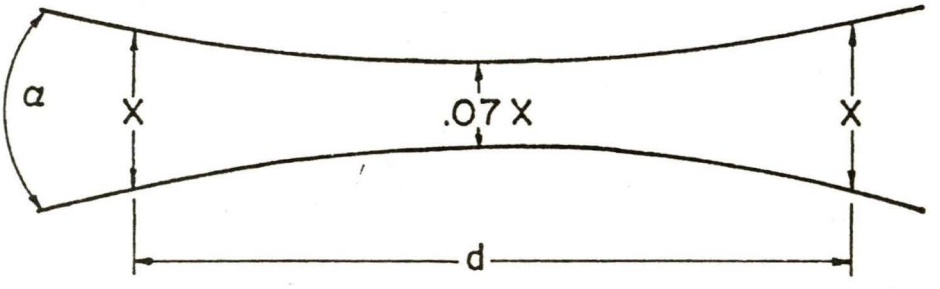

Figure 9 Waist of laser beam at the view volume.

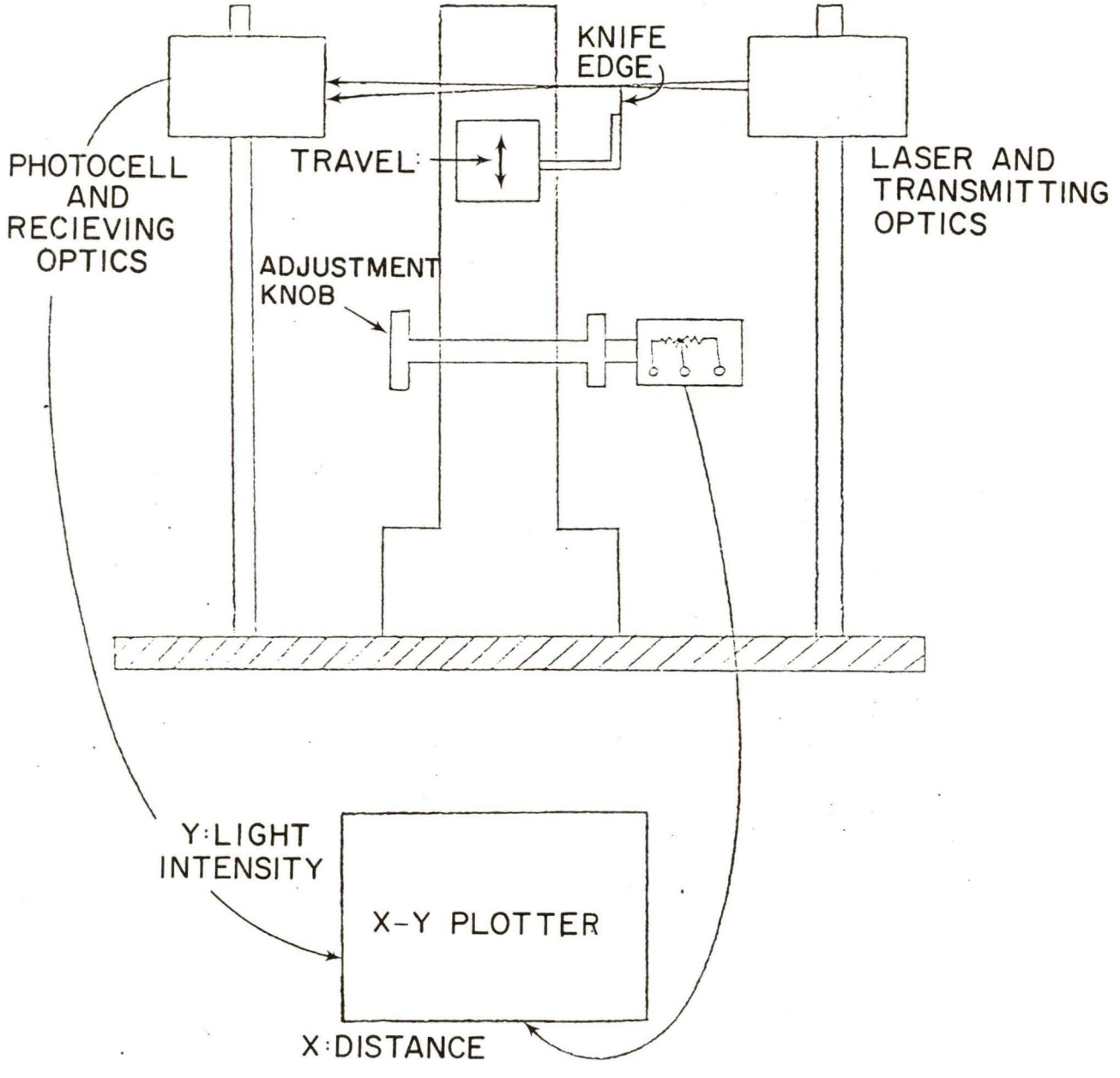

Figure 10 Schematic of microscope knife edge scanner.

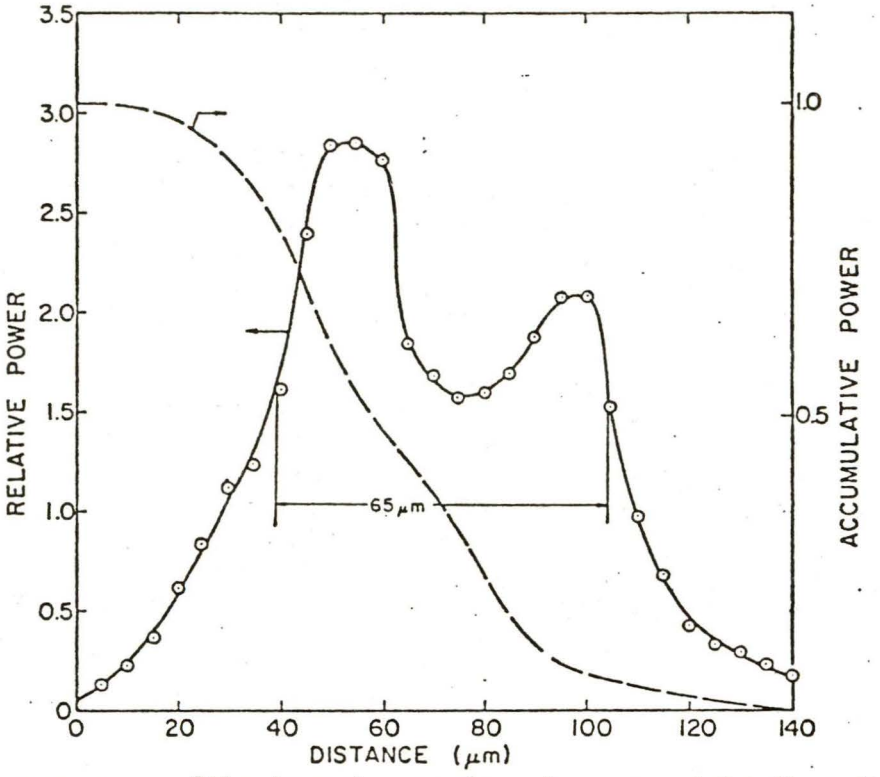

Figure 11 Beam power profile in waist region along particle flow direction.

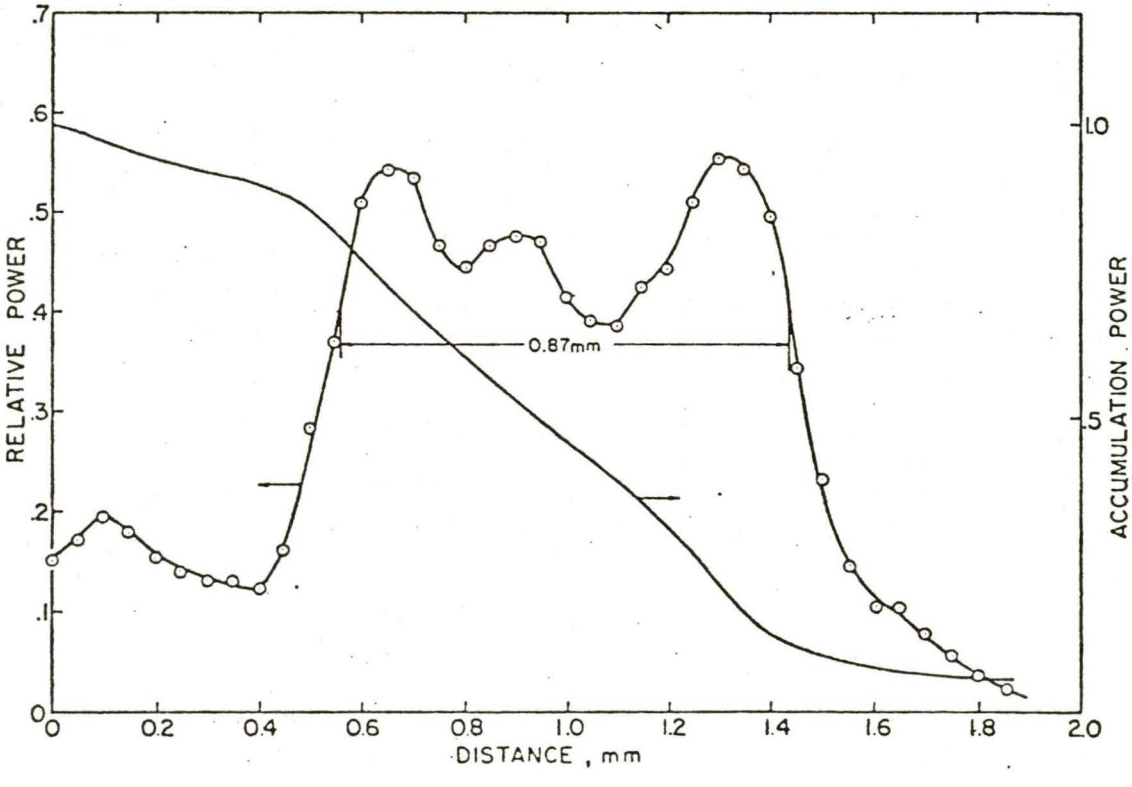

Figure 12 Beam power profile in waist region mutually perpendicular to the particle flow direction and laser beam axis.

To determine the beam profile along the beam, scans were made at 0.038 mm intervals. When reduced to intensity profile, the beam shapes were similar to those shown in Figures 11 and 12. The effect of the multiple sources can be seen in the profiles across the waist of the beam.

1.24 Beam Dump

The laser beam that passes through the sample chamber is absorbed in the beam dump chamber. The beam has a low divergence and is apertured at the cylindrical lens to remove the edges of the Gaussian distribution far enough from the receiver optic to prevent defracted light from entering the receiver photo cell. The inside of the beam channel from the cylindrical lens to the sample chamber is painted black to absorb this defracted light.

The beam exits the sample chamber through the hole in the spherical mirror receiver optics. The photo cell beam monitor (Section 1.12) is placed at an angle to the beam, so that surface reflected light remains in the beam dump chamber. The inside of the chamber is painted black with 3M Nextel 101-C10 black velvet-coating paint to absorb the beam energy that is not absorbed by the beam monitor. In addition, the monitor is placed as far as possible behind the aperture to minimize the beam energy that will be scattered due to diffuse scattering from dust and imperfections on the surface. The beam dump surface normal to the photo cell is an area that can only be illuminated after the radiation has been scattered at least twice inside the chamber and is very much attenuated. A schematic of the beam paths and apertures is shown in Figure 13.

1.3 Mechanical Design of Light Source

Although the individual components (laser diode, objective lens, and cylindrical lens) are accurately constructed, the magnification of the source image at the view volume dictates that provisions be made for adjustments during assembly to ensure focus of the light beam at the view volume.

The procedure used is to assemble the laser diode and the two lenses as a separate unit that projects a beam to the approximate location in space relative to these components (Figure 14). This unit is then mounted into the sample chamber by an adjustable mount that allows lateral and longitudinal adjustment of the beam waist location to intersect with the particle flow path. By making the adjustment in two steps, the 20:1 magnification does not limit the final adjustment accuracy which is a 1:1 ratio between beam location and movement of the component.

The laser diode is enclosed in a sealed chamber and is in close thermal contact with Fenwal Washer thermistors for current control. The low power dissipation from this assembly of only about 1 watt makes any special heat sinking unnecessary. The positive terminal of the diode is the diode heat sink stud, and the return current is via the aluminum encloser. The main power and the feedback control lines enter through hermetic feedthroughs.

2 Particle Sampling Port

The inlet was adapted from the modified design for the Royco 218[1] and is shown in Figure 15. A small bore tube isokinetically samples 0.28 lpm of the

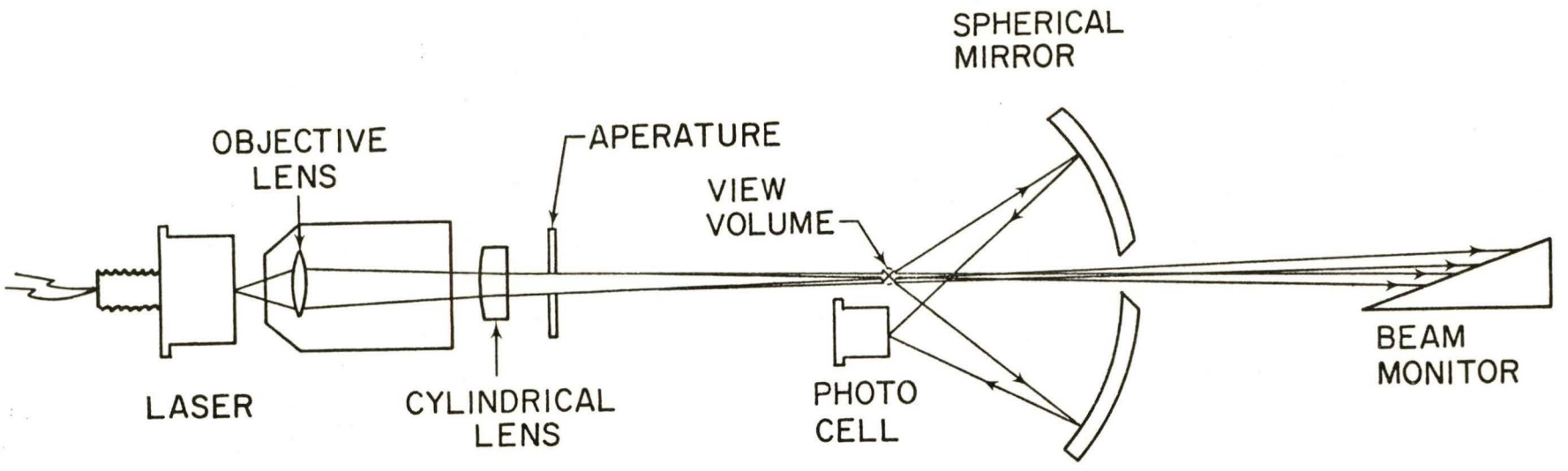

Figure 13. Schematic of optical system and light path.

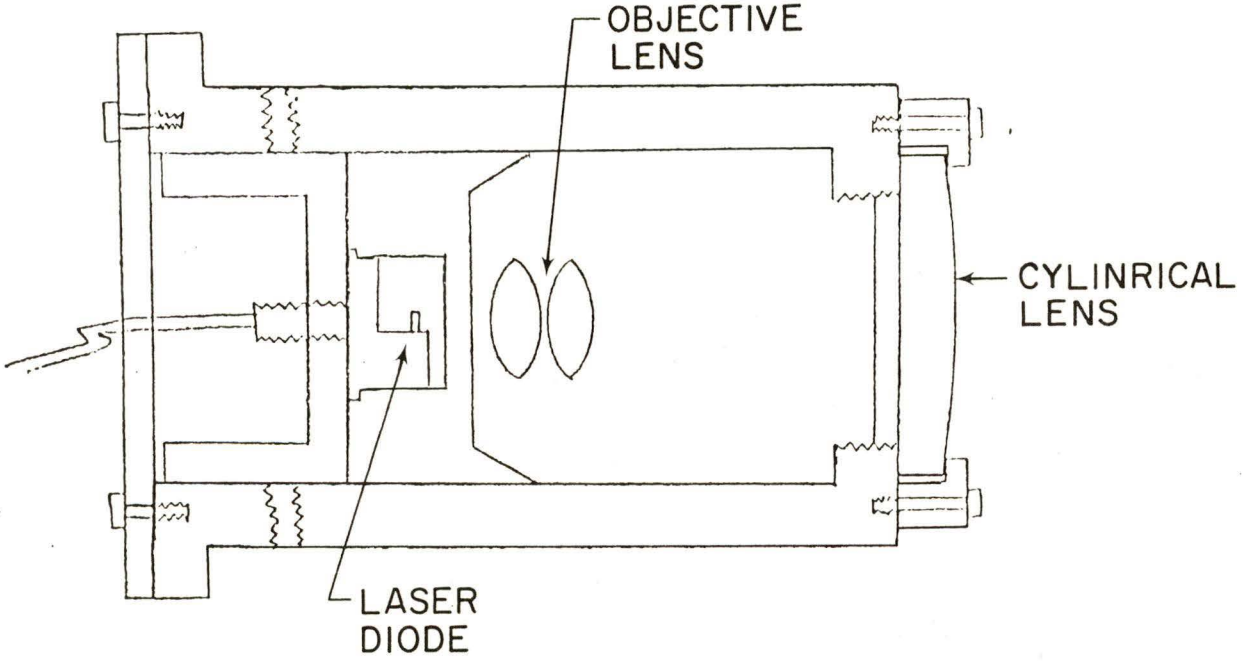

Figure 14 Schematic of laser light projector cell.

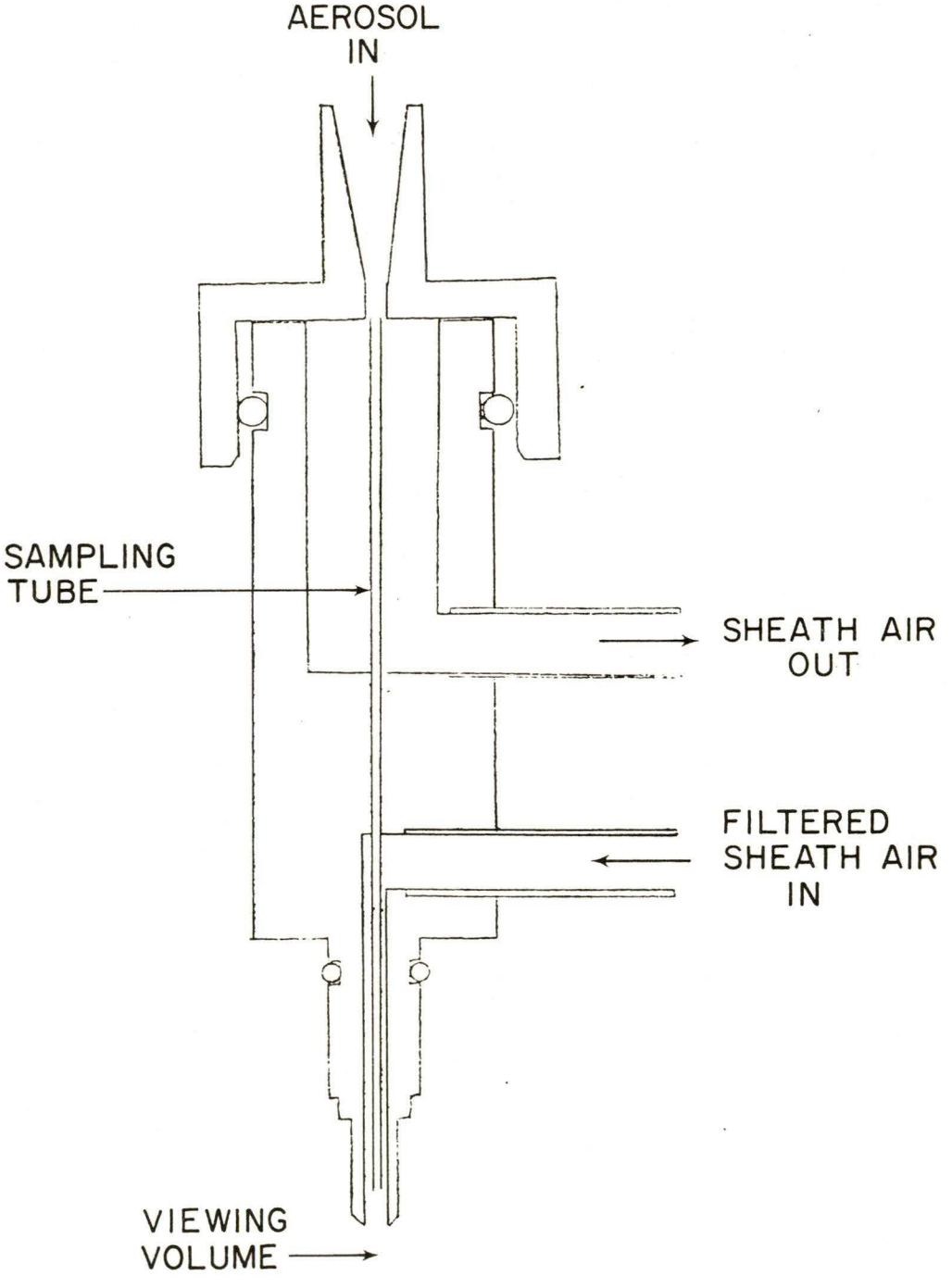

Figure 15 Schematic of modified Royco 218 inlet.

2 lpm inlet flow. The 0.28 lpm aerosol flow passes into the instrument, and the remaining flow passes through a filter and is returned as a clean air sheath surrounding the inlet tube where the particles enter the light beam. The pressure drop through the small bore inlet tube provides the driving force for the filter.

When this inlet assembly was used with the prototype laser particle counter, it was found that the flow was turbulent when operated at the design flow rate of 2 lpm. The incoherent and large beam used in the Royco does not detect this, but the slit optics of the present design indicates a much broader apparent particle size distribution at high velocity rather than at low velocity when monodisperse, ideal particles are sampled. In order to determine the best flow velocity for both the sample flow and the clean air sheath, a test set-up was constructed with separate controls on each air flow.

It was found that the ratio of sample to sheath flow is dictated by the area ratio at the exit. The aerosol sample flow velocity must be somewhat larger than the velocity of the surrounding coaxial sheath flow in order to maintain a velocity gradient from the center outward. If the sample velocity is less than the sheath velocity, an instability results, and the particle flow becomes turbulent, resulting in a wide range of particle velocities through the beam.

However, if the sample velocity is much larger than the sheath air velocity, there is a large gradient in the otherwise stable particle flow. This gives a range of individual particle velocities through the beam and the apparent particle size varies from some minimum corresponding to the center line velocity up to much larger apparent particle sizes corresponding to the slower particles near the edge of the sample flow. As the sheath flow is increased in velocity, the larger apparent sizes progressively disappear with the distribution becoming very narrow just before the sheath air velocity exceeds the sample velocity.

It was found that the best flow rate at the inlet of this test unit was 0.57 lpm with the sample flow at 0.21 lpm. The following aerosol test data was taken at these flow rates. If a 2.0 lpm inlet flow is needed, the dimension of the inlet can be adjusted to maintain the velocities determined to give stable flows.

The particle residence time in the beam as measured by the oscilloscope on the output photocell pulses is about 1 μsec. This is a little longer with larger particles, since the pulse starts when the particle enters the edge of the beam and the particle length in the direction of the flow is added to the 65 μm beam thickness. This residence time is important from the standpoint of particle coincidence loss, which results when two or more particles are simultaneously present in the view volume, since this particle counter is being designed for possible use to monitor extremely high dust concentrations. This subject is discussed in greater detail in Section 4.1.

2.1 Sample Tube Assembly

The final design of the inlet to be used with this instrument is shown in Figure 16. The center tube portion of the inlet assembly is removable for

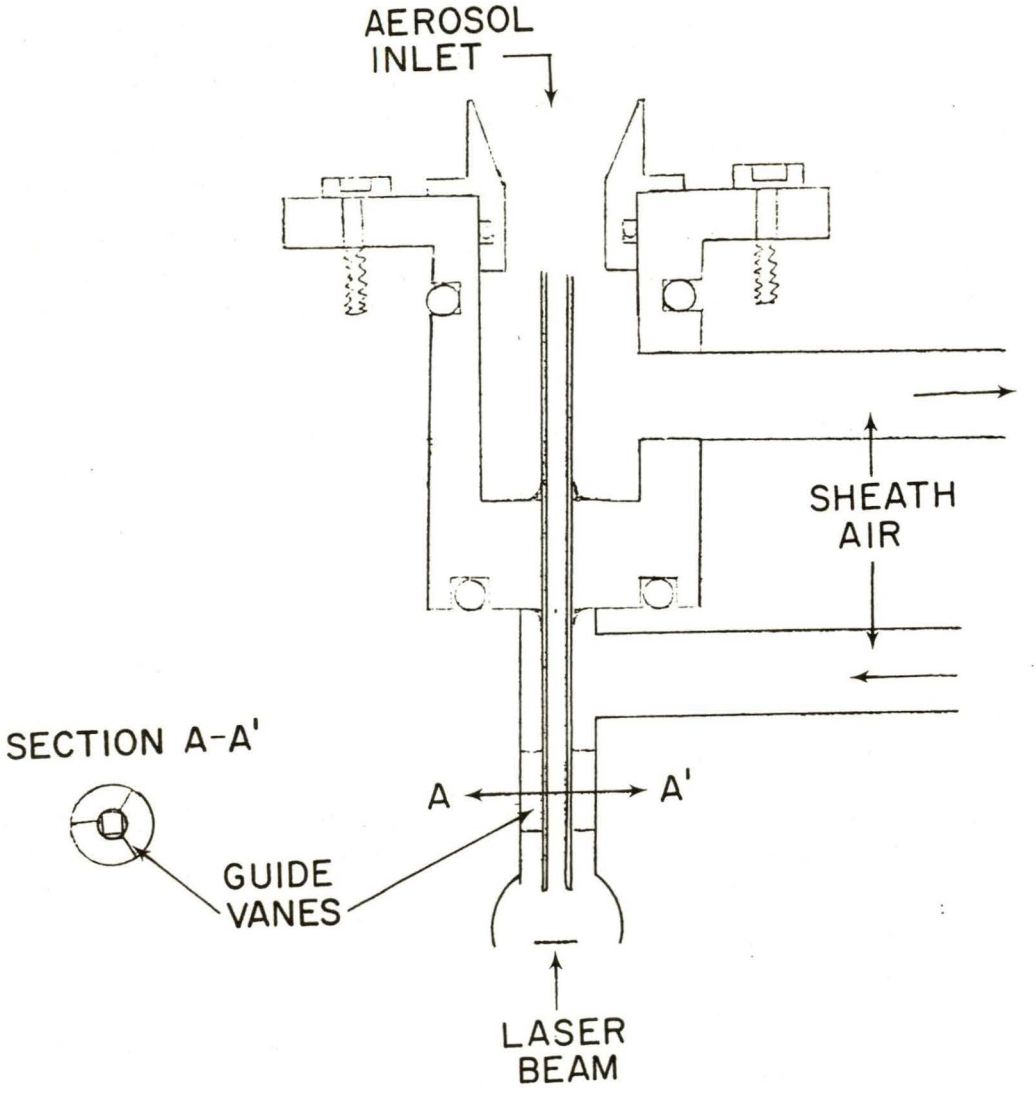

Figure 16 Removable inlet design.

cleaning, while the outside passageways to and from the filters are drilled into the inlet block. O ring seals are used on the inlet tube fitting.

The end of the sample tube extends into the beam chamber to about 1 mm above the slit beam, and is centered by guide vanes soldered to the tube. These vanes also serve as sheath flow straighteners.

2.2 Sheath Air

Some of the inlet sample flow is shunted through a filter element to provide a supply of clean air for the sheath air flow. This flow prevents particles from circulating in the beam chamber by purging it with a flow of clean air. The filter used is a Balston Model DFU, Grade B filter tube which is only 2.5 cm in diameter and 8.1 cm long. The filter pressure drop is low, so the filter flow rate must be regulated by a series valve. The overall flow system, which includes the filter, valve, and pump, is schematically shown in Figure 17.

In order to prevent condensation of water vapor on the optical components, the sheath air is also partially dried by a silica gel dryer element. A low resistance flow through design is used to minimize pressure drop.

2.3 Pump

The system is designed to be used with either an internal pump or a self-contained personal sampler pump. The system requires a pump capable of drawing 2.0 lpm at a pressure of 8 cm water. Currently, a Bendix Micronair II permissible personal sampler pump is being used.

2.4 Inlet Cleaning Rod

Since the inlet is exposed directly to the outside air, large particles can lodge in the small bore tube and block the flow. The laboratory technique is to clean the tube periodically with a wire. This would be difficult under field conditions, so an internal cleaning rod is incorporated in the inlet block (Figure 18). The beam chamber outlet to the pump is at an angle, so that a piston with a cleaning wire can be aligned with the inlet tube. The piston is stored retracted, so the wire is out of the flow path. The piston can be manually pushed up to its seated position, which will push the aligned cleaning wire up through the inlet tube and extend a small distance out of the inlet. Accumulated debris will be pushed backwards out of the inlet and can be brushed off of the wire before it is retracted.

This cleaning mechanism could be automated by using an air piston powered by the pump output to push the cleaning wire into the inlet tube at regular intervals.

2.5 Inlet Block Mechanical Design

The inlet block (as shown in Figure 19) is the support for the complete optical head assembly. The laser projector unit mounts on one side, and the optical receiver and beam dump on the other side. The printed circuit board containing the photo cell, preamp, and pulse shaping circuits is clamped between the two mounting plates. The top part of the inlet block bolts to the upper

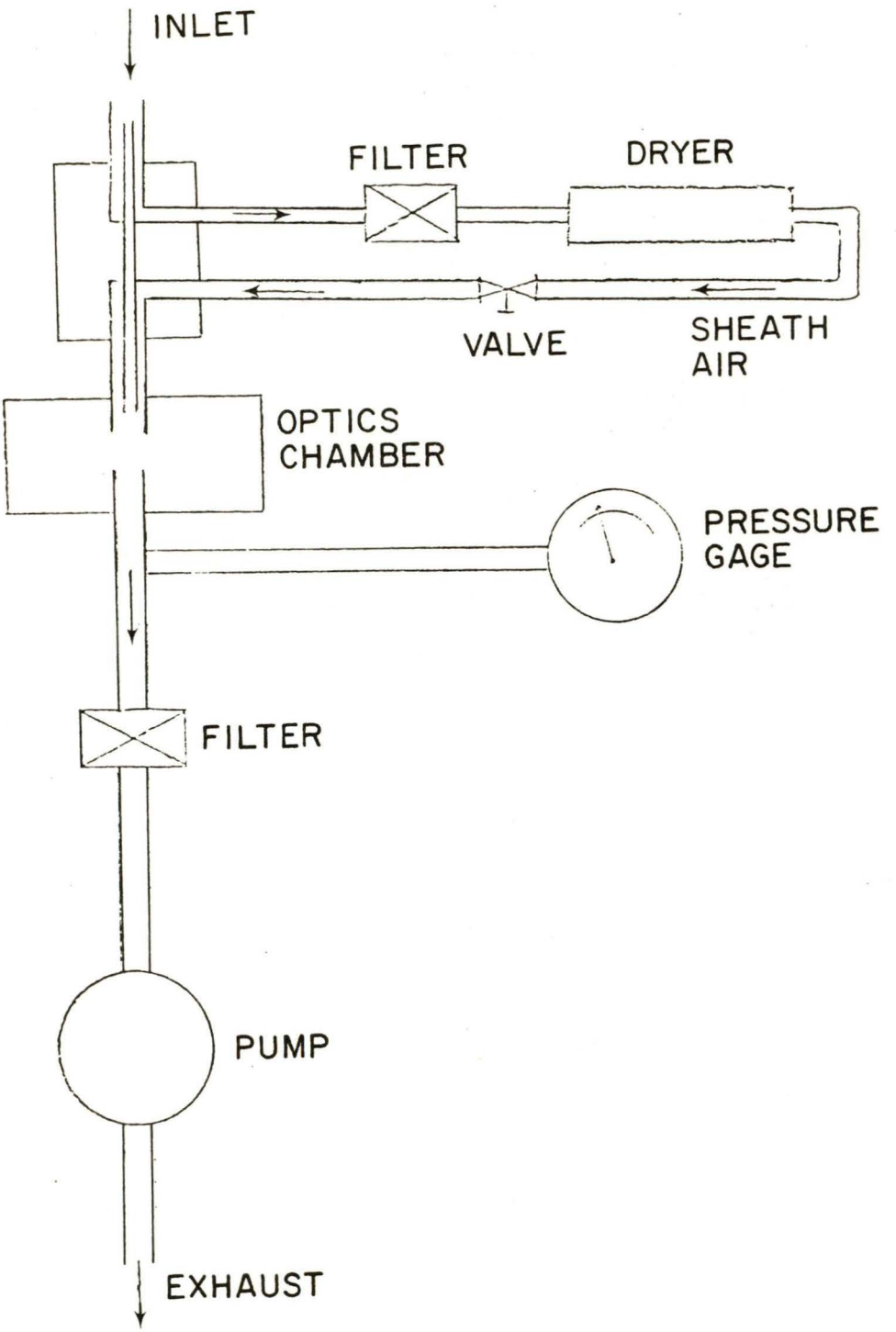

Figure 17 Air flow system.

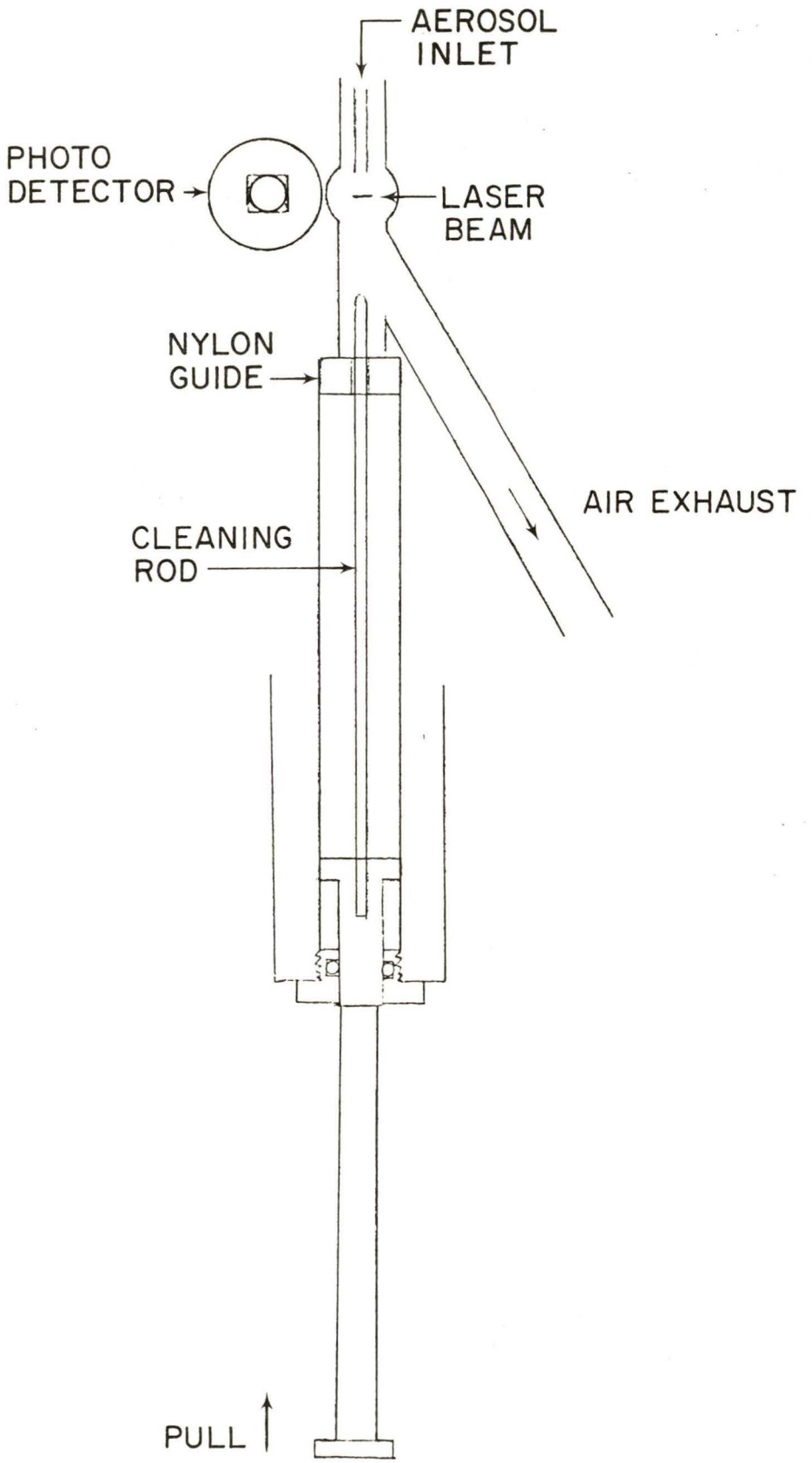

Figure 18 Cleaning rod mechanism.

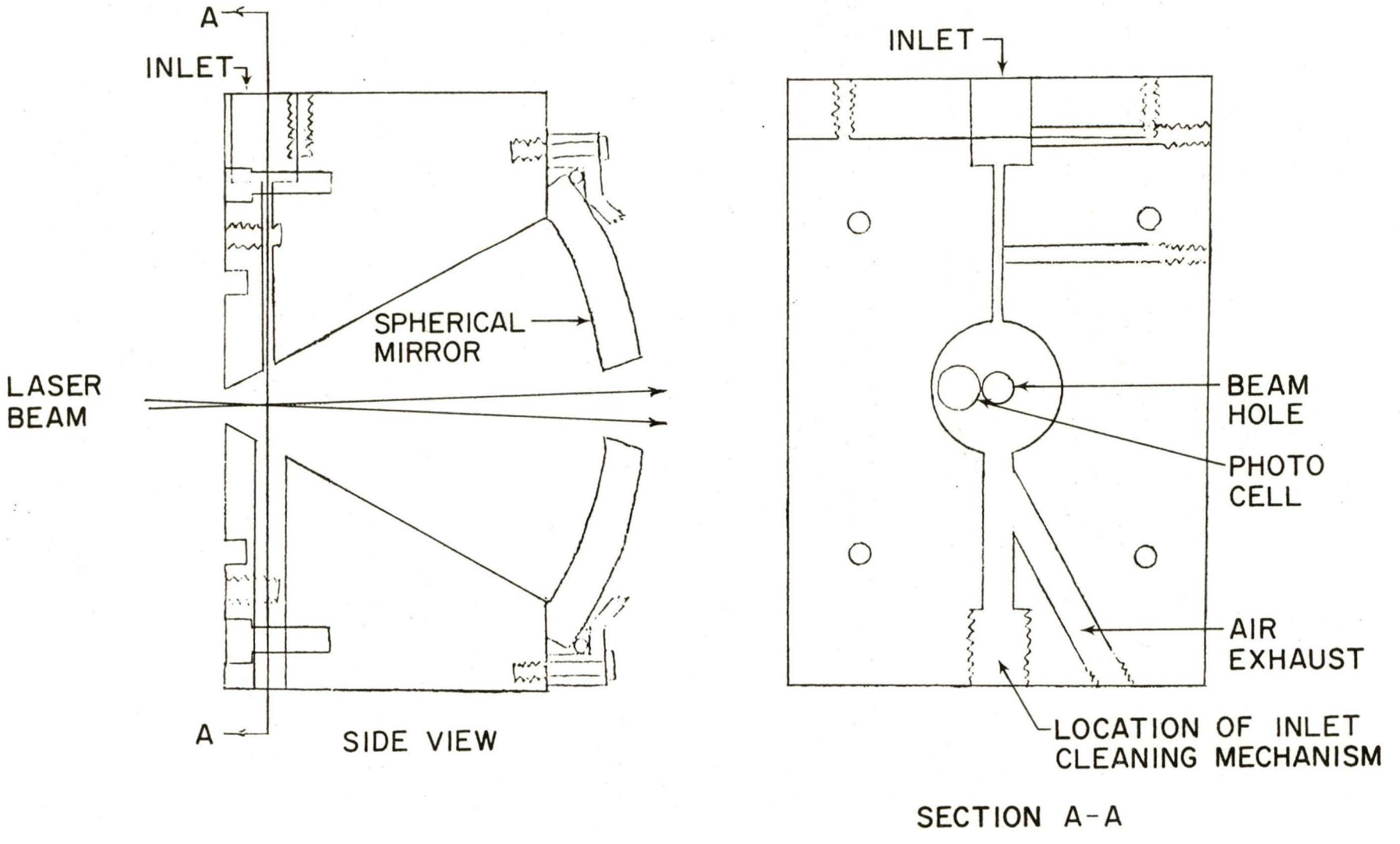

Figure 19 Inlet and receiver optic block design.

panel of the instrument, so that the inlet port extends through the panel.

The assembly sequence of the parts shown in Figure 20 is as follows:

1) The projector mounting ring is cemented to the printed circuit board, which contains all electrical components and is electrically checked. Silicone rubber is used to seal the printed electrical output leads from the photo cell.

2) The inlet block is bolted to the projector mounting ring, thus clamping the P.C. board in place. An O ring is used to seal between the P.C. board and the inlet block. The photo cell position is carefully aligned to place the photo sensitive surface at the point where the illuminated particle images appear.

3) The laser projector assembly which has previously been assembled and focused is now bolted onto the projector mounting flange. The bolt holes have enough adjustment to allow the projected beam to be aligned to intersect the center of the particle path.

4) The spherical mirror block can now be aligned and bolted in place. Since both the laser projector and the photo cell are in place, the alignment of the mirror can be functionally tested with either particles or by using the cleaning rod as a test scatterer. (The actual design of the mirror is described in Section 3.)

5) The beam intensity through the mirror hole can be measured with a photometer before the beam dump assembly is bolted in place. The output of the beam dump photo cell should agree with the photometer.

6) The tubes connecting the optical head to the filter and the air pump can now be connected.

7) The completed assembly can now be bolted to the front panel of the instrument. The filter, pump, and batteries also mount onto this panel.

3 Scattered Light Receiver

3.1 Theoretical and Experimental Light Scattering Evaluations

Particles that pass through the slit beam of coherent light each scatter a pulse of light that has an intensity and angular distribution that depends on its size, shape, and optical properties.

The scattering intensity as a function of angle for spherical particles with a specified complex index of refraction (a + i b) can be calculated from Mie scattering theory. In order to select optimum receiver optics for the wavelength used (0.82 μm) and the particulate type (coal), the scattering intensity as a function of angle and different particle size was numerically calculated using a computer program developed by Adrian and Earley[2]. For the purpose of this calculation, the index of fraction for coal was assumed to be equal to that of carbon, which is 1.95-0.66i. Figure 21 shows the calculated normalized accumulative scattering intensity for spherical particles from 0.3 to 12 μm diameter as a function of scattering half-angle relative to the forward

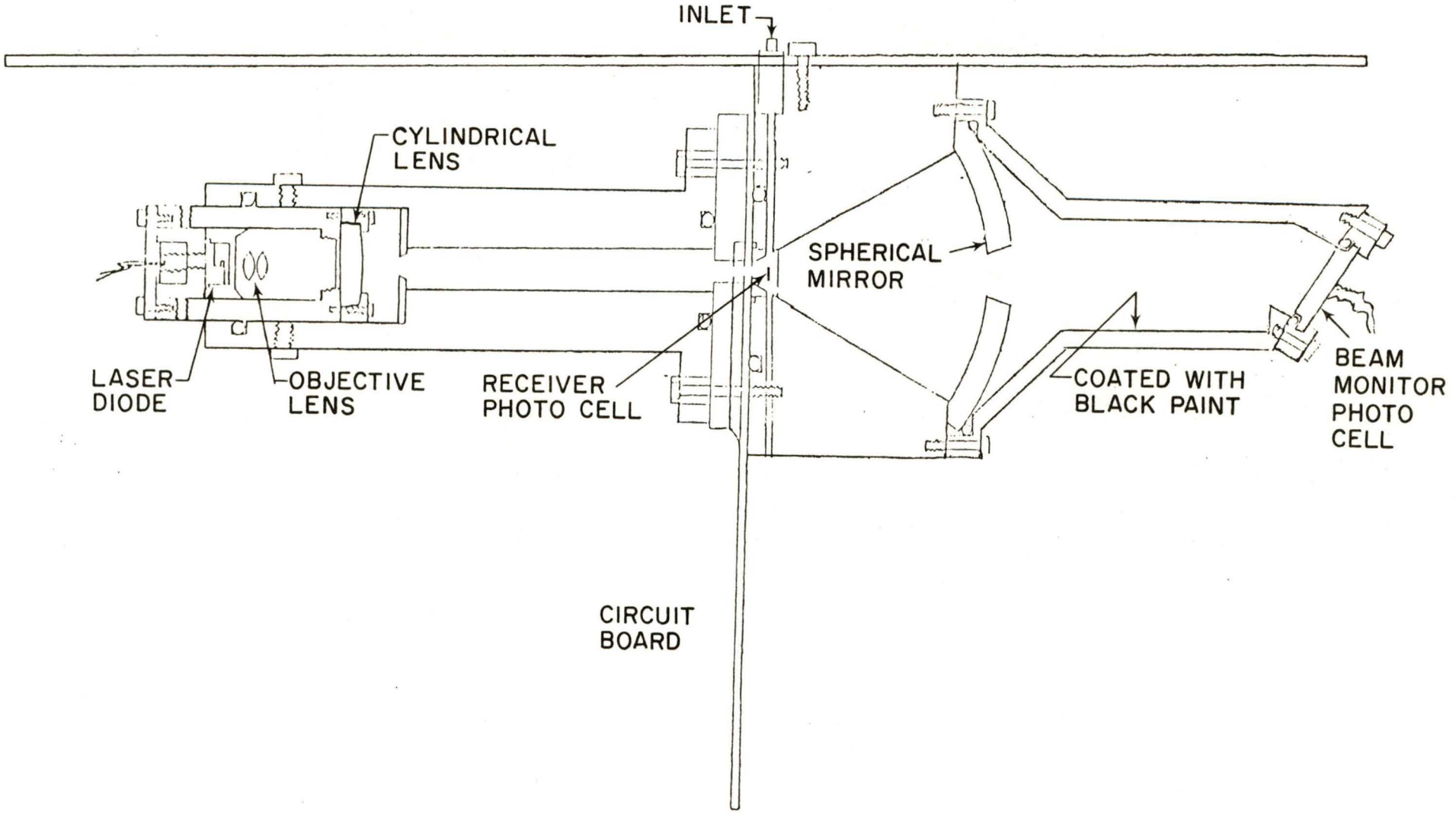

Figure 20 Schematic cross section of assembled optical head.

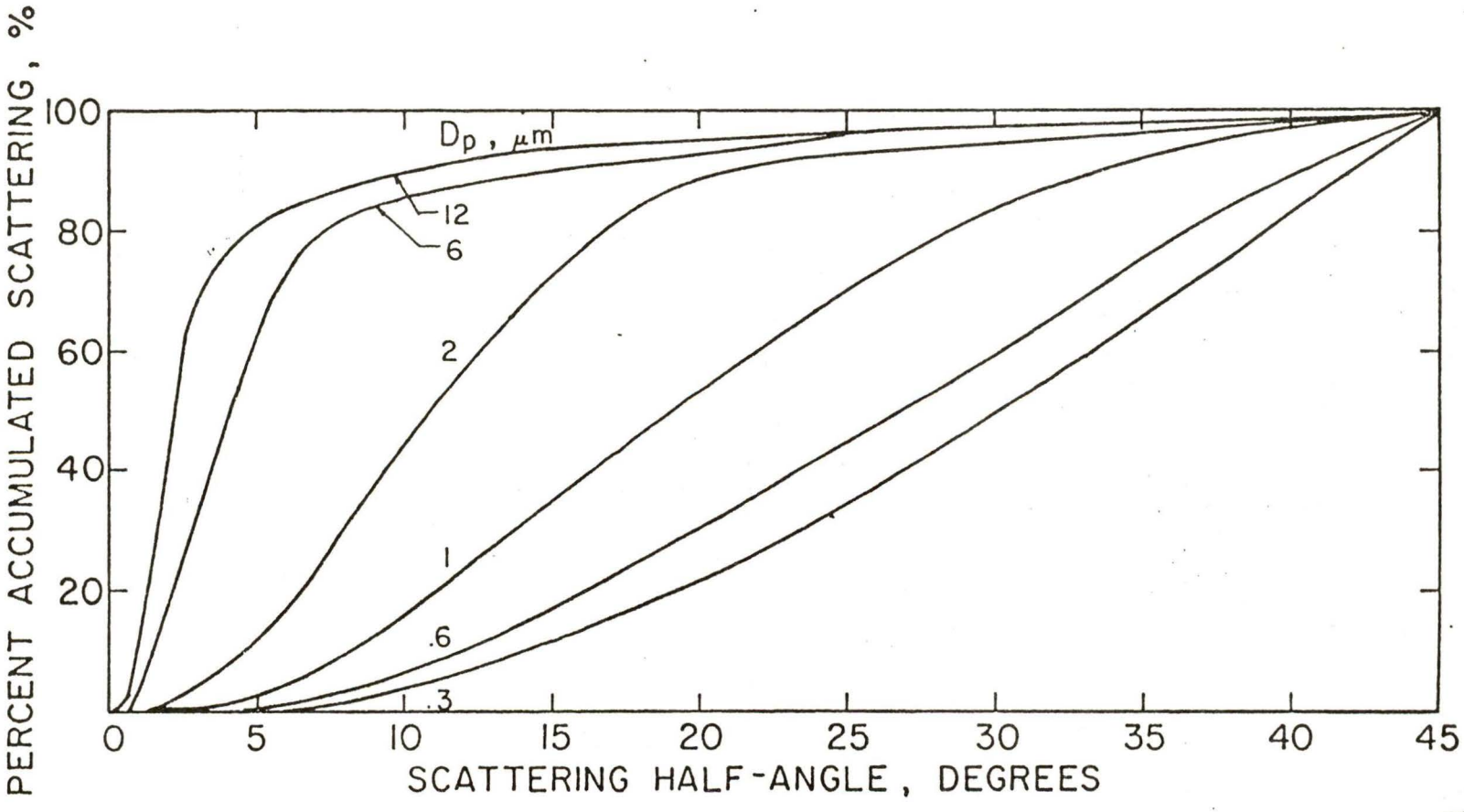

Figure 21 Normalized accumulative light scattering curves for coal dust.

direction. The data for each indicated particle diameter was normalized using the total accumulated scattered light from 0 to 45 degrees for that particle diameter.

The center portions of the forward-scattered light must be dumped along with the illuminating beam from the laser. The beam divergence of the slit-forming optics is much smaller than that of incoherent optic systems. As can be seen in Figure 21, the larger particles have a very intense forward scattering at low forward angles. Thus, the large difference in total scattered light from large and small particles can be reduced by using a large center beam trap area and as large as possible total aperture.

The unit has been designed with a 6° half-angle for the center beam trap and an average collecting aperture half-angle of 33°. This aperture half-angle is only an approximate average because the photo diode is not at the focal point of the spherical mirror.

The total light collected by the photo diode using monochromatic light with a wavelength of 0.82 μm was numerically calculated as a function of particle size for oleic acid (with an index of refraction of 1.46) and for coal dust over the size range from 0.3 μm to 12 μm. These theoretical curves are respectively shown in Figure 22 and Figure 23. Since the absolute value of the calculated scattered intensity can be arbitrarily set, the absolute values of the calculated scattering intensity as plotted in Figures 22 and 23 have been set to match the experimental output response of the prototype system. Thus, the relative shape of the calculated and experimentally determined calibration curves can be directly compared. One should note that the theoretical light scattering calculations were only made for a few particle diameters, so that the general shape of the response curve could be determined. As a consequence, with the exception of the large primary inflection point which occurs at approximately 1.5 μm, the fine oscillations in the response curve which are known to be present are not apparent.

The output voltage response of the instrument as a function of particle size has been experimentally determined using both ideal and coal dust aerosols. This calibration was performed using the same calibration techniques that were used for the original Royco 218 calibration.[1] The ideal monodisperse particles used were PSL and oleic acid, which ranged in size from 0.6 to 2.0 and 2.5 to 16 μm diameters, respectively. The oleic acid particles were generated using the vibrating orifice monodisperse aerosol generator.[3] The prototype calibration data for the ideal aerosol is presented in Figure 22.

The coal dust calibration was obtained using a polydisperse coal dust aerosol and inertial impactor technique which yields a calibration of the system based on the particle's Stokes' diameter as determined by an impactor.[4] The coal dust was generated using a fluidized bed dust generator.[5] Basically, for the inertial impactor calibration technique, two coal dust size distribution runs are made with the particle counter and the particle pulses accumulated with a multichannel analyzer (MCA). For the first run, the particle counter samples the dust aerosol through an impactor on its inlet, while in the second run, the impactor is removed. A ratio, R, for each MCA channel is then found by dividing the number of particles in each channel of the MCA for the first run by the number of particles in the corresponding channel of the second run. The channel

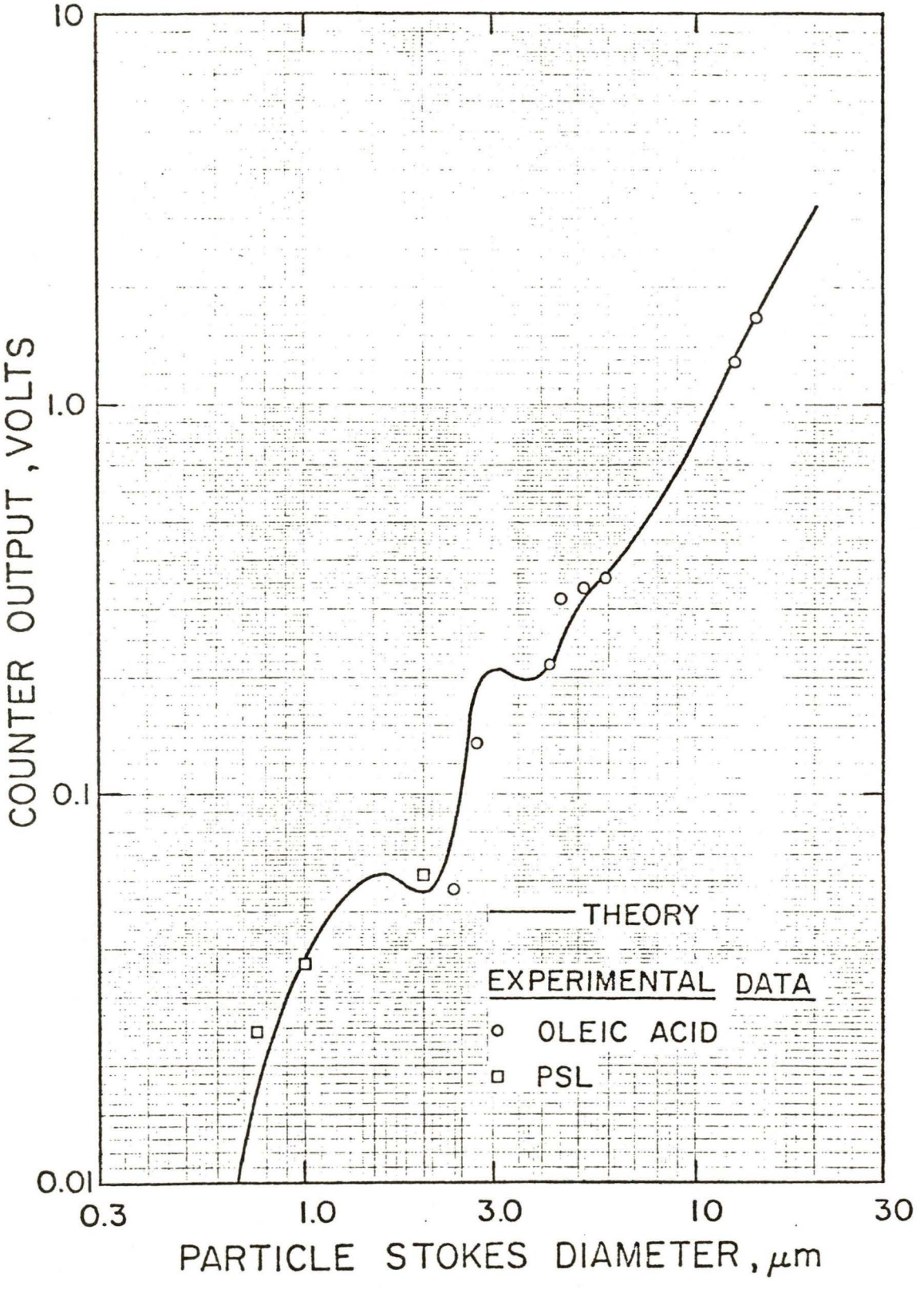

Figure 22 Laser Diode Optical Particle Counter
Ideal particle calibration curve

number, or the corresponding pulse voltage, for which this ratio is 0.5, corresponds to the 50% cut-off of the impactor. The resulting coal calibration data is presented in Figure 23. One should note that the system has only been calibrated in the particle size range of 1.5 to 12 μm. This calibrated range is not limited by the particle counter, but rather results from limitations in the current impactor calibration technique.

As one can see from the comparison between the theory and experimental data, there is agreement in the general slope of these two response curves for both the ideal and coal dust particles. However, there is some discrepancy in the finer structure of the curves. Nevertheless, since the response of the prototype system to ideal and coal dust particles behaves in a theoretically predictable manner, these comparisons confirm the integrity of the complete mechanical and electronic design. This also implies that, in general, it is possible to obtain a monotonically increasing relationship between particle size and the instrument response for coal dust aerosols. This coal calibration data also agrees well with the previously obtained coal calibration data for the Royco 218 with its white light source[1] which further confirms the feasibility of using this laser light source.

3.2 Receiver Optic

In order to make the instrument more compact, reflective receiving optics were selected for the portable instrument. As shown in the schematic of the optics (Figure 13), a spherical mirror is used to collect the scattered light and focus it onto on the photo cell. The small size of the silicon photo cell allows it to be placed to one side of the illuminative beam, and the mirror operates as a 1:1 reflector in which the two focal planes are superimposed. Light from a point on this plane is brought to a focus on a point equidistant on the other side of the optical axis. The image quality is good, since the two image points are separated by a little more than the diameter of the photo cell ($\approx$.64 cm). If the image points were on the axis, the image would have no geometric or chromatic distortion.

The center of the spherical mirror is removed to allow the illuminative beam to pass into the remotely placed beam dump. The off-axis location of both the illuminative beam and the photo cell allows the aperture in the mirror to shield the photo cell from direct view of the beam image in the beam dump. This makes it necessary for scattered light to make several reflections on the low reflection surface of the beam dump cavity before it can reach the photo cell.

The use of a spherical mirror gives a high quality large aperture receiver at low cost. The coated aluminum front surface reflection has a high reflection coefficient ($\approx$0.95) in the near I.R. (.82 μm).

3.3 Photo Cell and Preamp

The photo cell used is the Bell and Howell, Control Product Div. Type 539-01-5 integral silicon photo cell and operational amplifier. Externally connected feedback resistors and photo cell biasing connect the unit as a D.C. coupled light detector. The specification of this photo cell is given in the data sheet entitled "Type 539 data sheet". The photo cell is capacitor-coupled to the preamp as shown in Figure 24.

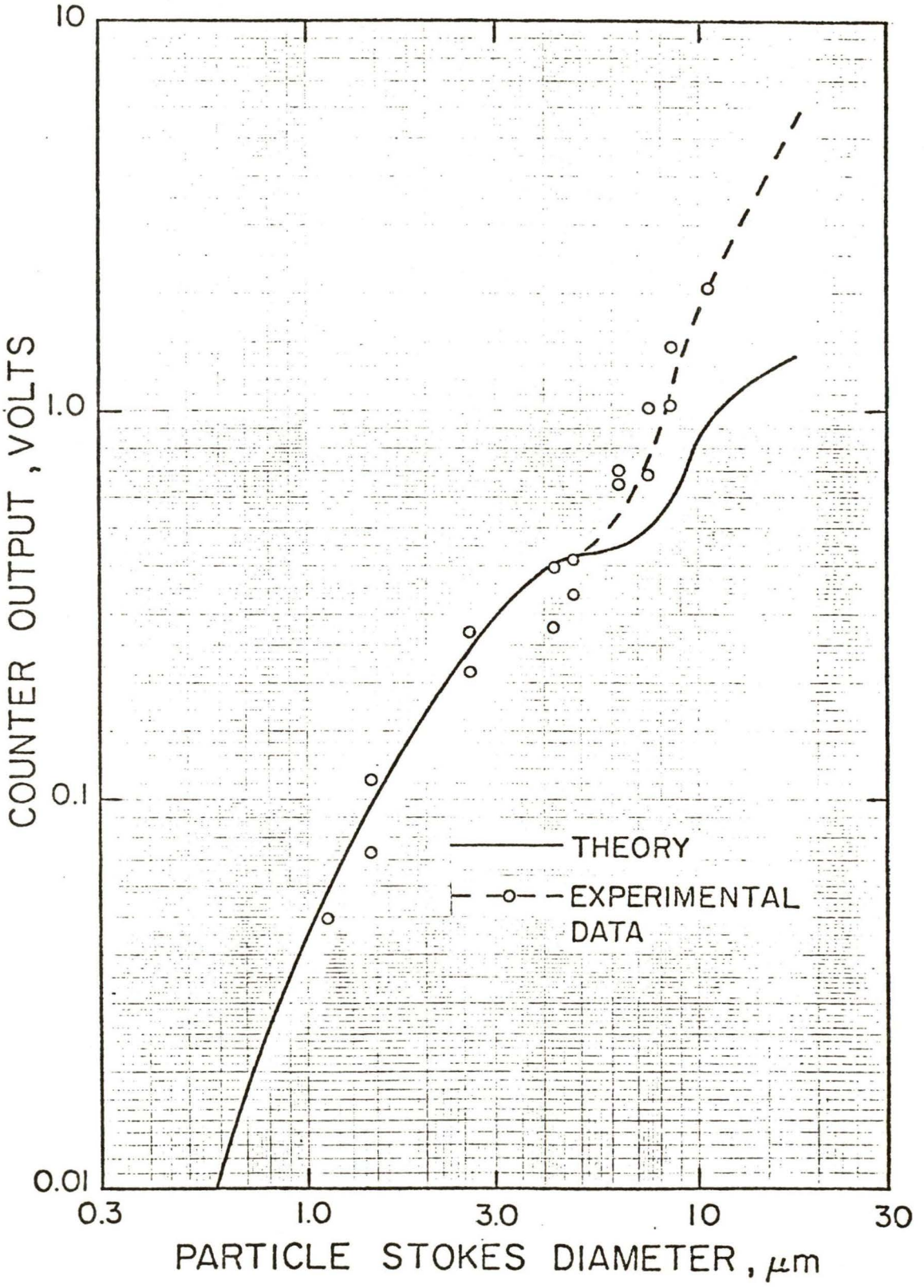

Figure 23 Laser Diode Optical Particle Counter Coal Calibration Curve

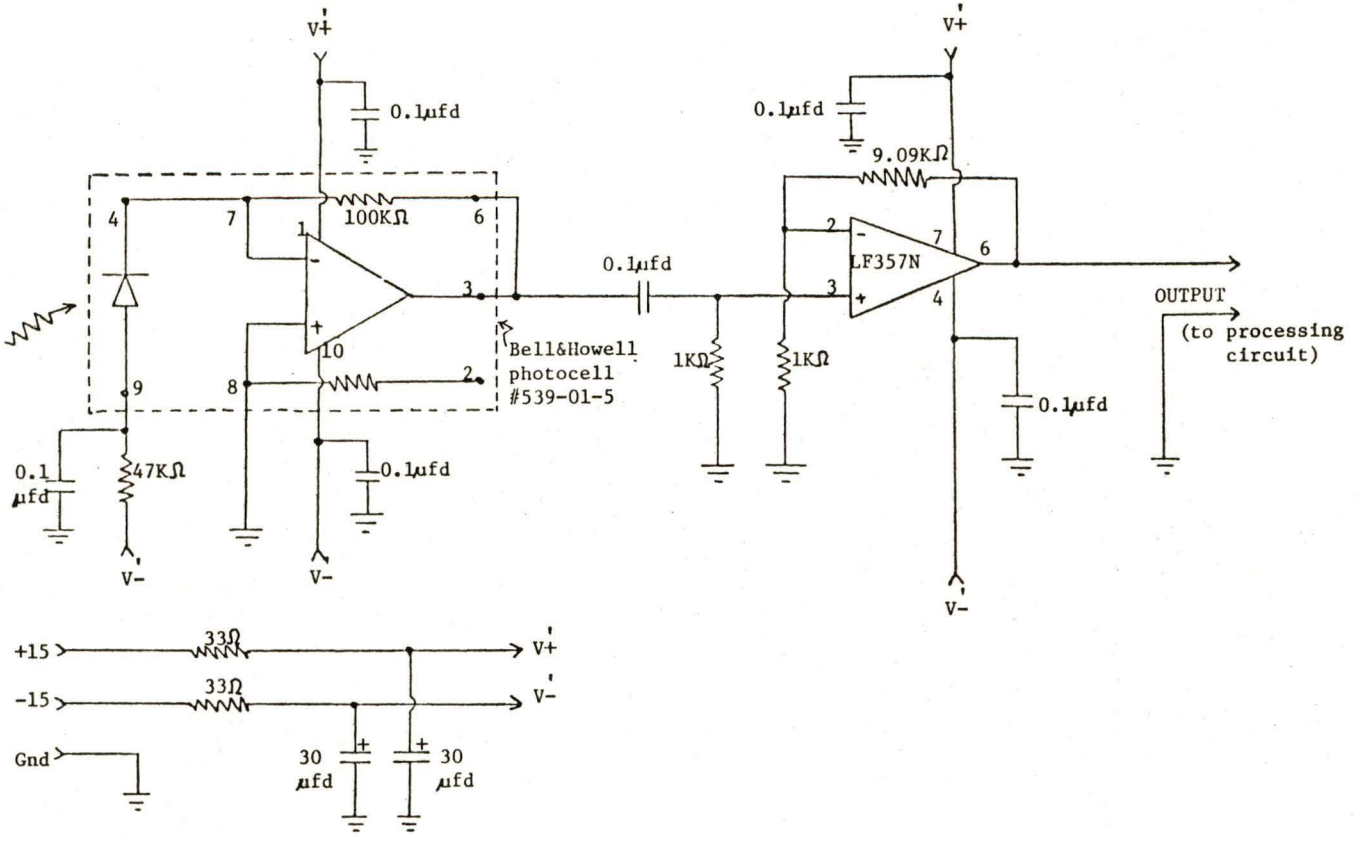

Figure 24. Circuit diagram for photo cell and preamp.

The photo cell response using the interval 100K feedback resistor is 60 mv/mw at the laser wavelength. The preamp is an LF 357 N connected as a noninverting amplifier with a gain of 10. This brings the system response to 0.6 V/mw. No filtering is used to maintain the maximum frequency response, since the light pulse duration is only about one microsecond.

3.4 Mechanical Design of Scattered Light Receivers

The side and end view of the spherical mirror mounting block is shown in Figure 19. The mirror is held in place with an O ring under the mounting flange to allow thermal expansion of the parts without stressing the glass. Lateral movement of the mirror is prevented by the machined recess. The spacer block thickness is such that the radius of the spherical surface falls at the plane of the photo cell surface and the particle beam path, and is not adjustable. Exact focusing is not needed, due to the photo cell surface area and mirror depth of field at the focal plane.

Lateral adjustment is made with the oversized mounting holes through the inlet block. Once this block is aligned, it will not be removed. The beam location is the only adjustment needed to get the particle image to fall on the photo cell. An O ring is used as a seal between the inlet and spacer blocks.

4 Signal Processing

After several attempts to increase the speed of the U of M 170 pulse shaping circuit, it was decided that the digital reset technique of this circuit could not be used at the response times made possible by the slit light beam. As a result of these response times, which were approximately 1 μsec, the signal processing time would be the limiting factor in determining the maximum allowable particle count rate for this counter. If the electronics could be designed to handle the high count rate associated with monitoring coal dust aerosol with a mass concentration of 20 mg/m^3 (see Section 4.1), then aerosol dilution would be unnecessary, thus greatly simplifying the instrument.

4.1 Calculated Maximum Allowable Signal Processing Time

The maximum particle concentration that can be monitored by a single particle counter sampling at a given aerosol flow rate is limited by the residence time of either the particle in the counter's view volume and/or the particle's resulting voltage pulse in the system's electronic processing circuit. The simultaneous presence of either more than one particle in the view volume or more than one particle's voltage pulses in the processing electronics is referred to as coincidence and will result in an indicated particle concentration less than the true concentration. Coincidence loss is then the difference between the true and indicated particle concentration. Using statistical probability and assuming that the number of particles (or voltage signals) present in the view volume (or processing electronics) at a given time can be represented by a Poisson distribution, one can calculate the coincidence loss, c, as a function of particle concentration, N, aerosol flow rate, q, and particle residence time, t.[6] The coincidence loss is then given by

$$c = N\,(1 - e^{-Nqt})$$

Thus, for a given coincidence loss, the residence time is inversely proportional to particle concentration and aerosol sample flow rate.

One of the design constraints for this particle counter system was that it be capable of monitoring particle size distributions of coal dust aerosols with mass concentrations up to 20 mg/m^3. The following numerical calculation was performed in order to determine the feasibility of designing a single particle counting instrument that would be capable of monitoring coal dust aerosols at this maximum concentration limit. The assumptions about the coal aerosol included:

1. Log-normal size distribution with a number median diameter of 1.0 μm and geometric standard deviation of 2.5. This corresponds to a mass median diameter of 10 μm.
2. Coal density of 1.45 gm/cm^3.
3. Coal particles are spherical.

The resulting particle number concentration is 600 particles/cm^3, with 500 particles/cm^3 greater than 0.3 μm. Based on this particle concentration for particles greater than 0.3 μm and an aerosol sample flow rate of 210 cm^3/min, the resulting maximum particle residence times in the system for percentage particle coincidence losses of 1% and 5% are 5.7 and 29 μsec, respectively.

In the current system, the particle residence time in the view volume is between 2.5 to 3.0 μsec, and the electronic pulse processing time is approximately 10 μsec. Since the view volume residence time is small compared to the signal processing time, the calculated maximum residence time for a given particle coincidence loss, in effect, determines the maximum allowable signal processing time. These actual residence times also mean that this prototype system would be able to accurately monitor coal dust particles with concentration up to the design criteria of 20 mg/m^3.

4.2 Pulse Shaping

The circuit that was developed produces an output pulse of fixed length and of an amplitude proportional to the total integral of the current pulse from the photo diode.

The output from the photo cell is a waveform that replicates the spatial distribution of light intensity in the laser beam. When the high frequencies that result from the multiple source interference are filtered out, the signal appears as a sine wave half-cycle.

This signal is introduced into an integrator via two paths (Figure 25). One path is direct, which causes the integrator to make a step increase in its output voltage level proportional to the integral of the applied pulse. The integrator now holds this value as the measured value of the scattered light from the particle.

The resetting of the integrator back to zero for the next particle is achieved with the second signal, which has passed through a 10 μsec delay line and inverted with an operational amplifier of gain 1X. The signal is DC-coupled to the input of the integrator. When this inverted and delayed version of the pulse arrives at the integrator, it produces an inverted step change that is

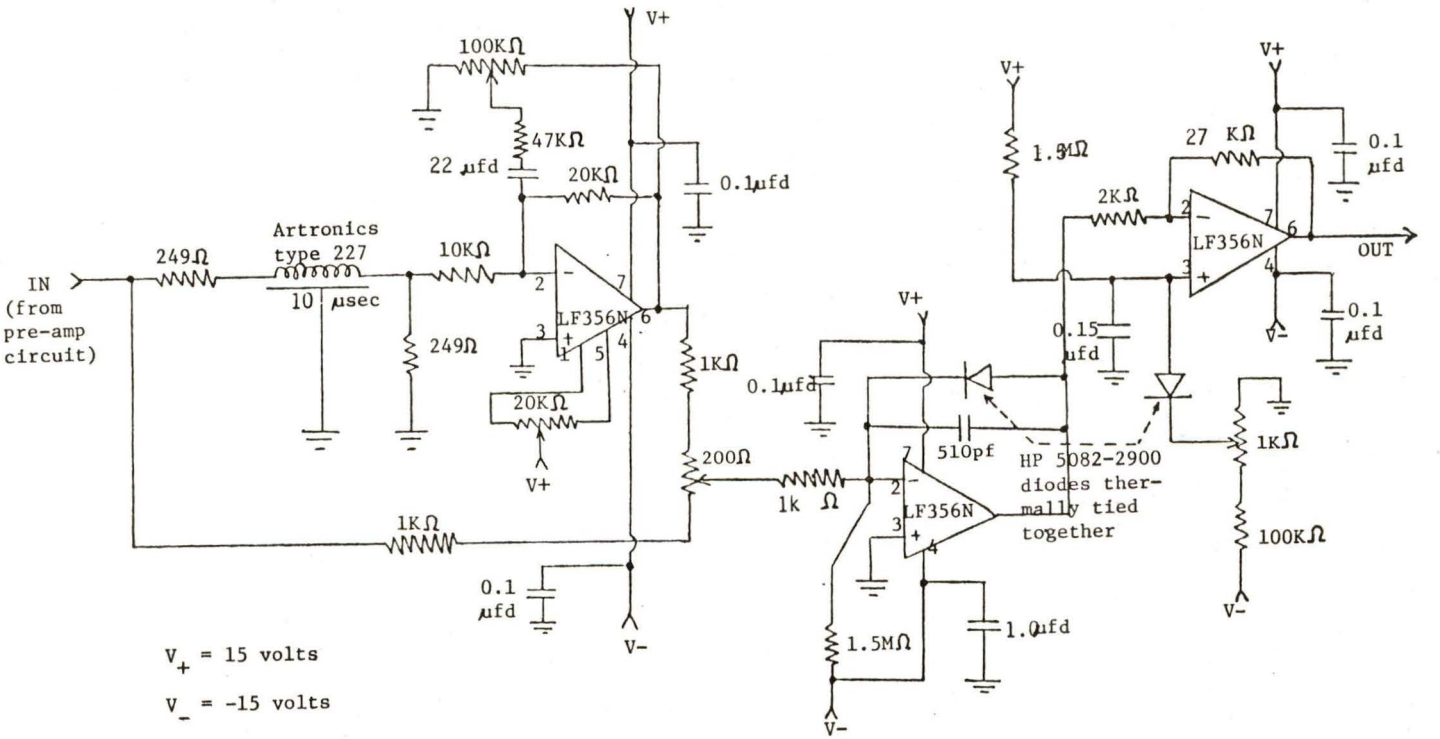

Figure 25. Output pulse shaping circuit diagram.

equal to the first step change. This brings the integrator output back to almost the original zero level. The pulse out of the integrator has a duration equal to the delay of the delay line plus the half-widths of the two integrate and reset pulses.

In order to maintain an exact output level, a diode is placed across the integrator feedback capacitator and a small bias current applied to the input to hold the integrator output clamped to the diode volt drop when a pulse is not present. The droop introduced by this bias current is removed by using several taps on the delay line and feeding in sustaining pulses while a signal is present. By adjustment of these resistors and by peaking the gain of the reset pulse amplifier, the integrator output can be made to return to ground level within one μsec for pulse amplitudes from a few mv up to 10 volts.

The offset and temperature sensitivity introduced by the diode clamp is removed by a second diode which offsets the input of the times 5 gain output amplifier.

The low frequency noise of the photo cell due to temperature or stray light is cancelled by the integrators even though the circuits are all DC coupled past the preamp. The low frequency gains of the integrators are zero since the signal path is both direct and inverted to its input. Only signals that have pulse widths less than the delay line time delay of 2.5 μsec are amplified.

Since no digital resets are used, the system is free of switching noise. A strobe generator was added to the input of the U of M multichannel analyzer (MCA) to allow its use to accumulate the output pulse in separate channels by pulse height. The high level and stretched pulses can be processed by this circuit.

4.3 Photometer/Particle Counter Output

The basic unit described in this report will be used for both the photometer and the particle counter. For the particle counter system, this unit can be used in conjunction with the portable, battery-powered multichannel analyzer (MCA) built in this laboratory and previously delivered to the Bureau of Mines. The system calibration data presented in Section 3.1 was obtained using the instrument together with an MCA similar to the portable MCA's.

A circuit was made to linearize the pulse so that simple integration would yield a voltage proportional to the particle volume (or mass). The pulse out of the 10 μsec pulse shaping circuit (Figure 25) was sent through a segmented linearizer consisting of four operation amplifiers sections set as half wave rectifiers with variable gain and threshold. The output of these four amplifiers plus a linear segment using a voltage divider allowed the linearization of the signal to the square root of volume (or mass). A commercial squaring circuit (RC4200) was used to provide a signal which was linear with volume (or mass). The output was then integrated with an operational amplifier circuitry which has a 10 sec. time constant. The output is displayed on the instrument panel meter.

More work is needed on this circuit to set up the proper gains for each stage. The wide dynamic range which is required made it difficult to cover both

the size and concentration range without serious noise and over range conditions.

References

1. Marple, V. A. and K. L. Rubow, "A Portable Optical Particle Counter System for Measuring Dust Aerosols," Am. Ind. Hyg. Assoc. J. 39:210-218 (1978).

2. Adrian, R. J. and W. L. Earley, "Evaluation of LDV Performance Using Mie Scattering Theory," pp. 426-454, Proc. of the Minnesota Symposium on Laser Anemometry, University of Minnesota, Department of Conferences, Minneapolis, Minnesota (1976).

3. Berglund, R. N. and B. Y. H. Liu, "Generation of Monodisperse Aerosol Standards," Environ. Sci. Technol. 7:147-153 (1973).

4. Marple, V. A. and K. L. Rubow, "Aerodynamic Particle Size Calibration of Optical Particle Counters," J. Aerosol Sci. 7:425-433 (1976).

5. Marple, V. A., B. Y. H. Liu and K. L. Rubow, "A Dust Generator for Laboratory Use," Am. Ind. Hyg. Assoc. J. 39:26-32 (1978).

6. Willeke, K. and B. Y. H. Liu, "Single Particle Optical Counter: Principle and Application," Fine Particles: Aerosol Generation, Measurement, Sampling and Analysis (B. Y. H. Liu, ed.), pp. 697-729, Academic Press, New York (1976).

APPENDIX C

EVALUATION OF THE SRI PORTABLE MINE DUST CONCENTRATION INSTRUMENT

By

Virgil A. Marple and M. Norman Chan
Particle Technology Laboratory
Mechanical Engineering Department
University of Minnesota
Minneapolis, Minnesota 55455

Introduction

The SRI portable mine dust concentration instrument determines dust concentration by monitoring the amount of low-angle forward light scattered from an aerosol cloud sampled by the instrument. As shown in Figure 1, the light from a lamp is focused onto a view volume through a system of lenses and a light baffle, and the light rays which are scattered by the dust cloud are focused by a detector lens onto a light detector. The output from the light detector is amplified and either read out on a panel meter located on the instrument, or monitored by a strip chart recorder. Full design details and some test data are presented in Reference 1.

The instrument has been designed so that the output of the light detector will be proportional to the mass concentration of the dust cloud passing through the instrument. However, because of the possibility that the amount of light scattered is not only a function of the aerosol mass concentration, but also may be a function of the type of aerosol and/or the aerosol size distribution, the instrument response must be calibrated experimentally.

Two of the units were supplied to our laboratory by the Bureau of Mines. This paper describes problems encountered in using the instruments, the types of tests performed, test results, conclusions which can be drawn from these test results, and finally, recommendations.

Initial Instrument Check-Out

In the initial check-out of the two instruments, problems were found with the stability of the instruments' baseline and with leakage of air into the viewing chamber of the instrument.

The baseline stability was checked by monitoring the instruments' output with a strip chart recorder while clean filtered air was passing through the instrument. In one of the units, the baseline drift was found to be approximately 0.2 mv over a period of 12 minutes, which is satisfactory. However, the second unit was found to have a widely varying baseline, making it impossible to evaluate. Therefore, it was returned to the Bureau of Mines without further evaluation and the availability of the units was reduced from two to one for the rest of the test program.

In addition, there was found to be aerosol leakage into the viewing chamber when the remaining instrument was operated on the clear mode of sampling, which should allow only clean filtered air to enter the viewing chamber. Also, it was found that when a finger was placed on the inlet of the unit to stop all flow at that point, the flow through the instrument dropped very little, indicating that the leak passage was large.

To correct the leakage, RTV adhesive was applied to all external seams of the instrument which could allow a leak into the viewing chamber. Although this did not eliminate the leakage entirely, it did reduce it to a level where the instrument could be evaluated.

Although the application of this adhesive would seemingly solve the leakage problem, leakage continued to be a problem throughout the test program due to

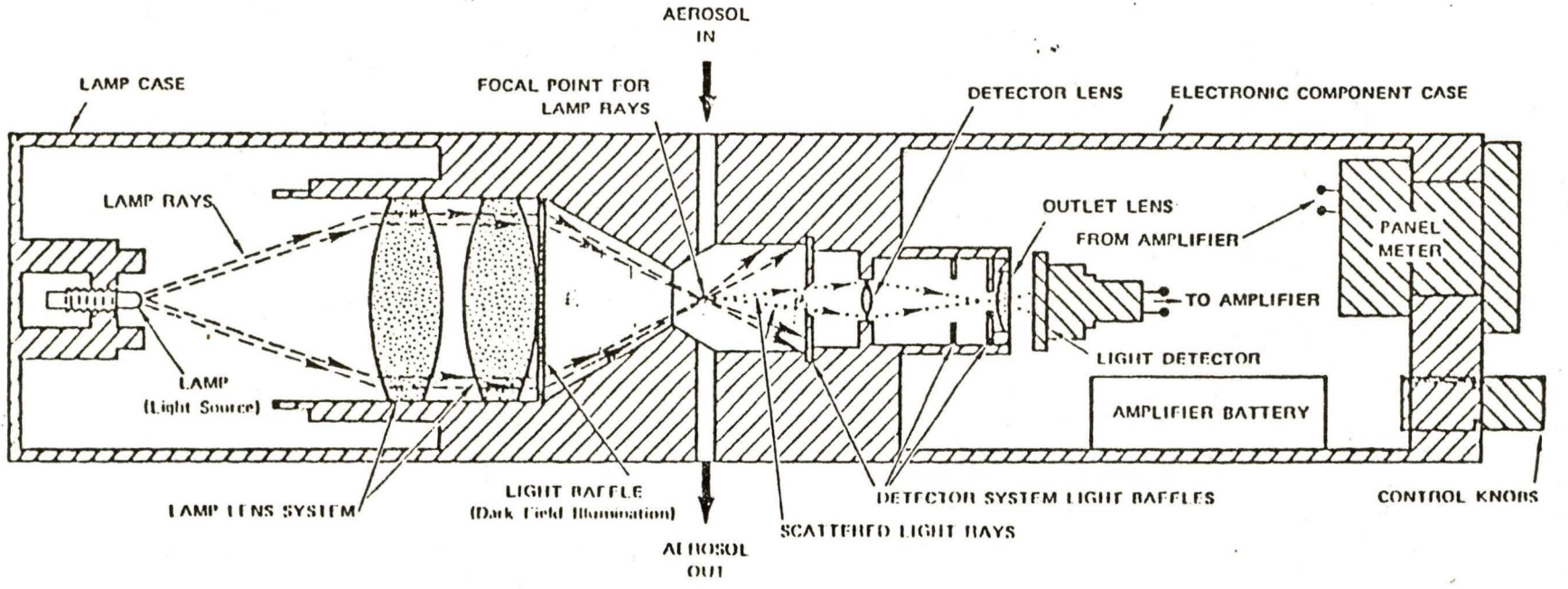

FIGURE 1. Schematic of SRI portable coal dust concentration instrument (from Reference 1).

the fact that the exterior surfaces of the instrument's case are very smooth and the adhesive did not adhere well to it. Therefore, leaks between the adhesive and the case would unknowingly appear during the course of a test, making testing difficult.

Due to the presence of the leaks in this instrument, it was very difficult to obtain an absolute calibration in millivolts output per mg/m^3 of dust concentration, since leakage of air into the viewing chamber diluted the dust concentration as will be shown in the following results. Thus, before an absolute calibration can be obtained, the instrument shoud be repackaged into a leak-tight case. However, even with some leakage into the optical chamber, the general influence of the types of dust and the dust size distributions on the instrument's operation can be obtained.

Test Methods

The evaluations were performed on the SRI instrument by comparing the output of the SRI to a mass concentration determined gravimetrically. The dusts, which consisted of coal or silicon particles, were generated in a fluidized bed dust generator.[2] The size distributions of the dusts generated are shown in Figure 2 and were determined by gravimetric analysis of the deposits from a cascade impactor. It should be noted in this figure that the total mass consists of all the particles being generated by the dust generator and the respirable mass includes the particles which have passed through a 9 lpm respirable cyclone. In the latter case, the large particles which can be considered nonrespirable are removed. It should also be noted in Figure 2 that the two total mass size distributions for coal, one being determined in the summer of 1977 and the other in the spring of 1978 are nearly identical. This indicates that the dust generator was providing a consistent size distribution over the time span of our testing.

Before each test, the SRI was allowed to warm up for at least one hour to establish temperature equilibrium and reach stable operation. Also, the flow rate was checked before each run to insure that the flow rate was 2 lpm through the instrument and the output of the SRI was zeroed on the strip chart at the desired range with the zero control of the instrument. Next, the range selector switch was set to four and the reference button fully depressed while the calibration control was adjusted to read full-scale on the SRI meter. The optical chamber was cleaned before each run by pumping clean air through an absolute filter on the inlet of the SRI instrument.

In our evaluation of this instrument, three basic types of test set-ups were used. In the first set-up, the output of the SRI instrument was compared directly to the mass concentration as determined by the aerosol divider[3] placed on the inlet of the instrument. For these tests, the particles passing through the central tube of the aerosol divider were passed through the SRI in a manner similar to that used for the evaluation of the GCA RDM 101-1.[4] In these tests, the dust generator was operated with 9 lpm of fluidizing air and 37 lpm of dilution air. At the aerosol divider, 2 lpm was passed through the central tube of the divider and then through the SRI instrument and 34 lpm was passed through the annular filter (0.8 μm pore size).

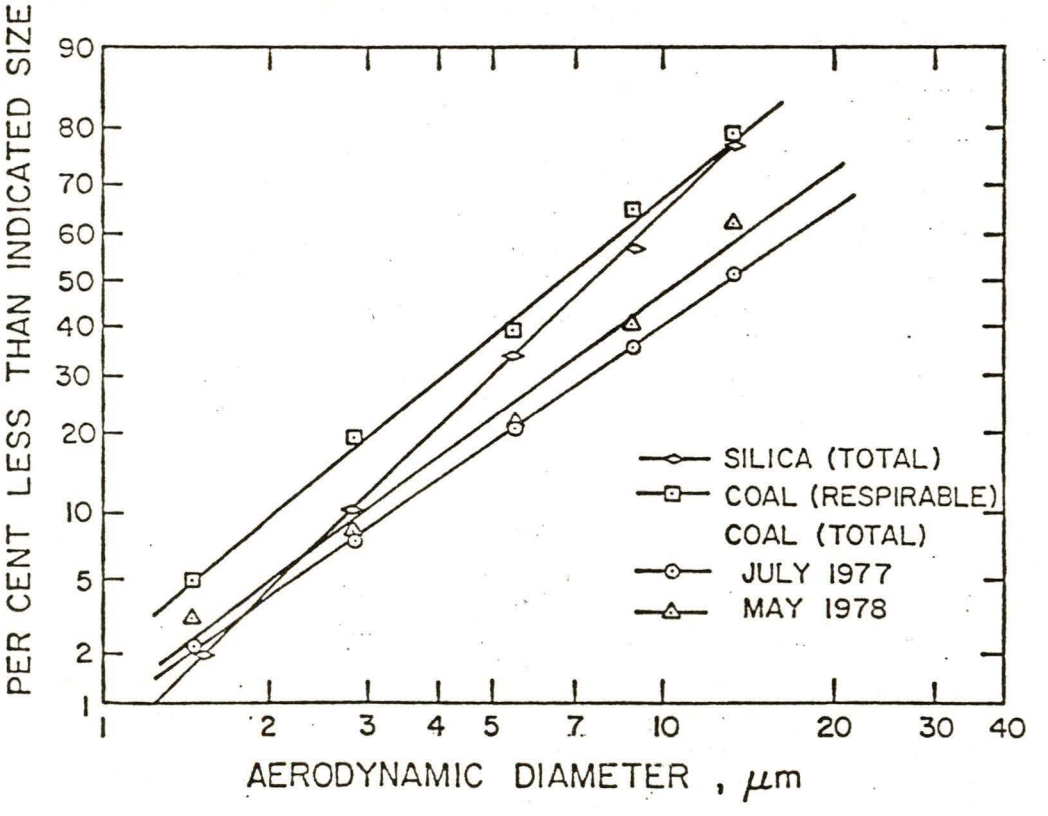

FIGURE 2. Particle size distribution of test dust aerosols.

In another set of tests, an impactor was placed between the aerosol divider and the SRI instrument, as shown in Figure 3. With the impactor in the line at this point, it was possible to remove large particles from the dust aerosol and to allow the SRI instrument to respond to the smaller particles. Due to the fact that the impactor was removing some particles, it was not possible now to use the aerosol divider as a gravimetric standard. Thus, a filter as shown in Figure 3 was used alternately with the SRI instrument in the sampling of the aerosol passing through the impactor. This filter then became the standard to which the SRI instrument was compared.

The impactor used for these studies is of the type used for the calibtration of optical particle counters,[5] which has interchangeable nozzles. Table 1 lists the nozzle sizes, the particle aerodynamic diameters at the 50% cut-point, and the corresponding Stokes diameters of the coal and silica particles. Incidentally, these same calibration impactors were used in a cascade arrangement to determine the mass size distributions of the dust aerosols shown in Figure 2.

Table 1
Impactor Cut-off Sizes (2 lpm)

Nozzle dia. (cm)	Aerodynamic dia. (μm)	Stokes dia. (μm)	
		(coal ρ = 1.45 gm/cm^3)	(silica ρ = 2.6 gm/cm^3)
0.137	1.45	1.20	0.90
0.213	2.84	2.36	1.76
0.328	5.50	4.57	3.41
0.450	8.94	7.42	5.54
0.590	13.4	11.1	8.31
0.688	21.4	17.8	13.2

In the third test set-up, shown in Figure 4, the SRI instrument was used in conjunction with a dichotomous impactor, which divides the aerosol stream into large and small particle fractions. Since only one SRI instrument was available, we alternately evaluated it with the large and small particle streams of the dichotomous impactor. In each case, the SRI instrument and a filter were alternated every five minutes as described with the previous test procedure. The filter then became the standard to which the SRI instrument was compared.

By using a cascade impactor to evaluate the large and small particle streams, it was found that the dichotomous impactor was removing the large particles from the small particle stream and allowing very few small particles to go through with the large particles. The cut-off size of the dichotomous impactor was approximately 3.5 μm. It was found that no particles larger than 5.5 μm were in the small particle stream, and only 24% of the particles in this stream were larger than 2.8 μm. When compared to the size distribution in Figure 2 of the total dust aerosol, it can be seen that the large particles were indeed removed. For the large particle stream, it was found that 70% of the particles were larger than 4 μm. This indicates that there was a high concentration of large particles in this air stream.

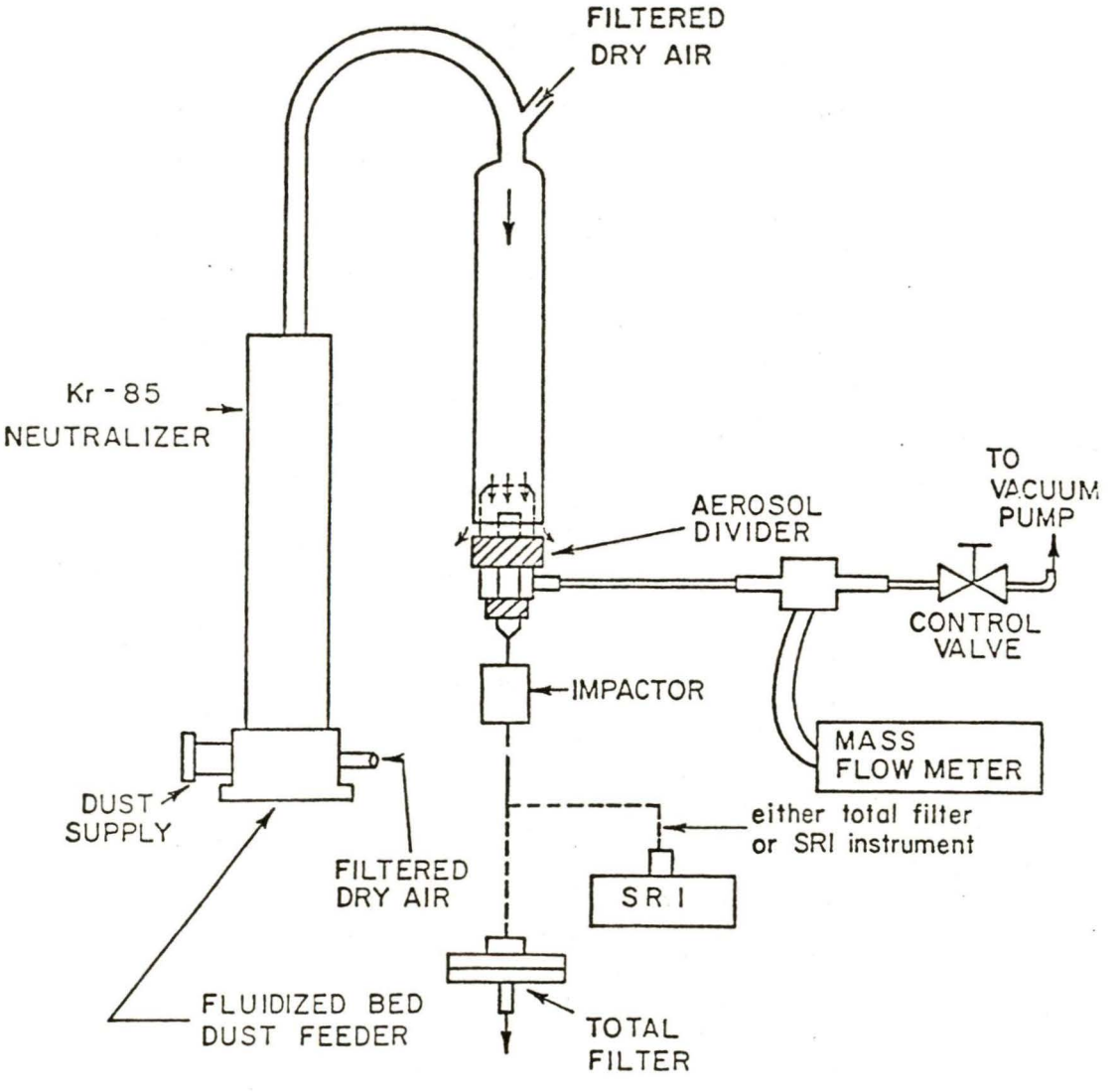

FIGURE 3. Test set-up for calibrating the SRI instrument with an impactor removing large particles.

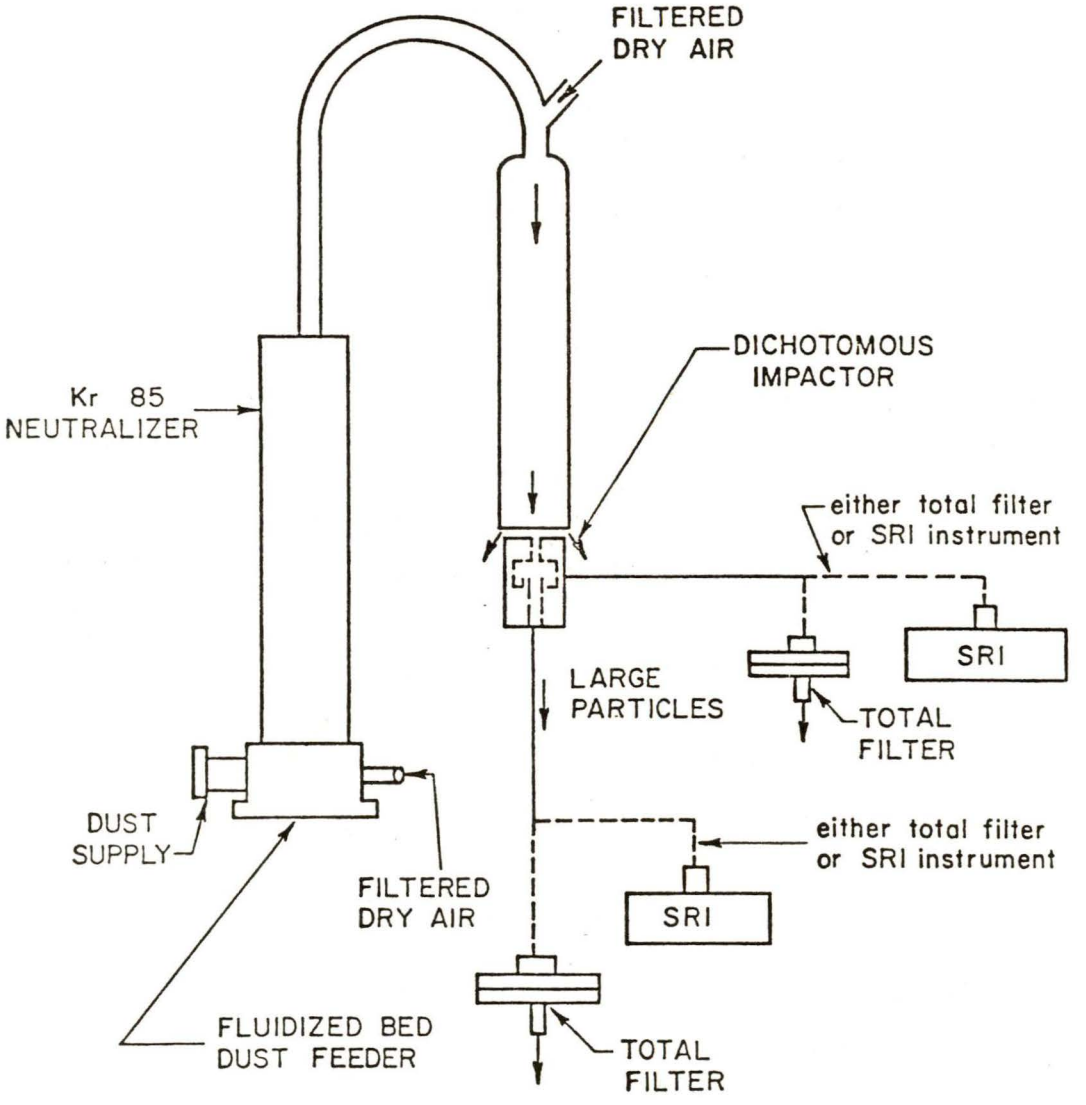

FIGURE 4. Test set-up for demonstrating use of SRI instrument with a dichotomous impactor.

Results

The previously described test set-ups were used in several different studies. The results of these studies are described in the following sections.

Response to Total and Respirable Dust

In this study, the output from the SRI instrument was compared directly to the gravimetric standard as determined from the aerosol divider filter. Tests were run at several different coal dust concentrations with and without the respirable cyclone in the dust generator and the particle size distributions are those shown in Figure 2. It should be noted that this set of tests were the first that were run after the unit had been sealed with RTV. Thus, the leakage was probably less in this set of runs than in any of the subsequent test series.

The response curve for these two size distributions are shown in Figure 5. It should be noted that the response curves do pass through the origin, indicating that the SRI instrument has zero output for zero concentration, and also that the data scatter for the respirable aerosol appears to be less than for the total aerosol. The reason for this behavior is believed to be that there is a better defined size distribution when the respirable cyclone is removing the large particles than when there is no classification device in the dust generator. When no classification device is used, there can be some fluctuation of large particles, giving the type of scatter seen in Figure 5.

The conclusion which can be drawn from this set of tests is that the response of the SRI instrument is proportional to the mass concentration, but is also a function of the size distribution of the aerosol. Thus, to further define the dependency upon the size distribution, the following set of tests were run.

Removal of Large Particles by an Impactor

In these tests, an impactor was placed between the aerosol divider and the SRI instrument to remove large particles. The aerosol passing through the impactor was sampled alternately by the impactor and by a filter which is used as a gravimetric standard. For these particular tests, silica dust as well as coal dust was used as the aerosol. The results are shown in Figures 6 and 7 for coal and silica dust, respectively. Again, the results are in terms of the SRI instrument output vs. the gravimetrically determined concentration from the filter. It should be noted that the SRI instrument range was 0 for the coal dust and 1 for the silica dust.

In both Figures 6 and 7, it can be seen that the response of the SRI instrument is different for dust with different size distributions. In both cases it shows that the sensitivity of the instrument increases as large particles are removed from the air stream. This again implies that the SRI instrument is more sensitive to small particles than large particles.

By studying the sensitivity of the SRI instrument to the aerosols of different size distributions, it is possible to obtain some information on the contributions of particles in different size ranges to the output of the instrument (Table 2). For example, in Table 2, the sensitivity for coal particles less than 4.57 μm is 10.5 mv/mg/m^3 calculated from the data in Figure 6.

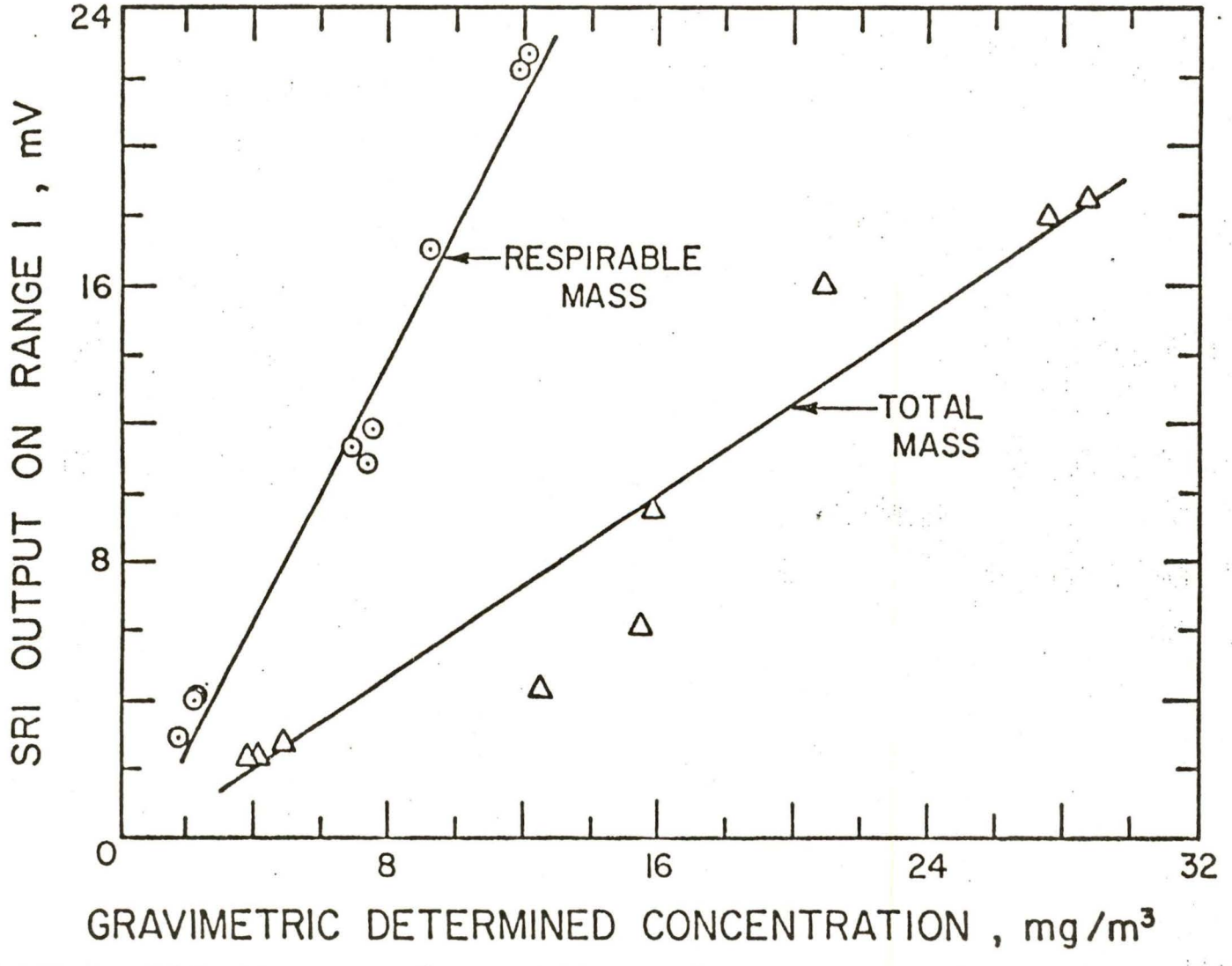

FIGURE 5. Calibration curve of SRI portable mine dust concentration instrument on coal dust

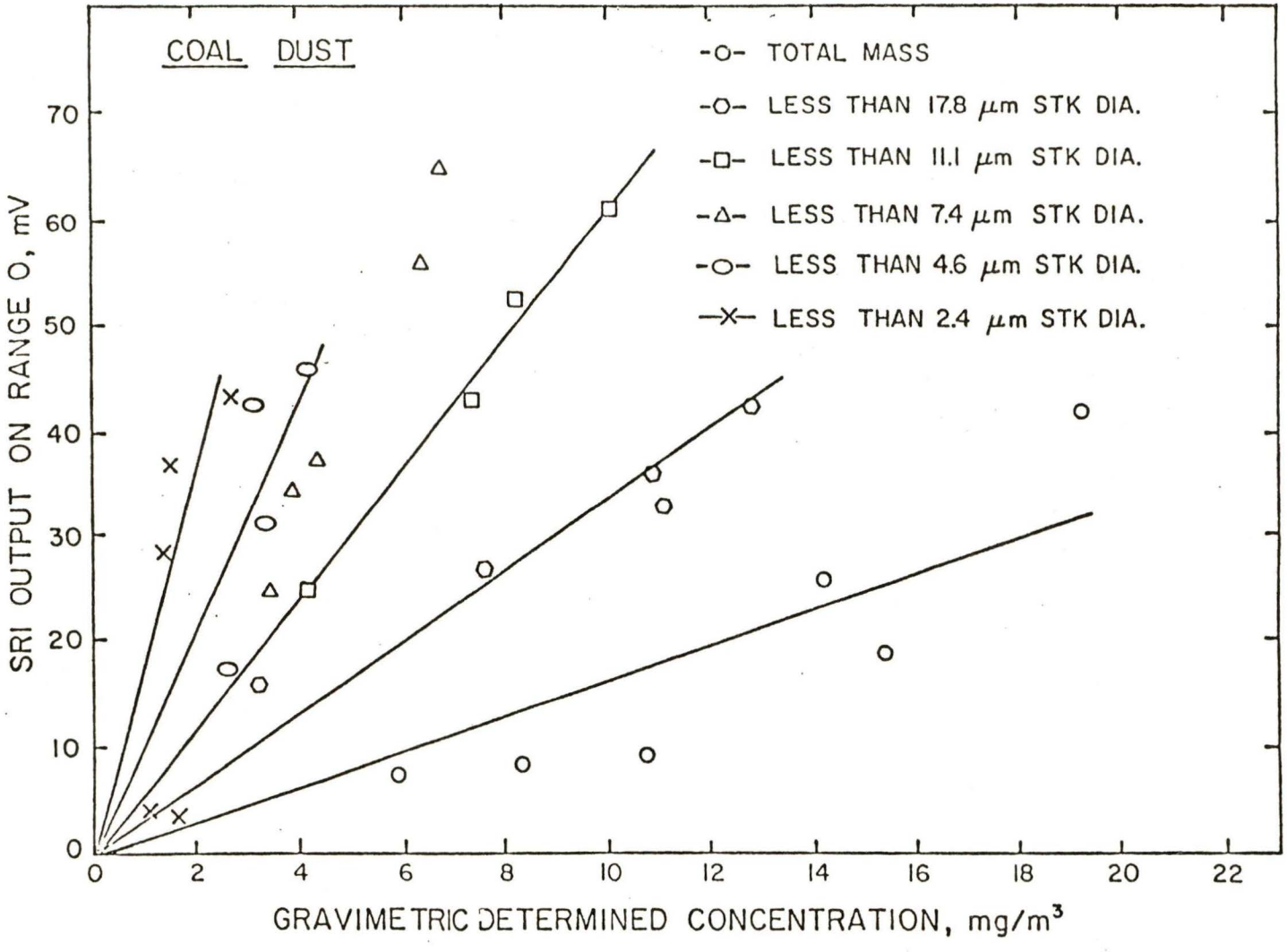

FIGURE 6. SRI portable coal dust concentration instrument response on coal dust, with large particles removed by an impactor.

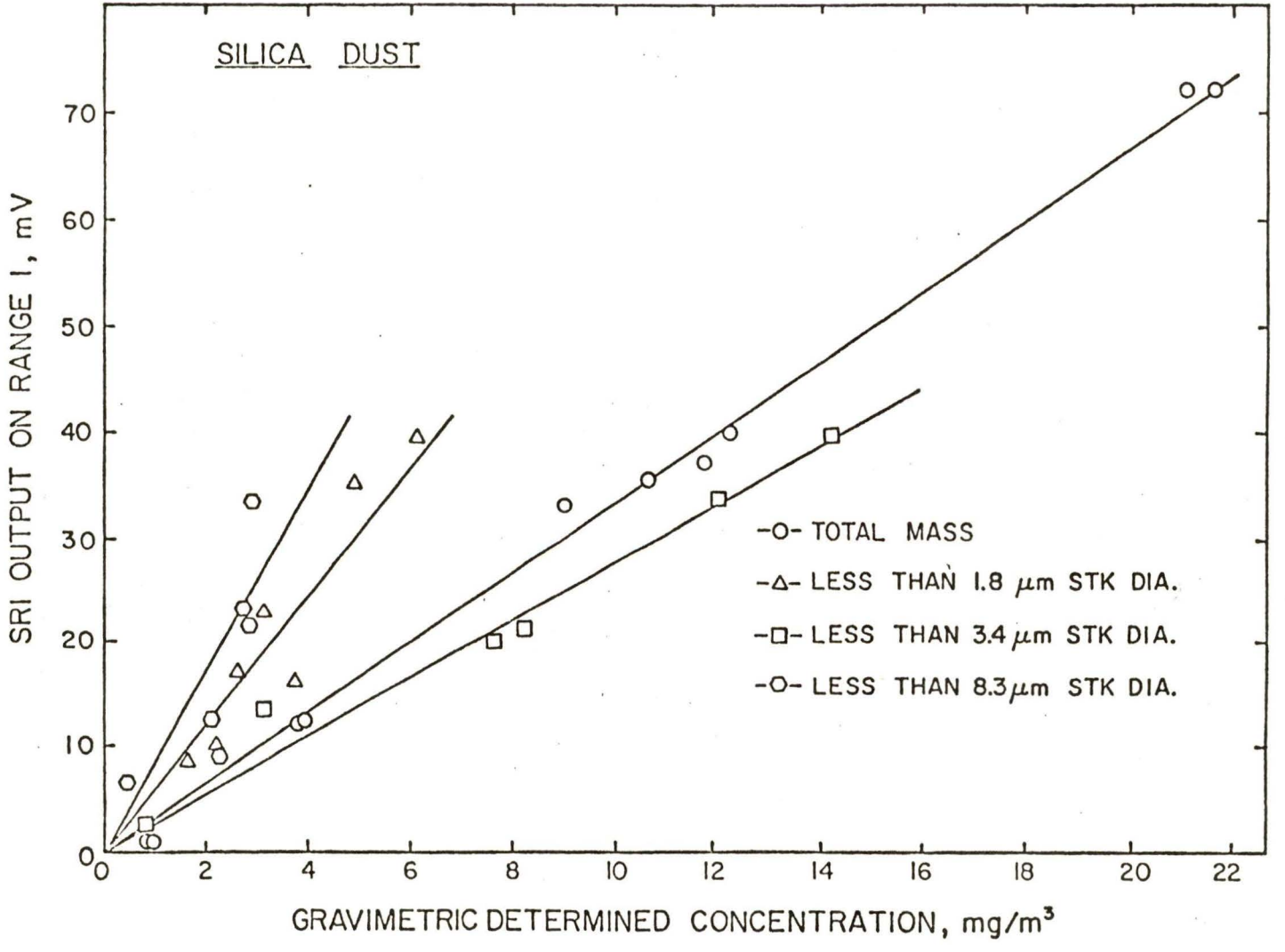

FIGURE 7. SRI port-ble coal dust concentration instrument response on silica dust, with large particles being removed by an impactor.

Table 2
Sensitivity of SRI Portable Coal Dust Concentration
Instrument in Different Size Ranges

Coal			Silica		
Size range Dst (μm)	% $<D_p$	Sensitivity mv/mg/m^3	Size range Dist (μm)	% $<D_p$	Sensitivity mv/mg/m^3
<2.36	8	16.7	<1.76	10	8.7
<4.57	20	10.5	<3.41	34	6.1
<7.42	35	9.5	<8.31	78	2.7
<11.1	51	6.1	Total	100	3.3
<17.8	68	3.4			
Total	100	1.7			
2.36-4.57		+6.4	1.76-3.41		+8.8
4.57-7.42		+8.2	3.41-8.31		+ .15
7.42-11.1		-1.3	8.31-Total		+5.3
11.1-17.8		-4.7			
17.8-Total		-1.9			

However, for particles less than 7.42 μm, the sensitivity is 9.5 mv/mg/m^3. Since the latter sensitivity must be from a combination of particles less than 4.57 μm and particles in the size range between 4.57 and 7.42 μm, the contributions to this sensitivity will be as follows:

$$s_{total} = m_1 s_1 + m_2 s_2 \qquad (1)$$

where m_1 and m_2 are the mass fractions contained in the two size ranges and s_1 and s_2 are the respective sensitivities in these size ranges. s_{total} is the combined sensitivity. The mass fractions of the particles in these two size ranges can be determined by referring to the size distributions as determined with the cascade impactor (Figure 2). Thus, equation 1 will become,

$$9.5 = \frac{20}{35}\,10.5 + \frac{15}{35}\,S_2 \qquad (2)$$

The solution of equation 2 is s_2 = 8.17 mv/mg/m^3, which will be the sensitivity of the particles in the size range from 4.57 to 7.42 μm. As can be seen from Table 2, the sensitivities for the particles in the larger ranges are negative. It is felt that the sensitivities in these larger ranges are actually near zero and the negative numbers are caused by the approximations of the slopes that were made in Figure 6.

The response of the SRI instrument on silica dust also shows a dependence on particle size. Again, sensitivities are given in Table 2. It is of interest to note here that the sensitivity for particles in the size range of 8.31 μm to "total" is greater than in the size range of 3.41 to 8.31 μm. This may be due to the shape of flux versus particle size curves for the particular index of refraction exhibited by silica.

From these sets of tests the conclusions that the output of the SRI instrument is sensitive to the size distribution of the aerosol can be drawn, as it was with the previous set of tests. Also, it appears as though the instrument has a higher sensitivity when sampling coal dust than when sampling silica dust. We feel, however, that this conclusion may be influenced somewhat by the leakage of air in the instrument since all of the coal dust tests were run at one time and all of the silica dust tests at a later time with several days separating the two tests. Thus, we would expect the coal runs to be comparable amongst themselves, and also the silica runs to be comparable amongst themselves; but it may be difficult to compare the coal and silica results with each other.

The fact that some leakage was present for the coal runs can be seen by comparing Figures 5 and 6. Although Figure 5 was run under conditions where the range setting of the SRI instrument was 1 and the range setting in Figure 6 was 0, these two ranges should be related by a factor of 10. That is, for a constant concentration, range 0 should give ten times the value of reading on range 1. Although, as described in the next section this factor may be different from 10, a comparison of the sensitivities in these two curves shows that the ratio is approximately 2.5, with the tests run at a later date giving the lower concentration. Since that data from the later tests gives the lower concentration, it is likely that at some time between the two sets of tests, a leak occured and room air leaked into the photometer, diluting the dust.

It should also be noted in Figure 6 that the scatter of the data for the total aerosol is larger than the scatter of the data when an impactor was used to remove the large particles, indicating again that the scatter is due to the fluctuation of the very large particles in the aerosols.

SRI Instrument Range Check

As discussed in the previous section, there appeared to either be an increased leakage in the instrument in the second set of runs, or switching from one range to a higher range does not decrease the output voltage by a factor of 10. To check this, several different concentrations were sampled by the SRI instrument and the range switch moved from 0 to 1 to 2 to 3 to 4.

The results of this test are shown in Table 3. The concentration levels in these runs are not known, but it is known that the concentration level is constant for all the ranges, since they were all checked at essentially the same time. From the data in Table 3, it can be seen that the factor between ranges 0 and 1 is approximately 5.5, the factor between ranges 1 and 2 is approximately 2.0, and the factor between ranges 2 and 3 is approximately 10. No concentrations were high enough to determine the factor between 3 and 4.

Table 3
Comparison Betwen SRI Instrument Ranges

RUN**	RANGE				
	0	1	2	3	4
1	*	72.5	36.5	3.0	0
2	*	51.0	25.5	1.5	0
3	*	46.5	24.0	1.5	0
4	*	28.5	15.5	0.5	0
5	*	21.5	12.5	0	0
6	68.5	11.0	6.5	0	0
7	44.0	8.5	5.0	0	0

* over scale
** For each run the dust concentration was constant for all ranges

The conclusion that can be drawn from these runs is that changing ranges does not change the output voltage factor of 10. The electrical schematic furnished in Reference 1 indicates that these ranges are changed by simply switching in a different resistance into the electrical circuit. These resistances are increased by a factor of 10 for each range, and thus, the signal is decreased by a factor of 10. Although the instrument was not disassembled and these resistances checked, it appears as though the resistances were not correct.

Influence of Flow Rate on Leakage

In the next set of tests, the SRI instrument was to be used in conjunction with a dichotomous impactor. However, with the dichotomous impactor, the flow rates for the large and small particle streams are 0.28 lpm and 13.7 lpm, respectively. Thus, since the SRI instrument would be used at two different flow rates, it was decided to determine the influence of this flow rate on the output of the instrument.

To perform this test, the concentration was set at approximately 3 mg/l and the flow rate increased from 2 to 14 lpm. Since this increase in flow rate will increase the pressure drop between the optical chamber and the outside of the instrument, the leakage flow rate should be proportional to the flow rate of the instrument. As shown in Figure 8, the SRI output on range 0 varies from approximately 30 mv at 2 lpm to approximately 6 mv at 14 lpm. It is felt that this is a good check on the influence of air leakage into the instrument, since the output of the instrument should not be influenced by the flow rate if the concentration remains constant. This simply indicates that leakage of room air into the optical chamber diluted the dust passing through the inlet.

It is also interesting to note in Figure 8 that if the calibration line is extrapolated to 0 flow rate, corresponding to no leakage, the error between this value and the value obtained at 2 lpm (the normal operating condition of the SRI) is approximately 10%.

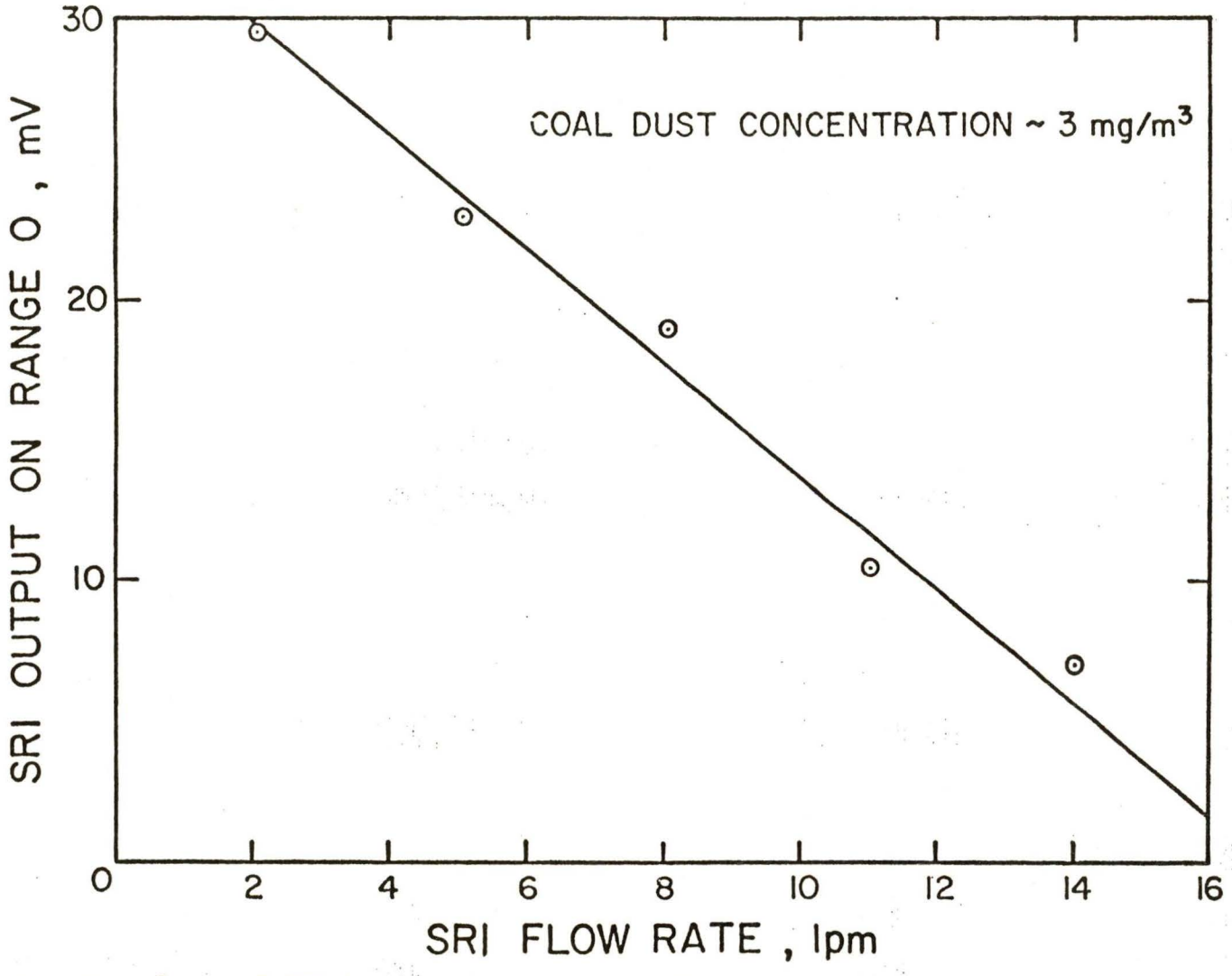

FIGURE 8. Dependency of SRI instrument response to flow rate due to leakage in the instrument

The conclusion which can be drawn from this test is that the leakage which will be experienced at 13.7 lpm will be sufficient to reduce the concentration from the true value by a factor of approximately 4.

The Use of the SRI Instrument with the Dichotomous Impactor

In this set of tests, the dichotomous impactor sampled coal dust and the SRI instrument was used to monitor the dust concentration in the large particle stream (particles greater than 3.5 μm) or the particles in the small particle stream (particles less than 3.5 μm). The flow rate of these two streams was 0.28 lpm and 13.7 lpm, respectively.

The instrument response to the large and small particles are shown in Figures 9 and 10, respectively. It can be seen from these two figures that the data points have very little scatter about a straight line passing through the origin. It is important to note in Figure 9 that the data points shown are the actual data taken in the experiment. If the leakage associated with the high flow rate in collecting these small particles is taken into consideration, and the calibration curve is adjusted by a factor of 4, as described in the previous section, then the calibration line for the particles that are less than 3.5 μm would be shown as the dotted line in this figure. It is interesting to note in Figure 10 that the concentrations of large particles experienced with the dichotomous impactor are very large. This is due to the dichotomous impactor concentrating large particles into a small percentage of the flow. Thus, the dichotomous impactor actually acts as a concentrator of large particles.

Theoretical Considerations

The reason that the instrument sensitivity decreases with increasing particle size can be seen more clearly if the response characteristics of light-scattering photometers are studied. Hodkinson and Greenfield[6] and Cooke and Kerker[7] have studied the response curves for various optical aerosol counters and photometers for particles with different indices of refraction. Although these two papers disagree somewhat on the exact values of the response from the instruments, they both show that photometers are expected to be more sensitive to particles of smaller sizes. Of particular interest is one set of curves by Hodkinson and Greenfield for an instrument which is similar to the SRI photometer. The response curves are shown in Figure 11 with the index of refraction of the aerosol particle being a parameter. The dashed-curve labeled 2-i is the index refraction corresponding to light absorbing particles and is of particular interest in our studies with coal. In the figure, α is a particle size parameter,

$$\alpha = \pi S D_p / \lambda \qquad (3)$$

where λ is the wave length of the incident light and D_p is the particle diameter. The scale of D shown in this figure is for a wave length of white light (λ = 0.5 μm) which we would have in the SRI instrument. The flux in this figure is the light scattered per unit surface area of the particle. Thus, flux is proportional to the instrument response divided by D_p^2. If we want the instrument response to be proportional to the mass of the particles, then the instrument response must be proportional to D_p^3, and thus, the flux should be proportional to D_p. In other words, in order for the response of this instru-

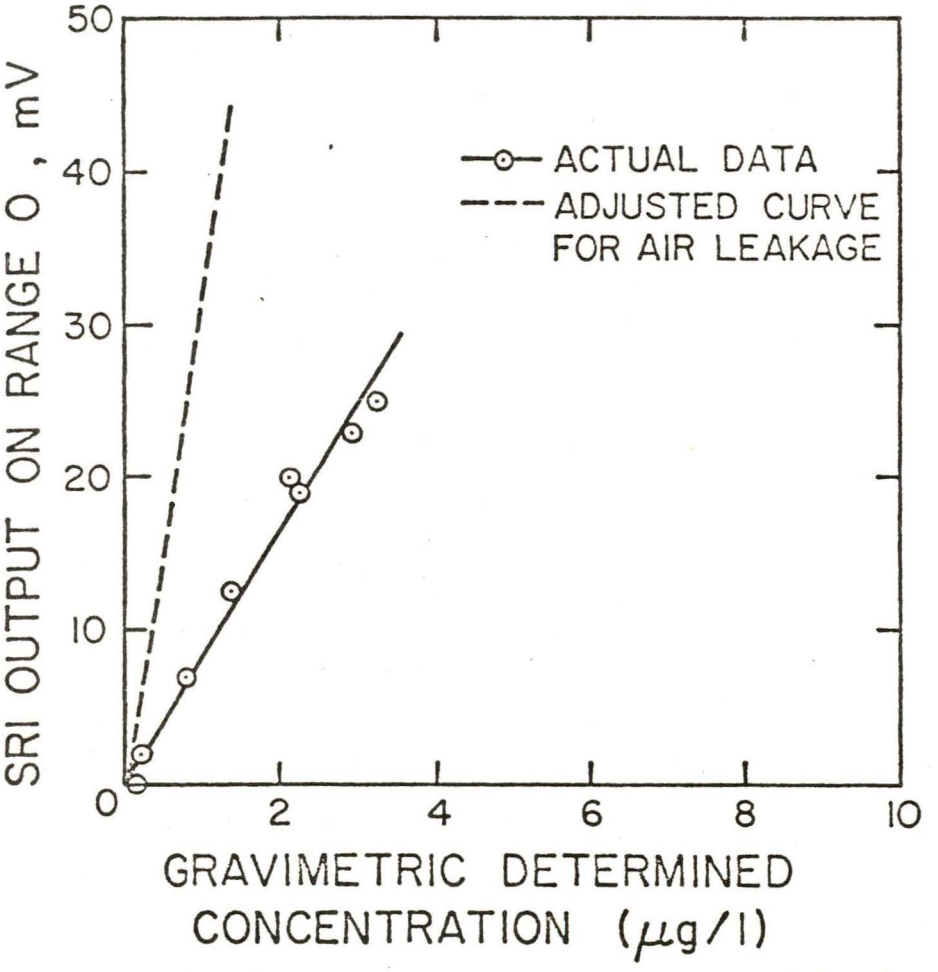

FIGURE 9. SRI instrument response to small particle air stream (<3.5 μm diameter) of dichotomous impactor (13.7 lpm flow rate)

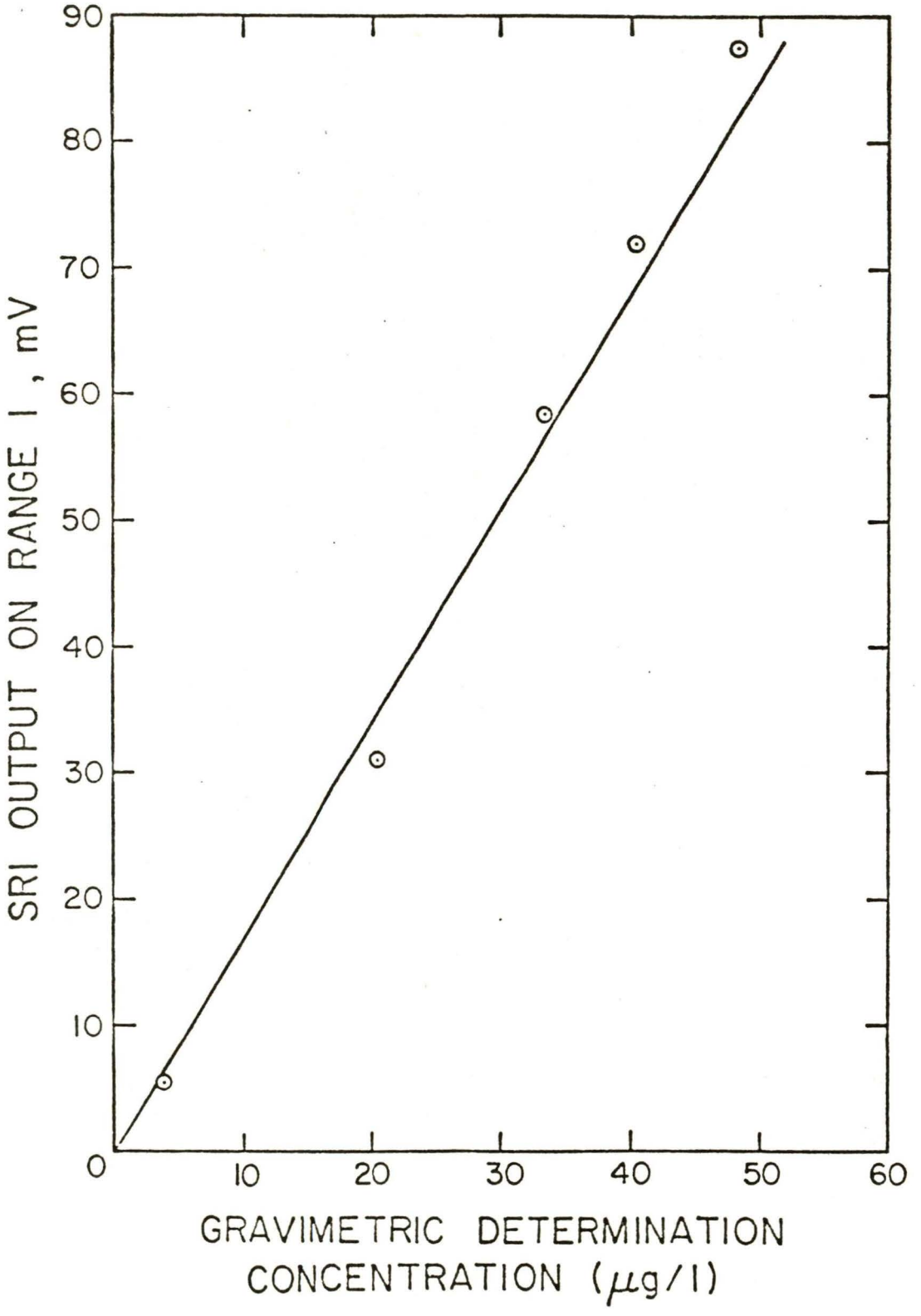

FIGURE 10. SRI instrument response to large particle air stream (>3.5 μm diameter) of dichotomous impactor (0.28 lpm flow rate)

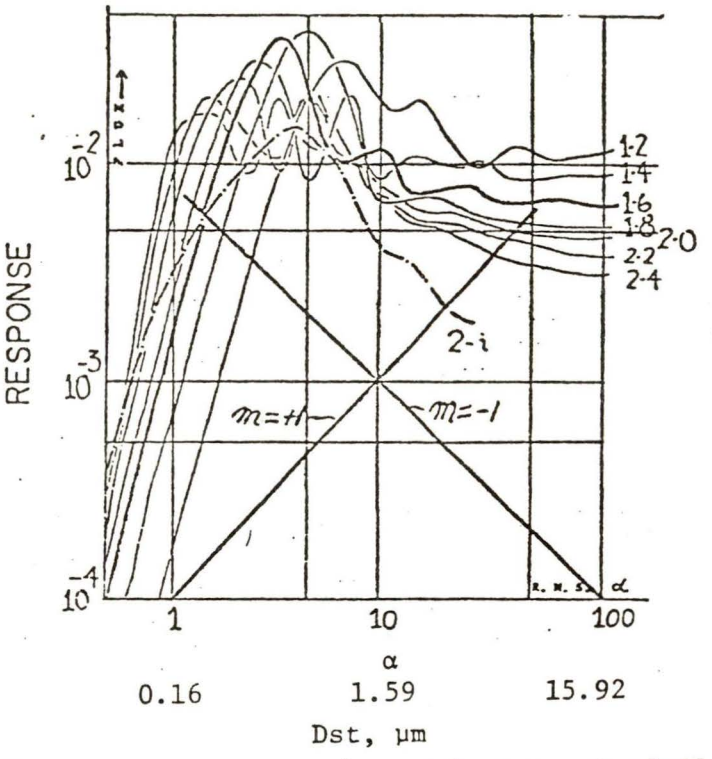

Figure 11. Response for an instrument similar to the SRI portable coal dust concentration instrument.

For Fig. 8	SRI*
β 6.26	15°
δ 16.25	55°
ε 26.25	48°

*Measured from Fig. A-1 of Final Report of portable mine dust concentration instrument.

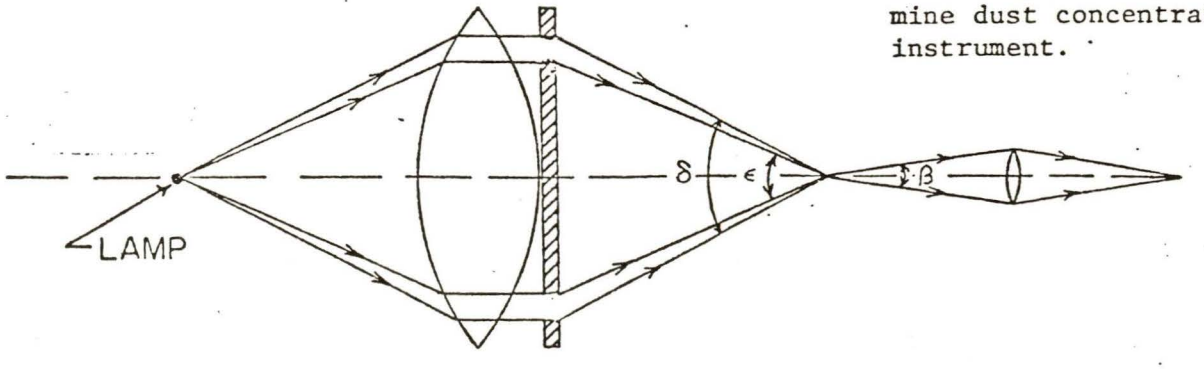

Figure 12. Schematic of optical system of SRI instrument.

ment to be insensitive to the size distribution, the dashed-line labeled 2-i, must have a slope parallel to the line labeled m = +1 (a line of slope one). As can be seen from Figure 11, the instrument would not be expected to have a response proportional to the mass of the particle for the larger sizes. By following the same reasoning, it can be seen that if the flux curve is horizontal (zero slope), the response of the instrument will be proportional to the surface area of the particle and if the flux curve has a slope of m = -1, the response curve will be proportional to the diameter of the particle.

For the index of refraction corresponding to silica, the slope of the flux curve for the size range from 3.41 to 8.31 μm must be less than the slope for particles larger than 8.31 μm. It should also be noted that the response curves shown in Figure 11 are for a collecting angle aperture $\beta = 6.25°$, illuminating cone (inside), $\delta = 16.25°$ and illuminating cone (outside), $\varepsilon = 26.25°$. In the SRI instrument, these values are $\beta = 15°$, $\delta = 55°$, and $\varepsilon = 48°$. These angles and a schematic of the optical system is shown in Figure 12.

In addition, due to the Tyndall effect, the light scattered per fixed volume of aerosol is proportional to the volume of aerosol, or proportional to the diameter of the particles cubed, for particles smaller than the wavelength of light. However, for particles much larger than the wavelength of light, which is what we are concerned with, the intensity per volume of aerosol is proportional to D_p^{-1}. Thus, for these large particles, the intensity per unit volume will decrease as the particle size increases.

Conclusions

First of all, the drifting baseline problem, the range change problem, and the leakage problem indicate that some mechanical and electrical design changes must be made on the instrument before it will be reliable. However, these are problems which can be overcome by a redesign of the instrument.

The second conclusion which can be drawn is that the sensitivity of the instrument is influenced by the size distribution of the dust aerosol and possibly by the material of the dust aerosol. The influence of the two materials tested (silica and coal), however, was much less than the influence of the size distribution. Thus, the influence of the size distribution appears to be the major factor in considering the usefulness of this instrument. It should be noted, however, that this instrument will be used with some type of a preclassifier to eliminate large particles. Thus, the size dependency of the instrument may not be extremely important, especially if the instrument is used with the dichotomous impactor, where the aerosol particles can be classified into distinct size ranges.

It should also be noted that in the testing which we performed on the instrument, we found the instrument to be easy to use and required little maintenance other than for the leakage problem. The instrument also proved to be very sensitive, and we were able to see small concentration fluctuations of the dust coming from the fluidized bed due to the nature at which the dust is fed into the bed by the feed chain conveyor. Thus, the instrument has a very rapid response and can follow changing dust concentrations much more readily than any other instrument we have tested.

Recommendations

In spite of the mechanical and electrical design problems of this instrument, we feel that it has promise as a mass monitor for dust aerosols, and recommend that a redesign of the instrument be made. After the redesign, the instrument should be calibrated again, so that an accurate calibration can be made. Also at this time, we feel that a monodisperse dust generator should be developed which will allow the instrument to be interrogated by particle sizes in a distinct size range (i.e., with the small particles being removed as well as the large particles).

REFERENCES

1. Lapple, C. E. and C. F. Schadt - Portable Mine Dust Concentration Instrument Final Report, Bureau of Mines, contract H0111688, Stanford Research Institute Project, PYU - 1267 (June 27, 1972).

2. Marple, V. A., B. Y. H. Liu, and K. L. Rubow, "A Dust Generator for Laboratory Use", Am. Ind. Hyg. Assoc. J. 39:26-32 (1978).

3. Marple, V. A., K. T. Whitby, B. R. Olson and J. L. Wolf, "Precision Aerosol Divider", Am. Ind. Hyd. Assoc. J. 37:69-72 (1976).

4. Marple, V. A. and K. L Rubow "An Evaluation of the GCA Respirable Dust Monitor 101-1" Am. Ind. Hyg. Assoc. J. 39:17-25 (1978).

5. Marple, V. A. and K. T. Rubow, "Aerodynamic Particle Size Calibration of Optical Particle Counters," J. Aerosol Sci. 7:425-433 (1976).

6. Hodkinson, J. R. and J. R. Greenfield, "Response Calculations for Light-Scattering Aerosol Counters and Photometers", Applied Optics, Volume 4, No. 11, 1463-1474 (Nov. 1965).

7. Cooke, D. D. and Kerker, M. "Response Calculations for Light-Scattering Aerosol Particle Counters," Applied Optics, Volume 14, No. 3, 734-739 (March 1975).

APPENDIX D

Evaluation of the MESA Plastic Disposable Respirable Impactor

Introduction

Theoretical and experimental evaluation of the impactor stage of the new two-stage respirable dust sampler [1] developed by Thomas Tomb and Harry Treaftis of MESA, U. S. Department of Interior, has been made. The impactor, shown schematically in Figure 1, has a round nozzle of 0.4 cm diameter and an S/W ratio of about 3, where S is the nozzle-to-plate distance and W is the nozzle diameter. The entire impactor is made from plastic including the impaction plate. Flow rate through the impactor is 2 lpm.

Theoretical Evaluation

The impactor was evaluated using a theoretical technique reported in References 2 to 4. In this theoretical procedure, the flow field within an impactor is determined by solving the full Navier-Stokes equations using finite difference methods. This method of determining the flow field has proven to be accurate since all viscous terms are included in the solution. The particle trajectories in these flow fields are then solved by expressing the particle's equations of motion in finite difference form and solving for the particle's path by numerical difference integration of these equations of motion. This method has proven to be very accurate in the prediction of the collection efficiency curves of inertial impactors.[4,5,6,7,8]

There are two ways in which this theory can be applied to an existing impactor. The first method would be to take the design of the impactor and apply the theoretical procedure to the solution of the flow field and then the solution of the particle trajectories while determining the collection efficiency curve in the process. The second method is to determine if certain governing parameters of the existing impactor matches that of parameters studied previously in the fundamental study of inertial impactors,[4] and then apply these predetermined efficiency curves to the impactor. The second method can only be applied if the governing parameters fall within a specific range.

For this particular impactor, it was found that the governing parameters were in a specific range allowing the use of the second method of evaluation of the impactor. These parameters are: 1) the S/W ratio which should be larger than 1.0 and was 3 for the existing impactor, 2) the throat length to nozzle diameter ratio which should be larger than a quarter and will certainly be satisfied by this impactor, and 3) the Reynolds Number which may be anywhere from 10 to 3,000 and was 700 in this impactor. Thus, an impactor with these governing parameters should have an efficiency curve which follows that of Figure 2. In this figure, the collection efficiency E is the fraction of the particles passing through the nozzle of the impactor which are collected upon the impaction plate. The particle diameter D_p is the aerodynamic diameter, which refers to a unit density spherical particle.

Experimental Evaluation

The impactor was also evaluated experimentally using monodisperse oleic acid particles with a uranine dye tracer. This procedure is similar to that described in Reference 8 and is a standard method for evaluating impactors in our Laboratory.

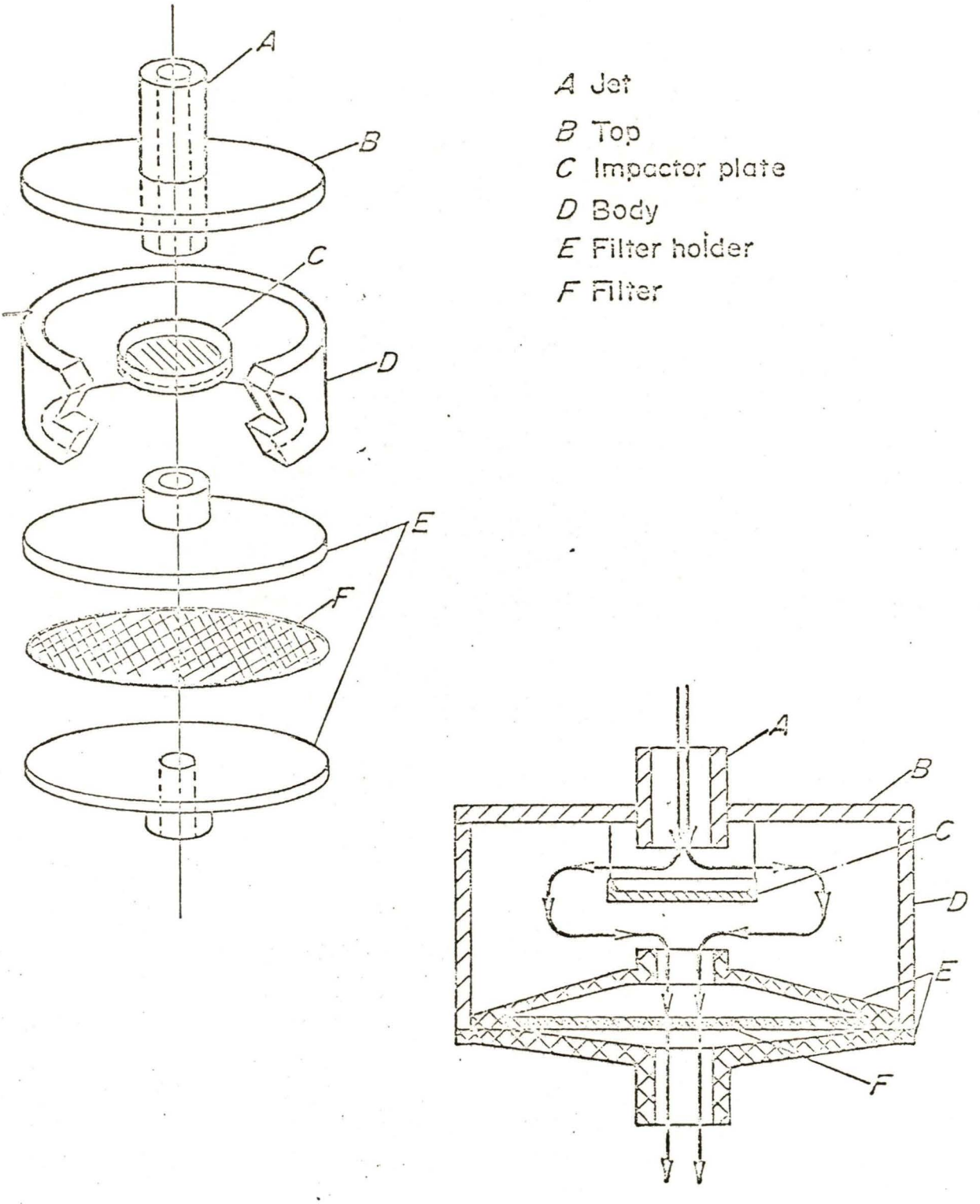

Figure 1. Schematic of the MESA Plastic Disposable Respirable Impactor (from Ref. 1).

In this procedure, monodisperse particles were generated in the range from 3 to 9 μm by use of a vibrating orifice monodisperse aerosol (VOMA) generator. A 20 μm diameter orifice was used in the VOMA generator to produce a liquid droplet of about 43 μm in diameter. The material of the droplets is a solution of alcohol, oleic acid and uranine with the uranine being about 10% of the oleic acid. The quantity of alcohol is such that when the alcohol is evaporated from the 43 μm droplet, the oleic-acid uranine particle of a desired size (3 to 8 μm) is obtained.

For each run, the monodisperse aerosol was passed through the impactor at a flow rate of 2 lpm. After several minutes of sampling the aerosol, the impactor is removed from the test set-up and disassembled. The cover, impaction plate, and filter assembly are then washed in known amounts of distilled water.

The amount of aerosol deposited on the different parts of the impactor is in proportion to the fluorescence of the uranine dye which will be found in the wash water. Thus, a quantitative analysis can be made by measuring the fluorescence of these wash solutions in a fluorometer (Model 110, G. K. Turner Associates, Palo Alto, California). The quantity of water used to wash the particles from the various parts of the impactor were such that all readings on the fluorometer would fall within one range of the fluorometer. This procedure eliminates any errors one may obtain by having to calibrate between different ranges of the fluorometer.

The mass of the uranine deposited upon each part of the impactor can then be calculated by multiplying a concentration by the quantity of the distilled water in the wash. The collection efficiency of the impactor is subsequently calculated by determining what fraction of the total mass deposited in the impactor is found on the impaction plate.

The results of this experimental work is shown in Figure 2. The agreement between the theory and experimental results is good for collection efficiencies of about 30%. Both the experimental and theoretical results indicate that the 50% cutoff point is at about 7.5 μm. At lower efficiencies (less than 30%) considerable differences between the theory and the experimental results were found.

In previous evaluations of impactors, we have not found as large a difference between experimental results and theory as we have seen for this impactor. Since the dimensions of this impactor are such that we would expect good agreement with the theory, the disagreement is difficult to explain. One possible explanation may be that the nonconducting plastic impaction plate could have acquired an electrical charge and influenced impaction at low efficiencies. The influence of nonconducting impaction plates has not been completely studied.

Results

The theoretical and experimental results of the impactor are shown in Figure 3 as the percent penetration through the impactor (100-percent efficiency) vs. the equivalent aerodynamic diameter. In this figure are three curves other than the experimental and theoretical curve just discussed. These three curves are the AEC and the BMRC respirable curves and the experimental penetration curve found by MESA for this particular impactor.

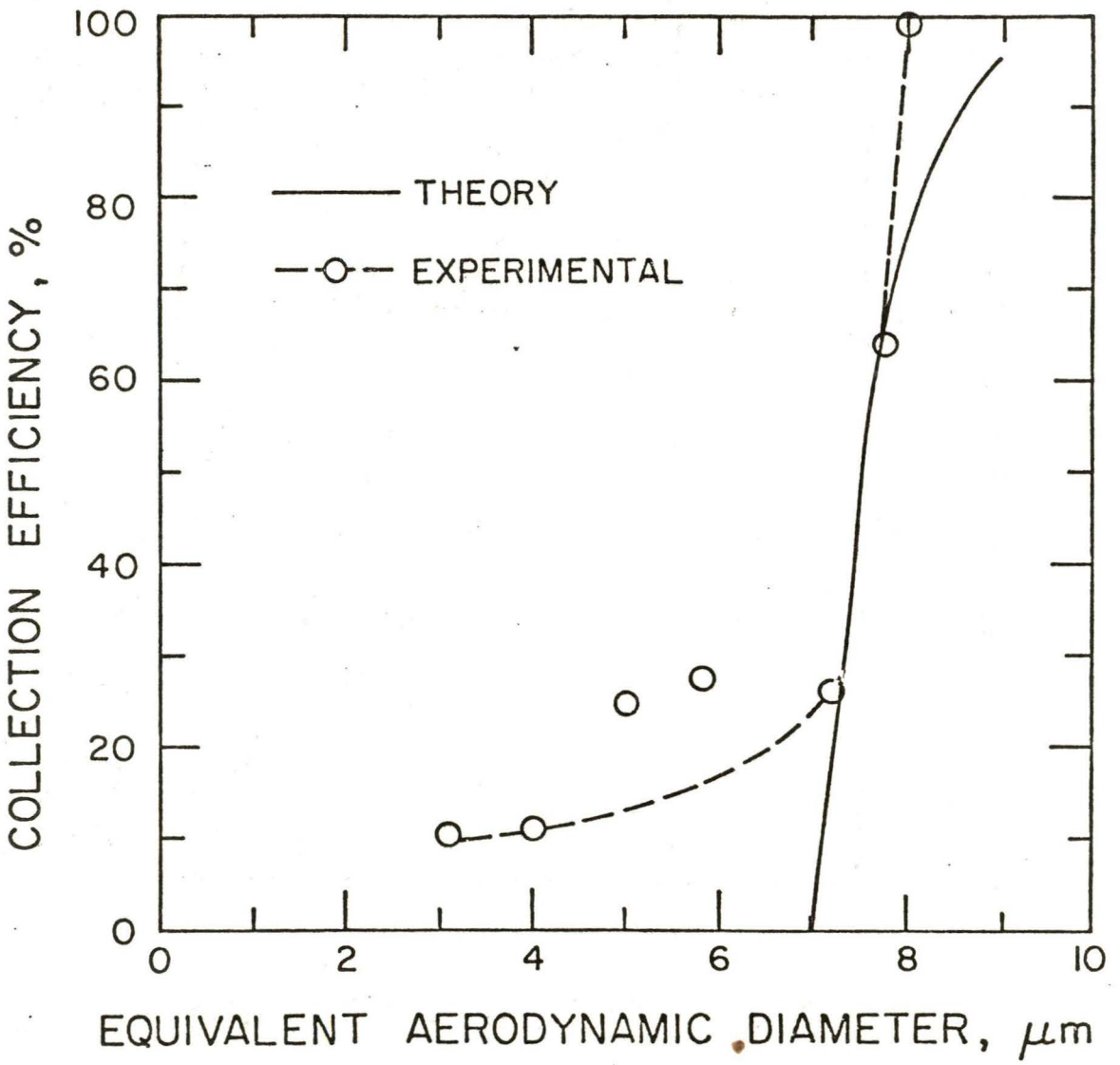

Figure 2. Theoretical and experimental collection efficiency curves for MESA Plastic Disposable Impactor.

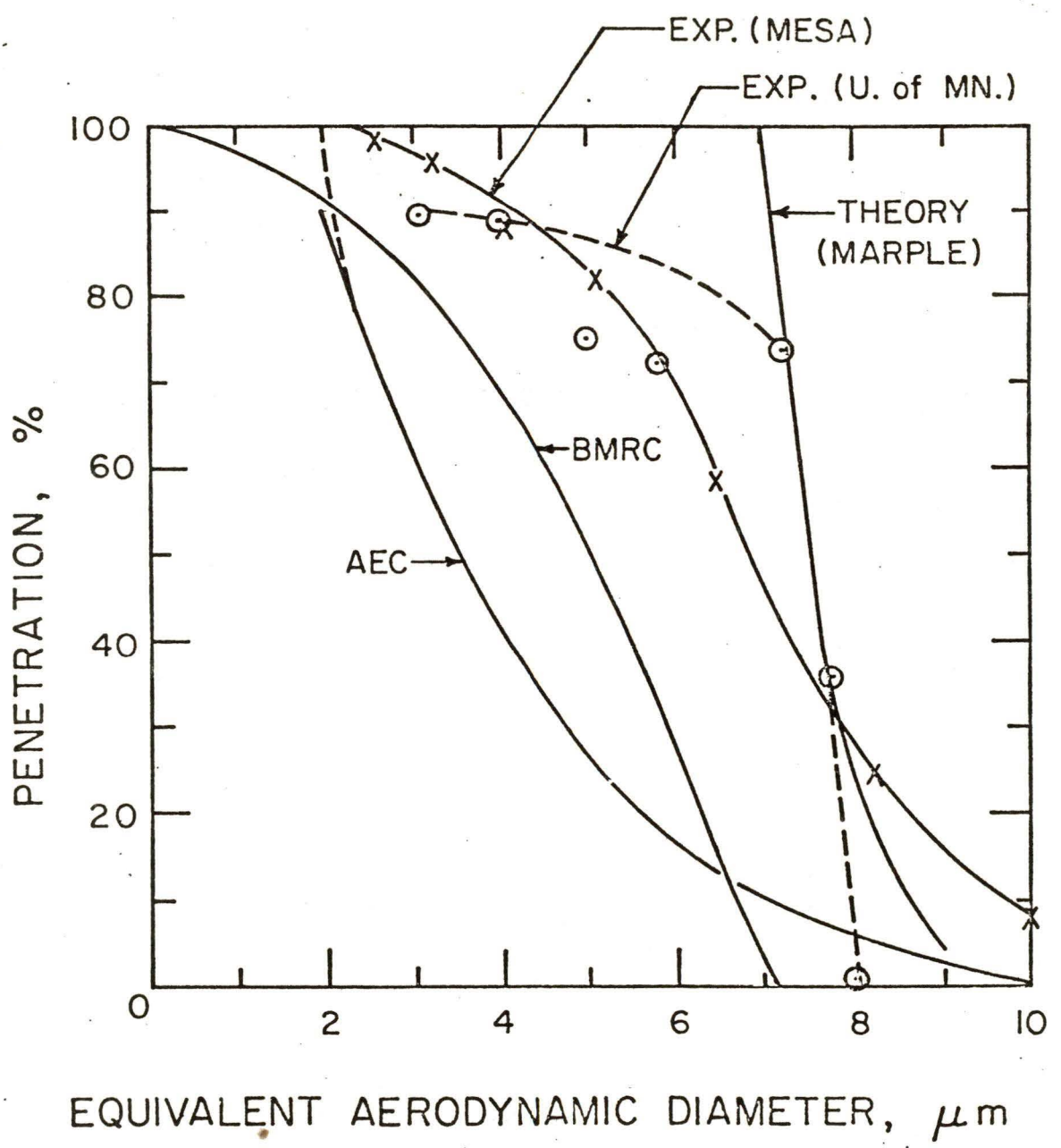

Figure 3. Comparison of penetration curves of the MESA Plastic Disposable Impactor with AEC and BMRC Respirable curves.

It is of interest to note in Figure 3, that the data points from these experiments agree fairly well with the data points that were found by MESA, with the exception that we found the penetration curve to be very steep for penetrations less than 70%. Another item of interest is that, for all particle sizes, the impactor has higher penetration than an impactor should have to follow either the BMRC or the AEC curve.

References

1. Tomb, Thomas F. and Harry N. Treaftis, "A New Two-Stage Respirable Dust Sampler", Am. Ind. Hyg. Assoc. J. 36:1-9 (November, 1975).

2. Marple, V. A., B. Y. H. Liu and K. T. Whitby, "On the Flow Fields of Inertial Impactors", presented at the ASME Symposium on Flow Studies in Air and Water Pollution, Atlanta, GA (June, 1973); J. Fluids Eng. 96:394-400 (1974). (COO-1248-36)

3. Marple, V. A., B. Y. H. Liu and K. T. Whitby, "Fluid Mechanics of the Laminar Flow Aerosol Impactor", J. Aerosol Sci. 5:1-16 (1973). (COO-1248-35) (Revised version of Publ. No. 175.)

4. Marple, V. A. and B. Y. H. Liu, "Characteristics of Laminar Jet Impactors", Environ. Sci. Technol. 8:648-654 (July, 1974). (COO-1284-40) (Revised version of Publ. No.'s 176, 177, and 178).

5. Jaenicke, R. and I. H. Blifford, "The Influence of Aerosol Chacteristics on the Calibration of Impactors", J. Aerosol Sci. 5:457 (1974).

6. Willeke, K. and J. J. McFeters, "The Influence of Flow Entry and Collecting Surface on the Impaction Efficiency of Inertial Impactors", J. Colloid and Interface Science, in print (1975).

7. Schott, J. H., "Jet-Cone Impactors as Aerosol Partcle Separators", M. S. Thesis, University of Minnesota (1973).

8. Willeke, K., "Performance of the Slotted Impactor", Am. Ind. Hyg. Assoc. J. (September, 1975).

Appendix E

IMPACTORS WITH RESPIRABLE PENETRATION CHARACTERISTICS: PERSONAL SAMPLER SIZE

By

Virgil A. Marple and James E. McCormack

Particle Technology Laboratory
Mechanical Engineering Department
University of Minnesota
Minneapolis, Minnesota 55455

ABSTRACT

Single stage impactors with penetration characteristics approximating those of the BMRC, AEC and ACGIH respirable criteria have been developed for use as personal samplers. Three impactors were built for flow rates of 2 l/min. Calibration of these impactors shows good agreement with the respirable penetration curves. Experiments with coal dust indicated little particle bounce when an oil soaked porous impaction plate was used. Finally, a procedure is introduced by which samplers can be designed with penetration characteristics that differentiate between the AEC and ACGIH respirable criteria.

Introduction

In determining health hazards from inhaled aerosol particles, it is the respirable particulate matter, defined as that which penetrates to the alveolated regions of the lungs, which are of primary importance. Due to the size selective nature of the particle removal mechanisms in the nasal passages and lungs airways, criteria defining respirable particles must be a function of the particle size. Three commonly used criteria defining respirable particle penetration are shown in Figure 1. These criteria, discussed in detail by Lippmann[1], have been defined by the British Medical Research Council (BMRC), the United States Atomic Energy Commission, (AEC), and the American Conference of Governmental Industrial Hygienists (ACGIH).

The quantity of respirable particles in an aerosol can be measured by use of two-stage respirable dust samplers. The first stage consists of a particle classifier with penetration characteristics corresponding to one of the respirable penetration curves in Figure 1 and the second stage which has a high collection efficiency for all particle sizes penetrating the first stage. In practice, only the quantity of particles collected on the second stage, representing the respirable fraction is measured. Cyclones[2] and horizontal elutriators[3] have been commonly used for the first stage while filters are generally used for the second stage.

Furthermore it is often advantageous if the two-stage samplers are small enough to be worn by the worker as a personal sampler, enabling the sampler to be located in the workers breathing zone. This implies the further requirement that the flow rate through the sampler be on the order of 2 l/min so as to be compatible with battery operated personal sampling pumps. The cyclones have generally been used as the first stage of this type of sampler since they are lightweight and being an inertial classifier can operate in any position, an important requirement for any personal sampler.

Another inertial classifier which has potential as a personal sampler is the inertial impactor[4]. Although the penetration characteristics of inertial impactors are generally much sharper than those shown in Figure 1, a technique has recently been developed where respirable penetration curves can be approximated through the use of a single stage impactor with multiple nozzles of different sizes[5].

Since the AEC and ACGIH respirable curves are often considered equivalent for practical purposes[1], a sampler with penetration characteristics approximating the AEC curve may be assumed to also approximate the ACGIH curve. However, if distinction between the two curves is necessary, a technique is described in the addendum by which the personal sampler impactor can be designed to approximate the ACGIH curve, including the characteristic that only 90% of the particles smaller than 2 μm are respirable.

Impactor Nozzle Designs

Normally, inertial impactors have penetration characteristics which are much sharper than those shown in Figure 1. However, a design procedure has been recently developed by which the penetration characteristics of single stage inertial impactors could be designed to approximate respirable penetration

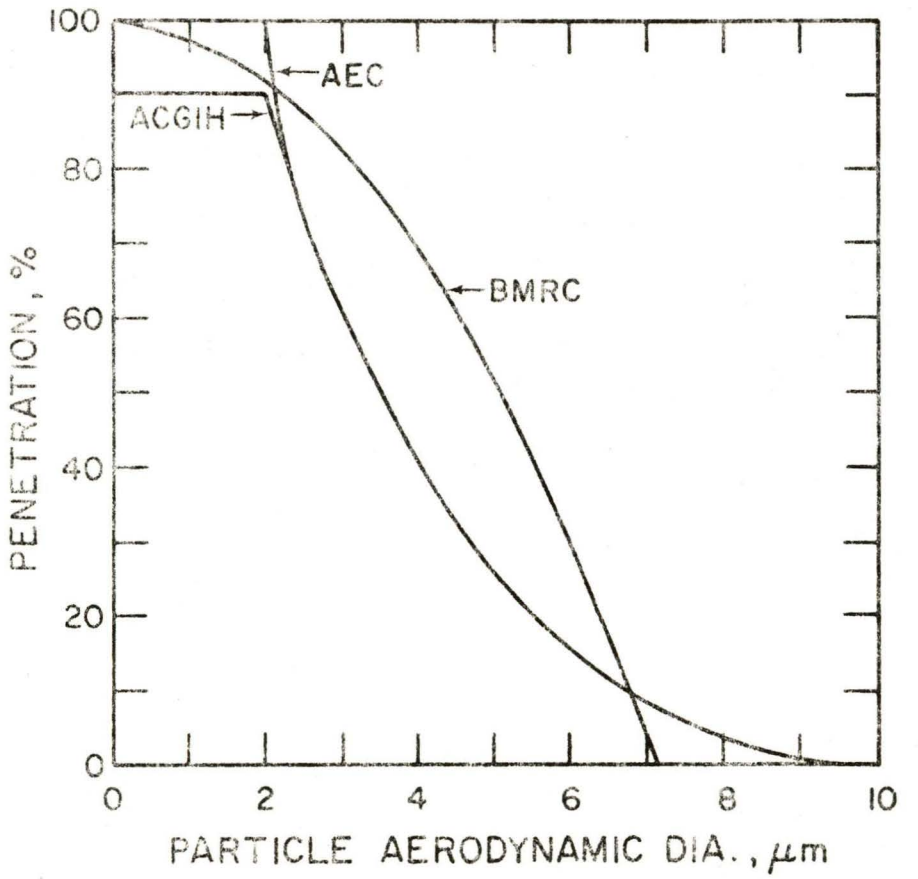

Figure 1. BMRC, AEC and ACGIH respirable penetration curves.

curves.[5] This design procedure involves using several impactors with different nozzle sizes in a parallel flow arrangement, as shown in Figure 2. Since the pressure drops across the nozzles are the same, each nozzle will have a different particle cutoff size, depending upon the size of the nozzle. The combined penetration curve will then be a function of the number and the size of the nozzles used, and the total flow rate through the nozzles. For example, shown in Figure 2, a single stage impactor with three sizes of nozzles would possess cut-off characteristics which approximate the respirable curve in three steps. The number of nozzles of each size must be sufficient to pass the quantity of flow dictated by the size of each step. For the three steps shown in Figure 2, there must be enough nozzles of each size to pass one third of the flow.

The stepwise curve in Figure 2 represents impactor cutoff characteristics determined from theoretical analysis. In the work presented in Ref. 5 the theoretical curves were based on the work by Marple[6] whereas in this paper the curves are based on a more recent theoretical study[7] which is a slight modification of the original theory. The major difference is that the modified theory does not predict cutoff characteristics that are as sharp as those predicted by the original theory. However, the predicted particle diameter at 50% collection efficiency remained essentially the same for both theoretical studies.

In reference 5, the nozzle sizes and number of nozzles for impactors operating at 2 l/min were determined for impactors with penetration characteristics which approximate the AEC (or ACGIH) curve using from one to five nozzle sizes (steps). Those values are tabulated in Table 1 of this paper. The results for similar calculations made for impactors with penetration characteristics approximating the BMRC criteria are presented in Table 2.

Since impactors can be designed with either round or rectangular nozzles, Tables 1 and 2 present nozzle dimensions for both. Either the round or rectangular nozzles in these tables will provide the same particle cutoff size and are interchangeable. For example, in Table 1 if two nozzle sizes are to be used, a round impactor with one 0.25 cm diameter nozzle and sixteen 0.063 cm diameter nozzles could be used. However, similar characteristics would be obtained for an impactor with one 0.10 cm by 0.40 cm rectangular nozzle and one 0.042 cm by 2.0 cm rectangular nozzle. In addition, since the round and rectangular nozzles are interchangeable an impactor could be designed with one 0.25 cm diameter round nozzle and one 0.024 cm by 2.0 cm rectangular nozzle.

In most cases, two or three nozzle sizes are sufficient to approximate a respirable curve. Although closer approximations to the respirable penetration curves can be obtained by going to four or five nozzle sizes, the nozzle diameters become very small and, therefore, may not be practical.

Personal Sampler Design

Three impactor designs with round nozzles were chosen for construction and evaluation. These are the two and three nozzle size designs approximating the AEC (or ACGIH) criteria and the three nozzle size design approximating the BMRC criteria as indicated by the boxed cases in Tables 1 and 2, respectively.

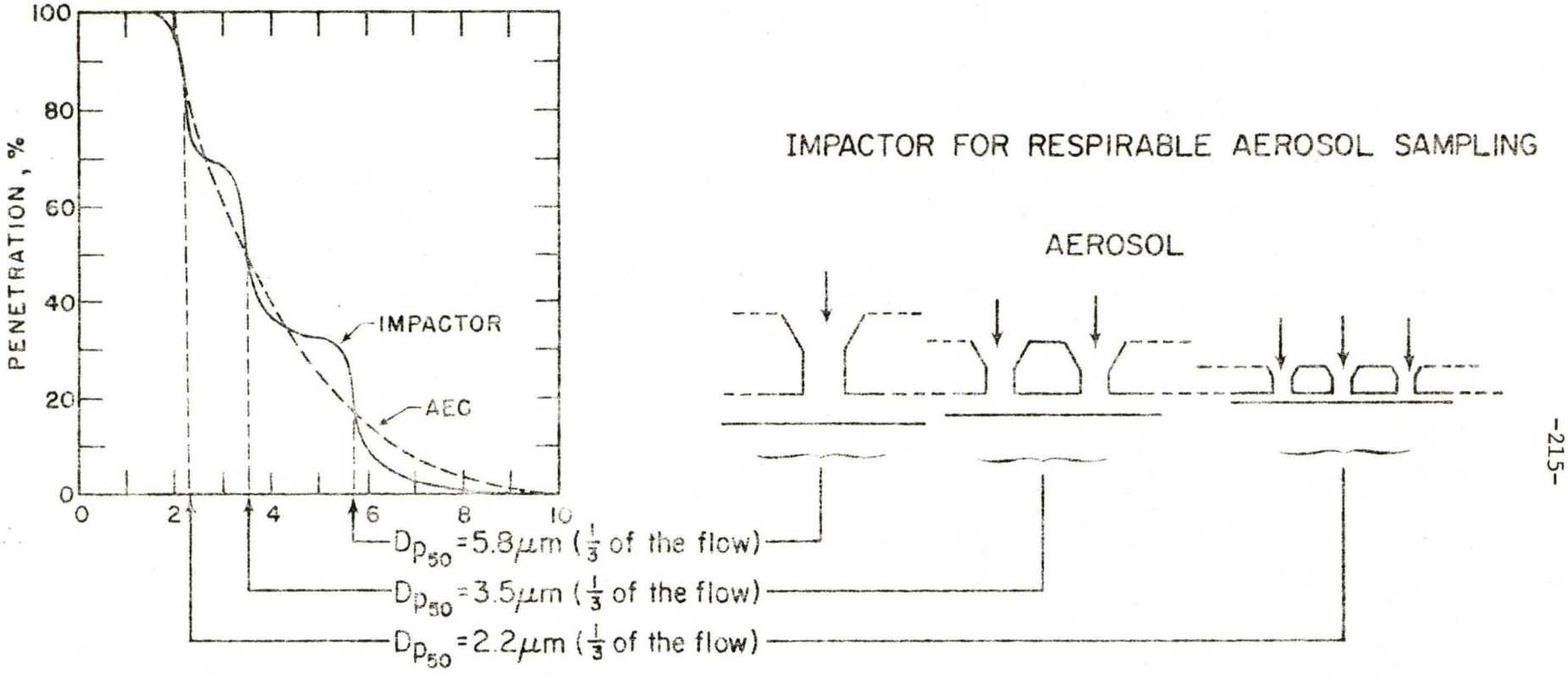

Figure 2. Approximation of a respirable curve by a single stage impactor with three nozzle sizes.

Table 1
Impactor Designs With
Penetration Characteristics at 2 l/min Flow Rates
Which Simulate the AEC (or ACGIH) Respirable Penetration Curve

		ROUND		RECTANGULAR	
Number of nozzle sizes	Particle Cut-off Diameter, μm	Nozzle Diam., cm	Number of Nozzles,	Nozzle Width, cm	Nozzle Length, cm
1	3.5	0.25	1	0.10	0.49
2	5.0	0.25	1	0.10	0.49
	2.5	0.063	16	0.024	2.0
	5.8	0.24	1	0.097	0.47
3	3.5	0.087	8	0.033	1.4
	2.2	0.033	53	0.012	3.8
	6.4	0.23	1	0.093	0.45
	4.2	0.10	5	0.038	1.1
4	3.0	0.048	23	0.019	2.2
	2.1	0.022	109	0.0083	5.0
	6.7	0.22	1	0.086	0.44
	4.6	0.11	4	0.042	0.91
5	3.5	0.057	15	0.022	1.7
	2.7	0.033	44	0.012	3.2
	2.0	0.017	167	0.0066	5.8

Table 2

Impactor Designs With Penetration Characteristics at 2 l/min Flow rate Which Simulates the BMRC Respirable Penetration Curve

		ROUND		RECTANGULAR	
Number of nozzle sizes	Particle Cut-off Diameter, µm	Nozzle Diam., cm	Number of Nozzles,	Nozzle Width, cm	Nozzle Length, cm
1	4.9	.31	1	.13	.60
	6.1	.28	1	.11	.55
2	3.5	.093	9	.035	1.8
	6.4	.26	1	.10	.50
3	5.0	.15	3	.060	.85
	2.9	.048	28	.019	2.7
	6.6	.24	1	.093	.47
	5.5	.16	2	.062	.71
4	4.3	.10	6	.037	1.2
	2.5	.030	63	.011	3.4
	6.6	.22	1	.086	.44
	5.9	.17	2	.066	.57
5	5.0	.13	3	.047	.81
	3.8	.072	9	.027	1.4
	2.2	.019	132	.0075	5.1

A cross-sectional view of an impactor is shown in Figure 3. Photographs of the components and an assembled unit are shown in Figure 4. The impactors are constructed from plastic with nozzle lay-outs as shown in Figure 4a. In all cases, the nozzles are placed symetrically so that the flow will be symmetrical on the impaction plate. The impaction plate shown in Figure 4b is designed to be attached to the nozzle plate by four pegs. The after-filter and the base plate are those that have been used by Tomb and Treaftis[4] in a single nozzle impactor. The filter is from a model Type 457193 MSA filter cassette.

Two types of impaction plates have been designed and used in the impactors. These are a plastic impaction plate used in the calibration of the impactor with liquid droplets and an oil impregnated porous impaction plate[8] used for the collection of coal dust particles. With the porous impaction plate, oil wicks upward continuously through the deposited particles always presenting the incoming dust particles with a fresh oil surface, reducing the particle bounce problem often associated with impactors.

Sampler Calibration

The particle cutoff characteristics of the personal sampler impactors were experimentally determined using monodisperse particles generated by the vibrating orifice monodisperse aerosol generator [9]. The particles were oleic acid with a uranine dye tracer. The quantity of particles penetrating through the impactors were determined by fluorometric analysis of the deposited particles on the impaction plates and the after-filters. The procedure was identical to that described in reference 5. The experimental results for each of the three impactors are shown as data points in Figures 5, 6, and 7. The theoretical curves are also presented in these figures. A comparison between the experimental data and theoretical curves indicates good agreement with the best agreement being for the three nozzle sizes as expected.

Test of the Oil Impregnated Impaction Plate

Experiments were performed sampling coal dust particles to test the effectiveness of the oil impregnated impaction plate to control particle bounce. Coal dust was generated at a concentration of about 9 mg/m^3 by a fluidized bed type of dust generator[10]. The concentration of the respirable fraction of the dust was about 2 mg/m^3, leaving 7 mg/m^3 to be removed by the impactor. The impactor used in this test was the two nozzle size unit which approximates the AEC respirable penetration curve. The test was run for a total of 6.5 hours with evaluations of particle bounce being made at 0.5, 2.25, 4.0 and 6.5 hours into the test.

The evaluations for particle bounce were made by measuring the dust concentration and size distribution with an optical particle counter system specifically calibrated for coal particles[11]. At 0.5. 2.25, 4.0 and 6.5 hours into the test, the coal particle number size distribution and concentration was measured upstream and downstream of the impactor and the penetration as a function of particle size calculated. Sampling bias was reduced by normalizing the concentration at each particle diameter by the concentration at 1 μm aerodynamic diameter, which should represent close to 100% penetration.

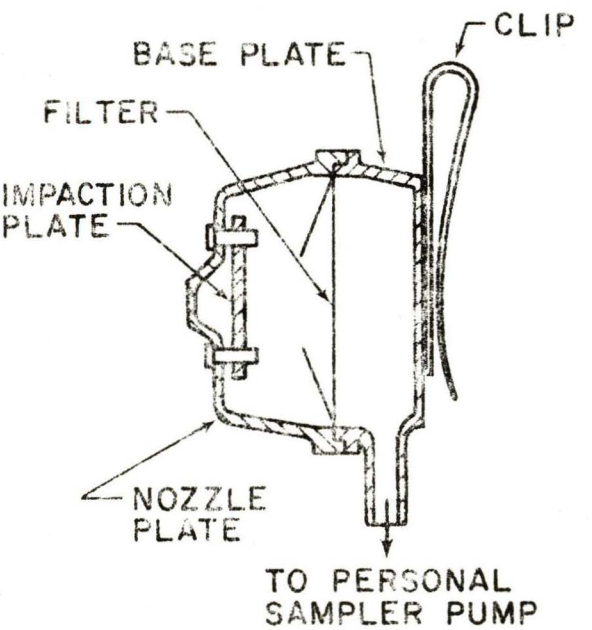

Figure 3. Cross-sectional view of a personal sampler.

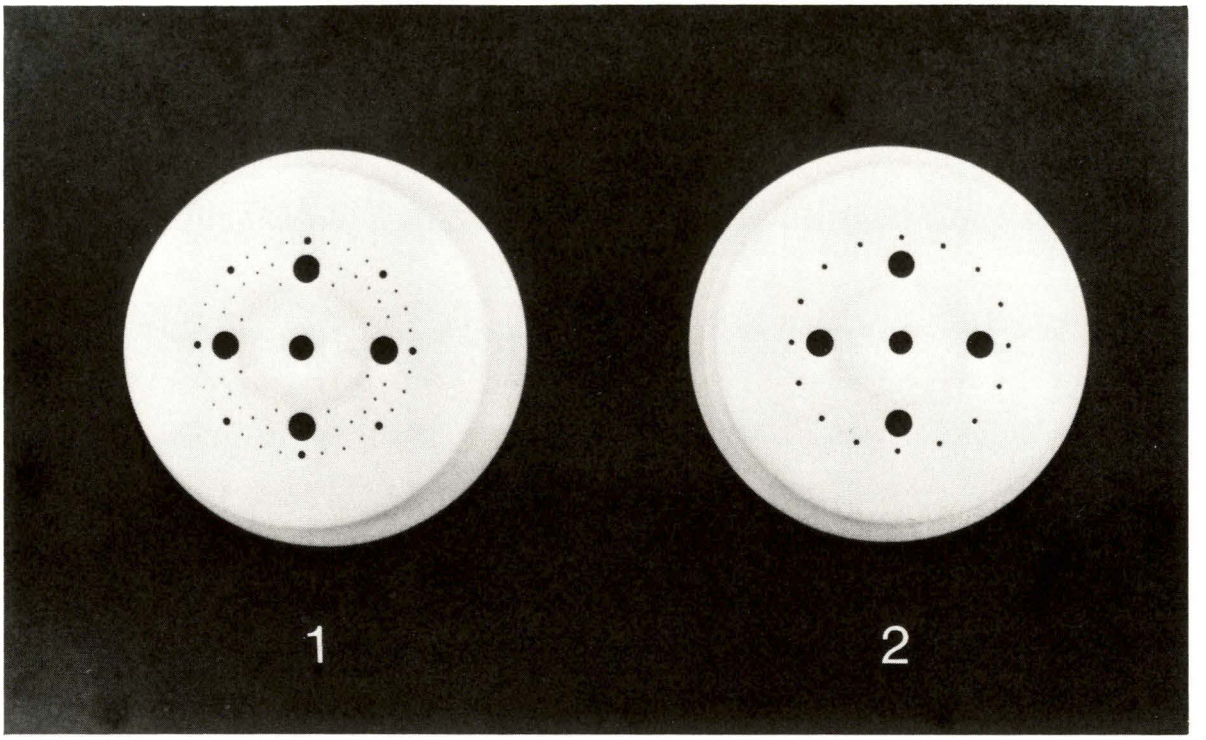

a. Nozzle plates with two (2) and three (1) nozzle sizes. (The four equally spaced large holes are for the impaction plate mounting pegs.)

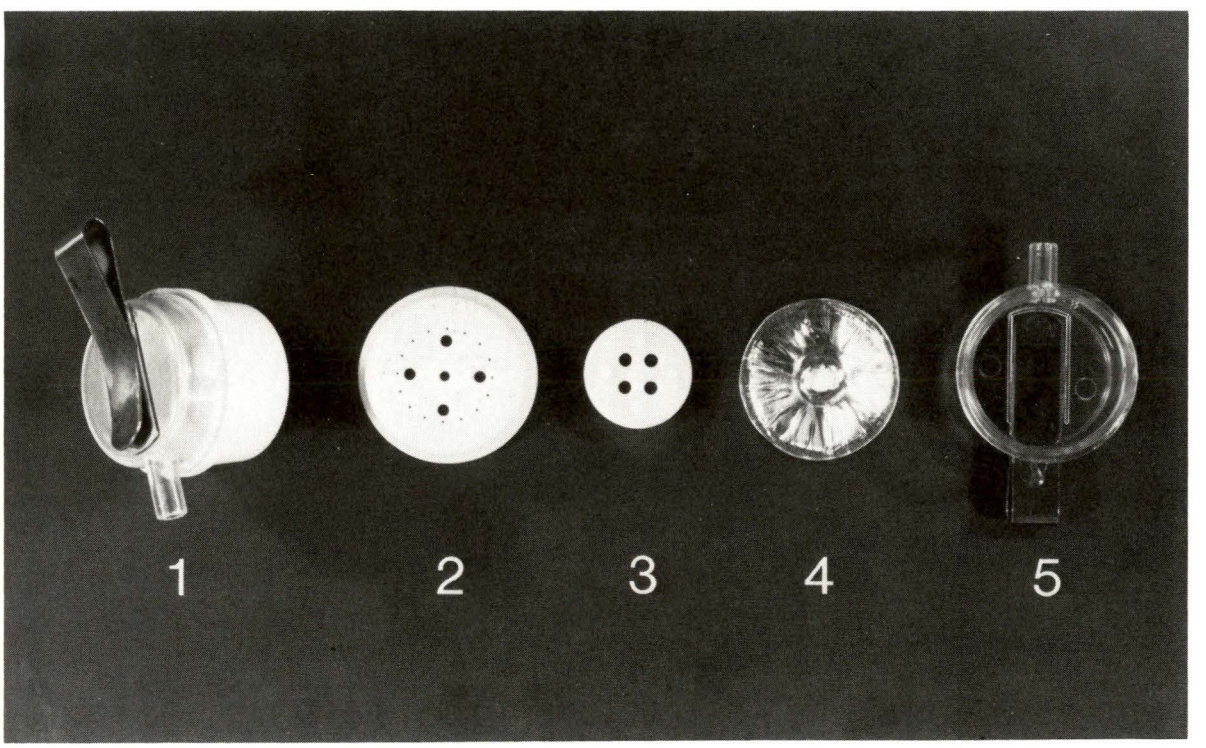

b. Impactor components (1- assembly, 2- nozzle plate, 3- impaction plate, 4- filter, 5- base plate).

Figure 4. Respirable personal sampler.

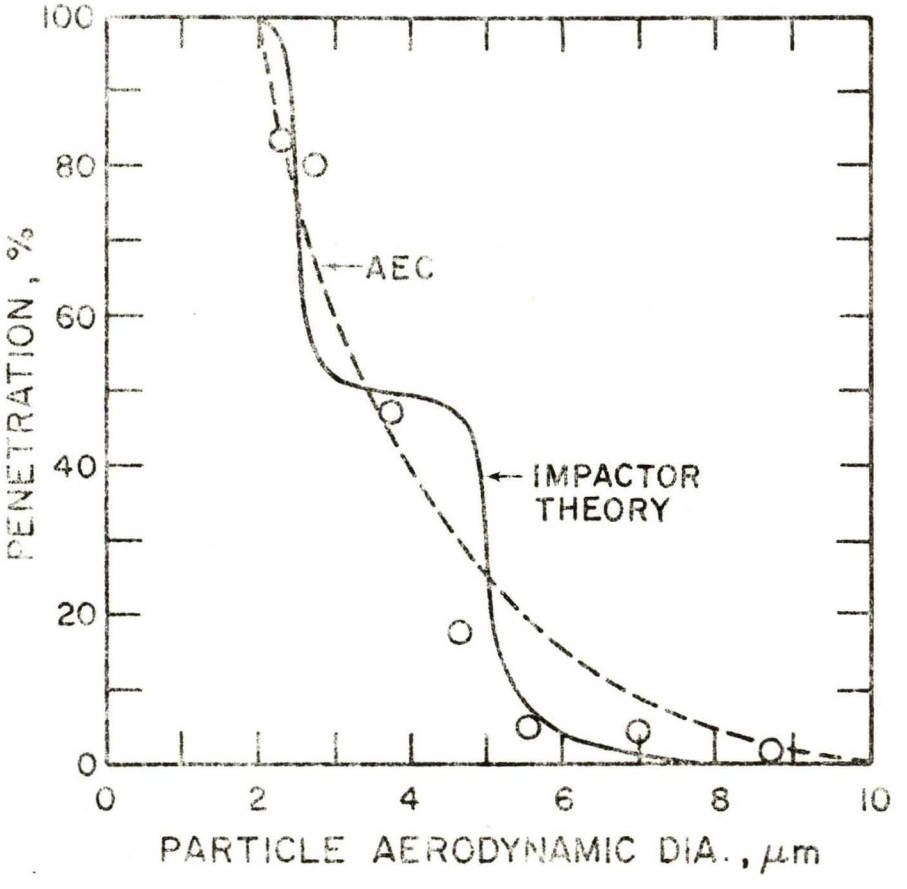

Figure 5. Comparison of experimental data and the theoretical penetration curve to the AEC respirable curve for the two nozzle size impactor.

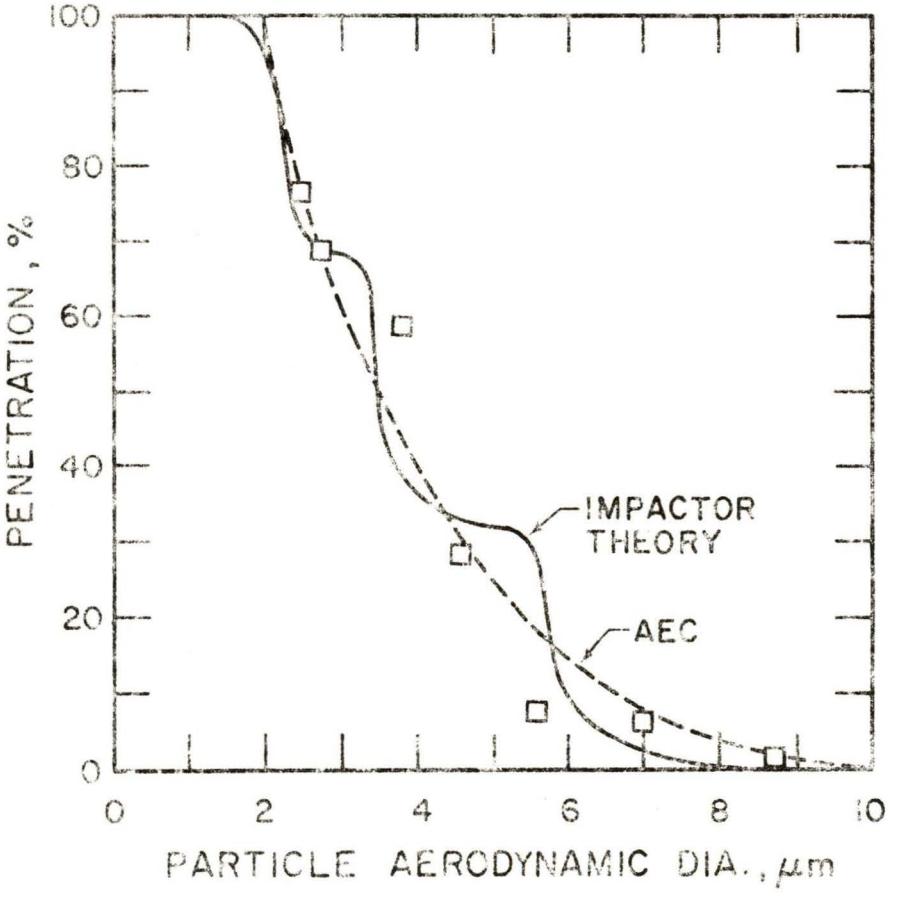

Figure 6. Comparison of experimental data and the theoretical penetration curve to the AEC respirable curve for the three nozzle size impactor.

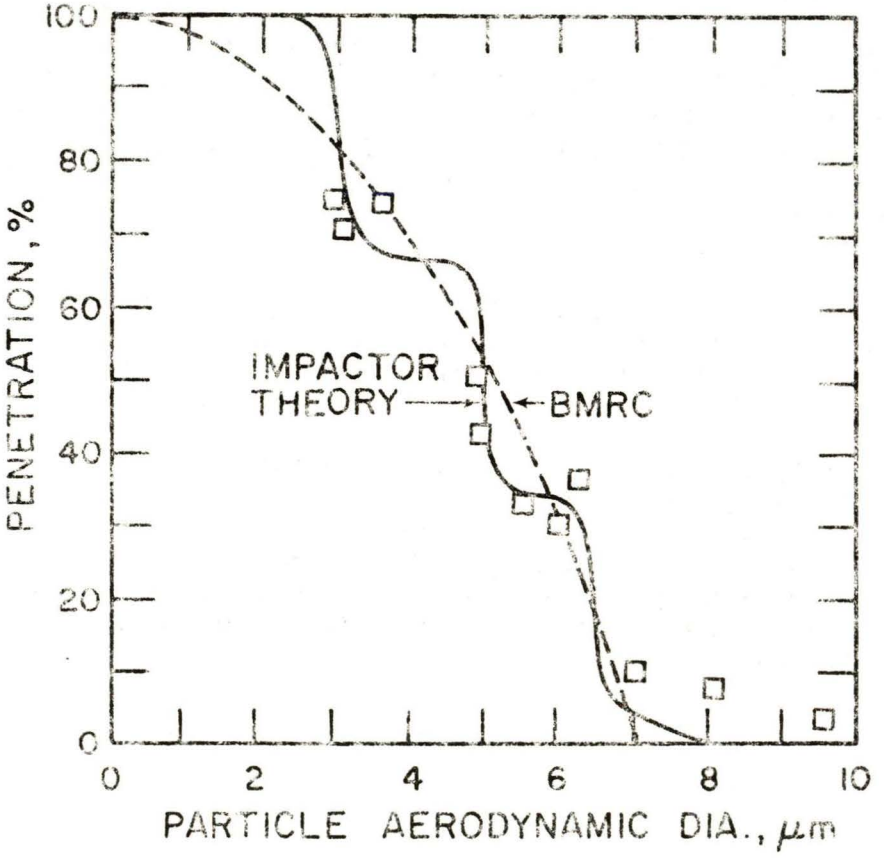

Figure 7. Comparison of experimental data and the theoretical penetration curve to the BMRC respirable curve for the three nozzle size impactor.

The resulting penetration curves, shown in Figure 8, indicate that not only did the penetration remain constant over the test period but that the measured penetration does agree well with the AEC respirable penetration curve. Thus, there is no indication of particle bounce or particle reintrainment.

In addition to the measurement of the particle size distribution, the test was stopped at 1, 2 and 6.5 hours and the impaction plate removed for inspection of the deposits. Photographs of the deposits from the smaller nozzles are shown in Figure 9. The deposits appear to form spikes and in some cases the spikes bend and a new spike grows from the base. This bending of the spikes may have been caused by the removal of the impaction plate from the impactor and may not happen if the impaction plate is not disturbed.

Conclusions

It was found that personal sampler impactors can be designed with penetration curves that approximate either the BMRC or AEC (or ACGIH) respirable penetration curves. Experimental determination of the penetration curves of three impactors showed close agreement to theoretically predicted curves. As expected, an impactor with three cutoff sizes approximates the respirable curve closer than does an impactor with two cutoff sizes but both are sufficiently close approximations. Even better approximations could be obtained with more nozzle sizes but the small nozzle diameters at the low flow rate of 2 l/min would not be practical.

Experiments with an oil impregnated porous impaction plate showed that large amounts of dust particles could be collected without experiencing particle bounce. An impactor collecting approximately 7 mg/m^3 of coal dust at a flow rate of 2 l/min for 6.5 hours showed no signs of particle bounce.

Finally, it is important to note that impactors with respirable cutoff characteristics can be designed for any flow rate. The flow rates for the impactors in this paper were chosen to be 2 l/min to be compatible with standard personal sampling pumps. However, personal samplers with larger flow rates could be designed if larger flow rate pumps were used. If 4 l/min were used for personal sampling, the mass of particles collected on the filter would be doubled and the gravimetric accuracy increased.

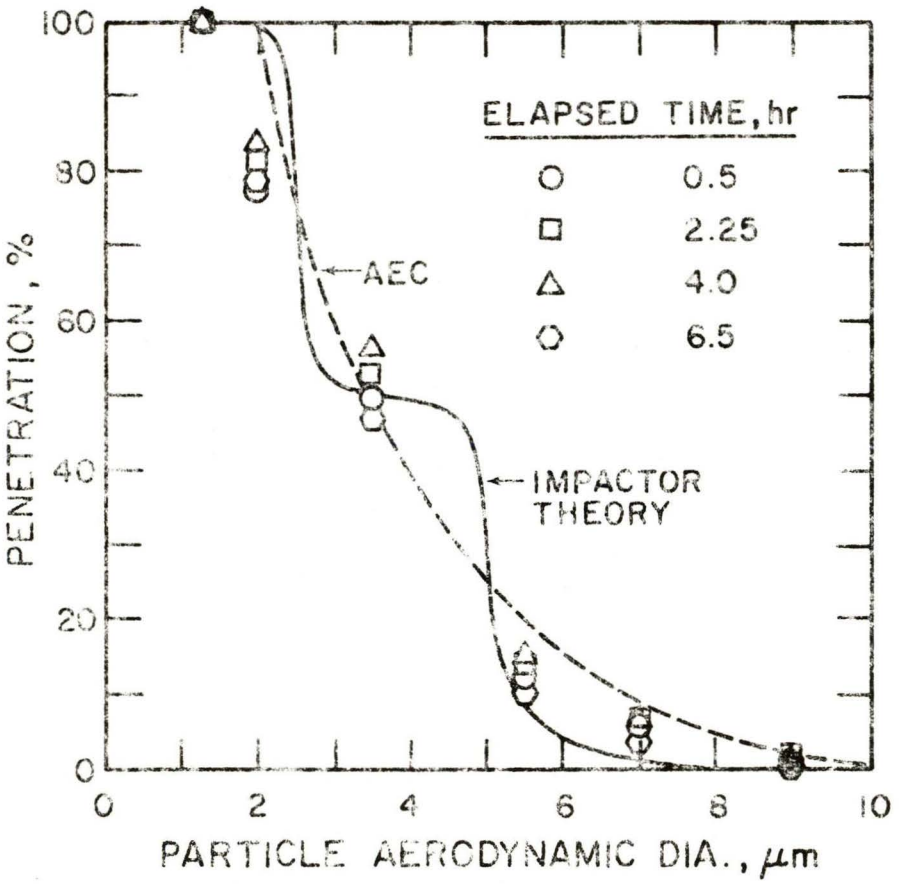

Figure 8. Penetration of particles through the impactor with an oil impregnated porous impaction plate as a function of time.

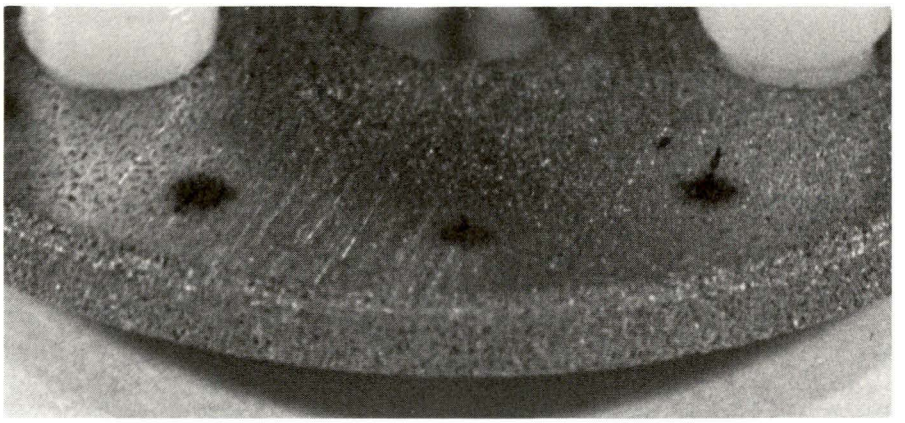

A. 1.0 HOUR

B. 2.0 HOURS

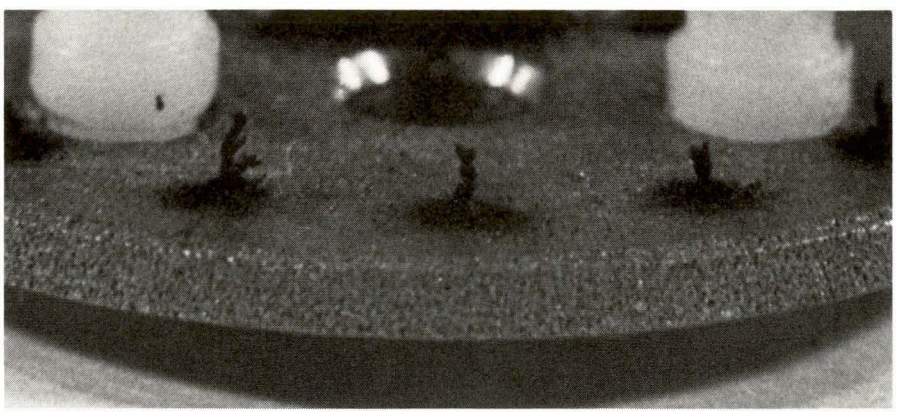

C. 6.5 HOURS

Figure 9. Deposits on the oil impregnated porous impaction plate after sampling a coal dust aerosol (9 mg/m^3) for 1.0, 2.0 and 6.5 hours.

REFERENCES

1. Lippmann, M., "Section G "Respirable" Dust Sampling", Sampling Instruments Fifth Edition, American Conference of Governmental Industrial Hygienists (1978).

2. Lippmann, M., "Size-Selective Sampling for inhalation Hazard Evaluations", in Fine Particles: Aerosol Generation, Measurement, Sampling, and Analysis (B. Y. H. Liu, ed.), pp. 287-310, Academic Press, New York (1976).

3. Wright, B. M. (1954) Br. Jr. Ind. Med. 11, 284

4. Tomb, T. F. and H. N. Treaftis, "A New Two-Stage Respirable Dust Sampler", Am. Ind. Hyg. Assoc. J. 36:1 (1975).

5. Marple, V. A., "Simulation of Respirable Penetration Characteristics by Interial Impaction", J. Aerosol Sci. 9:125-134 (1978).

6. Marple, V. A., "A Fundamental Study of Inertial Impactors", Ph.D. thesis, University of Minnesota, Mechanical Engineering Department, Minneapolis, Minnesota (19).

7. Rudin, E. (1981) "Interception Effects in the Collection Characteristics of Inertial Impactors" M.S. thesis, University of Minneosta, Particle Technology Laboratory Publication No. 458.

8. Reischl, G. P. and W. John "The Collection Efficiency of Impaction Surfaces: A New Impaction Surface", Staub Reinhalt Luff 38:55 (1978).

9. Berglund, R. N. and B. Y. H. Liu, "Generation of Monodisperse Aerosol Standards", Environ. Sci. Technol. 7:147-153 (Feb., 1973).

10. Marple, V. A., B. Y. H. Liu and K. L. Rubow, "A Dust Generator for Laboratory Use", Am. Ind. Hyg. Assoc. J. 39:26-32 (Jan., 1978).

11. Marple, V. A. and K. L. Rubow, "A Portable Optical Counter System for Measuring Dust Aerosols", Am. Ind. Hyg. Assoc. J. 39:210-218 (March, 1978).

Addendum

Designing a Classifier with Penetration Characteristics Which Approximate the ACGIH Respirable Penetration Criteria

The respirable penetration curves for the AEC and ACGIH criteria are identical except for particle sizes less than 2 μm aerodynamic diameter. For the AEC and the ACGIH criteria the penetration in this range is 100% and 90%, respectively.

Due to the particle collection principles of classification devices such as cyclones, horizontal elutriators and impractors, the penetration continually decreases from 100% to 0% as the particle size increases. Thus, they can be designed to approximate respirable penetration criteria which also decreases from 100% to 0% such as the AEC criteria but are difficult to design for criteria not having 100% penetration for small particles such as the ACGIH criteria.

However, one method which can be used to obtain a classifier with penetration characteristics approximating the ACGIH criteria is to first increase the penetration values of the ACGIH criteria by a factor of 1/0.9 defining the modified ACGIH curve shown in Figure 1A. The penetration values for the modified curve are tabulated in Table 1A.

A classifier can now be designed with respirable penetration characteristics of the modified ACGIH curve. The number of nozzles and nozzle sizes for personal sampler impactors with penetration characteristics of this criteria are tabulated in Table 2A. The mass of particles penetrating classifiers of this design will be 1/0.9 times greater than the mass of particles that would penetrate a classifier with penetration characteristics of the original ACGIH curve. Thus, the ACGIH respirable concentration will be simply 90% of the concentration determined by a classifier with penetration characteristics of the modified ACGIH curve.

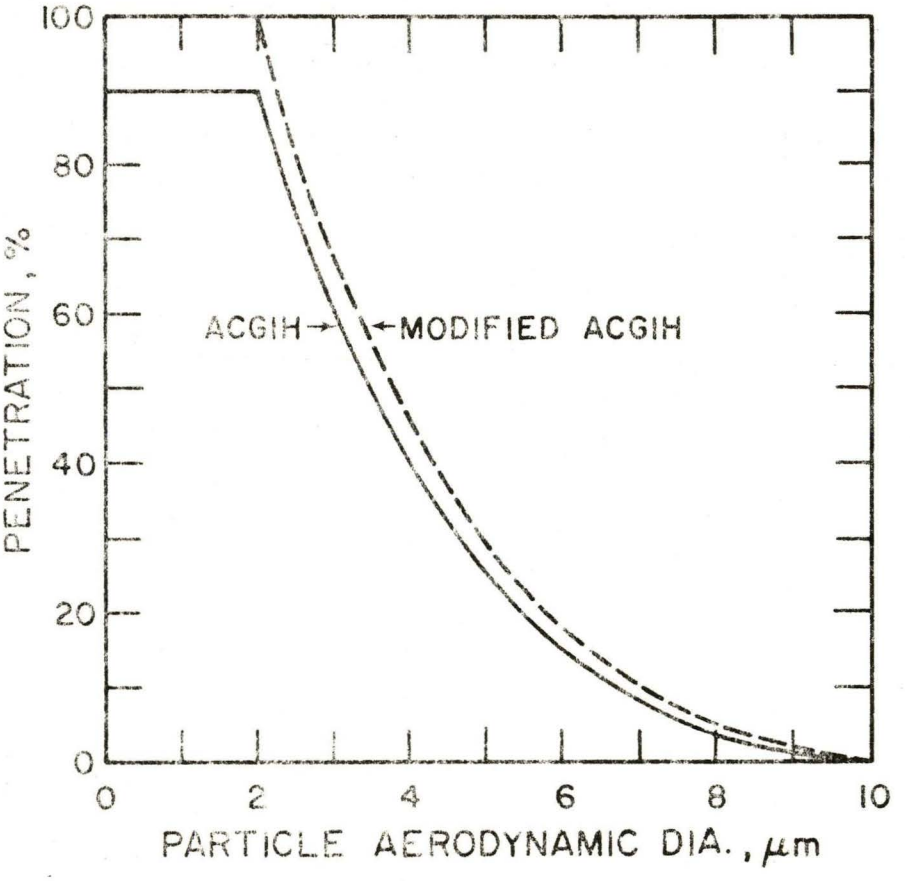

Figure 1A. ACGIH respirable penetration curve and modified ACGIH curve.

Table 1A

Impactor Designs With Penetration Characteristics at 2 l/min Flow Rates Which Simulate the Modified ACGIH Respirable Penetration Curve

		ROUND		RECTANGULAR	
Number of nozzle sizes	Impactor Cut-off Size μm	Nozzle Diam., cm	Number of Nozzles,	Nozzle Width, cm	Nozzle Length, cm
1	3.8	0.26	1	0.10	0.53
2	5.2	0.26	1	0.10	0.53
	2.8	0.068	15	0.026	2.1
3	5.9	0.24	1	0.097	0.47
	3.8	0.092	7	0.035	1.3
	2.5	0.036	44	0.013	3.4
4	6.5	0.23	1	0.093	0.45
	4.4	0.10	5	0.038	1.1
	3.3	0.051	20	0.020	2.0
	2.4	0.024	92	0.0091	4.6
5	6.8	0.22	1	0.086	0.44
	4.8	0.11	4	0.042	0.91
	3.8	0.060	13	0.023	1.6
	3.0	0.035	40	0.013	3.0
	2.3	0.019	134	0.0074	5.1

APPENDIX F

A UNIFORM DEPOSIT IMPACTOR

by

Virgil A. Marple
Benjamin Y. H. Liu
Gregory A. Kuhlmey

Particle Technology Laboratory
Mechanical Engineering Department
University of Minnesota
Minneapolis, Minnesota 55455

Introduction

Inertial impactors of various designs are widely used for collecting aerosol particles. The collected particles can be analyzed by a variety of techniques to determine such properties as the mass size distribution or the chemical composition of the particles.

In this paper, the design of a cascade impactor is described which has the unique feature that the particles can be collected uniformly over a large impaction area of any reasonable size. This is important for several reasons. First, the problem of particle bounce is reduced because there is no overloading of a single spot on the impaction plate. Secondly, more particles can be collected before overloading and blow-off occurs by spreading the deposit over nearly the entire area of a sticky surface impaction plate substrate as compared to the quantity of particles collected in localized deposits of a conventional impactor. Thus, the ratio of the substrate weight to the deposit weight can be minimized and the accuracy of gravimetric analysis maximized. Finally, by depositing the particles uniformly over a large area, the deposit can be analyzed for elemental chemical composition more easily by the technique of X-ray fluorescence, (Dzubay, 1978), which has special substrate and sample requirements.

Other features of this impactor include nozzle diameters of small sizes, so that the size distribution of submicron aerosols can be determined, and a design which allows all of the impaction plates to be on one assembly, increasing the ease with which the impaction plates can be changed, and reducing the possibility of damaging the deposited particles.

Although some of these features have been incorporated into previously described impactors, the present design integrates all of these features into a new cascade impactor design which takes advantage of recent advances in techniques of gravimetric and elemental analysis, as well as extends the range of the impactor to submicron aerosols and increases the ease of use of the cascade impactor. These various features of the impactor are described in greater detail in the following sections.

Uniform Deposit Impaction

The usual method for spreading out a deposit on an impaction plate is to move the impaction plate below the nozzle of a rectangular nozzle impactor, (May, 1956 and Lundgren, 1967). However, this has generally been a means of determining the time resolution of the aerosol rather than obtaining a uniform deposit. Round nozzle impactors have also been designed with moving impaction plates, (Carson, 1974), but this was not necessarily designed to obtain a uniform deposit on the impaction plate.

In the impactor described here, a uniform deposit on the impaction plate is obtained from multiple round nozzle impaction stages by locating the nozzles at predetermined radial distances from the centerline of the stage and rotating the impaction plate about the centerline. Several rotations of the impaction plate are necessary so that any fluctuations which would be present as a function of time will be masked by the multiple passing of the nozzles over the impaction plate.

The radial position of the holes are placed so that, for any annular area, the number of nozzles per unit area is constant. Thus, for any of the annular areas bounded by r_i and $r_i + 1$ shown in Figure 1,

$$\frac{\text{Number of nozzles}}{\pi(r_{i+1}^2 - r_i^2)} = \text{constant} \tag{1}$$

Equation (1) can be changed to a more useful form by letting the number of nozzles equal one. Thus, for each nozzle

$$r_{i+1}^2 - r_i^2 = \text{constant} \tag{2}$$

and the radius of the position of any nozzle, R_i, can be expressed as

$$R_i = r_i + \frac{1}{2}\Delta r_i \tag{3}$$

where

$$\Delta r_i = r_{i+1} - r_i \tag{4}$$

From Equation (2), it follows that

$$r_i = \sqrt{2\, r_{i-1}^2 - r_{i-2}^2} \tag{5}$$

since

$$r_i^2 - r_{i-1}^2 = r_{i-1}^2 - r_{i-2}^2$$

By combining Equations (3), (4), and (5), an expression for R_i can be found to be

$$R_i = \frac{1}{2}\left[r_i + \sqrt{2r_i^2 - r_{i-1}^2}\right] \tag{6}$$

From the above analysis, it can be seen that Equations (5) and (6) must be satisfied to obtain a uniform deposit on the rotating impaction plate. However, to start the calculations of the r and R values, some initial conditions must be assumed. Normally these assumed conditions are the values for r_1, r_2, and R_1. Now Equations (5) and (6) can be used to obtain all r_i and R_i values respectively. The selection of the values of r_1, r_2, and R_1 may have to be a trial and error process, if the number of holes, N, is fixed and the position of the nozzle farthest from the centerline, Rn is limited by the size of the impaction plate.

It should be noted that the radial separation between adjacent nozzles decreases as the radial position increases. Thus, by placing the nozzles sufficiently close together near the center of the stage, the deposits from adjacent nozzles will overlap, providing a uniform layer of particles over the entire impaction plate.

An example of a uniform deposit impactor is shown in Figure 2 for an impactor with 200 nozzles. A partial list of the nozzle positions is given in Table 1. It has been assumed that r_1 = .08000 cm, r_2 = .08886 cm, and R_1 = .08443 cm to start the calculations. These assumptions were necessary to limit R_{200} to less than 0.5523 cm, a requirement of this particular design.

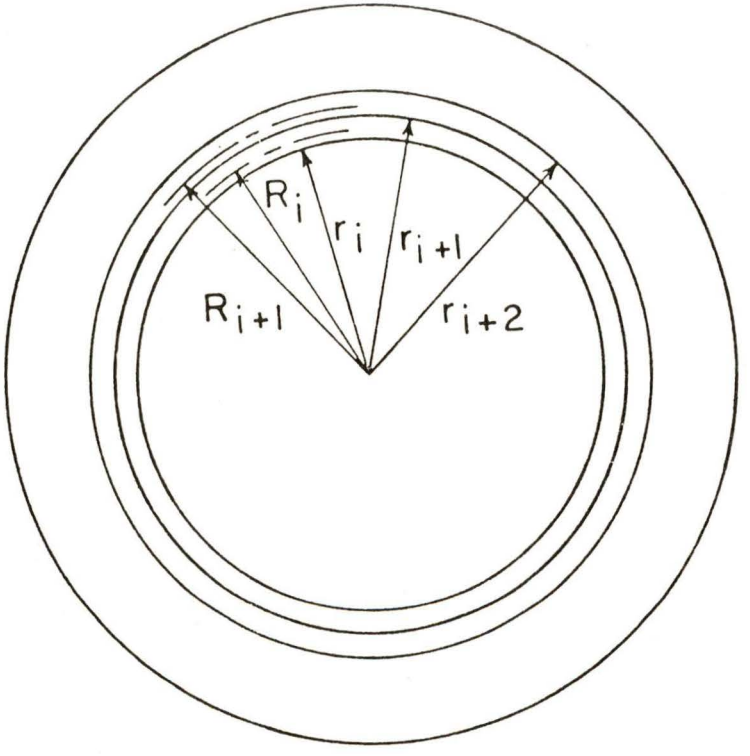

Figure 1. Annular rings of equal area.

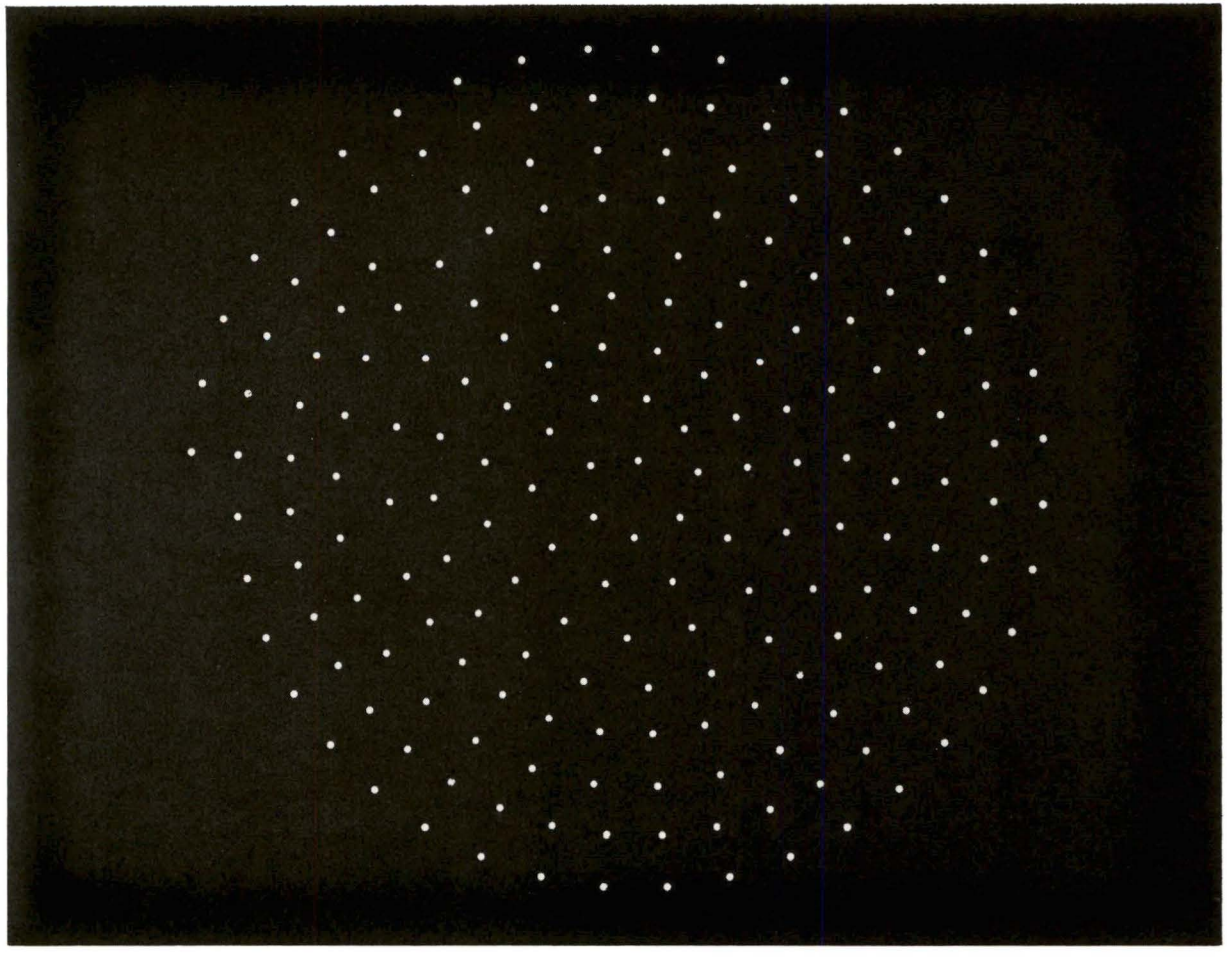

Figure 2. Photographs of a 200 hole uniform deposit impactor nozzle plate.

Table 1. Example of uniform deposit impactor nozzle placement (200 nozzles of 100 μm diameter)

Hole number	R, cm
1	.08443
2	.09289
3	.10064
⋮	⋮
99	.39218
100	.39408
101	.39598
⋮	⋮
198	.54951
199	.55087
200	.55223

Micro-Orifice Nozzles

The collection of particles in impactors is governed by the ratio of the particle stopping distance at the average fluid velocity in a nozzle to some characteristic length such as the nozzle radius. This ratio, commonly known as the Stokes number (Fuchs, 1964), St, is also the dimensionless parameter one defines by expressing the particle's equations of motion in dimensionless form. The equation for St is

$$St = \frac{4Q \rho_p C D_p^2}{9 \pi \mu W^3} \qquad (7)$$

where Q is the flow rate through a nozzle, ρ_p is the particle density, C is the Cunningham slip correction, D_p is the particle diameter, μ is the fluid viscosity, and W is the nozzle diameter.

By rearranging Equation (7), an expression which can be used to predict the size of the particles collected can be found as:

$$D_p = \sqrt{\frac{9 \pi \mu W^3}{4Q \rho_p C}} \sqrt{St} \qquad (8)$$

For round nozzles, particles with values of $\sqrt{St}$ larger than approximately 0.45 to 0.55 will be collected, while particles with smaller values will not (Marple and Liu, 1974). The exact value of $\sqrt{St}$ for collection will depend upon the particular nozzle design, the Reynolds number of the fluid flowing through the nozzle, and to a lesser extent upon the radial position of the particle as it passes through the nozzle, (Marple and Liu, 1975).

One method of collecting small particles is to operate the impactor at low pressures so that the particles can more easily slip through the air molecules and be collected. Thus, in Equation (8) as the pressure is decreased, the Cunningham slip correction will increase and D_p will decrease, in Equation (8).

Further inspection of Equation 8 indicates that another method of collecting small particles is to use nozzles of small diameters. It was this method which has been used in the impactor described here. For example, the 200 nozzle array described in Table 1 was designed for nozzle diameters of 100 µm, which will collect approximately 0.10 µm diameter aerosol particles at a flow rate of 10 lpm.

The construction of such an impactor would be difficult if the nozzles must be drilled in the conventional manner. However, the nozzles in the impactor nozzle plate shown in Figure 2 were machined in a 50 µm thick stainless steel plate by photochemical etching. With this technique, the nozzles are slightly conical, providing a tapered inlet to the nozzle. The nozzle diameters are controlled by the length of time the etching process is allowed to continue.

Impactor Design

A cascade impactor which incorporates the above features has been designed and is under development in our Laboratory. A sketch of the cascade impactor is shown in Figure 3. The flow passes through the impactor in a saw-tooth fashion so that the impactor nozzles of all stages are in one plane.

This horizontal design of the impactor simplifies the design of a mechanism for rotating the impaction plates. As shown in Figure 3, this is done by using a series of bevelled gears. We are currently investigating alternate methods of performing this function, such as worm gears, but the same basic layout is being preserved.

In addition, special consideration has been given in the design of the impactor to its ease of use and to minimizing the chance of damaging the deposits while changing the impaction plates between runs. As shown in Figure 3, the cascade impactor is comprised of three assemblies; nozzle, impaction plate and drive. Thus, between runs, all of the impaction plates can be changed by changing just one assembly, instead of changing each impaction plate one at a time, as is standard practice with conventional impactors. This impaction plate arrangement also reduces the chance of deposit damage, since the impaction plates themselves need not be handled from the time they are prepared in the laboratory to the time they are returned to the laboratory for analysis. A cover on the impaction plate assembly can be used to protect the plates during transport.

Summary

An inertial impactor has been designed with the specific purpose of providing a uniform deposit of particles over the entire impaction plate, which makes maximum use of the impaction plate and makes the particles available for X-ray fluorescent analysis. Since the technique to obtain uniform deposits employs the use of multiple nozzle impactor stages with the impaction plate rotating below the nozzles, the design could be extended to cover a wide range of uniform deposit diameters, being limited by the number of nozzles and flow rate chosen.

In addition, the impactor employs the features of very small diameter nozzles, so that sub-micron particles can be collected, and a design which allows the changing of all impaction plates by changing only one assembly. By changing the impaction plates in this manner, the risk of damaging the deposits from the time they are prepared in a laboratory to the time they are returned for analysis is kept at a minimum.

References

Carson, G. A., and H. J. Paulus, "A high volume cascade sieve impactor," AIHA Jour. 35:262-268 (May, 1974).

Dzubay, T. G. and D. G. Rickel, "X-ray Fluorescence Analysis of Filter-Collected Aerosol Particles," Electron Microscopy and X-ray

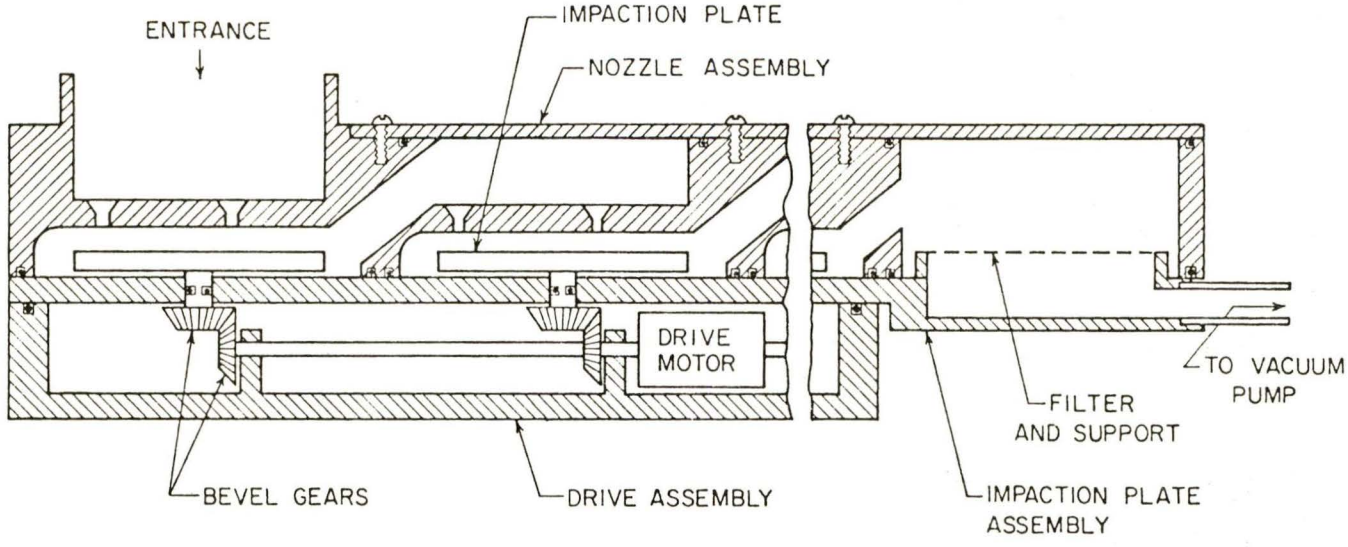

Figure 3. Design schematic of the uniform deposit impactor.

Applications edited by P. A. Russell and A. E. Hutchings, Ann Arbor Science 1978, pp.3-20.

Fuchs, N. A., The Mechanics of Aerosols, Pergamon Press, New York, (1964).

Lundgren, D. A., "An aerosol sampler for determination of particle concentration of size and time," J. Air Poll. Cont. Assoc. 17:225 (1967).

Marple, V. A., and B. Y. H. Liu, "Characteristics of laminar jet impactors," Environ. Sci. Technol. 8:648-654 (July, 1974).

Marple, V. A., and B. Y. H. Liu, "On fluid flow and aerosol impaction in inertial impactors," J. Colloid Interface Sci. 53:31-34 (1975).

May, K. R., "A cascade impactor with moving slides," A.M.A. Arch. Ind. Health 13:481 (1956).